# Optimization Under Uncertainty and Total Predictive Uncertainty for a Tractor-Trailer Base-Drag Reduction Device

Jacob A. Freeman

Dissertation submitted to the faculty of the Virginia Polytechnic Institute and State University in partial fulfillment of the requirements for the degree of

Doctor of Philosophy
in
Aerospace Engineering

Christopher J. Roy, Chair
Robert Canfield
Russell M. Cummings
William H. Mason

7 August 2012
Blacksburg, Virginia

Keywords: optimization under uncertainty, predictive uncertainty, aerodynamic shape optimization, drag reduction, verification & validation, evolutionary algorithm, uncertainty quantification

Optimization Under Uncertainty and Total Predictive Uncertainty
for a Tractor-Trailer Base-Drag Reduction Device

Jacob A. Freeman

# Abstract

One key outcome of this research is the design for a 3-D tractor-trailer base-drag reduction device that predicts a 41% reduction in wind-averaged drag coefficient at 57 mph (92 km/h) and that is relatively insensitive to uncertain wind speed and direction and uncertain deflection angles due to mounting accuracy and static aeroelastic loading; the best commercial device of non-optimized design achieves a 12% reduction at 65 mph. Another important outcome is the process by which the optimized design is obtained. That process includes verification and validation of the flow solver, a less complex but much broader 2-D pathfinder study, and the culminating 3-D aerodynamic shape optimization under uncertainty (OUU) study.

To gain confidence in the accuracy and precision of a computational fluid dynamics (CFD) flow solver and its Reynolds-averaged Navier-Stokes (RANS) turbulence models, it is necessary to conduct code verification, solution verification, and model validation. These activities are accomplished using two commercial CFD solvers, Cobalt and RavenCFD, with four turbulence models: Spalart-Allmaras (S-A), S-A with rotation and curvature, Menter shear-stress transport (SST), and Wilcox 1998 k-ω. Model performance is evaluated for three low subsonic 2-D applications: turbulent flat plate, planar jet, and NACA 0012 airfoil at $\alpha = 0°$.

The S-A turbulence model is selected for the 2-D OUU study. In the 2-D study, a tractor-trailer base flap model is developed that includes six design variables with generous constraints; 400 design candidates are evaluated. The design optimization loop includes the effect of uncertain wind speed and direction, and post processing addresses several other uncertain effects on drag prediction. The study compares the efficiency and accuracy of two optimization algorithms, evolutionary algorithm (EA) and dividing rectangles (DIRECT), twelve surrogate models, six sampling methods, and surrogate-based global optimization (SBGO) methods. The DAKOTA optimization and uncertainty quantification framework is used to interface the RANS flow solver, grid generator, and optimization algorithm. The EA is determined to be more efficient in obtaining a design with significantly reduced drag (as opposed to more efficient in finding the true drag minimum), and total predictive uncertainty is estimated as ±11%. While the SBGO methods are more efficient than a traditional optimization algorithm, they are computationally inefficient due to their serial nature, as implemented in DAKOTA.

Because the S-A model does well in 2-D but not in 3-D under these conditions, the SST turbulence model is selected for the 3-D OUU study that includes five design variables and evaluates a total of 130 design candidates. Again using the EA, the study propagates aleatory (wind speed and direction) and epistemic (perturbations in flap deflection angle) uncertainty within the optimization loop and post processes several other uncertain effects. For the best 3-D design, total predictive uncertainty is +15/-42%, due largely to using a relatively coarse (six million cell) grid. That is, the best design drag coefficient estimate is within 15 and 42% of the true value; however, its improvement relative to the no-flaps baseline is accurate within 3-9% uncertainty.

# Dedication

For her unwavering devotion to mission accomplishment, unflappable perseverance in bearing a sixth child during our sojourn, undaunted bravery in home-educating our flock of younglings, frequent selfless service to family and friends, and gentle encouragement, I gratefully dedicate this work to my companion and wife.

For the many, many times I went home or for a short walk with little clue how to proceed or what to do about a specific technical challenge or how to fix a pesky bug in my code or how in the world to push those thousands of computational solutions to completion, an infinitely knowledgeable and everlastingly gracious God in Heaven patiently provided inspiration and quietly opened the way. I gratefully and humbly present this small work at His feet.

For their love and trust and sweet smiles and innocence (mostly), I also dedicate this work to our six wonderful children.

# Acknowledgments

I gratefully acknowledge my advisor and committee chair, Chris Roy, for his patient mentorship, enabling leadership, technical depth, and steady academic standards. I thank the Department of Aeronautics, US Air Force Academy, for their financial sponsorship of this advanced degree and for their faith that the investment will prove worthwhile. For their encouragement and technical expertise, I acknowledge the committee members, Bill Mason, Russ Cummings, and Bob Canfield. For their close cooperation and prompt support, I thank the following: RavenCFD developer, Jimmy Carpenter of Corvid Technologies; Cobalt developers, Bob Tomaro and Bill Strang of Cobalt Solutions; DAKOTA developers, Brian Adams, William Bohnhoff, Keith Dalbey, John Eddy, and Laura Swiler; bestowers of millions of Air Force computing hours, Bobbi Ruf and Steve Senator; local technical support professional, Steve Edwards; Department of Transportation for granting access to some of their raw data, Ed Strocko, Jeff Short, and Rolf Schmitt; technical support at the Department of Defense (DoD) computing center, David Dumas and Duncan Schulze; and occasional technical assistance from fellow members of Dr Roy's research team. I also acknowledge the work of Chris Rumsey, his colleagues at NASA-Langley, as well as partners in industry and academia, for their efforts to develop and maintain the collaborative website, "Turbulence Modeling Resource," http://turbmodels.larc.nasa.gov.

This work was supported significantly by and could not have been completed without a generous grant of computer time and software usage from the DoD High Performance Computing Modernization Program at the US Army Engineer Research and Development Center, a DoD Supercomputing Resource Center in Vicksburg, Mississippi. Specifically, over the course of three years, I used 3,153,110 computing hours (2.7M in FY2012) granted by the DoD. Nearly all of those hours used the commercial Cobalt flow solver, translating to a significant monetary value.

And not least of all, I thank our good man Flori, from Albania, for his ready smile, encouraging word, and uncomplaining service to keep the floors shiny, restrooms clean, and waste receptacles ever ready for more.

# Table of Contents

# List of Figures

**Chapter 1**



**Chapter 2**



**Chapter 3**

**Chapter 4**

**Appendix**

# List of Tables

# Nomenclature

**Symbols**

| Letter | Description |
|---|---|
| $a$ | speed of sound |
| $C_D$ | body-axis drag coefficient, 3-D |
| $C_{D_{\delta+2^\circ}}$ | body-axis drag coefficient, with nominal flap deflection + 2°, 3-D |
| $C_{D_{\delta-2^\circ}}$ | body-axis drag coefficient, with nominal flap deflection - 2°, 3-D |
| $\bar{C}_D$ | wind-averaged body-axis drag coefficient, 3-D |
| $\bar{C}_{D_{\delta\pm2^\circ}}$ | wind-averaged body-axis drag coefficient, with flap deflection perturbations, 3-D |
| $C_d$ | body-axis drag coefficient, 2-D |
| $\bar{C}_d$ | wind-averaged body-axis drag coefficient, 2-D |
| $\bar{C}_{d,RE}$ | Richardson-extrapolated body-axis drag coefficient, 2-D |
| $C_f$ | skin friction coefficient |
| $c$ | chord length |
| $F_s$ | factor of safety |
| $F_x$ | axial force or body-axis force in axial direction |
| $H$ | height of tractor-trailer |
| $H_1$ | distance from trailer base centerline to flap attachment point |
| $h$ | grid refinement parameter |
| $h_i$ | grid level, *i*=1,2,3, etc.; fine to coarse |
| $I$ | turbulence intensity |
| $k$ | turbulent kinetic energy |
| $L$ | length of combined tractor and trailer (Chap 3, Chap 4) |
| $L$ | length of flat plate (Chap 2) |
| $L_1$ | axial length of trailer base flap |
| $M$ | Mach number |
| $P$ | Pressure |
| $\hat{p}$ | observed order of accuracy |
| $p_f$ | formal order of accuracy |
| $Re$ | Reynolds number |
| $r$ | grid refinement factor |
| $St$ | Strouhal number |
| $T$ | Temperature |
| $\Delta t$ | time step |
| $\Delta t^*$ | nondimensional time step |
| $U$ | Uncertainty |
| $u$ | velocity in *x*-direction |

| | |
|---|---|
| $u_{max}$ | planar jet centerline velocity |
| $V$ | speed or velocity magnitude |
| $V_y$ | speed of wind normal to tractor-trailer direction of motion |
| $W$ | width of tractor-trailer |
| $\Delta x$ | cell spacing in *x*-direction |
| $y^+$ | nondimensional cell spacing in surface-normal direction |
| $z$ | height above ground |
| $z_0$ | surface roughness length |

| **Greek Symbols** | |
|---|---|
| $\alpha$ | angle of attack |
| $\beta$ | sideslip angle |
| $\gamma$ | ratio of specific heats |
| $\delta$ | trailer base flap deflection angle |
| $\varepsilon$ | turbulence dissipation |
| $\bar{\varepsilon}_{DE,RE}$ | Richardson-extrapolated estimation of discretization error |
| $\theta_1$ | slope at flap leading edge, 2-D & 3-D studies |
| $\theta_2$ | slope at flap mid-chord, 2-D study |
| $\theta_2$ | slope at flap trailing edge, 3-D study |
| $\theta_3$ | slope at flap trailing edge, 2-D study |
| $\theta_{wind}$ | direction of wind |
| $\mu$ | dynamic viscosity |
| $\nu$ | kinematic viscosity |
| $\tilde{\nu}$ | Spalart-Allmaras viscosity |
| $\rho$ | density of air |
| $\sigma$ | standard deviation |
| $\tau_w$ | wall shear stress |
| $\psi$ | weighting function |
| $\omega$ | turbulent specific dissipation rate |

| **Subscripts** | |
|---|---|
| *0* | total or stagnation |
| *e* | Edge |
| *gauge* | gauge (static minus reference or freestream) |
| *ref* | Reference |
| *t* | turbulent eddy |
| $\infty$ | Freestream |

**Acronyms**

| Abbreviation | Description |
|---|---|
| ANN | artificial neural network |
| BB | Box-Behnken sampling |
| CCD | Box-Wilson central composite design sampling |
| CDF | cumulative distribution function |
| CFD | computational fluid dynamics |
| CFL | Courant-Friedrichs-Lewy number |
| CFL3D | NASA structured 3-D CFD solver |
| CHC | crossover hill climber genetic algorithm |
| COLINY | common optimization library interface |
| DAKOTA | design analysis kit for optimization and terascale applications (Sandia National Laboratories) |
| DE | discretization error |
| DES | detached eddy simulation turbulence model |
| DIRECT | dividing rectangles optimization algorithm |
| DoD | US Department of Defense |
| EA | evolutionary algorithm |
| EDF | empirical distribution function |
| FUN3D | NASA unstructured 3-D CFD solver |
| GA | genetic algorithm |
| GB | Gigabytes |
| GCM | generic conventional model, tractor-trailer |
| GFLOPS | gigaflops, floating point operations per second |
| GP | Gaussian process data fit |
| GTS | ground transportation system |
| HLLC | Harten-Lax-van Leer-Contact solver |
| LE | leading edge |
| LHS | Latin hypercube sampling |
| MARS | multivariate adaptive regression spline data fit |
| MOAT | Morris one-at-a-time sampling |
| NCSU | North Carolina State University |
| NOAA | National Oceanic and Atmospheric Administration |
| OAS | orthogonal array sampling |
| OUU | optimization under uncertainty |
| PSUADE | problem solving environment for uncertainty analysis and design exploration |
| QP | quadratic polynomial data fit |
| RAM | random access memory |
| RANS | Reynolds-averaged Navier-Stokes |

| | |
|---|---|
| RE | Richardson extrapolation |
| RSM | Reynolds stress turbulence model |
| S-A | Spalart-Allmaras turbulence model |
| SAE | Society of Automotive Engineers |
| SARC | Spalart-Allmaras turbulence model with corrections for rotation and curvature |
| SBGO | surrogate-based global optimization |
| SOGA | single objective function genetic algorithm |
| SST | Menter shear-stress transport turbulence model |
| SST-V | SST with modified vorticity source term |
| UQ | uncertainty quantification |
| USAF | United States Air Force |
| VTDIRECT | Virginia Tech DIRECT optimization algorithm |

# Attribution

Christopher J. Roy is co-author for the manuscripts of Chapters 2, 3, and 4. His contributions include strategic advice and review of the articles for technical accuracy, completeness, and grammatical correctness.

# Chapter 1: Introduction

## 1.1 Motivation

The Chief Scientist of the United States Air Force (USAF) in 2010 prioritized 19 research focus areas for the coming decade [1]. Priorities 1 and 2 mention the need to advance technologies that help reduce USAF operating and sustainment costs; priority 19 is more specific in suggesting the need to push technologies that enable fuel cost savings. In addition to USAF current and projected needs, commercial transportation companies and the US Department of Energy have for decades been working to reduce aerodynamic drag on tractor-trailers. More recently the commercial, government, and military sectors have revived and are re-focusing effort on reducing consumption of fossil fuels. For tractor-trailers, these drag-reduction efforts include devices such as a cab roof deflector, cab side extenders, skirt between cab and trailer, trailer front-end fairing, trailer front-end edge-rounding, trailer side skirts, wheel fairings, trailer underbody fairing, trailer vortex generators, slotted wheel flaps, wheel coverings, and the object of this study – trailer boat-tail or flaps extending from the trailer base [2, 3]. Several of these devices are illustrated in Fig. 1.

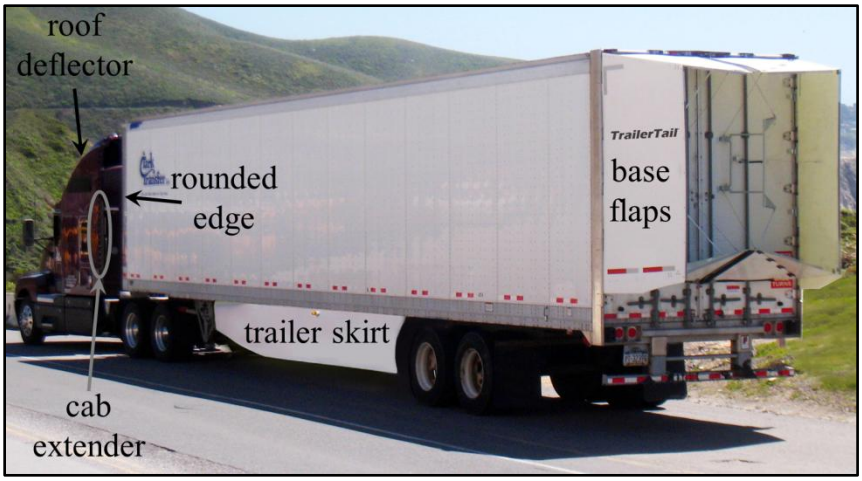


**Figure 1.** Example of straight trailer base flaps and other aerodynamic drag-reduction devices [4] (Used with permission of Steven Rodger, 2012, ATDynamics, www.ATDynamics.com)

At the base of a tractor-trailer, flow features include massive separation and turbulent shear flow that lower the static pressure and generate significant pressure drag because of the pressure differential between tractor front and trailer base. While base flaps add skin-friction drag and regions of adverse pressure gradient, more significantly they force the trailing wake to shrink and stabilize, resulting in a region with pressure a little larger than the freestream [2], which in turn creates less pressure drag. Figure 2 illustrates this with flow visualization from 3-D computational time-averaged solutions at highway speed 57.2 mph (92 km/h) and sideslip angle, $\beta$ = 9.1°, one of the angles used for wind averaging, where Fig. 2a shows velocity streamlines and gauge pressure ($P_{gauge} = P - P_{\infty}$, where $P_{\infty}$ is freestream pressure) contours for the trailer base without flaps, and Fig. 2b shows results for the trailer with base flaps. Addition of the base flaps visibly reduces the wake size and strength, as indicated by the smaller region of recirculating flow and higher static pressure.

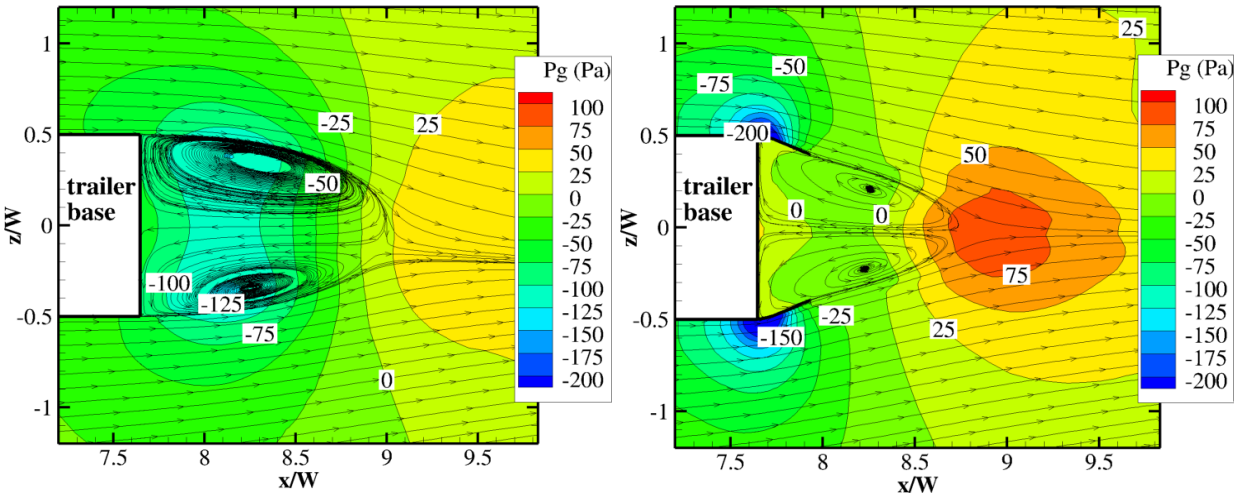


(a) Baseline, no flaps, $C_D$ = 0.3287. (b) Side flaps deflected inward 20°, $C_D$ = 0.2005.

**Figure 2.** Time-averaged 3-D computational solutions of simplified tractor-trailer with and without base flaps, showing reduced region of low pressure and stabilized base flow. Horizontal slice at $y/W$ = 0.695 for $\beta$ = 9.1° (one of angles used for wind averaging) showing velocity streamlines atop contours of gauge pressure. Highway speed, $V_\infty$ = 57.2 mph (92.1 km/h), and trailer-width-based Reynolds number, $Re_W$ = 4.4 x $10^6$.

To put this in perspective, consider the impact of a drag-reduction device implemented by numerous commercial trucking fleets. In 2010, tractor-trailers on US interstates averaged 5.9 miles per gallon and traveled 85 billion miles [5]; this equates to 14.4 billion gallons of diesel per year. If 1/3 of tractor-trailers traveling on US interstates install a base drag-reduction device that cuts drag by 20%, for about 10% reduction in fuel consumption, and based on the average cost of diesel in the US in 2011 ($3.84/gallon) [6], the trucking industry would conserve $1.8 billion and 480 million gallons of diesel fuel annually. While there is not a large fleet of trucks in the USAF, a *process* by which we may rigorously optimize aerodynamic shapes to minimize drag may be readily extended to aircraft and other air weapons systems.

Numerous computational and experimental studies have been conducted to quantify the drag reduction associated with base flaps (refer to Introductions for Chapters 3 and 4), but as demonstrated in Fig. 1, these flaps are generally straight. Straight flaps may not provide an optimal reduction in aerodynamic drag; thus, this study includes flap curvature in the design space and seeks to optimize shape, orientation and position of these base flaps to provide minimum aerodynamic drag for the tractor-trailer. Further, because some of the model input variables are uncertain, whether aleatory (inherent randomness) or epistemic (due to a lack of knowledge) in form [7], this study includes and quantifies several sources of uncertainty within the design optimization loop.

### 1.2 Literature Review

We sub-divide the overall research into the following components: verification and validation of turbulence models and verification of models in commercial flow solvers; aerodynamic shape optimization, specifically tractor-trailer base flaps; total predictive uncertainty; optimization under uncertainty; optimization algorithms; and surrogate-based global optimization. Details of the various turbulence models are available in later chapters.

### 1.2.1 Verification and Validation of Turbulence Models in Commercial Flow Solvers

For code and solution verification, we employ the methods of Oberkampf and Roy [7]. To conduct code verification, the preference is to verify a code's formal order of accuracy by computing the solution to a problem with an exact solution. We may use the exact analytical solution or an exact manufactured solution to accomplish this code verification. Veluri et al. [8] completed a detailed code verification study using an exact manufactured solution for a 3-D unstructured finite-volume computational fluid dynamics (CFD) code with Reynolds-averaged Navier-Stokes (RANS) two-equation turbulence models; they cite numerous studies using manufactured solutions for 2-D inviscid, laminar and turbulent cases. However, without access to source code, in the case of commercial flow solvers evaluated in this dissertation, namely Cobalt [9, 10] by Cobalt Solutions, LLC, and RavenCFD [11, 12] by Corvid Technologies, the user may conduct a lesser degree of code verification by carefully comparing results with those from a flow solver that has been rigorously verified for a RANS turbulence model, such as the NASA-Langley unstructured (FUN3D) and structured (CFL3D) finite-volume CFD codes that are verified 2$^{nd}$-order accurate for the Spalart-Allmaras (S-A) one-equation turbulence model [13, 14]. To conduct solution verification, users may then compute solutions with the verified code for various applications and estimate the numerical error in those solutions [7].

In model validation, we assess how accurately the model represents the physical flow by comparing the computed solution with experimentally obtained data. Since this study utilizes simplified 2-D and 3-D tractor-trailer geometries, based on the 1/8$^{th}$ scale Ground Transportation System (GTS) model developed by Sandia National Laboratories [15], we conduct validation based on studies that utilize RANS and detached-eddy simulation (DES) turbulence models, for both time-averaged and time-accurate flow solutions, for highway Reynolds number based on trailer width, $Re_W$ = 5.2x10$^6$ for the 2-D study and $Re_W$ = 4.4x10$^6$ for the 3-D study. The Generic Conventional Model (GCM), which is also 1/8$^{th}$ scale, is somewhat more detailed than the GTS, as it includes the gap between cab and trailer, more cab form and detail, and rounded wheels (vs. the GTS cylindrical posts in place of wheels) [16]. Table 1 compares results for body-axis drag coefficient, $C_D$, from several computational studies with wind-tunnel test data using 3-D GTS, GCM or similar geometry, all without base flaps. These results indicate poor performance by the RANS S-A turbulence model in 3-D, while other steady RANS turbulence models perform with an acceptable degree of accuracy (see noted references for details of these turbulence models), not greater than 12% difference from experiment. The RANS Reynolds stress model appears to be most accurate for sideslip angle, $\beta$ = 0°, but its five (for 2-D) to seven (for 3-D) transport equations, compared with one or two for the other RANS turbulence models, makes it less computationally efficient. We also include some time-accurate, detached-eddy simulation (DES) comparisons to show that steady RANS models (except S-A for 3-D) perform as well as or better than a time-accurate model for this case and under these conditions, and we note that while the time-accurate DES more accurately models the unsteady flow structures, it requires 2-9 times (depending on required time-step size) the number of iterations or time steps for a converged solution. Spalart and Rumsey [17] and Freeman and Roy [18] show the RANS S-A turbulence model *in 2-D* agrees well with experiment and performs suitably well (computes relatively fast and stably) under similar flow conditions, thus we select the S-A turbulence model for the 2-D study and Menter shear-stress transport (SST) for the 3-D study.

**Table 1.** Computational predictions vs. experiment for 3-D simplified tractor-trailer at varied sideslip angles[a]

| Turbulence Model, 3-D Cases | $C_D$ Difference from Experiment (%) | | | |
|---|---|---|---|---|
| | $\beta$ = 0° | $\beta$ = 1-2° | $\beta$ = 4-8° | $\beta$ = 10° |
| **RANS S-A** [19, 20, 21] | 22 - 65 | | | 58 |
| **RANS k-ω** [19, 21] | 4.4 - 8 | | | |
| **RANS k-ε** [21, 22, 23][b] | 2.3 - 10 | 0.5 - 1.0 | 10 - 12 | 9 |
| **RANS Reynolds Stress** [22] | 0.6 | | | |
| **RANS SST** [23][b] | 0.8 - 2.6 | 0.5 - 1.0 | 10 - 12 | 9 |
| **DES, unsteady** [20, 24, 25] | 2 - 12 | | | 12 - 39 |

[a] Random winds can result in different flow angles seen by the tractor-trailer, and these uncertainties are propagated from input to output by considering different sideslip angles (see Section 2.6 of Chapter 3 for additional information).

[b] Pointer et al. [23] do not specify which turbulence model is used for results at $\beta \neq 0°$.

All of the cases noted above evaluate tractor-trailer models (or similar) with no drag-reduction devices or other geometrically complicating elements. Pankajakshan et al. [26] add complexity to the GCM computational model by including symmetric 3-D trailer base flaps (straight; axial length, $L_1 = 0.25W$, where $W$ is trailer width; and deflected inward, $\delta = 15°$), cab extenders, and rear axle with smooth wheels (rotating or fixed) in contact with a moving ground plane (both wheels and ground have a slip boundary condition). They also include a 7-mph cross-wind at $\beta$ = 15, 45, 75, 105, 135 and 165°, wind-average (refer to Section 2.6 of Chapter 3) the drag coefficient ($\bar{C}_D$), and model turbulence using the time-accurate DES with Menter one-equation Scale-Adapted Simulation. Unsurprisingly, these additional sources of complexity and time-accurate simulations add considerably to the computational expense; compared with using simplified 3-D geometry, time-averaging, a two-equation RANS turbulence model, and roughly equivalent computing hardware, each solution by Pankajakshan et al. [26] requires nearly 20 times the number of computing core-hours. Pankajakshan et al. [26] estimate a 5.4% increase in $\bar{C}_D$ for fixed vs. rotating rear wheels. With the addition of base flaps, rotating wheels/axle and at $\beta$ = 0°, their computational results differ only 1.2% from experiment, and 3.4-6.3% from road tests. The base flaps give a relatively constant improvement in drag performance for the range of sideslip angles, though improvement is greatest for $\beta$ = 0°. Pankajakshan et al. [26] make no comparison between fixed and rotating rear wheels for the case with base flaps. The experimental study of Ortega and Salari [27] shows a 38% reduction in $\bar{C}_D$ for a simplified tractor-trailer model without wheels, and similar wind-tunnel tests of Gutierrez et al. [28] show 29% reduction for the configuration without wheels. For both of these cases (Ortega and Salari [27] and Gutierrez et al. [28]), the magnitude of $\bar{C}_D$ vs. $\beta$ differs, but the shape is approximately the same for configurations with and without wheels (sting-mounted). Thus, if we desire to accurately predict values for tractor-trailer drag coefficient, our model should include rotating wheels and wind-averaging, but if we desire to predict relative differences in drag coefficient, a simplified model without wheels is adequate.

A concluding note for validation: because the geometry for the computational simulations is simplified and includes forebody rounding, we expect a geometrically complex, full-scale tractor-trailer to experience roughly half that amount of drag reduction; this observation is based on comparing wind-tunnel experiments with nearly identical base flaps for 1/8-scale simplified geometry, which showed 19% reduction in $\bar{C}_D$ [15], and for an actual full-scale tractor-trailer, which showed 10% reduction in $\bar{C}_D$ [29].

### 1.2.2 Aerodynamic Shape Optimization

Many studies have been conducted to optimize aerodynamic shapes, but we focus on minimizing drag (specifically base pressure drag) for tractor-trailers or similar bodies. Doyle et al. [30] optimize a curved (cubic polynomial) tractor-trailer base flap using five design variables and a genetic algorithm for a 2-D symmetric half-truck computational domain, and they compute a total of 200 design points. Their CFD computations are steady and use the two-equation Menter SST k-ω RANS turbulence model. They conduct a mild grid sensitivity study, involving only two grid levels that are not systematically refined and that maintain the same first-cell spacing. The optimized design of Doyle et al. [30] results in a 59% reduction in predicted 2-D drag coefficient (and they estimate 29% reduction for 3-D), compared against the baseline configuration with no flaps. The best design full-scale flap has $L_1 = 0.36W$ and $\delta = 15°$.

Using add-on humps optimized from their earlier study, Hsu and Davis [31] optimize fixed-curvature base flaps using two design variables ($L_1$ and $\delta$) for a four-flap configuration on a 3-D modified Ahmed body, shown in Fig. 3. While the Ahmed body is similar in form to a simplified tractor-trailer, it likely would not be utilized in commercial transportation because of its departure from a rectangular parallelepiped that is easily transported, stacked and stored. Hsu and Davis [31] time-average results from a combined unsteady RANS k-ε and DES turbulence model using a relatively coarse mesh (2.55 million cells following grid and time-step sensitivity studies) and for 12 design points. Their best design, with equivalent full-scale $L_1 = 0.20W$ and $\delta = 9°$, results in 51% reduction in predicted 3-D body-axis drag coefficient, $C_D$. Neither Doyle et al. [30] nor Hsu and Davis [31] consider the effect of cross-flow in their optimization studies, meaning their designs are not optimized to include uncertainty in wind speed and direction. We note that 3-D computational and experimental designs generally produce less drag reduction than 2-D designs because of pressure relief around 3-D bodies.

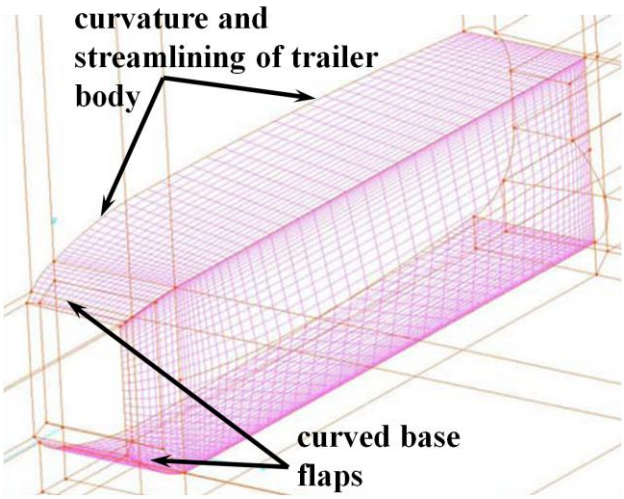


**Figure 3.** Optimized Ahmed-body-based design of Hsu and Davis [31] with curved trailer base flaps (Used with permission of Roger Davis, 2012)

While the following optimization studies are experimental, they provide insight for computational investigation. Cooper [2] summarizes findings from full- and reduced-scale wind-tunnel tests and some road tests for various drag-reduction devices on tractor-trailers, and he emphasizes the value of including wind-averaging in examining the devices' effect on drag, since a great deal of drag results from cross-winds passing under the trailer and between cab and trailer. Using a full-scale truck at highway speed of 65 mph, wind-tunnel testing of Cooper [2, 32] shows 6-8% reduction in $\bar{C}_D$ for straight flaps with $0.19W \leq L_1 \leq 0.25W$ and $10 \leq \delta \leq 18°$. The addition of the bottom flap gives only a slight improvement in $\bar{C}_D$ reduction. The addition of a cab-trailer gap seal and trailer side skirts increases $\bar{C}_D$ reduction to 25% [2]. He presents no results for deflections of the bottom flap. Leuschen and Cooper [3] conduct full-scale wind-tunnel tests of several drag-reduction devices for tractor-trailers, including base flaps on trailer top and sides. They perform some optimization of device combinations, rather than optimizing device shapes or placement. Leuschen and Cooper [3] do not reveal dimensions for the commercial flaps, but from the image provided, they appear to be $0.23W \leq L_1 \leq 0.35W$ and $15 \leq \delta \leq 20°$. If we assume the same baseline value for $\bar{C}_D$ as for Cooper [2], the base flaps give a drag reduction of 7%. Using the Society of Automotive Engineers (SAE) road-test procedures for heavy trucks [33], with base flaps of $L_1 = 0.47W$ and $\delta = 15°$, a commercial company claims 12% reduction in $\bar{C}_D$ at 65 mph [4, 34]. Browand et al. [35] road testing shows 8% reduction in $\bar{C}_D$ (compared with the baseline from Cooper [2]) for straight flaps of $L_1 = 0.24W$ and best $\delta = 13°$. Hsu et al. [36] wind tunnel testing, with a streamlined geometry and at 1/12 full-scale Reynolds number, shows 30% reduction in $C_D$ at zero sideslip (assuming baseline $C_D = 0.25$) for straight flaps of $L_1 = 0.27W$ and $0.53W$ and $9 \leq \delta \leq 12°$. Ortega and Salari [27] wind tunnel testing, with streamlined geometry and non-rotating wheels, shows 16% reduction in $\bar{C}_D$ for straight flaps of $L_1 = 0.35W$, $\delta_{side\ flaps} = 10°$, $\delta_{top\ flap} = 11°$, and $\delta_{bottom\ flap} = 0°$. Ortega and Salari [27] further show 19% reduction in $\bar{C}_D$ for flaps with constant-radius curvature of $0.91W$ and $L_1 = 0.30W$.

Numerous results confirm the observation that drag reduction from add-on devices and aerodynamic shaping is greater for geometries with front-edge rounding [27, 31, 32, 36]. All of

these studies test a relatively small number of design configurations, and most of them include wind-averaging to account for variability in wind speed and direction. Cooper [32] shows that straight deflected flaps are slightly better than curved flaps, while Ortega and Salari [27] show that a curved flap is best. Most of these studies show that $L_1 = 0.25W$ is best, but ATDynamics [4] and Hsu et al. [36] show good results for $L_1 \approx 0.5W$. We observe there is considerable variation among researchers regarding the optimal shape (curved or straight), length (0.19-0.53$W$), and deflection of the base flaps ($0 \leq \delta \leq 20°$ and whether all flaps should be deflected the same amount). Thus, we conduct a computational optimization study to minimize drag due to the addition of trailer base flaps that may have relatively wide ranges of curvature, length, and deflection angles.

### 1.2.3 Total Predictive Uncertainty and Optimization Under Uncertainty

Oberkampf and Roy [7] and Roy and Oberkampf [37] define the uncertainty framework as identifying and characterizing sources of uncertainty, estimating uncertainty due to numerical approximations, propagating input uncertainty through the model, and estimating model form uncertainty (difference between experiment and computation). These three elements – numerical approximation uncertainty, model input uncertainty, and model form uncertainty – comprise total predictive uncertainty. Roy and Oberkampf [37] and Roy and Balch [38] apply this framework to relatively simple and computationally inexpensive examples for a quasi 1-D hypersonic converging-diverging nozzle and a quasi 1-D supersonic nozzle, respectively. Larger-scale, but less robust examples include the following: Roy et al. (GTS truck model) [19] and Veluri et al. (truncated GTS) [21] estimate uncertainty due to numerical approximation and model form but do not propagate uncertainty; and Pankajakshan et al. (modified GCM) [26] propagate uncertainty via wind-averaging but include no explicit uncertainty estimation. Robust but simple and smaller-scale examples include the Model Validation Challenge Workshop, as reported by Hills et al. [39]. For this workshop, intending to help develop a standardized approach to model validation, 18 individuals or teams provide a vast array of solutions to three uncertain, albeit simple engineering problems: 1-D linear heat conduction, a statically determined four-beam structure, and a three degree-of-freedom substructure known only by measured behavior under known conditions. Employed methods include surrogate modeling, Bayesian calibration, multivariate approaches, model calibration under uncertainty, and probabilistic analyses. Thus, the engineering community lacks rigorous treatment of predictive uncertainty for a large-scale, complex application.

The next logical step is to incorporate the uncertainty framework and predictive uncertainty estimation into the design optimization process. Yao et al. [40] provide an excellent review, including 366 references, of current thought and state-of-the-practice for optimization under uncertainty (OUU). They explain for problems like those of this dissertation, which have nonlinear, non-convex form, uncertain inputs, and computationally expensive flow solutions, that attention must be paid to selection of an appropriate optimization algorithm and to the "organizational procedures" for dealing with the varied forms and "cross propagation" of uncertainties. The organizational procedures refer, in part, to the practice of using a nested double-loop, where the inner loop involves uncertainty propagation and the outer loop is the optimization algorithm. In our case, the inner-loop uncertainty propagation also includes two loops, an outer loop for epistemic uncertainty and an inner loop for aleatory uncertainty. Yao et al. [40] note three essential parts in representing uncertainties: (1) identify all uncertainties; (2) select mathematical models to represent those uncertainties; and (3) filter the uncertainties via

sensitivity analysis and/or sampling to reduce the scope of uncertainty. For problems that require a gradient-free approach, they suggest that genetic algorithms (GA) and evolutionary algorithms are promising because of their strengths in global optimization, treatment of multiple objective functions, and distributed or concurrent architecture for parallel computing; however, GA convergence efficiency is not ideal and needs additional evaluation. Yao et al. [40] recommend exploring approximate or surrogate models in lieu of or in concert with high-fidelity simulations, thereby conserving computational time and transforming a discrete model into a continuous form, upon which more efficient gradient-based methods may be operated.

Following are example studies using OUU. In the wind-tunnel experiment of Ortega and Salari [27], they conduct coarse optimization (few samples) of straight or curved base flaps for a simplified tractor-trailer with wheels and include uncertainty propagation via wind-averaging for every design configuration. While the numerical optimization studies of Zhang et al. [41] and Han and Hosder [42] involve relatively simple case studies (optimization of a 2-D airfoil and synthetic jet actuators, respectively) with few design variables, they propagate both aleatory and epistemic uncertainty and create surrogate models using stochastic expansion and polynomial chaos that is mathematically complex but more computationally efficient than a sampling-based approach, such as Monte Carlo sampling. However, they do not employ the nested double-loop noted above, since they conduct a simple, gradient-based search of the surrogate model to locate the minimum. Li et al. [43] conduct a 2-D airfoil OUU study with 20 design variables and using a low-fidelity Euler flow solver with uncertain Mach number range; they use a trust-region, gradient-based profile optimization method with a simple double-loop (propagation of uncertain Mach number for inner loop and optimization outer loop). Gumbert et al. [44] follow the recommendation to use a lower-fidelity model for their multidisciplinary OUU study with transonic flow over a 3-D flexible wing with uncertain geometric parameters (two and four design variables). They use an extremely coarse computational mesh, a coupled Euler CFD flow solver and finite element structural code, a gradient-based optimization algorithm, and statistical propagation of the uncertain inputs. Gumbert et al. [44] reference other aerodynamic OUU studies involving simple geometry (airfoils and plates). Schillings et al. [45] use a finer mesh (nearly 6 million cells) for a 3-D wing in transonic flow, where the design variables include more than 100,000 surface nodes; they use polynomial chaos to treat the aleatory uncertainty and reduce the sampling population from 343 to 21, showing a result that is slightly improved over the result from the larger population. They do not address epistemic uncertainty, and they use an Euler flow solver and gradient-based optimization algorithm. Lacking are studies that combine OUU with both aleatory and epistemic uncertainty, relatively complex 3-D geometry and flow physics, and total predictive uncertainty.

### 1.2.4 Optimization Algorithms

Due to the expected discontinuities among the solutions, we initially assume this problem is non-convex and cannot guarantee a unique solution; we confirm this assumption from our 2-D study shown in Chapter 3, Section 4.1. Further, we seek the design with global minimum $\bar{C}_D$ if possible, though the reality of a limited number of function evaluations suggests we may determine a *good* design that is better than existing solutions and that is not necessarily the *best* design. Because we seek an efficient optimization method that can be applied to the more complex, more computationally expensive 3-D version of this problem, we consider more than one design optimization method. Linearized methods do not apply due to discontinuous input/output relationships (associated with discontinuous flow separation effects on drag), partial

differential equations, and a complex flow field with large gradients. Gradient-based methods are less effective because of discrete design selection, where prediction of boundary-layer separation on the base flap will rule out a design, and since the mesh must be regenerated with each design. Branch-and-bound methods are less effective because the design space is continuous. And since the viscous solutions are computationally expensive, we can only afford to run tens or hundreds of design points, not thousands. Hence, we investigate an evolutionary or genetic algorithm and DIviding RECTangles (DIRECT) – both are nonlinear, non-gradient-based, conveniently coded within DAKOTA, and have shown promising results even with a small population of samples [40]. Refer to Arora [46] for a more detailed discussion of the optimization methods mentioned above.

*Genetic Algorithms (GA).* While not necessarily a perfect fit because they may require a large number of solutions and do not guarantee finding the global minimum, genetic algorithms apply to both discrete and continuous problems, *may* find the global minimum, and tend to find a "good" design [40, 47, 48]. GAs are based on Darwin's theory of "survival of the fittest," in that the most fit candidates – in this case, those with the smallest $\bar{C}_D$ – survive from one generation to the next and remain in the mating pool, while the others are eliminated. However, the algorithm allows candidates with lower fitness to be selected as well, although with lower probability, since they may contain a trait or traits that may prove useful when crossed with another candidate. The algorithm starts with a randomly generated population of candidates drawn from the design space, evaluates the fitness of each candidate then creates a new population by selecting two parent candidates, crossing them to form new offspring or making an exact copy of the parent, allowing for mutations in the offspring, and placing the offspring in the new population for the next fitness evaluation. The success of this algorithm depends on the size of the initial population and the number of generations computed [46]. Some GA options include the single-objective function genetic algorithm (SOGA) [48] and the common optimization library interface evolutionary algorithm (COLINY-EA) [47]. The COLINY-EA designs may converge more efficiently to the optimum design because of its "self-adaptive mutation, which modifies the mutation scale dynamically" [47], as well as its ability to select design points that cover much of the design space. As part of the COLINY-EA, DAKOTA recommends the crossover hill-climber (CHC) genetic algorithm [47, 49], for engineering applications, rather than the elitist algorithm that sometimes biases the parent pool with the best candidates at the expense of discovering a favorable trait that may be found in a "less desirable" candidate. COLINY-EA allows a mix of continuous and discrete design variables, whereas SOGA requires continuous design variables.

Janiga [50] uses an EA with computational fluid dynamics (CFD) for three relatively complex examples: 2-D heat exchanger, 2-D laminar burner, and 2-D turbulence modeling. For the examples, he completes 800, 280, and 10,000 design point evaluations, respectively, based on 2-8 design variables and 2-4 objective functions. All computational grids are coarse but the flow solutions are relatively expensive because of coupled equations. Janiga [50] includes no consideration of uncertainty in his optimizations; in none of the cases does the EA find a global minimum, but it does determine a good or acceptable design in each of the cases. Dumas [51] also uses an EA with CFD, but he shows a more efficient approach by coupling the EA with a local search using a "deterministic descent method." For the CFD he specifies for the turbulence modeling the seven-equation Reynolds stress model with a wall function and obtains a converged solution within 14 core-hours, which is 40% more computationally expensive than using a two-equation RANS turbulence model. The application is a 3-D automotive shape with a mesh of six million cells. Dumas [51] shows the EA alone finds an acceptable design after 160

design points and the EA coupled with local search finds the same design after 60 design points. He does not consider uncertainty in the optimizations.

*DIviding RECTangles (DIRECT) Algorithms.* Gablonsky's version of DIRECT implemented at North Carolina State University (NCSU-DIRECT) [52] combines local search in regions of the design space that indicate good fitness levels with global search in unexplored areas to increase likelihood that the global minimum is found. The algorithm begins at the design space center of a normalized hyper-cube, subdivides, and evaluates the objective function at those points. Figure 4 illustrates this process and shows two of the six design variables for the 2-D study. The starting point is illustrated by the center point in Fig. 4, for $L_1$ = 0.75 m and $\theta_1$ = 15°. Regions with better fitness levels are further subdivided in hyper-rectangles and evaluated until the optimum is found. The results in Fig. 4 represent 157 design points or 28 iterations of NCSU-DIRECT; several points in the figure are coincident because these variables are held constant while the effect of variation in the other design variables are evaluated. Our 2-D studies [53] show that NCSU-DIRECT does not determine the same design obtained by COLINY-EA but comes within 5-12% of $\bar{C}_d$. However, its algorithm required 12% fewer design candidates to arrive at this slightly inferior solution. An additional limitation of NCSU-DIRECT is that maximum sample size may not exceed twice the number of design variables, whereas for COLINY-EA we may specify the sample size according to our method of concurrent solutions. Because of this limitation, a future study may consider implementing the VTDIRECT algorithm of He et al. [54] that is designed to evaluate significantly more concurrent design points using the DIRECT method.

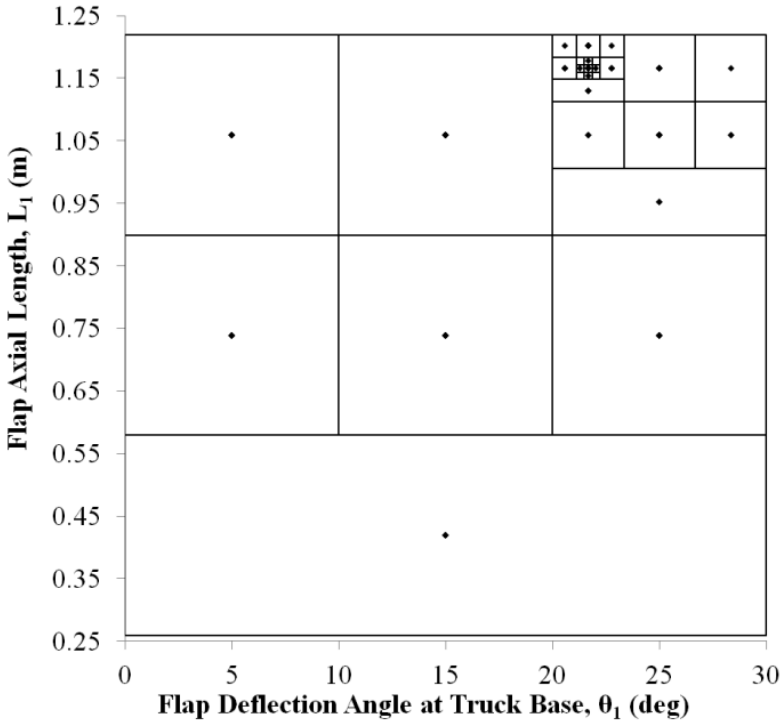


**Figure 4.** Illustration of DIviding RECTangles (DIRECT) algorithm, showing two of six design variables for the 2-D optimization study, representing 28 iterations of the DIRECT algorithm or 140 design points

### 1.2.5 Surrogate-Based Global Optimization

Surrogate-based global optimization (SBGO) combines the accuracy of the nonlinear, coupled, and possibly discontinuous computational flow solutions (or the truth model results) with the computational efficiency of searching a simpler, potentially smooth representation of the truth model output. To obtain the surrogate model, otherwise known as a data fit or a response surface approximation, we start with a dataset of solutions that is generated by the truth model; the design points may be determined by stochastic sampling, design of experiment, user-determined methods, or by some combination of these three approaches. Based on the nature of the dataset, if it is known, the user may select an appropriate data fitting scheme; since in our case the dataset is not smooth due to the discontinuous behavior associated with flow separation at larger flap deflection angles, we try numerous data fitting methods available in DAKOTA to determine which one provides the best data fit or surrogate model. The optimization algorithm of choice is then able to inexpensively query or evaluate the surrogate millions of times, if needed, to determine a minimum or set of minima. We next use the more expensive and more accurate truth model to evaluate this design point or points, update the surrogate model with those values, and repeat until the global or an acceptable minimum is located. [47, 55, 56]

For this portion of the study – assessing surrogate models, sampling methods, and SBGO methods – we significantly reduce computational expense by using a surrogate model in place of the truth model (viscous CFD simulations). For example, one sampling method may specify 100 design points. We query the surrogate model at those points and, in less than one second, receive 100 values for $\bar{C}_d$. Those returned values are used to generate the various surrogate models, or secondary surrogates. We may then evaluate the secondary surrogates by comparing them with the initial surrogate model, and we may use the secondary surrogates as the starting point for the various SBGO methods.

*Data-Fitting Algorithms*. We compare surrogate models generated by 12 DAKOTA data fitting algorithms, namely, polynomial regression models (linear, quadratic, and cubic) [57], Gaussian process fits (constant, linear, and reduced-quadratic) [58], kriging spatial interpolation (constant, linear, and quadratic), artificial neural network [59], and multivariate adaptive regression spline or MARS (linear and cubic) [60]; we do not evaluate the moving least squares method because the DAKOTA team notes it does not yet work well for global optimization [47].

Since it is not our purpose to conduct a comprehensive assessment of each fitting method, we briefly discuss only the two data fitting algorithms that yield the best fits for our specific datasets. The most accurate fits for our data come from DAKOTA's implementation of Gaussian process (GP) and kriging interpolation. Both GP and kriging algorithms are interpolation based and are designed to handle surfaces that are multimodal, discontinuous, and noisy – such as we expect in this study. Both algorithms assume a multivariate normal distribution in the dataset, and we specify DAKOTA's zeroth-order additive correction that forces the surrogate model to match the truth data points. The kriging method uses the maximum likelihood estimation procedure [61] that is effective for fitting data with slope discontinuities and multiple minima/maxima. [47, 58]

*Sampling Methods*. For a complex engineering problem, the quality of the surrogate model is a direct function of the dataset upon which it is based. Therefore, we must find an acceptable balance between a large, more representative dataset and one that is smaller, less computationally expensive, and sufficiently accurate. With this balance in mind, we evaluate the following sampling methods that are available in DAKOTA: Latin hypercube sampling (LHS); orthogonal array sampling (OAS); combined OAS and LHS (OA-LHS); Box-Wilson central

composite design (CCD); Box-Behnken design (BB); and problem solving environment for uncertainty analysis and design exploration with Morris one-at-a-time sampling (PSUADE-MOAT). LHS randomly samples from a uniform distribution within discrete intervals in the design space [7]. OAS creates orthogonal arrays of the inputs where any two of the columns contain an equal number of all possible combinations, and it is well suited to sensitivity analysis [62]. CCD is based on a factorial design with additional center points and selects one point at the center of the design space, at each of the constraint endpoints, and at the constraint midpoints [63]. BB is a quadratic design and selects one point at the center of the design space and at each of the constraint endpoints [64]. PSUADE is a more encompassing tool for optimization, UQ, sensitivity analysis, and surrogate modeling, but we use only its MOAT sampling procedure, designed to discriminate input variables that insignificantly affect the output [65].

*SBGO Methods*. In our earlier study [53], we use the linear GP data fit of the flow solver results as the truth model and compare nine of DAKOTA's gradient-free SBGO algorithms after one global iteration; within that single global iteration, each optimizer queries the surrogate between 70 and 20,000 times, requiring only seconds of physical time on a single processor. Because there is one objective function, each optimization algorithm returns one design point that should be the minimum point in the surrogate model. While six of the optimizers fare better than the other three after a single global iteration, we believe that with enough global iterations, all nine would likely arrive at the truth design (in the case where it is known *a priori*) – and there is no significant computational penalty because this would require seconds or minutes, not days or weeks. This approach has merit in the sense of automation, but the outcome is the same, which is a recommendation for one design point that needs to be assessed with the truth model (flow solver or initial data fit) and returned to the database to create an updated surrogate model; the optimizer then repeats the process on this updated response surface [55]. Therefore, we abandon this process in favor of evaluating each updated surrogate model using a multidimensional parameter study, which is known to compute within a few minutes. The SBGO methods that merit further investigation should predict a design point similar in form and close in value to the surrogate model minimum design point.

### 1.3 Approach for Problem Investigation

Based on the preceding section, the problem we are attempting to solve involves: a 3-D, relatively complex geometry with automated grid generation and assembly; coupled, nonlinear flow physics, approximated with a 3-D, RANS CFD flow solver and turbulence models which should be verified and validated; gradient-free design optimization under uncertainty that includes both aleatory and epistemic uncertainty and needs to incorporate novel ways to approximate the sampling-heavy uncertainty propagation; consideration and evaluation of more efficient optimization schemes, such as surrogate-based optimization; and estimates of total predictive uncertainty. Each of these items has individually been addressed in numerous studies, but it is the integrated combination of all these activities, applied to a real engineering problem, that renders this research unique.

We start at the bottom and build upward. We conduct verification and validation of the CFD flow solver and several RANS turbulence models; this includes more turbulence models than are actually needed, as we down-select to one turbulence model for the 2-D study and a different, more applicable one for the 3-D study. We conduct grid and time-step sensitivity studies for the geometries of interest to select appropriate computational grids and time-step, as well as to

assess numerical accuracy of the associated solutions. We develop automated grid generation and assembly to accommodate the hundreds of tractor-trailer base flap design configurations; and we automate the data-mining and wind-averaging processes for the CFD flow solutions. We use wind-averaging to approximate propagation of aleatory uncertain wind speed and direction, and we modify the wind-averaging to employ a worst-case condition for propagation of epistemic uncertainty in flap deflection angles due to installation tolerances. To develop and refine the design optimization process, we initially reduce the problem to two dimensions then expand it to three dimensions after we select the most accurate and efficient optimization approach for this specific application, whether based on a surrogate model or other optimization algorithm. This selection process involves several non-gradient-based optimization methods, 12 surrogate models with six data sampling methods, and nine SBGO algorithms.

### 1.4 Outline of Dissertation

Following the manuscript format for this dissertation, Chapters 2, 3 and 4 contain articles that have been submitted and are being peer-reviewed for publication in professional technical journals, namely *AIAA Journal* for Chapter 2, *International Journal for Numerical Methods in Fluids* for Chapter 3, and *Computers and Fluids* for Chapter 4. Chapter 2 details the verification and validation of several RANS turbulence models used for time-averaged computations in two commercial CFD flow solvers: Cobalt and RavenCFD. Chapter 3 details the 2-D optimization under uncertainty study for the simplified tractor-trailer with curved (quartic polynomial) base flaps, six design variables, inner-loop aleatory uncertainty (approximated by wind-averaging), various other epistemic uncertainties, total predictive uncertainty for the best design configuration, and evaluation of the possibilities for SBGO. Chapter 4 details the 3-D optimization under uncertainty study for the simplified tractor-trailer with curved (cubic polynomial) base flaps, five design variables that include independent flap deflection angles for the side- and top/bottom-flaps, inner-loop aleatory uncertainty (approximated by wind-averaging), inner-loop epistemic uncertainty, and various other aleatory and epistemic uncertainties applied to and total predictive uncertainty estimated for the best design configuration. Chapter 5 includes a summary, conclusions, and recommendations for future work. Appendices include information not included in the papers, such as the derived cubic and quartic polynomial coefficients for flap geometry and representative files for the flow solver input, optimization algorithms, and automation scripts.

**Chapter 2**: In review for publication in *AIAA Journal*

# Verification and Validation of Reynolds-Averaged Navier-Stokes Turbulence Models for External Compressible Flow

Major Jacob A. Freeman, USAF* and Christopher J. Roy†
*Virginia Tech, Blacksburg, Virginia 24061*

**The Spalart-Allmaras (S-A) turbulence model in the NASA-Langley CFL3D and FUN3D flow solvers has been previously verified 2nd-order accurate. For low subsonic 2-D applications (turbulent flat plate, planar jet, and NACA 0012 airfoil at $\alpha = 0°$), solutions from the S-A, S-A with Rotation and Curvature (SARC), Menter Shear-Stress Transport (SST), and Wilcox 1998 k-ω turbulence models in commercial flow solvers, Cobalt and RavenCFD, are compared with the NASA results for code verification. Of the 80 case evaluations, each of which uses 5 systematically refined computational meshes, only 7 approach 2nd-order observed accuracy, but 41 cases show 1st-order or better, indicating the formal order may be less than 2 for these applications. Since Cobalt and RavenCFD turbulence models perform comparable to NASA's verified models and since rigorous code verification is not possible without access to source code, the presented evidence suggests these turbulence models are implemented correctly for these or similar flow conditions and configurations. For solution verification, estimates of numerical uncertainty are less than 0.5% for 90% of the cases. For validation, the turbulent flat plate solutions match experiment skin friction within 4.8% for $x/L > 0.05$; for planar jet shear-layer velocity profiles, S-A and SARC match experiment within 2-3% full-scale, and SST and k-ω are within 10%; and for airfoil drag coefficient, S-A and SST agree within 1.2% of experiment, SARC 2%, and k-ω 4%.**

## I. Introduction

WITH initial and subsequent versions of flow solvers, developers and users subject the code to a suite of regression tests and case validations, such as the 1-D Riemann shock-tube problem [1]; in 2-D, an inviscid supersonic inlet with compression ramp [1], inviscid airfoil in transonic flow, inviscid base flow [2], laminar flat plate [1], viscous, turbulent boundary-layer flow for the flat plate, supersonic ramp, and an airfoil [2 – 12], or various types of jet and shear flow [13, 14]; then well tested 3-D applications such as a supersonic missile with fins [1], a wing [7, 8], or a civil air transport in transonic cruise [15]. Often, however, little attention is given to code verification (to determine the code's observed order of accuracy, as compared with its formal order) or to solution verification (to quantify numerical accuracy of the code's predicted solutions) [16]. The preference is to verify a code's formal order of accuracy by computing the solution to a problem with an exact solution. The exact analytical solution or an exact manufactured solution may then be used to accomplish this code verification [16]. Without access to source code, in the case of commercial flow solvers, the user may conduct code verification by carefully comparing results with those from a flow solver that has been rigorously verified. To conduct solution verification, users may then use the verified code to compute solutions for various applications and estimate the numerical error in those solutions, effectively placing "error bars" on the computational predictions. As the last step in the verification and validation process, the user validates the model to assess how accurately the model represents the physical flow; this is accomplished by comparing the computed solution with experimentally obtained data.

The purpose of this study is to verify turbulence models in the commercial flow solvers, Cobalt and RavenCFD, which are derived separately from the Air Force Research Lab's *Cobalt*$_{60}$, by comparing their solutions and behavior with those obtained from the previously verified NASA-Langley flow solvers, CFL3D (cell-centered structured) and

* Graduate Student, jacobf72@vt.edu, Department of Aerospace & Ocean Engineering, Senior Member AIAA.
† Associate Professor, cjroy@vt.edu, Department of Aerospace & Ocean Engineering, Associate Fellow AIAA.

FUN3D (node-centered unstructured) [17, 18]. The code and solution verification are performed using three subsonic, 2-D turbulent applications: flat plate, planar jet, and NACA 0012 airfoil at angle of attack, $\alpha = 0°$. These applications were selected because their combined features may represent a more complex, 3-D subsonic flow field. These verification activities compare results from four Reynolds-Averaged Navier-Stokes (RANS) turbulence models: Spalart-Allmaras (S-A), S-A with corrections for Rotation and Curvature (SARC), Wilcox 1998 k-ω, and Menter Shear-Stress Transport (SST). Model validation is not stressed in this study, but there is some validation for each of the cases.

## II. Background and Methods

### A. Flow Solvers

Cobalt [19] solves the 3-D unsteady, compressible Euler and Navier-Stokes equations at cell centers, uses the method of finite volumes, and is parallelized. It is designed to use structured or unstructured mesh topologies, including prisms, tetrahedra, and hexahedra in 3-D, or quadrilaterals and triangles in 2-D, all with arbitrary cell skewness, curvature and/or stretching rates. Cobalt combines the exact Riemann solver of Gottlieb and Groth [20] and the approximate Riemann solver of Harten-Lax-van Leer-Contact (HLLC) [21] with a least-squares method to attain $2^{nd}$-order spatial accuracy, and it uses a point-implicit method with Newton sub-iterations for $2^{nd}$-order temporal accuracy. Its implicit method allows for Courant-Friedrichs-Lewy (CFL) numbers as large as $1x10^6$. Specifying $1^{st}$-order accuracy in time typically provides a time-averaged solution. Cobalt offers eight turbulence models, including the four used for this study, which have formally $2^{nd}$-order accurate numerical implementations but may revert to $1^{st}$-order in the presence of discontinuities, contact surfaces, large flow gradients, or singularities. Cobalt offers one discontinuous flux limiter which may influence the solution observed order of accuracy [1, 15, 19].

RavenCFD [22] also solves the 3-D unsteady, compressible Euler and Navier-Stokes equations at cell centers, uses finite volumes, is parallelized, may use structured or unstructured mesh topologies, is formally $2^{nd}$-order accurate in space and time, uses Newton sub-iterations with its implicit solver, and allows the following options to users: fully implicit or explicit using a 4-stage Runge-Kutta solver; flux-splitting schemes of either Gottlieb and Groth [20] or Edwards Low-Diffusion (LDFSS) [23], which is designed primarily for reacting and multi-phase flows; local or global time-stepping; wall functions; and various flux limiters (Carpenter, J.R., "RavenCFD by Corvid Technologies," Flow Solver Documentation, URL: http://fileserver.corvidtec.com/dokuwiki/doku.php?id=ravencfd, accessible with permission, [cited 7 June 2012]). All RavenCFD simulations in this study use the minmod limiter. RavenCFD offers nine turbulence models, including three used for this study, all with $2^{nd}$-order numerical implementations that may reduce to $1^{st}$-order when exposed to the effects noted above. RavenCFD does not include the SARC turbulence model.

### B. Turbulence Models

To reduce computational mesh cell count and overall computation time for applications with large Reynolds-number flow, all scales of turbulent flow are modeled with RANS turbulence models in this study. The turbulence models include the S-A one-equation (meaning one transport partial differential equation), S-A with corrections for Rotation and Curvature (SARC), Wilcox 1998 k-ω two-equation, and Menter SST two-equation. For the detailed equations and coefficients used by these turbulence models, see [2, 17, 24]. Care is taken to ensure turbulence model equations and coefficients are common among all flow solvers in this study, including one revision to a RavenCFD SST coefficient for conformity.

The S-A turbulence model is often applied to aircraft applications, including predicting separation due to adverse pressure gradients. The S-A model is a function of velocity, kinematic viscosity, vorticity, and wall distance. In the laminar sub-layer it uses a wall-destruction function to reduce turbulent viscosity, and to transition the boundary layer from laminar to turbulent it includes trip functions. The S-A model relies on 11 empirical constants [2]. The SARC model includes a modification in the production term which is a function of kinematic strain and rotation rates, as well as three additional constants [24]. The S-A and SARC models show good agreement with experiment for subsonic flow over a flat plate, sub- and transonic flow over airfoils and wings, rotating and curved channels, turbulent shear flow, and a supersonic impinging jet [4 – 12, 14].

Wilcox's 1998 k-ω turbulence model is often used for wall-bounded flow, regions of large separation, and terms were added to better model planar shear layers. The two transport variables are turbulent kinetic energy, $k$, and turbulent specific dissipation rate, $\omega$, and the model is a function of velocity, kinematic viscosity, and turbulent shear stress. The model includes low Reynolds number corrections for transition from laminar to turbulent boundary layer. The k-ω model also relies on 11 empirical constants [2]. The k-ω model shows good agreement with

experiment, though generally not as good as the S-A, SARC, and SST models, for subsonic flow over a flat plate and an airfoil, and turbulent shear flow [4, 9, 13].

Menter's SST turbulence model combines the accuracy of the k-ω model for wall-bounded flow with that of the k-ε model for shear flow; the 2nd transport variable is turbulence dissipation, $\varepsilon$. Away from the wall, the $\varepsilon$-equation is transformed into an $\omega$-equation, and the model relies on a computationally expensive switching function between the two sub-models. The SST model is a function of velocity, kinematic viscosity, turbulent shear stress, vorticity, and distance from the wall, and it relies on 10 empirical constants [2]. The SST model shows good agreement with experiment for subsonic flow over a flat plate, sub- and transonic flow over airfoils, and a supersonic impinging jet [4, 7, 9 – 11, 14]. For the comparisons in this study, Cobalt and RavenCFD use the version of SST discussed above, while FUN3D and CFL3D both use (for the flat plate and planar jet cases, not for the airfoil) a variant form of the SST model, noted SST-V. To improve numerical stability, the SST-V model transport equations include a modification to the vorticity source term [17].

### C. Case Descriptions

The unit tests include a 2-D flat plate to verify and validate boundary layer modeling, a 2-D planar jet for free shear modeling, and a 2-D airfoil for adverse or non-zero pressure gradient modeling.

Figure 1 shows the 2-D flat plate formulation from NASA-Langley [17], which includes five levels of systematically refined structured meshes; Fig. 1b shows the 2nd coarsest of those grids, the finest being *545x385*. Values for the average $y^+$ for the first cell along the surface range between 0.68 for the coarsest grid to 0.04 for the finest; $y^+$ is defined as

$$y^+ = \frac{y}{\nu}\sqrt{\frac{\tau_w}{\rho}} = yRe_{/x}\sqrt{\frac{C_f}{2}} \tag{1}$$

where $y$ for this case is the height of the first cell (m), $\nu$ is kinematic viscosity ($m^2/s$), $\tau_w$ is wall shear stress ($N/m^2$), $\rho$ is density ($kg/m^3$), $Re_{/x}$ is Reynolds number per length ($m^{-1}$), and $C_f$ is skin friction coefficient. Freestream Mach, $M_\infty$ = 0.2, is selected to ensure essentially incompressible flow, though the flow solvers all use compressible equations. Reynolds number is $Re_{/x} = 5x10^6$ $m^{-1}$. Specified at the inflow boundary are total pressure, $P_0$ = 117,684.90 Pa, and total temperature, $T_0$ = 302.4 K; they are based on specified $T_{ref}$ = 300 K and calculated $P_{ref}$ = 114,448.3 Pa (from given $M_\infty$ and $Re_{/x}$). At the outflow boundary, $P = P_{ref}$. The plate has no thickness, length is $L$ = 2.0 m, and skin friction coefficient values are extracted at $x$ = 0.97008 m, or $x/L$ = 0.48504. A point singularity at the plate leading edge poses a potential problem with the setup; the singularity makes it difficult, particularly for node-centered codes, for observed order of accuracy to match the formal order [17]. From the flow solvers, skin friction ($C_f$) and drag ($C_d$) coefficients are calculated as

$$C_f = \frac{2\tau_w}{\rho u^2} \text{ and } C_d = \frac{2F_{x,avg}}{\gamma P_{ref} M_\infty^2 L} \tag{2}$$

where $u$ is local velocity magnitude (m/s), $\gamma$ is ratio of specific heats (for air, $\gamma$ = 1.4), and $F_{x,avg}$ is average force in the axial direction (N).

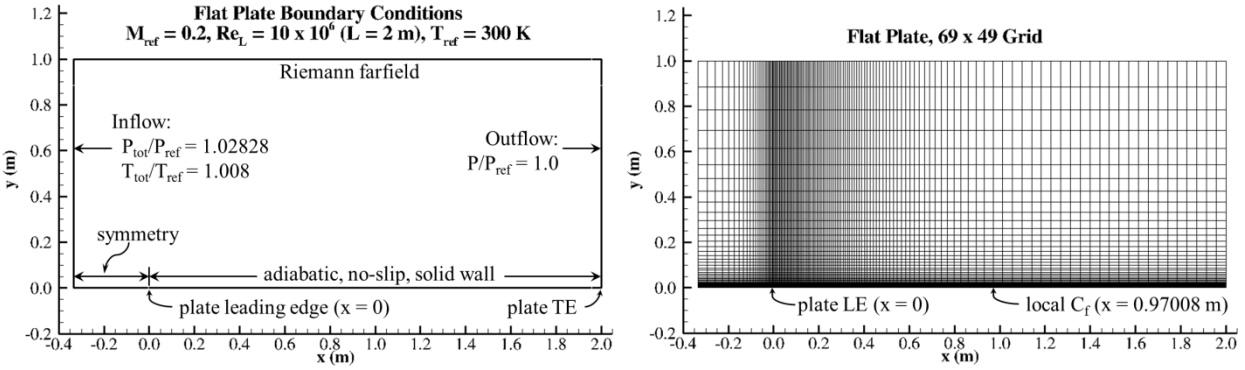


**a) Boundary conditions** **b) 2nd coarsest grid**

**Fig. 1 Turbulent flat plate case.**

Figure 2 shows the 2-D planar jet case from NASA-Langley [17], which includes five levels of systematically refined curvilinear structured meshes; Fig. 2c shows the 3rd finest of those grids with 20,480 cells, the finest having

327,680 cells. Values for the average $y^+$ for the first cell along the solid plate range between 4.2 for the coarsest grid to 0.21 for the finest. For the entire model, $Re_{/x}$ = 5x10$^4$ cm$^{-1}$, $T_{ref}$ = 300 K, and calculated $P_{ref}$ = 457.79 Pa. For the flow above the plate, $M_\infty$ = 0.25, $P_{0,upper}$ = 478.85 Pa, and $T_{0,upper}$ = 300 K. For flow below the plate, $M_{jet}$ = 0.5, $P_{0,jet}$ = 543.035 Pa, and $T_{0,jet}$ = 315 K. The plate has no thickness, length is $L$ = 10.0 cm, and it is positioned at the inflow boundary in the $x$-direction and at $y$ = 0.5 cm above the $y$ = 0 symmetry boundary. This models the 2-D planar jet from the experiment of Bradbury and Riley [25], which is used for model validation. For the verification, comparisons are made among $C_d$ values for the plate and $u/a_{ref}$ values at three locations along the jet centerline, $y$ = 0: $x/L$ = 0.271623, 2.92468, and 9.5501, where $u$ is local velocity in the $x$-direction (cm/s) and $a_{ref}$ is the speed of sound (cm/s), based on $T_{ref}$. For validation with experiment, velocity profiles are compared at approximately $x/L$ = 2.9, 6.4 and 9.5; the profiles are nondimensionalized as $(u-u_e)/(u_{max}-u_e)$, where $u_e$ is edge velocity (cm/s) and $u_{max}$ is jet centerline velocity (cm/s). This setup also has point singularities at the plate leading and trailing edges. From the flow solvers, drag coefficients are calculated as in Eq. (2).

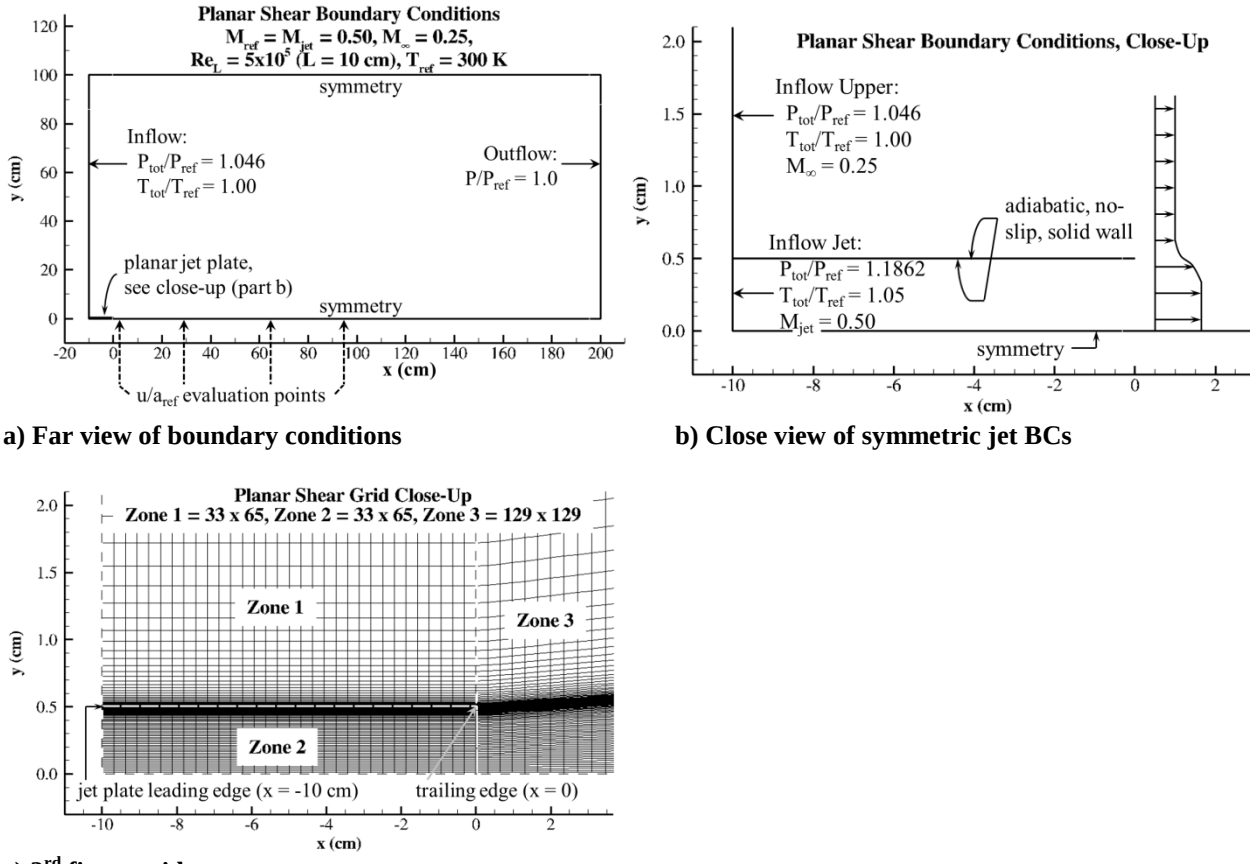


**a) Far view of boundary conditions** **b) Close view of symmetric jet BCs**




**c) 3rd finest grid**

**Fig. 2 Planar jet case.**

Figure 3 shows the NACA 0012 airfoil setup from NASA-Langley [17], which includes five levels of systematically refined curvilinear structured meshes; Figs. 3b and 3c show the 3rd finest of those grids, the finest being *1,793x513* or 917,504 cells. The computational domain extends 500 chord lengths in all directions to fully capture circulation effects. Values for the average $y^+$ for the first cell along the surface range between 1.19 for the coarsest grid to 0.048 for the finest. Freestream Mach, $M_\infty$ = 0.15, is selected to ensure essentially incompressible flow, and Reynolds number per chord length is $Re_{/c}$ = 6x10$^6$/c, where $c$ = 1.0 m. At the Riemann farfield boundary, $T_{ref}$ = 300 K and $P_{ref}$ = 183,117.4 Pa. Because the primary interest is code verification using this model, only the $\alpha$ = 0° case is evaluated and only $C_d$ and $C_f$ are considered, since $C_l \approx 0$ at this angle for a symmetric airfoil. $C_f$ is evaluated locally at a point on the upper surface ($x/c$ = 0.5121166, $y/c$ = 0.0513979503). For the single validation point, $C_d$ at $\alpha$ = 0°, comparison is made with Ladson's experimental results [26] because the boundary layer is tripped and thus fully turbulent. From the flow solvers, $C_d$ and $C_f$ are calculated as in Eq. (2), since $\alpha$ = 0° and for $L$

= *c*. This case differs from the flat plate case by incorporating a non-zero pressure gradient on the surfaces, by removing the leading edge singularity, and by changing the boundary conditions from inflow/outflow to farfield.

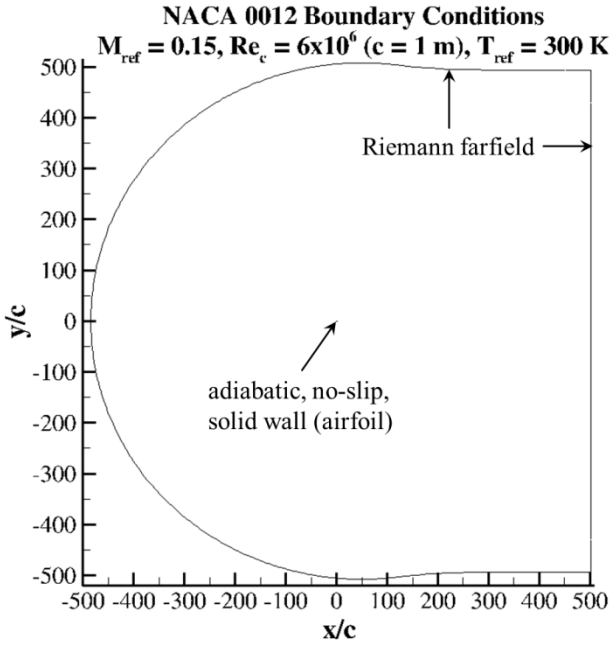


**a) Boundary conditions**

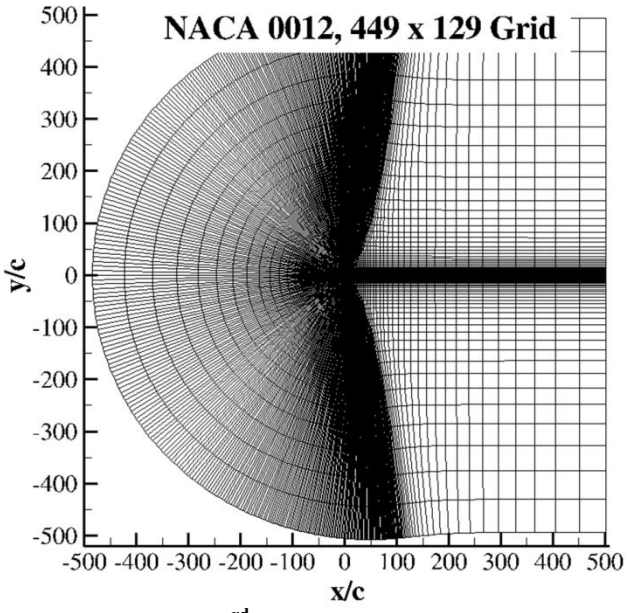


**b) Far view of 3rd finest grid**

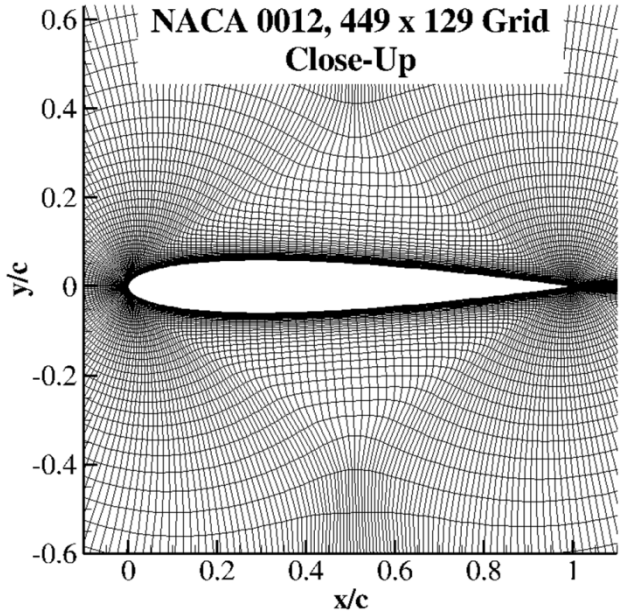


**c) Close view of 3rd finest grid**

**Fig. 3 NACA 0012 airfoil case.**

### D. Code Verification

Two primary intents of code verification include (1) ensuring a code is correct and bug-free, and (2) proving that systematic mesh refinement results in improved observed order of accuracy, i.e., as the cell spacing approaches zero, the observed order of accuracy should approach the formal order of accuracy [16, 27]. Since the commercial codes being evaluated are well tested and free of blatant errors, the second intent is addressed in this study. To accomplish this, multiple, systematically refined mesh levels are used; systematic refinement requires uniformity (constant

refinement factor in all spatial directions) and consistency (as cell size approaches zero, the mesh quality – cell aspect ratio, stretching factor, skewness and curvature – remains the same or improves) [16]. For all three cases, NASA-Langley [17] generated a fine grid, removed every other grid point in each spatial direction for the next coarser grid, and repeated until five grid levels were created. From the flow solvers' integrated values for $C_d$, for example, the observed order of accuracy [16] is calculated as

$$\hat{p} = \frac{ln\left|\frac{C_{d,3}-C_{d,2}}{C_{d,2}-C_{d,1}}\right|}{ln(r)} \tag{3}$$

where the indices 1, 2, and 3 denote solutions from systematically coarser grids, respectively, 1 being the solution from the finest of the three grids; and $r$ is grid refinement factor, or $r = \left(\frac{N_{cells,1}}{N_{cells,2}}\right)^{1/2} = 2$ for all of these grids. Thus, if the observed order of accuracy approaches the formal order within an acceptable margin (e.g., 10%), or if the observed order behaves similarly to that of a verified code, the code of interest may not be declared unequivocally verified but the model is probably implemented correctly.

### E. Solution Verification

To verify the solution, numerical error must be quantified, where numerical error consists of error due to round-off, iterations, discretization, and statistical sampling. Numerical uncertainty can be quantified by applying a factor of safety to the absolute value of the numerical error [27]. The cases examined do not result in any statistical sampling error, but using double-precision computations in the flow solvers generally keeps round-off error to much less than 1% of the discretization error. Iterative error is the difference between the current iterative approximate solution and the exact solution to the discrete equations, and the "machine-zero method" is used to estimate this error. With the machine-zero method, the solution residuals are iteratively converged either to machine zero (14 orders of magnitude for double-precision) or as far as the solver permits with its stabilizing functions (flux limiters and damping), then that deeply converged solution is compared with the solution at the current iterative level to estimate the iterative error [16, 27]. For the cases in this study, iterative error estimates are assumed to be zero because every solution is converged as far as the schemes allow, between 6 and 10 orders of magnitude reduction in the iterative residual for the continuity equation.

Before estimating the discretization error and uncertainty in the numerical error, the exact solution is first approximated via Richardson Extrapolation [27]. Richardson Extrapolation generally provides an estimate that is one order more accurate than the computed results; e.g., if using a formally 2nd-order method, Richardson Extrapolation estimates a solution that is 3rd-order accurate, and it requires solutions from the two finest systematically refined grids. Again using $C_d$ as an example, the extrapolated value $\bar{C}_{d,RE}$ is calculated as

$$\bar{C}_{d,RE} = C_{d,1} + \frac{(C_{d,1} - C_{d,2})}{r^{p_f} - 1} \tag{4}$$

where $p_f$ is formal order of accuracy (here $p_f = 2$). We then use the extrapolated value to estimate the discretization error,

$$\bar{\varepsilon}_{DE,RE} = \left|C_{d,i} - \bar{C}_{d,RE}\right| \tag{5}$$

where $i$ is the respective grid level.

Lastly the uncertainty due to numerical error is approximated according to the sum of its parts, $U_{Numerical} = U_{DiscretizationError} + U_{Iterative\ Error} + U_{Round\text{-}off\ Error}$, where $U_{Iterative\ Error} = \left|C_{d,iter\ level} - C_{d,machine\ zero}\right| = 0$ for these cases, $U_{Round-off\ Error} \approx 0.01\left(\bar{\varepsilon}_{DE,RE}\right)$, and using Roache's Grid Convergence Index with a modified implementation by Oberkampf and Roy [27] for the factor of safety, $F_s$, when using solutions on three or more systematically refined meshes,

$$U_{Discretization\ Error} = \frac{F_s}{r^{p_f} - 1}\left|C_{d,i} - C_{d,i+1}\right| \tag{6}$$

where $F_s = 1.25$ for $\chi = \left|\frac{\hat{p}-p_f}{p_f}\right| \leq 0.1$, or $F_s = 3$ for $\chi > 0.1$

and where $i$ is the grid refinement level and $\hat{p}$ is defined in Eq. (3).

## III. Results and Discussion

### A. 2-D Turbulent Flat Plate

For code verification, Fig. 4a shows the turbulent flat plate's predicted drag coefficients from the four flow solvers using two to four RANS turbulence models on five systematically refined meshes (Note: There are no data for FUN3D and CFL3D using k-ω, and SARC results are available only for Cobalt.); Fig. 4b shows predicted skin friction coefficient at $x/L$ = 0.48504. Solid-black lines represent the S-A model, solid-gray lines represent SST, and dotted-black lines represent k-ω. Dashed-black lines mark ±1% of the average $C_d$ or $C_f$ from the NASA solutions, or benchmark numerical solution. The grid refinement parameter, $h$, is defined spatially [5] as

$$h = {\Delta x}/{\Delta x_{ref}} \tag{7}$$

where $\Delta x_{ref}$ refers to the finest grid spatial node spacing; e.g., $h$ = 1 corresponds to the finest grid. Cobalt and RavenCFD S-A solutions coincide for both $C_d$ and $C_f$ within 0.01% or less; thus, they appear as one line in each plot. On the finest grid for the S-A model, each of the four codes predicts a value for $C_d$ and $C_f$ within 0.3% of the others. Cobalt SARC results also nearly coincide with Cobalt S-A results (less than 0.2% for $C_d$ and $C_f$ for all grid levels); the small difference between S-A and SARC is unsurprising because neither curvature nor significant rotation is present. On the finest grid for the SST model, each of the four codes predicts a value for $C_d$ and $C_f$ within 0.5% of the others; although small, most of that gap comes from the difference between the SST and SST-V models. On the finest grid for the k-ω model in Cobalt and RavenCFD, however, differences range between 2.0 and 4.5% from the NASA average for the S-A and SST models; the k-ω model creates greater eddy viscosity within the boundary layer, as shown in more detail in Fig. 5. Further, since Cobalt and RavenCFD k-ω results on the finest grid differ from each other by 1.4% for both $C_d$ and $C_f$, there must be a slight difference in their implementation and/or an effect of flux limiter switching (in Cobalt) which is most likely.

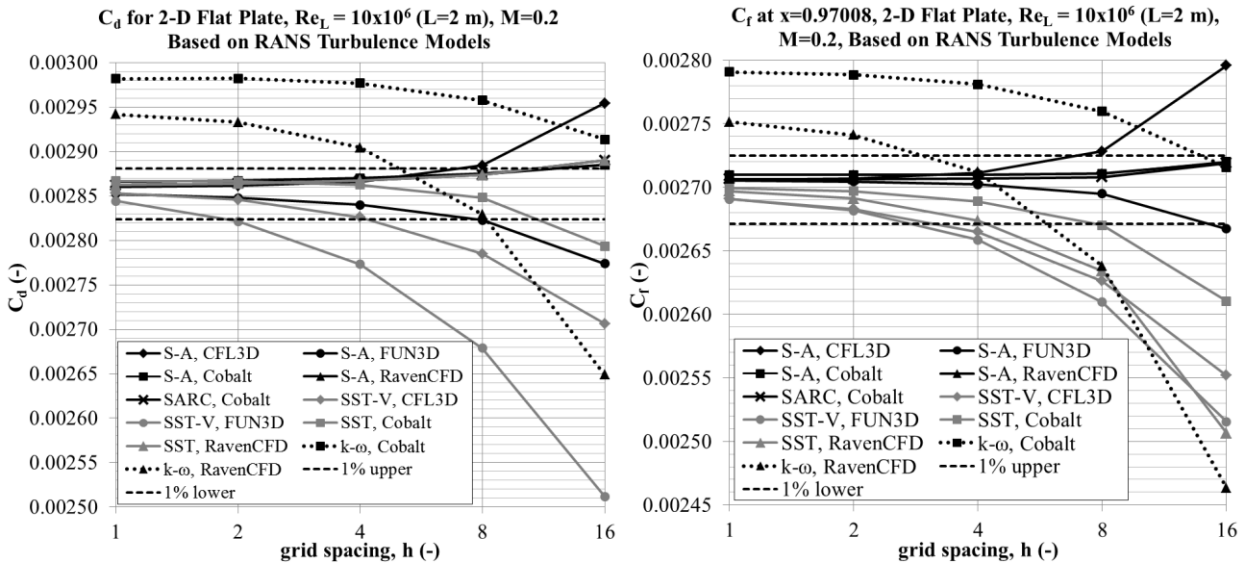


**a) Drag coefficient** **b) Skin-friction coefficient at $x/L$ = 0.48504**

**Fig. 4 Turbulent flat plate using RANS turbulence models on 5 systematically refined meshes.**

In Fig. 5, ratios of turbulent eddy viscosity to freestream viscosity ($\mu_t/\mu_\infty$) are compared for the various RANS turbulence models. Figures 5a and 5b show contours of the difference between the k-ω, S-A, and SST models, indicating clearly larger values for eddy viscosity within the flat plate boundary layer generated by the k-ω turbulence model; for reference, the dashed line shows the k-ω boundary layer thickness, noted as $\delta_{0.99}$ and based on where the local velocity (in the $x$-direction) magnitude is 99% of the freestream velocity. Figure 5c further illustrates that the k-ω model generates the most turbulent eddy viscosity within the boundary layer, and it strengthens the argument that the commercial flow solvers' turbulence models are implemented correctly for the turbulent flat plate case, since the results and behavior match so closely with the benchmark codes. Specifically at streamwise location, $x/L$ = 0.48504, the eddy viscosity ratio for Cobalt's S-A model differs from that of FUN3D by less than 1.7% full-scale (< 0.1% for ¾ of the shear layer), and Cobalt SST differs from FUN3D SST-V by less than 4.3% full-scale

(< 0.2% for ¾ of the shear layer); Cobalt S-A and SARC differ by less than 1.6% full-scale throughout the shear layer, and Cobalt S-A and k-ω differ by as much as 39% full-scale. While not plotted in Fig. 5c, RavenCFD turbulence models predict an eddy viscosity ratio at that location that differs from the Cobalt results by less than 0.02% full-scale for S-A, 0.8% for SST, and 8% for k-ω.

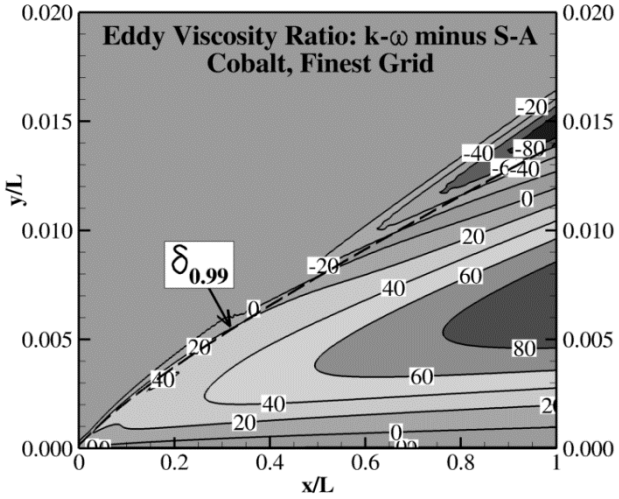


**a) Difference between k-ω and S-A turbulence models**

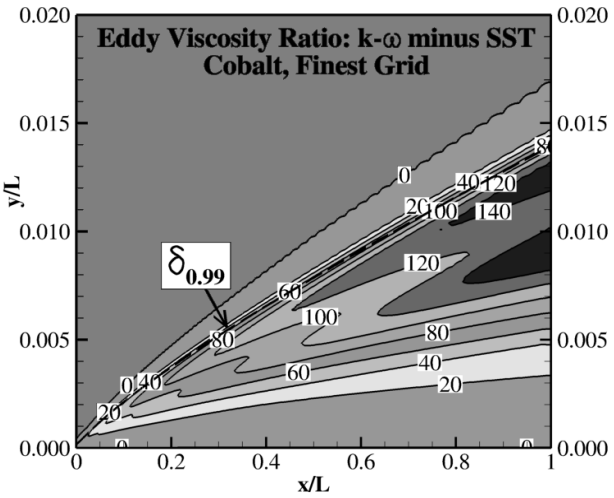


**b) Difference between k-ω and SST**

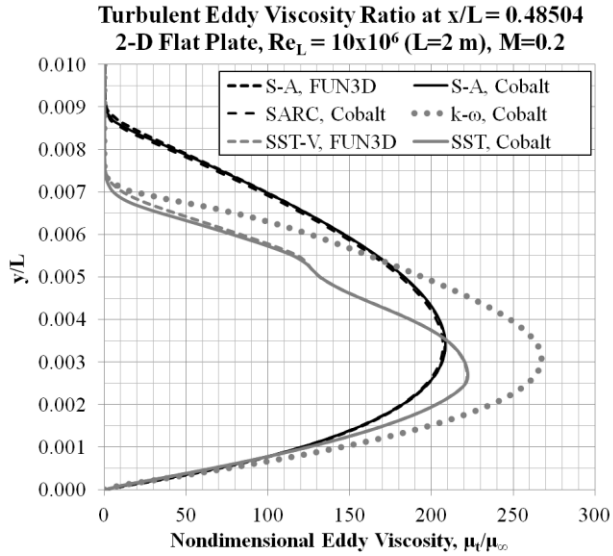


**c) Values at *x/L* = 0.48504**

**Fig. 5 Turbulent eddy viscosity ratios ($\mu_t/\mu_\infty$) normal to flat plate surface, finest grid.**

Figure 6 shows the local value for $C_f$ along the flat plate surface from each of the turbulence models, as well as an empirically-based integral solution, noted "MOSES, fully turbulent," and experimental results from Wieghardt and Tillmann [28], which are discussed later. The integral method [29] uses Moses' turbulent mean-flow momentum integral equations, neglects the effects of a transition region, is based on empirical data to model the turbulent eddy viscosity, approximates the wake function to provide a more representative boundary layer velocity profile, assumes steady (in the mean) turbulent flow, and treats all dependent variables as mean values. The associated solvers [30] assume incompressible flow but allow a viscous calculation for the surface flow. As noted in [17], agreement suffers at the leading and trailing edges because of the point singularities; however, along the rest of the surface the S-A, SARC, and SST models agree with each other within less than 0.4%, and the k-ω models differ from each other by 1.1-1.6%.

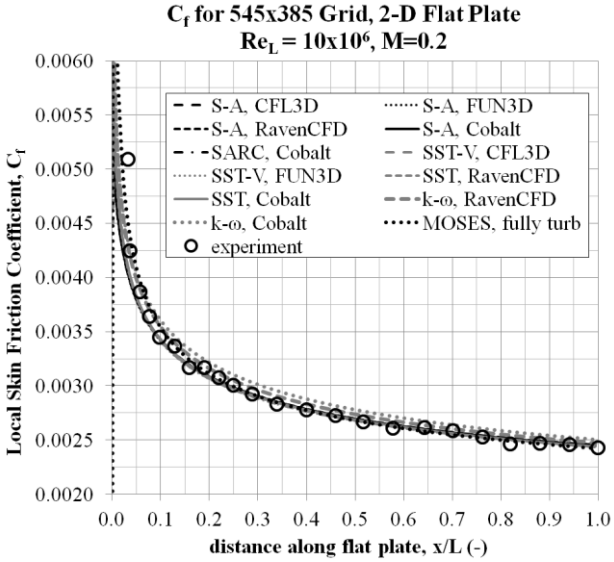


**Fig. 6 Skin friction coefficient along flat plate surface from solutions on finest grid.**

For code verification, observed order of accuracy for $C_d$ and $C_f$ is shown in Table 1, based on the solutions to the three finest grids (with two noted exceptions), for the several turbulence models and flow solvers; for solution verification, Table 1 also shows total estimated uncertainty due to numerical error. A negative value for observed order of accuracy means the difference between solutions from grid levels 2 and 3 is smaller than the difference from grid levels 1 and 2. Accuracy for $C_f$ at a point is generally better than or comparable to $C_d$ because the local $C_f$ value is less affected by the leading edge singularity. Observed order of accuracy near unity is noted in several cases, likely due to that singularity ($C_f$ approaches infinity at the leading edge). In general, numerical uncertainty is less than 1% for all cases and is smaller for cases where the observed order is close to the formal order of accuracy, which is assumed to be 1.0 for the error and uncertainty calculations for the integrated coefficient, $C_d$. That is, if $0.9 \leq \hat{p} \leq 2.2$, then $F_s$ = 1.25 for Eq. (6) since 1st-order effects are present. It is imprecise to declare that these flow solvers display 2nd-order accuracy for all the turbulence models evaluated, and the results in Table 1 suggest the formal order for this case is likely between 1 and 2. It may be concluded that the results from these Cobalt and RavenCFD RANS turbulence models closely match results from the numerical benchmark codes, CFL3D and FUN3D, which have been verified for the S-A turbulence model [18], and that the turbulence models have been correctly implemented for turbulent boundary layer flow.

**Table 1 Turbulent flat plate observed order of accuracy and total numerical uncertainty.**

| **Turbulent Flat Plate, M=0.2, $Re_L$ = 10x10$^6$ (L = 2 m)** | | | | | |
|---|---|---|---|---|---|
| Turbulence Model | Flow Solver | $C_d$ | | $C_f$ at $x$=0.97008 m | |
| | | $\hat{p}$ | $U_{Tot,Num}$ | $\hat{p}$ | $U_{Tot,Num}$ |
| S-A | CFL3D | 1.75 | 0.03% | 1.98 | 0.02% |
| | FUN3D | 0.80 | 0.65% | 1.34 | 0.03% |
| | Cobalt | 0.83 | 0.19% | < 0 | 0.03% |
| | RavenCFD | 1.00 | 0.06% | < 0 | 0.03% |
| SST-V | CFL3D | 1.34 | 0.22% | 1.21 | 0.28% |
| | FUN3D | 1.07 | 0.92% | 1.39 | 0.26% |
| SST | Cobalt | 1.75[a] | 0.08%[a] | 1.84 | 0.04% |
| | RavenCFD | 0.93 | 0.04% | 1.60 | 0.13% |
| k-ω | Cobalt | 1.87[a] | 0.07%[a] | 1.65 | 0.05% |
| | RavenCFD | 1.63 | 0.19% | 1.50 | 0.26% |
| SARC | Cobalt | 0.93 | 0.08% | 2.17 | 0.001% |

[a] Results taken from coarser level of grids due to oscillatory behavior on finest level.

For validation, Fig. 6 shows the local $C_f$ comparison with the experiment of Wieghardt and Tillmann [28]. The computational results for the finest grid do not agree well with experiment at the two measured points closest to the leading edge, $x/L < 0.05$, where the results differ from experiment by 5-20%; this is possibly due to interference from the pressure rake in the boundary layer transition region. At every other measured location, the simulations from all four flow solvers and all turbulence models differ from the experiment by less than 4.0%, with the one exception of Cobalt k-ω, which differs by as much as 4.8%. Again disregarding the two points nearest the leading edge, the average difference between computation and experiment for $C_f$ is 0.9-1.0% for the S-A, SST, and SARC turbulence models; Cobalt and RavenCFD results for k-ω differ on average from experiment by 3.2% and 1.8%, respectively. These results are consistent with other subsonic-flow flat-plate comparisons between computation and experiment for these four turbulence models [4, 5, 9 – 11]. Thus, it may reasonably be concluded for the turbulent flat plate skin friction that the RANS turbulence models all compare well with experiment for $x/L > 0.05$.

### B. 2-D Planar Jet

For code verification, Fig. 7a shows the planar shear plate predicted drag coefficients from the several turbulence models and flow solvers on five systematically refined meshes; Figs. 7b, 7c, and 7d show predicted pseudo-local Mach (where $u$-velocity is normalized by the reference sound speed rather than local sound speed) at three locations downstream and along the jet centerline. As with the turbulent flat plate results, solid-black lines represent the S-A and SARC model, solid-gray lines represent SST, dotted-black lines represent k-ω, and dashed-black lines mark ±1% of the average $C_d$ or $u/a_{ref}$ from the NASA numerical benchmark solutions. For the S-A model predicted $C_d$ on the finest grid, FUN3D and CFL3D differ by 1.8%, while RavenCFD and Cobalt differ by only 0.2%, and Cobalt differs from CFL3D by 0.4%. SARC and S-A $C_d$ for Cobalt differ by 0.01% on the finest grid. For the SST model finest grid $C_d$, the variation is less polarized and all solvers lie within 1.0% of each other. For the k-ω model finest grid $C_d$, RavenCFD and Cobalt differ by 1.0% and from the average NASA data by 4.1%, indicating once again its tendency to predict greater eddy viscosity in the boundary layer. Further, the coarse-mesh variation in $C_d$ results suggests the need to investigate local mesh refinement around the plate if a coarser grid is selected for additional simulations. Fig. 7b shows that all solvers and models on the finest grid predict $u/a_{ref}$ values within 0.02% of each other, an uninteresting result where flow is essentially free of turbulence.

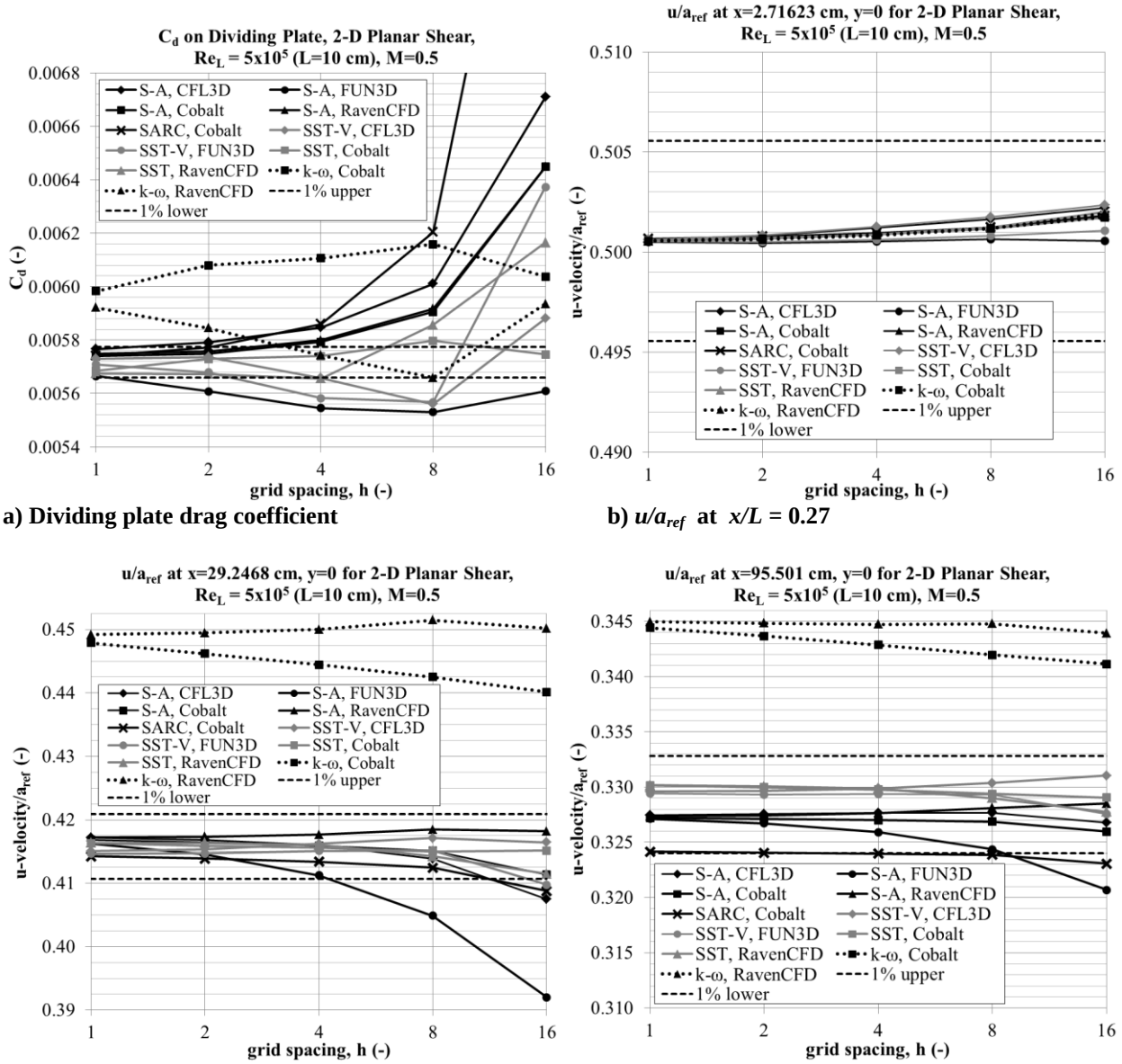


**a) Dividing plate drag coefficient** **b) $u/a_{ref}$ at $x/L$ = 0.27**

**c) $u/a_{ref}$ at $x/L$ = 2.92** **d) $u/a_{ref}$ at $x/L$ = 9.55**

**Fig. 7 Planar shear drag coefficient and pseudo-local Mach for RANS turbulence models.**

Farther downstream for the finest grid, shown in Figs. 7c and 7d, agreement is excellent among the solvers for each respective turbulence model, where the predictions differ by no more than 0.4%; at $x/L$ = 2.92, S-A differs from SST and SARC by no more than 0.6%, but k-ω is 7.6% greater than the average NASA data for SST and S-A; and at $x/L$ = 9.55, S-A, SST, and SARC differ by less than 0.9% and k-ω is 5.3% greater than the average NASA data for SST and S-A. While the k-ω model predicts less turbulence dissipation in the boundary layer (refer to Fig. 5c), roughly three plate-lengths downstream at $x/L$ = 2.925 above the jet centerline, Fig. 8 shows the Cobalt k-ω model has notably greater turbulence dissipation than S-A, SARC, or SST models, where its turbulent eddy viscosity ratio is 27-60% smaller than S-A full-scale. The SARC model predicts 5-10% full-scale greater eddy viscosity ratio than the S-A models, while the SST and SST-V models predict greater peak eddy viscosity but generally smaller levels throughout the mixing region shown in Fig. 8. To enhance the commercial code verification, Fig. 8 shows that Cobalt S-A differs from FUN3D S-A by less than 1%, and Cobalt SST differs from FUN3D SST-V by 2.4%. While not included in Fig. 8, the RavenCFD results closely follow those of Cobalt: S-A results differ by less than 0.05%, SST results differ by less than 0.2%, and k-ω results differ by 2-7% full-scale. This suggests that both Cobalt and

RavenCFD k-ω models have similar implementation for shear flow, whereas it was noted previously that they show different behavior in the near-wall region.

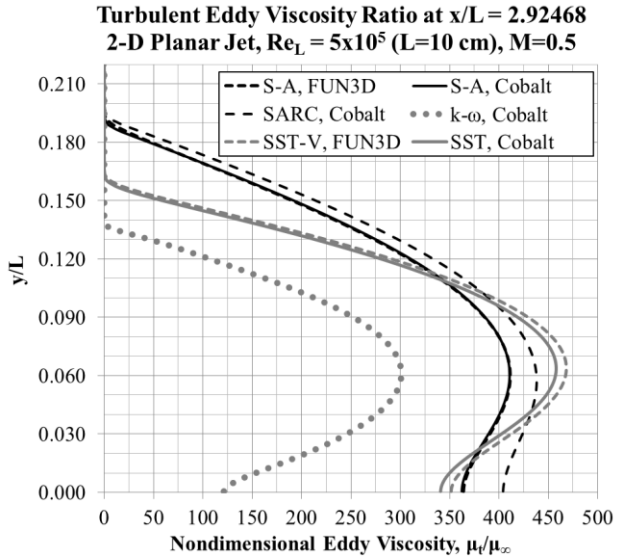


**Fig. 8 Turbulent eddy viscosity ratio downstream and along centerline of planar jet at *x/L* = 2.92468.**

Figure 9 shows $u/a_{ref}$ along the jet centerline, $y = 0$, for all the solvers and turbulence models from the finest grid solution. In the region far downstream of the jet exit ($x/L > 4.0$), S-A and SST results differ by no more than 1.5%, SARC and S-A differ by less than 1.0%, and k-ω differs from S-A by 5-6%. A notable difference among the turbulence models is where they predict the change from non-turbulent jet flow (horizontal portion of data in Fig. 9) to a turbulent mixing region. The k-ω models predict this location 74% farther downstream than do the S-A models, likely because the k-ω turbulent wake is more energetic and delays mixing; the SST models predict it 32% farther downstream than the S-A models; and SARC predicts it 2% farther downstream than the S-A models. As a comparison with similar experimental data [20], where the experimental $u_{max}/u_e \approx 5$ versus the computational $u_{max}/u_e \approx 2$, the S-A models predict this transition point 28% farther downstream – a result readily explained by the more gradual disruption of the wake by the slower moving jet flow.

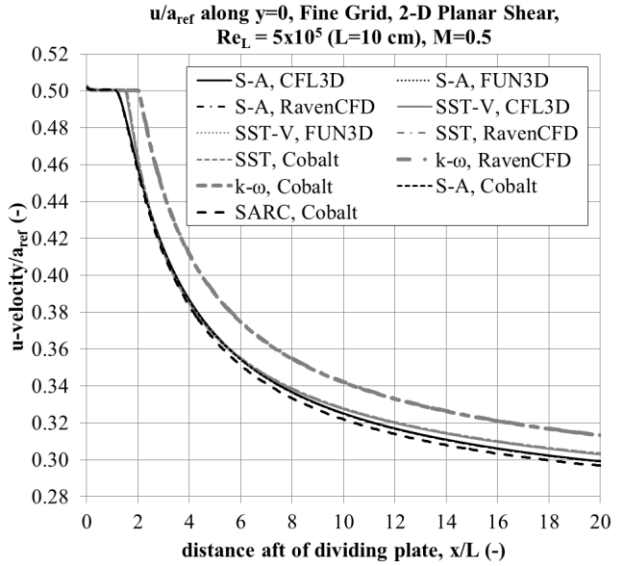


**Fig. 9 Pseudo-local Mach along centerline, aft of planar jet exit, from solutions on finest grid.**

Table 2 presents observed order of accuracy for code verification and numerical uncertainty estimates for solution verification. Regarding $C_d$ predictions, since the observed orders of accuracy do not behave like those in the turbulent flat plate case, the flow solvers must deal differently with the changed configuration: three different boundary conditions meet at the plate leading edge followed by a singularity at the trailing edge, different velocities on upper and lower surfaces, and information propagated from downstream flow structures. Some general observations include: there is smaller numerical uncertainty in the local $u/a_{ref}$ quantities than with the integrated $C_d$ for the plate, possibly due to mesh resolution around the plate; all models appear to predict roughly 1st-order effects in the region closest to the trailing edge singularity and where the flow is steady; while there is no clear "best performing" turbulence model or flow solver, RavenCFD S-A and SST models appear to estimate consistently reasonable values; and none of the models or flow solvers consistently display its formal order of accuracy, most likely due to the plate singularities, but due also to possible unsteady structures in the flow. These results demonstrate the modeling complexity of even seemingly simple flow. Regarding Cobalt and RavenCFD turbulence models and based on the results shown in Figs. 7 – 9, it may be concluded they perform comparably with those of CFL3D and FUN3D, and they are thus likely implemented correctly for the case of a planar jet and shear flow.

**Table 2 Planar shear observed order of accuracy and total numerical uncertainty.**

| **Planar Shear, $M_{jet}$=0.5, $Re_L$ = 5x10$^5$ (L = 10 cm)** | | | | | | | | | |
|---|---|---|---|---|---|---|---|---|---|
| Turbulence Model | Flow Solver | $C_d$ | | $u/a_{ref}$ at $x/L$=0.272 | | $u/a_{ref}$ at $x/L$=2.925 | | $u/a_{ref}$ at $x/L$=9.550 | |
| | | $\hat{p}$ | $U_{Tot,Num}$ | $\hat{p}$ | $U_{Tot,Num}$ | $\hat{p}$ | $U_{Tot,Num}$ | $\hat{p}$ | $U_{Tot,Num}$ |
| S-A | CFL3D | 1.13 | 0.47% | 0.96 | 0.06% | 1.35 | 0.06% | < 0 | 0.03% |
| | FUN3D | 0.12 | 1.01% | 0.81[a] | 0.05%[a] | 0.96 | 0.54% | 0.94 | 0.17% |
| | Cobalt | 2.25 | 0.16% | 0.65 | 0.02% | 0.61 | 0.08% | 0.26 | 0.03% |
| | RavenCFD | 2.48 | 0.13% | 1.46 | 0.01% | 1.61 | 0.02% | 1.52 | 0.02% |
| SST-V | CFL3D | 0.32[a] | 0.49%[a] | 0.88 | 0.05% | 1.38 | 0.06% | 2.77 | 0.01% |
| | FUN3D | 1.70 | 0.29% | 0.59[a] | 0.02%[a] | 4.58 | 0.004% | 6.38[a] | 0.01%[a] |
| SST | Cobalt | < 0 | 0.78% | 0.39 | 0.02% | < 0 | 0.10% | 0.07 | 0.06% |
| | RavenCFD | 2.60 | 0.57% | 1.23 | 0.02% | 2.45[a] | 0.12%[a] | 0.75 | 0.12% |
| k-ω | Cobalt | < 0 | 1.62% | 0.70 | 0.02% | 0.01 | 0.38% | 0.07 | 0.22% |
| | RavenCFD | 0.42 | 1.30% | 1.20 | 0.02% | 1.10 | 0.06% | < 0 | 0.04% |
| SARC | Cobalt | 1.42 | 0.42% | 0.56 | 0.02% | 0.35 | 0.09% | < 0 | 0.03% |

[a] Results taken from coarser level of grids due to oscillatory behavior on finest level.

The planar shear results to this point help verify Cobalt and RavenCFD compared with the NASA benchmark solutions but do not validate any of the turbulence models. In Fig. 10, the computational results from the finest grid are compared with Bradbury and Riley [25] experimental results; the 1967 data contain no quantified experimental uncertainty. Figure 10 shows results only from the Cobalt flow solver for the S-A, SST and k-ω turbulence models; while not shown, the three other flow solvers and Cobalt SARC match the Cobalt results within 1%. The black lines show computational results at $x/L$ = 2.92468, where the flow is not far enough downstream of the jet to be fully self-similar (independent of scale) [17], so those results are excluded from the following discussion. At the other two downstream locations (gray and dark-gray lines), all the turbulence models compare within 0.5% of experiment full-scale for $0 \le y/(\textit{half-width}) < 1.1$, where *half-width* is defined as the location where $(u-u_e) = \frac{1}{2}(u_{max}-u_e)$, indicating the turbulence models do well in the shear layer where there is less mixing and turbulence scales are fine, but that they have more difficulty modeling the outer region of the shear layer where the plate wake mixes with the planar jet and where turbulence scales are larger. The S-A (dashed lines) and SARC models compare within 2-3% of experiment full-scale even in this outer region of the shear layer. Because the SST (solid lines) and k-ω (dotted lines) models produce less eddy viscosity in most or all of the shear layer (refer to Fig. 8), they predict a smaller region of turbulent shear, where the local velocity matches the edge velocity closer to the centerline than are predicted by S-A and SARC and indicated by experiment; SST and k-ω match within 10% of experiment full-scale. Similarly, Barone et al. [13] show this moderate agreement between experiment and the Wilcox 1998 k-ω model in turbulent shear flow. Thus, while there are nuances among their implementations, each of the evaluated RANS turbulence models in Cobalt and RavenCFD compares well with experiment for fully turbulent shear flow, which includes the mixing of a wake and a planar jet.

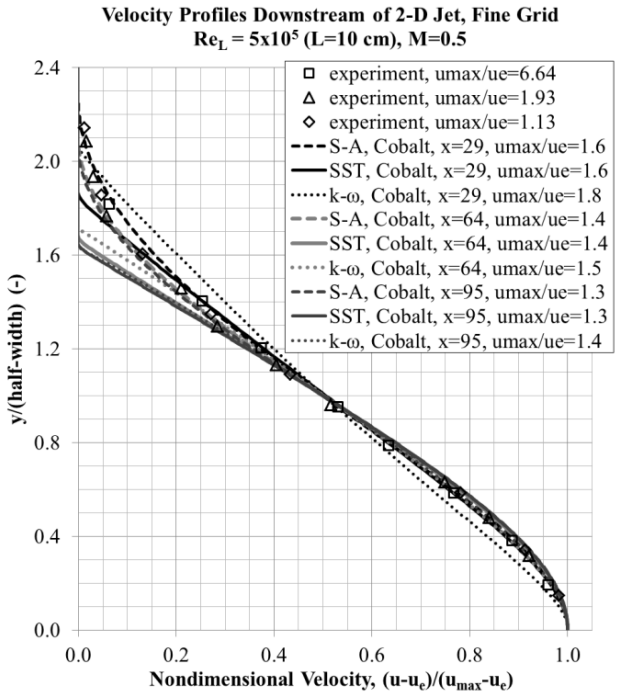


**Fig. 10 Planar jet velocity profiles downstream of planar jet ($M_{jet} = 0.5$).**

### C. 2-D NACA 0012 Airfoil at $\alpha = 0°$

For the airfoil case, NASA-Langley [17] conducted primarily a validation study so verification data are less complete; specifically, they provide $C_d$ results from CFL3D and FUN3D for only the 2nd finest grid and $C_f$ results from only CFL3D on the 2nd finest grid. However, $C_d$ results on that grid are included from one additional flow solver, from the Russian NTS. Also, CFL3D and FUN3D results include the SST turbulence model without the additional vorticity source term. For code verification, Fig. 11a shows the NACA 0012 predicted drag coefficients; Fig. 11b shows the predicted skin friction coefficient at the upper-surface location noted in Section II.C. Solid-black lines represent the S-A and SARC model, solid-gray lines represent SST, and dotted-black lines represent k-ω. Dashed-black lines mark ±1% of the average $C_d$ or $C_f$ from the NASA benchmark numerical solutions, again for the 2nd finest grid in this case. Some coarse-grid results are truncated from Fig. 11 to accentuate the more pertinent results on the finer grids. For $C_d$ predictions on the finest grid, the SST solutions from Cobalt and RavenCFD differ from each other by 0.03%. S-A results for $C_d$ predictions on the finest grid differ from each other by 0.08%, and SARC results differ from S-A by 2.6% showing that this turbulence model slightly under-predicts the eddy viscosity. (Refer to Fig. 5c, where SARC predicts boundary-layer eddy viscosity ratios 1.6% less than S-A.) The k-ω results for $C_d$ on the finest grid differ from each other by 0.5%. There should be negligible influence of pressure drag at this angle of attack for a symmetric airfoil; thus discrepancies must be attributed to boundary layer and surface shear.

Solutions from Cobalt and RavenCFD on the 2nd finest grid for both $C_d$ and $C_f$ differ from the benchmark values by less than 0.1% for S-A, 0.2% for SST, 3.2% low for SARC (vs. S-A), and 3.4% high for k-ω (vs. S-A and SST). These comparisons primarily indicate that the k-ω and SARC turbulence model results are relatively close to the other models but highlight differing implementations for modeling the eddy viscosity.

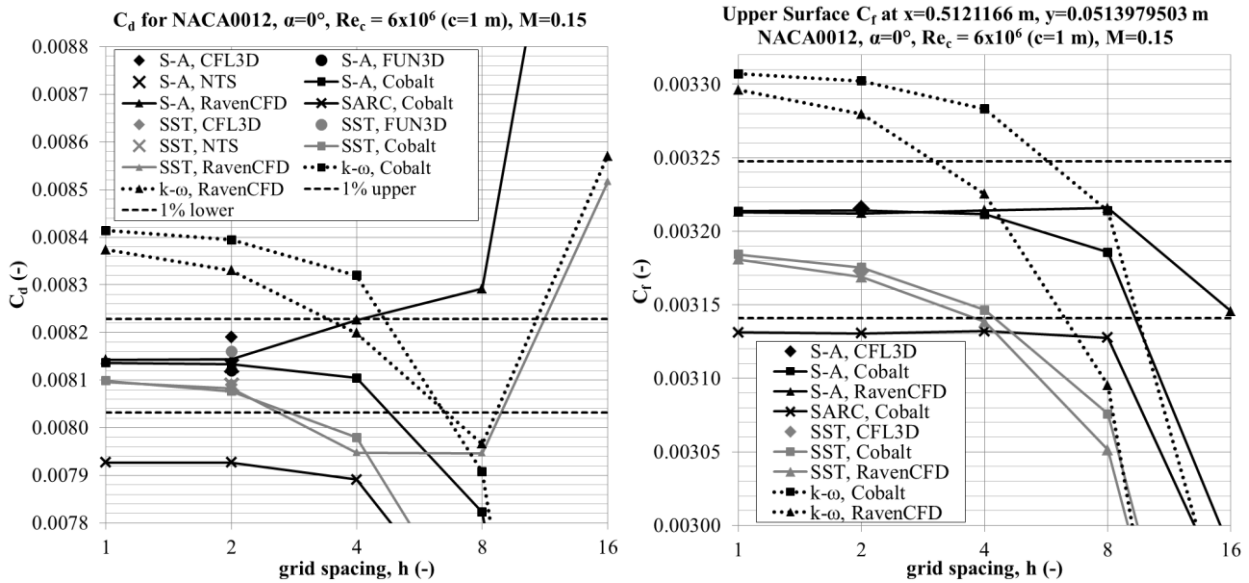


**a) Airfoil drag coefficient** **b) Skin friction coefficient at a point**

**Fig. 11 NACA 0012, $\alpha = 0°$, $C_d$ and $C_f$ from RANS turbulence models.**

Figure 12 shows the local $C_f$ predicted values for the NACA 0012 at $\alpha = 0°$ from the flow solvers' various RANS turbulence models for the 2nd finest grid; Fig. 12b shows a closer view, where the scale zooms to 10% chord length. Over nearly the entire upper surface, differences among the same turbulence models but different solver stay below 0.5% for S-A and SST and below 1.0% for k-ω. Among the turbulence models, differences between S-A and SST remain below 1.5%, below 3% between S-A and k-ω, and 2-6% between S-A and SARC. Differences are significantly larger inside the region of predicted transition from laminar to turbulent boundary layer. For the SST model in this region, the maximum difference between Cobalt and CFL3D is 15%; 35% between RavenCFD and CFL3D; and 44% between Cobalt and RavenCFD. For the k-ω model in this region, the maximum difference between Cobalt and RavenCFD is 19%. The S-A models compare well with each other, even in this region, with maximum differences not exceeding 1.0%. Thus, it may be generally concluded the turbulence models are implemented correctly in the various flow solvers for a non-zero pressure gradient; however, further evaluation and validation would be prudent in cases where flow information must be accurate within and around the transition region.

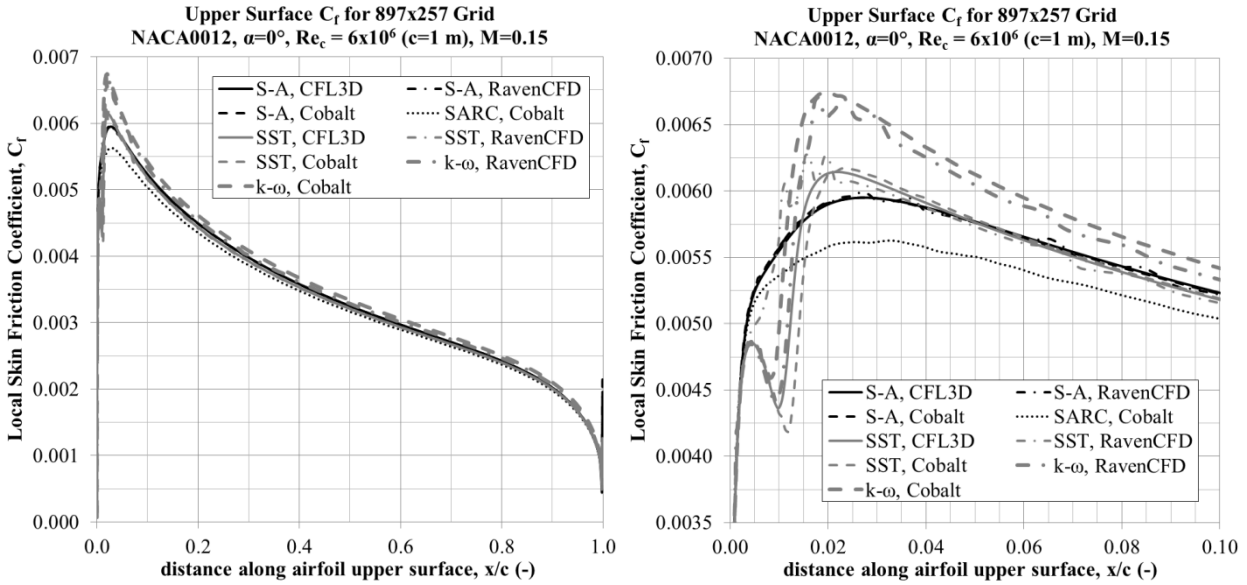


**a) Skin friction profile** **b) Close-up view of skin friction values**

**Fig. 12 $C_f$ along NACA 0012 upper surface at $\alpha$ = 0° from solutions on 2nd finest grid.**

For code verification, Table 3 shows observed order of accuracy, and for solution verification it shows total estimated uncertainty due to numerical error for $C_d$ and $C_f$ for several turbulence models in Cobalt and RavenCFD. All turbulence model results are better than or comparable to those for the turbulent flat plate and show less 1st-order behavior, most likely because the leading-edge singularity and intersecting boundary conditions are absent in this application. Because there are no FUN3D and CFL3D observed-order and uncertainty data for comparison, one cannot confidently declare verified turbulence models for this case; however, since their performance is comparable to that of Cobalt and RavenCFD for the flat plate, which in turn were comparable to the NASA benchmark solutions for the flat plate, verification or at least some degree of confidence may be inferred. All evaluated turbulence models for this case display significantly less numerical uncertainty (≤ 0.5%) than the experiment's measurement uncertainty (2.5%) [26]. Such solution behavior further confirms that the turbulence models are implemented correctly for this case.

**Table 3 NACA 0012 at $\alpha$ = 0° observed order of accuracy and total numerical uncertainty.**

| NACA 0012 Airfoil, $\alpha$=0°, $M$=0.15, $Re_c$ = 6x10^6 | | | | | |
|---|---|---|---|---|---|
| Turbulence Model | Flow Solver | $C_d$ | | $C_f$ at $x/c$=0.51, $y/c$=0.051 | |
| | | $\hat{p}$ | $U_{Tot,Num}$ | $\hat{p}$ | $U_{Tot,Num}$ |
| S-A | Cobalt | 3.55 | 0.03% | 2.25 | 0.02% |
| | RavenCFD | 5.78 | 0.02% | 1.35 | 0.02% |
| SST | Cobalt | 2.14 | 0.11% | 1.70 | 0.28% |
| | RavenCFD | 3.43 | 0.16% | 1.33 | 0.02% |
| k-ω | Cobalt | 1.94 | 0.10% | 2.00 | 0.06% |
| | RavenCFD | 1.59 | 0.52% | 1.74 | 0.50% |
| SARC | Cobalt | 6.84 | 0.004% | 0.99 | 0.02% |

Table 4 summarizes the model validation activity by comparing the RANS results with the experimental data of Ladson [26]. The SST results, except for FUN3D (albeit for the 2nd finest mesh rather than for the finest), all predict within 0.1% of the experimental measurement, an excellent agreement. For all flow solvers presented in the table, S-A, SST, and SARC predict $C_d$ within the experimental uncertainty of 2.5%. Even the k-ω predictions match closely to experiment, differing by less than 4%. Thus, for the NACA 0012 airfoil at $\alpha$ = 0°, all the $C_d$ predictions from the turbulence models under consideration match well with experiment. Additional comparisons of these four turbulence models show fair to good agreement with experiment for subsonic flow over various airfoils [6 – 9].

**Table 4 NACA 0012 at $\alpha$ = 0° RANS Turbulence Models vs. Experiment [26].**

| NACA 0012 Airfoil, $\alpha$=0°, $M$=0.15, $Re_c$ = 6x10$^6$ | | | | |
|---|---|---|---|---|
| Turbulence Model | Flow Solver | Grid | $C_d$ | Diff (%) |
| Experiment, Ladson (1988) | | - | 0.008092 | - |
| S-A | Cobalt | $h_1$ | 0.008137 | 0.55 |
| | RavenCFD | $h_1$ | 0.008143 | 0.63 |
| | CFL3D | **$h_2$** | 0.008190 | 1.21 |
| | FUN3D | **$h_2$** | 0.008120 | 0.35 |
| | NTS | **$h_2$** | 0.008130 | 0.47 |
| SST | Cobalt | $h_1$ | 0.008099 | 0.09 |
| | RavenCFD | $h_1$ | 0.008096 | 0.05 |
| | CFL3D | **$h_2$** | 0.008090 | -0.02 |
| | FUN3D | **$h_2$** | 0.008160 | 0.84 |
| | NTS | **$h_2$** | 0.008090 | -0.02 |
| k-ω | Cobalt | $h_1$ | 0.008414 | 3.98 |
| | RavenCFD | $h_1$ | 0.008374 | 3.48 |
| SARC | Cobalt | $h_1$ | 0.007927 | -2.04 |

## IV. Summary and Conclusions

The S-A turbulence model in NASA-Langley's CFL3D and FUN3D flow solvers has been previously verified 2nd-order accurate [18], and for three unit-level applications this study has compared the NASA numerical benchmark solutions with solutions obtained from S-A, SARC, SST, and k-ω turbulence models in Cobalt and RavenCFD. Of the 80 total number of case evaluations (refer to Tables 1 through 3), the following seven cases clearly demonstrate solutions that approach 2nd-order observed accuracy ($1.8 \leq \hat{p} \leq 2.2$): for the flat plate, CFL3D S-A $C_f$, Cobalt SST $C_f$, Cobalt SARC $C_f$, and Cobalt k-ω $C_d$; none for the planar jet; for the airfoil, Cobalt SST $C_d$, Cobalt k-ω $C_d$, and Cobalt k-ω $C_f$. This 2nd-order asymptotic behavior is not present in any other cases, despite the systematic mesh refinement. Considering that formal order of accuracy of the code may reduce to 1st order in the presence of the singularities noted, mixed-order solutions ($0.9 \leq \hat{p} \leq 2.2$) may be included; thus, 41 of the 80 evaluations make the case for asymptotic behavior between 1st and 2nd order. Further, numerical uncertainty is estimated to be less than 1.7% in all of the 80 cases and is less than 0.5% in 90% of the cases. Thus, since Cobalt and RavenCFD turbulence models perform comparable to NASA's verified models and since a majority of the case evaluations demonstrate reasonably asymptotic behavior, it is suggested that these turbulence models are implemented correctly (or are "pseudo-verified") for these or similar flow conditions and configurations. Along with the pseudo-verification, this study identifies for these turbulence models where the largest errors exist and where to focus efforts to reduce the uncertainty. This study has also provided some turbulence model validation by comparing computational results with experiment. Specifically, this was accomplished by showing good agreement with experiment for the turbulent flat plate, where all the turbulence models show no more than 4.8% difference from experiment $C_f$ values for $x/L > 0.05$, and where the models average between 1% (S-A, SST, SARC) and 2-3% difference from experiment. For the downstream velocity profiles in the planar jet case, the computed solutions show excellent agreement (within a few percent) with experiment for the S-A and SARC turbulence models and good agreement (within 10%) for the SST and k-ω models. For the NACA 0012 case $C_d$ at $\alpha$ = 0°, the S-A and SST models agree within 1.2% of experiment, the SARC model agrees within 2%, and k-ω within 4%.

For future code verification studies, whether pure or comparative like this one, this study highlights the need for case models which are free of singularities and/or potentially coupled or conflicting boundary conditions. Even so, the absence of singularities and intersecting boundary conditions does not guarantee clean verification, as noted in the airfoil case. An additional consideration is 2-D versus 3-D code verification. While flow velocities are low and geometries are simple in these cases, both turbulent flow and experimental measurement are fundamentally 3-D; thus, 2-D turbulence models may not accurately or correctly represent the actual flow physics, such that 3-D models should be considered for further verification and validation.

## Acknowledgments

The authors gratefully acknowledge the close cooperation and prompt support of RavenCFD developer, James Carpenter of Corvid Technologies, and Cobalt developers, Robert Tomaro and William Strang of Cobalt Solutions. This work was supported in part by a grant of computer time from the Department of Defense (DoD) High Performance Computing Modernization Program at the US Army Engineer Research and Development Center, a DoD Supercomputing Resource Center in Vicksburg, Mississippi. The authors also acknowledge the work of Chris Rumsey, his colleagues at NASA-Langley, as well as partners in industry and academia, for their efforts to develop and maintain the collaborative website, "Turbulence Modeling Resource," URL: http://turbmodels.larc.nasa.gov.

## References

[1] Grismer, M.J., Strang, W.Z., Tomaro, R.F., and Witzeman, F.C., "Cobalt: A parallel, implicit, unstructured Euler/Navier-Stokes solver," *Advances in Engineering Software,* Vol. 29, No. 3-6, 1998, pp. 365-373. doi: 10.1016/S0965-9978(97)00075-6

[2] Forsythe, J.R., Strang, W.Z., and Hoffmann, K.A., "Validation of Several Reynolds-Averaged Turbulence Models in a 3D Unstructured Grid Code," AIAA Paper 2000-2552, June 2000.

[3] Kotapati-Apparao, R.B., Squires, K.D., and Forsythe, J.R., "Prediction of the Flow over an Airfoil at Maximum Lift," AIAA Paper 2004-0259, January 2004.

[4] Bigarella, E.D.V., and Azevedo, J.L.F., "Advanced Eddy-Viscosity and Reynolds-Stress Turbulence Model Simulations of Aerospace Applications," *AIAA Journal*, Vol. 45, No. 10, October 2007, pp. 2369-2390. doi: 10.2514/1.29332

[5] Kitamura, K., and Shima, E., "Simple and Parameter-Free Second Slope Limiter for Unstructured Grid Aerodynamic Simulations," *AIAA Journal*, Vol. 50, No. 6, June 2012, pp. 1415-1426. doi: 10.2514/1.J051269

[6] Ghoreyshi, M. Jirasek, A., and Cummings, R.M., "Computational Investigation into the Use of Response Functions for Aerodynamic-Load Modeling," *AIAA Journal*, Vol. 50, No. 6, June 2012, pp. 1314-1327. doi: 10.2514/1.1J051428

[7] Garbaruk, A., Shur, M., Strelets, M., and Spalart, P.R., "Numerical Study of Wind-Tunnel Walls Effects on Transonic Airfoil Flow," *AIAA Journal*, Vol. 41, No. 6, June 2003, pp. 1046-1054. doi: 10.2514/2.2071

[8] Yang, J.-Y., Hsieh, T.-J., and Wang, C.-H., "Implicit Weighted Essentially Nonoscillatory Schemes with Antidiffusive Flux for Compressible Viscous Flows," *AIAA Journal*, Vol. 47, No. 6, June 2009, pp. 1435-1444. doi: 10.2514/1.38148

[9] Celic, A., and Hirschel, E.H., "Comparison of Eddy-Viscosity Turbulence Models in Flows with Adverse Pressure Gradient," *AIAA Journal*, Vol. 44, No. 10, October 2006, pp. 2156-2169. doi: 10.2514/1.14902

[10] Rumsey, C.L., and Spalart, P.R., "Turbulence Model Behavior in Low Reynolds Number Regions of Aerodynamic Flowfields," *AIAA Journal*, Vol. 47, No. 4, April 2009, pp. 982-993. doi: 10.2514/1.39947

[11] Bassina, I., Strelets, M., and Spalart, P.R., "Response of Simple Turbulence Models to Step Changes of Slip Velocity," *AIAA Journal*, Vol. 39, No. 2, February 2001, pp. 201-210. doi: 10.2514/2.1301

[12] Shur, M.L., Strelets, M.K., Travin, A.K., and Spalart, P.R., "Turbulence Modeling in Rotating and Curved Channels: Assessing the Spalart-Shur Correction," *AIAA Journal*, Vol. 38, No. 5, May 2000, pp. 784-792. doi: 10.2514/2.1058

[13] Barone, M.F., Oberkampf, W.L., and Blottner, F.G., "Validation Case Study: Prediction of Compressible Turbulence Mixing Layer Growth Rate," *AIAA Journal*, Vol. 44, No. 7, July 2006, pp. 1488-1497. doi: 10.2514/1.19919

[14] Alvi, F.S., Ladd, J.A., and Bower, W.W., "Experimental and Computational Investigation of Supersonic Impinging Jets," *AIAA Journal*, Vol. 40, No. 4, April 2002, pp. 599-609. doi: 10.2514/2.1709

[15] Wurtzler, K.E., and Morton, S.A., "Accurate Drag Prediction Using *Cobalt*," AIAA Paper 2004-0395, January 2004.

[16] Oberkampf, W.L., and Roy, C.J., *Verification and Validation in Scientific Computing*, Cambridge University Press, Cambridge, England, 2010, Chaps. 2, 5, 7, 8, 10, 13.

[17] Rumsey, C.L., "Turbulence Modeling Resource," NASA-Langley Research Center, Hampton, Virginia, URL: http://turbmodels.larc.nasa.gov [cited 7 June 2012].

[18] Rumsey, C.L., and Thomas, J.L., "Application of FUN3D and CFL3D to the Third Workshop on CFD Uncertainty Analysis," NASA TM-2008-215537, November 2008.

[19] "Cobalt Version 5.0 User's Manual," Cobalt Solutions, LLC., Ohio, 2010.

[20] Gottlieb, J.J., and Groth, C.P.T., "Assessment of Riemann Solvers for Unsteady One-Dimensional Inviscid Flows of Perfect Gases," *Journal of Computational Physics*, Vol. 78, 1988, pp. 437-458. doi: 10.1016/0021-9991(88)90059-9

[21] Toro, E.F., Spruce, M., and Speares, W., "Restoration of the Contact Surface in the HLL-Riemann Solver," *Shock Waves*, Vol. 4, No. 1, 1994, pp. 25-34. doi: 10.1007/BF01414629

[22] "Computational Fluid Dynamics," Corvid Technologies, URL: http://www.corvidtec.com/index.html [cited 7 June 2012].

[23] "Unique Contributions to the CFD Discipline," Aerospace Engineering Computational Fluid Dynamics Laboratory, North Carolina State University, Raleigh, North Carolina, URL: http://www.mae.ncsu.edu/cfd/overview/intro.html [cited 7 June 2012].

[24] Spalart, P.R., and Shur, M.L., "On the Sensitization of Turbulence Models to Rotation and Curvature," *Aerospace Science and Technology*, Vol. 1, No. 5, 1997, pp. 297-302. doi: 10.1016/S1270-9638(97)90051-1

[25] Bradbury, L.J.S., and Riley, J., "The spread of a turbulent plane jet issuing into a parallel moving airstream," *Journal of Fluid Mechanics*, Vol. 27, Part 2, February 1967, pp. 381-394. doi: 10.1017/S0022112067000400

[26] Ladson, C.L., "Effects of Independent Variation of Mach and Reynolds Numbers on the Low-Speed Aerodynamic Characteristics of the NACA 0012 Airfoil Section," NASA TM-4074, October 1988.

[27] Roy, C.J., and Oberkampf, W.L., "A Comprehensive Framework for Verification, Validation, and Uncertainty Quantification in Scientific Computing," *Computer Methods in Applied Mechanics and Engineering*, Vol. 200, No. 25-28, 2011, pp. 2131-2144. doi: 10.1016/j.cma.2011.03.016

[28] Wieghardt, K., and Tillmann, W., "On the Turbulent Friction Layer for Rising Pressure," NACA TM-1314, October 1951.

[29] Schetz, J.A., *Boundary Layer Analysis*, Prentice-Hall, New Jersey, 1993, Chaps. 2, 7.

[30] Devenport, W.J., Schetz, J.A., and Vadapalli, B., "Boundary Layer Codes for Students in Java, Version 2.1," Department of Aerospace and Ocean Engineering, Virginia Tech, Blacksburg, Virginia, URL: http://www.engapplets.vt.edu [cited 7 June 2012].

[31] Bradbury, L.J.S., "The Structure of a Self-Preserving Turbulent Plane Jet," *Journal of Fluid Mechanics*, Vol. 23, Part 1, 1965, pp. 31-64. doi: 10.1017/S0022112065001222

**Chapter 3**: In review for publication in *International Journal of Computational Fluid Dynamics*

# Optimization Under Uncertainty: 2-D Tractor-Trailer Base Flaps

Major Jacob A. Freeman, USAF (jacobf72@vt.edu) and Christopher J. Roy (cjroy@vt.edu)

*Virginia Tech, Blacksburg, Virginia 24061*

**Abstract** As precursor to a more complex 3-D design optimization, this 2-D tractor-trailer study seeks primarily to develop an effective and efficient methodology, as well as a good design for trailer base flaps that reduce the aerodynamic drag. The model includes six design variables with generous constraints, and this study includes the following uncertain effects on drag prediction: wind speed and direction, truck speed and elevation, turbulence model parameters, steady Reynolds-averaged Navier-Stokes (RANS) approximation, and numerical approximation. To down-select models for the 3-D study and to provide greater confidence that a global minimum is found, this study also compares efficiency and accuracy of two optimization algorithms (evolutionary algorithm (EA) and dividing rectangles (DIRECT)), twelve surrogate models, six sampling methods, and surrogate-based global optimization (SBGO) methods. This study uses the DAKOTA optimization and uncertainty quantification framework to interface the RANS flow solver, grid generator, and optimization algorithm. The computational model is a simplified full-scale tractor-trailer with flow at highway speed. Compared with the no-flaps result, the optimized design yields 36.3% reduction in wind-averaged drag. For the optimized design, the estimate of total predictive uncertainty is $^{+11.3\%}_{-11.2\%}$; 11% of this uncertainty comes from model form (computation vs. experiment) and numerical approximation (due in this case to significant flow unsteadiness). The total predictive uncertainty is also presented in the form of a probability box, which may be used to decide how to improve the model and reduce uncertainty. The linear Gaussian process best fits the data set generated by EA and DIRECT, and the most promising surrogate-sampling combinations for use by SBGO methods are presented.

*Keywords: optimization under uncertainty, predictive uncertainty, aerodynamic shape optimization, base-drag reduction, evolutionary algorithm, surrogate-based global optimization*



# 1 Introduction

With no indication of future reduction in global fuel prices, commercial transportation companies and the US Department of Energy have for decades been working to reduce aerodynamic drag on tractor-trailers. More recently global commercial, government, and military sectors are focusing effort on reducing consumption of fossil fuels. For tractor-trailers, aerodynamic drag occurs primarily in four areas (Mason and Beebe 1978): tractor forebody; tractor-trailer gap; trailer underbody; and trailer base. The trailer underbody and base account for more than half of that aerodynamic drag (Mason and Beebe 1978). While many drag-reduction shapes and devices have been designed and analyzed (Cooper 2003; Leuschen and Cooper 2006), most companies have focused on modifications to the tractor, where the largest return-on-investment is achieved. With our research, we hope to develop geometry that will significantly reduce aerodynamic drag at the base of the tractor-trailer. Figure 1 illustrates several tractor and trailer modifications and add-on devices, including the truncated boat-tail or base flaps that are the focus of this study.

At the base of a tractor-trailer, flow features include massive separation and turbulent shear flow that lower the static pressure and generate significant pressure drag because of the pressure differential between tractor front and trailer base. While base flaps add skin-friction drag and regions of adverse pressure gradient, more significantly they force the trailing wake to shrink and stabilize, resulting in a region with pressure a little larger than the freestream, which in turn creates less pressure drag (Cooper 1985). Figure 2 illustrates this with flow visualization from 3-D computational time-averaged solutions at highway speed 57.2 mph (92 km/h) and sideslip angle, $\beta = 9.1°$. Figure 2a shows velocity streamlines and gauge pressure ($P_{gauge} = P - P_\infty$, where $P_\infty$ is freestream pressure) contours for the trailer base without flaps, and Fig. 2b shows results for the trailer with base flaps. Addition of the base flaps visibly reduces the wake size and strength, as indicated by the smaller region of recirculating flow and higher static pressure, resulting in 39% reduction in the body-axis drag coefficient for a 3-D body, $C_D$, at that sideslip angle and 36% reduction in wind-averaged drag coefficient for a 3-D body, $\bar{C}_D$. (We explain wind averaging in Section 2.6.) Because the geometry for the computational simulation is simplified and includes forebody rounding, we expect a geometrically complex, full-scale tractor-trailer to experience roughly half that amount of drag reduction; this observation is based on comparing wind-tunnel experiments with nearly identical base flaps for 1/8-scale simplified geometry that showed 19% reduction in $\bar{C}_D$ (Storms et al. 2001), and for an actual full-scale tractor-trailer that

showed 10% reduction in $\bar{C}_D$ (Lanser et al. 1991). Ten percent reduction in $\bar{C}_D$ translates to about 5% reduction in fuel consumption (ATDynamics 2012; Cooper 2003).

Numerous experimental and some computational studies have been conducted to quantify the drag reduction associated with base flaps. Using a full-scale truck at highway speed of 65 mph, wind-tunnel testing of Cooper (1985, 2003) shows 6-8% reduction in $\bar{C}_D$ for straight flaps of length $0.19W$-$0.25W$ (where $W$ is trailer width) and inward deflection of the flaps, $10 \leq \delta \leq 18°$. Using the Society of Automotive Engineers (SAE) road-test procedures for heavy trucks (SAE J1321 2012), with base flaps that are $0.47W$ in length and at $\delta$ = 15°, a commercial company claims 12% reduction in $\bar{C}_D$ at 65 mph (ATDynamics 2012; Visser et al. 2011). Road testing of Browand et al. (2005) shows 8% reduction in $\bar{C}_D$ (compared with the baseline from Cooper (2003)) for straight flaps of length $0.24W$ and best $\delta$ = 13°. Wind-tunnel testing of Hsu et al. (2004), with streamlined geometry and at 1/12 full-scale Reynolds number, shows 30% reduction in $C_D$ at zero sideslip (assuming baseline $C_D = 0.25$) for straight flaps of lengths $0.27W$ and $0.53W$ and at $9 \leq \delta \leq 12°$. Wind-tunnel testing of Ortega and Salari (2004), with streamlined geometry and non-rotating wheels, shows 16% reduction in $\bar{C}_D$ for straight flaps of length $0.35W$, $\delta_{side\ flaps}$ = 10°, $\delta_{top\ flap}$ = 11°, and $\delta_{bottom\ flap}$ = 0°. Ortega and Salari (2004) further show 19% reduction in $\bar{C}_D$ for flaps with constant-radius curvature and length $0.30W$. The 3-D computational study of Hsu and Davis (2010) with streamlined geometry (for both tractor and trailer portions of the simplified geometry, instead of only for the tractor forebody) and curved flaps shows 51% reduction in zero-sideslip $C_D$ for a flap length of $0.20W$ and $\delta$ = 9°; we expect a traditional, straight trailer body, with comparable base-drag reduction devices, to yield a smaller reduction in drag. The 2-D computational study of Doyle et al. (2008) shows 59% reduction in the body-axis drag coefficient for a 2-D body, $C_d$, at zero sideslip, for a flap length of $0.36W$ and $\delta$ = 15°. Note that 3-D computational and experimental designs produce less drag reduction because of pressure relief around 3-D bodies.

Numerous results confirm the observation that drag reduction from add-on devices and aerodynamic shaping is greater for geometries with front-edge rounding (Cooper 1985; Hsu et al. 2004; Ortega and Salari 2004; Hsu and Davis 2010). All of these studies test a relatively small number of design configurations, and most of them include wind-averaging to account for variability in wind speed and direction. Cooper (1985) shows that straight deflected flaps are slightly better than curved flaps, while Ortega and Salari (2004) show that a curved flap is best. Most of these studies show that a flap length of $0.25W$ is best, but ATDynamics (2012) and Hsu et al. (2004) show good results for a length closer to $0.5W$. We observe there is considerable variation among researchers regarding the optimal shape (curved or straight), length ($0.19$-$0.53W$), and deflection ($0 \leq \delta \leq 18°$ and whether all flaps should be deflected the same amount) of the base flaps. Thus, we conduct a computational optimization study to maximize drag reduction due to the addition of trailer base flaps that may have relatively wide ranges of curvature, length, and deflection angles. In addition, because some of the model input variables are uncertain, whether aleatory (inherent randomness) or epistemic (due to a lack of knowledge) in form (Oberkampf and Roy 2010), we propagate some sources of uncertainty within the design optimization loop. Specifically, we include within the optimization loop the aleatory uncertainty associated with side winds to predict a wind-averaged drag coefficient; our 3-D study includes both aleatory and epistemic uncertainty within the design loop (Freeman and Roy 2013).

Compared with a fine 2-D viscous solution for the simplified tractor-trailer geometry (mesh with 637,000 cells), a relatively coarse 3-D solution (mesh with 5,750,000 cells) requires 5.4 times the number of computational hours to properly converge. In terms of physical time, solutions for 240 2-D design points complete within 6-9 weeks (depending on availability of computing resources), whereas that number of 3-D design points would require 24-36 weeks. It would be desirable to accomplish the 3-D study with considerably fewer design points. Because of this 3-D computational expense and to develop and refine the design optimization process, we initially reduce the problem to two dimensions. The present study extends the work of Doyle et al. (2008) by accomplishing the following: includes within the optimization loop the uncertain effect of side winds to predict a wind-averaged drag coefficient; compares two gradient-free optimization methods; evaluates 12 surrogate models and six sampling methods; assesses the efficiency of surrogate-based optimization methods; adds a 6$^{th}$ design variable; relaxes constraints on the design variables; quantifies uncertainty for several other effects; and employs a different turbulence model. Thus, the primary goal of this 2-D study is to determine an approach that yields a good candidate design (not necessarily the global optimum) at an acceptable computational expense. The current study consists of two sub-studies: (1) determination of an appropriate approach for optimization under uncertainty using computational simulations for the truth model – results in Section 3; and (2) evaluation of optimization approaches using a surrogate model, or response surface approximation, created from the simulations of (1) – results in Section 4. We then apply these findings to our 3-D study (Freeman and Roy 2013).

# 2 Background and Methods

## 2.1 Framework and Model

The optimization framework is managed by Sandia National Laboratories' Design Analysis Kit for Optimization and Terascale Applications (DAKOTA) (Adams et al. 2009) and includes automated computational mesh generation using Gridgen (Pointwise 2006), flow calculations via the Cobalt flow solver version 5.0 (Cobalt Solutions 2010),

and design optimization by a few of DAKOTA's algorithms. Based on user-specified input parameters for the DAKOTA algorithm of choice, the optimization scheme determines appropriate design candidates (base-flap shape, orientation, and location) then awaits the returned model evaluations (wind-averaged drag coefficient for a 2-D body or $\bar{C}_d$). While it waits, we generate the model geometry and flow solver input file, feed that grid and input deck to the flow solver at the appropriate flow conditions, extract $\bar{C}_d$, and return that value to the optimization algorithm. These design candidates may be executed concurrently, depending on the algorithm. The algorithm then assesses the returned values, determines the next design points, and repeats. We illustrate this process in Fig. 3, where dashed lines represent user activity.

For the physical model, we assume a constant freestream velocity ($V_\infty$ = 30 m/s ≈ 67 mph), standard temperature ($T_\infty$ = 293.15 K), pressure ($P_\infty$ = 101.325 kPa), and density ($\rho_\infty$ = 1.204 kg/m$^3$) – corresponding to Reynolds number, $Re_{/x}$ = 1.992x10$^6$ m$^{-1}$, or $Re_W$ = 5.161x10$^6$ (Reynolds number based on trailer width), and Mach number, $M_\infty$ = 0.0874. The computational model assumes a fully turbulent boundary layer along the trailer sides and consists of a simplified Class-8 cab-over-engine tractor-trailer geometry of standard length ($L$ = 19.812 m = 65 ft*)* and width (*W* = 2.5908 m = 8.5 ft). We neglect the cab-trailer gap and other excrescence drag components (side mirrors, exhaust stack, etc.) to simplify the model and flow physics in regions not being investigated. We include the effects of uncertain wind speed and direction, based on the National Oceanic and Atmospheric Administration (NOAA) collection of average monthly wind speed measurements in 250 continental US cities between 1927 and 2002 (Dellinger 2008) and on the SAE standard practice for wind-averaging drag coefficients for trucks (SAE J1252 1981).

We use the 2-D study of Doyle et al. (2008) as a starting point then add one geometric design variable, expand the design constraints, model the effects of uncertain wind speed and direction, and compare multiple design optimization algorithms. Figure 4 shows one notional base flap geometry with six design variables that are described in Table 1: $H_1$, $L_1$, $\theta_1$, $\theta_2$, $\theta_3$, and $\delta$. We use $H_1$, $L_1$, $\theta_2$, and $\delta$ to determine three points in Cartesian space, according to Eqs. (1) through (3), where point 1 is the flap intersection at the trailer base, point 2 is the flap mid-chord, and point 3 is the flap trailing edge. These three points are then used with slopes, $\theta_1$ and $\theta_3$, to solve a system of five equations to determine the five coefficients of a quartic polynomial describing the flap geometry, $y = Ax^4 + Bx^3 + Cx^2 + Dx + E$.

$$x_1 = L; \quad y_1 = H_1 \tag{1}$$

$$x_2 = L + \frac{L_1 \cos\theta_2}{2\cos\delta}; \quad y_2 = H_1 - \frac{L_1 \sin\theta_2}{2\cos\delta} \tag{2}$$

$$x_3 = L + L_1; \quad y_3 = H_1 - L_1 \tan\delta \tag{3}$$

For the objective function, we minimize the 2-D body-axis drag coefficient,

$$C_d(\beta_i) = \frac{F_x(\beta_i)}{\frac{1}{2}\rho_\infty V_\infty^2 W} > 0 \tag{4}$$

where $F_x(\beta_i)$ is the axial force (N) at the respective sideslip angle, $\beta_i$ (deg), which is a function of pressure and viscous forces (skin friction) acting over the body surface and flaps. This force is predicted using the Cobalt flow solver (Cobalt Solutions 2010).

Table 1 describes the base flap design variables and we now explain the constraints. The non-load-bearing flap is constrained by federal regulation to not extend more than 5 ft (1.524 m) from the trailer base (US Code of Federal Regulations 2004), but we further constrain that length, $L_1$, to 4 ft (1.219 m) to reduce the likelihood of overlapping the trailer base centerline, which may preclude the added complexity, weight, and expense of a secondary hinge. $H_1$ must be at least the flap chord length, or $L_1/\cos\delta$, and since we specify an arbitrary minimum $L_1 = 0.1W$ = 25.9 cm, the minimum $H_1$ must also be 25.9 cm (in the case of a straight flap). We constrain the maximum $H_1$ to 0.5 cm shy of the trailer edge, to allow space for the flap computational mesh. We require positive angles for $\theta_1$, $\theta_2$, and $\delta$ to reduce likelihood of extension beyond the trailer sides, where the flap would be certain to increase drag, and we limit them to 30° to avoid extremely adverse pressure gradients and limit unwelcome skewness in the computational mesh. We grant a healthy range of values for $\theta_3$ to avoid inappropriately limiting the problem. Since each computational simulation is expensive, we eliminate infeasible design candidates before they are submitted to the flow solver. Thus, we exclude the nonlinear minimum constraint, $H_1 \geq L_1/\cos\delta$, from the optimization model and determine whether a design candidate is infeasible (overlaps the centerline); if it is, we assign it a large value, $C_d$ = 10, thereby penalizing that combination of design parameters.

For the computational model, we modify a structured C-grid for the 2-D flow field around the simplified tractor-trailer geometry by inserting a point-matching block aft of the trailer. The computational domain extends 10 tractor-trailer lengths forward and to each side of the vehicle and 11.5 lengths downstream. The mesh used for the optimization study, shown in Fig. 5, features 205 points normal to the vehicle, 885 points along the front and side surfaces, 641 points along the trailer base, and 437 points normal to the base – for a total of 637,264 quadrilateral

cells. We place 80 cells within the estimated boundary layer region and computations reveal an average first cell $y^+ \approx 0.4$; rule of thumb for viscous modeling is 20 cells to resolve the boundary layer with first cell $y^+ \leq 1$. (Refer to Schetz (1993) for further explanation of $y^+$.) In Figs. 5a and 5b, we show the domain "shell", where the flap geometry and its corresponding domains are missing. After the optimization algorithm selects flap design candidates, we use those flap shape variables to determine the 97 *tanh*-spaced coordinates that are in turn used to generate and insert the final piece of the mesh puzzle, shown for one flap shape in Fig. 5c. All vehicle surfaces and flaps have a no-slip, adiabatic wall boundary condition, and the exterior boundaries are modified Riemann farfield at the specified $P_\infty$, $T_\infty$, and $M_\infty$. All values for $\beta$ are positive, such that the simplified tractor-trailer port side is windward for $\beta > 0°$. We select this grid based on the grid resolution study in Section 2.5.

### 2.2 Flow Solver and Turbulence Model

Cobalt solves the 3-D unsteady, compressible Euler and Navier-Stokes equations at cell centers, uses the method of finite volumes, and is parallelized. It is designed to use structured or unstructured mesh topologies, including prisms, tetrahedra, and hexahedra in 3-D, or quadrilaterals and triangles in 2-D, all with arbitrary cell skewness, curvature, and/or stretching rates. Cobalt combines the exact Riemann solver of Gottlieb and Groth (1988) and the approximate Riemann solver of Harten-Lax-van Leer Contact (HLLC) (Toro et al. 1994) with a least-squares method to attain 2nd-order spatial accuracy, and it uses a point-implicit method with Newton sub-iterations for 2nd-order temporal accuracy. Its implicit method allows for Courant-Friedrichs-Lewy (CFL) numbers as large as $1x10^6$. Specifying 1st-order accuracy in time, as we do in this study, typically provides a time-averaged solution. Cobalt offers eight turbulence models, including the one used for this study, that have formally 2nd-order accurate numerical implementations but may revert to 1st-order in the presence of discontinuities, contact surfaces, large flow gradients, or singularities. Cobalt offers one discontinuous flux limiter that may influence the solution observed order of accuracy. (Cobalt Solutions 2010; Grismer et al. 1998; Wurtzler and Morton 2004)

To reduce computational mesh cell count and overall computation time for applications with large Reynolds number flow, as in this study, all scales of turbulent flow are modeled with the one-equation Spalart-Allmaras (S-A) Reynolds-averaged Navier-Stokes (RANS) turbulence model. For the S-A model detailed equations and coefficients, see Forsythe et al. (2000). The S-A turbulence model is often applied to aircraft applications, including predicting separation due to adverse pressure gradients. The S-A model is a function of velocity, kinematic viscosity, vorticity, and wall distance. In the laminar sub-layer it uses a wall-destruction function to reduce turbulent viscosity, and to transition the boundary layer from laminar to turbulent it includes trip functions. The S-A model relies on 11 empirical constants (Forsythe et al. 2000).

In addition to its accuracy for predicting separated flow, we select the S-A turbulence model according to the results of the verification and validation study of Freeman and Roy (2012a). In that earlier study involving 2-D cases that are representative of the flow properties of interest in the current study (a turbulent flat plate, a planar shear layer, and an NACA 0012 airfoil, all in low subsonic flow), we accomplish the following: verify that Cobalt has correctly implemented the S-A model, compared with implementations by two separate NASA codes; verify that Cobalt S-A solutions display nearly asymptotic behavior (as the computational mesh is refined, the solution observed order of accuracy approaches the code formal order of accuracy (Oberkampf and Roy 2010)) and maintain total numerical uncertainty less than 0.2%; and validate the Cobalt S-A solutions against experimental data – within an average of 1% (3.6% maximum) for the local skin friction coefficient on the flat plate, within 1% for ¾ of the shear layer velocity profile for the planar shear case (and within 2-3% for the rest), and within 0.6% for the drag coefficient of the airfoil at 0° angle of attack. These results suggest the RANS S-A turbulence model is suitable for this optimization study.

### 2.3 Optimization Schemes

Due to the expected discontinuities among the solutions, we initially assume this problem is non-convex and cannot guarantee a unique solution; we later confirm this assumption after numerous solutions are generated. Further, we seek the design with global minimum $\bar{C}_d$ if possible, though the reality of a limited number of function evaluations suggests we may determine a *good* design that is better than existing solutions and that is not necessarily the *best* design. Because we seek an efficient optimization method that can be applied to the more complex, more computationally expensive 3-D version of this problem, we consider more than one design optimization method. Linearized methods do not apply due to discontinuous input/output relationships (associated with discontinuous flow separation effects on drag), partial differential equations, and a complex flow field with large gradients. Gradient-based methods are less effective because of discrete design selection, where prediction of boundary-layer separation on the base flap will rule out a design (see Fig. 6 for a depiction of separated flow on the base flap when the deflection angle becomes too large), and since the mesh must be regenerated with each design. Branch-and-bound methods are less effective because the design space is continuous. And since the viscous solutions are computationally expensive, we can run tens or hundreds of design points, not thousands (note for this study, we complete nearly 2,300 simulations, where each design point requires six simulations). Hence, we investigate an evolutionary or genetic algorithm and DIviding RECTangles (DIRECT) – both are nonlinear, non-gradient-based,

coded within DAKOTA, and have shown promising results even with a small population of samples (Yao et al. 2011). We also investigate surrogate-based global optimization (SBGO) methods, where the surrogates may be linear and gradient-based; we detail SBGO separately in Section 2.8.

### *2.3.1 Genetic Algorithms*

While not necessarily a perfect fit because they may require a large number of solutions and do not guarantee finding the global minimum, genetic algorithms apply to both discrete and continuous problems, *may* find the global minimum, and tend to find a "good" design (Adams et al. 2009; Eddy and Lewis 2001; Yao et al. 2011). Genetic algorithms are based on Darwin's theory of "survival of the fittest," in that the most fit candidates – in this case, those with the smallest $\bar{C}_d$ – survive from one generation to the next and remain in the mating pool, while the others are eliminated. However, the algorithm allows candidates with lower fitness to be selected as well, although with lower probability, since they may contain a trait or traits that may prove useful when crossed with another candidate. The algorithm starts with a randomly generated population of candidates drawn from the design space, evaluates the fitness of each candidate then creates a new population by selecting two parent candidates, crossing them to form new offspring or making an exact copy of the parent, allowing for mutations in the offspring, and placing the offspring in the new population for the next fitness evaluation. The success of this algorithm depends on the size of the initial population and the number of generations computed (Arora 2004). From results of a preliminary study we conducted with two of the design variables, we rule out using DAKOTA's single-objective function genetic algorithm (SOGA) (Eddy and Lewis 2001) in favor of the common optimization library interface evolutionary algorithm (COLINY-EA) (Adams et al. 2009), because, according to our implementation, the COLINY-EA designs converged more efficiently to the optimum design. This may be due in part to COLINY-EA's "self-adaptive mutation, which modifies the mutation scale dynamically" (Adams et al. 2009), as well as its ability to select design points that cover much of the design space.

Table 2 details the specific settings for the COLINY-EA algorithm, where we select many randomization parameters to increase the likelihood of discovering the global minimum. DAKOTA recommends the crossover hill-climber (CHC) genetic algorithm (Lozano et al. 2004; Adams et al. 2009), incorporated within COLINY-EA, for engineering applications, rather than the elitist algorithm that sometimes biases the parent pool with the best candidates at the expense of discovering a favorable trait that may be found in a "less desirable" candidate; we thus select CHC but with zero design candidates carried from the existing and newly generated population, thereby maximizing the total number of random design candidates. COLINY-EA allows a mix of continuous and discrete design variables, so we specify continuous $L_1$ and $H_1$ and discrete $\theta_1$, $\theta_2$, $\theta_3$, and $\delta$, in increments of 1°.

### *2.3.2 DIviding RECTangles (DIRECT)*

Gablonsky's version of DIRECT implemented at North Carolina State University (NCSU-DIRECT) (Finkel 2003) combines local search in regions of the design space that indicate good fitness levels with global search in unexplored areas to increase likelihood that the global minimum is found. The algorithm begins at the design space center of a normalized hyper-cube, subdivides, and evaluates the objective function at those points. Figure 7 illustrates this process and shows two of the six design variables. The starting point is illustrated by the center point in Fig. 7, for $L_1$ = 0.75 m and $\theta_1$ = 15°. Regions with better fitness levels are further subdivided in hyper-rectangles and evaluated until the optimum is found. The results in Fig. 7 represent 157 design points or 28 iterations of NCSU-DIRECT; several points in the figure are coincident because these variables are held constant while the effect of variation in the other design variables are evaluated. In our preliminary 2-D study using two design variables, we found that NCSU-DIRECT did not determine the same design obtained by COLINY-EA but came within 12%. However, its algorithm required only 25% of the number of design candidates to arrive at a slightly inferior solution, so we include it for further investigation. An additional limitation of NCSU-DIRECT is that maximum sample size may not exceed twice the number of design variables, whereas for COLINY-EA we may specify the sample size according to our method of concurrent solutions. NCSU-DIRECT requires all continuous design variables, and its specific settings are detailed in Table 3.

## 2.4 Uncertainty Due to Numerical Error

For the most promising candidate design, we estimate the uncertainty due to numerical error. To do this, we quantify the numerical error that consists of round-off error, iterative error or statistical sampling error, and discretization error; we then quantify the numerical uncertainty by applying a factor of safety to the numerical error. We do not directly address round-off error in this study, but using double-precision computations in the flow solver should keep round-off error to well below 1% of the discretization error. For statistical sampling error, since the solution output oscillates about a steady-state value due to vortex shedding in the flow (addressed in Section 2.5), we perform time-averaging of the forces output. Statistical error may arise based on sample size or total number of iterations. However, since we converge each solution to the equivalent of machine zero – which for this case Cobalt reduces the iterative continuity residual by 6-8 orders of magnitude – and average over only the oscillatory steady

state, we assume zero error due to statistical sampling. This averaging process precludes estimation of iterative error. (Oberkampf and Roy 2010)

We approximate the uncertainty due to numerical error according to its definition,

$$U_{Numerical} = U_{Discretization\ Error} + U_{Round\text{-}off\ Error} + U_{Sampling\ Error} \quad (5)$$

where $U_{Sampling\ Error} = 0$ for these cases, and $U_{Round\text{-}off\ Error} \approx 1\%$ of the discretization error. Using Roache's Grid Convergence Index with a modified implementation by Oberkampf and Roy (2010) for the factor of safety, $F_s$, when using solutions from three or more systematically refined meshes,

$$U_{Discretization\ Error} = \frac{F_{s_i}}{r^{p_f} - 1}\left|C_{d,i} - C_{d,i+1}\right| \quad (6)$$

where $F_{s_i} = 1.25$ for $\chi = \left|\frac{\hat{p}_i - p_f}{p_f}\right| \leq 0.1$, or $F_{s_i} = 3$ for $\chi > 0.1$

where observed order of accuracy, $\hat{p}_i = \frac{ln\left|\frac{C_{d,i+2} - C_{d,i+1}}{C_{d,i+1} - C_{d,i}}\right|}{ln(r)}$, (7)

and where $r$ is the grid refinement factor, or $r = \left(\frac{N_{cells,i}}{N_{cells,i+1}}\right)^{1/2} = 2$ for these 2-D grids, $p_f$ is the formal order of accuracy (here $p_f = 2$), and $i$ is the respective grid level (e.g., 1 is finer than 2).

### 2.5 Solution Convergence and Computational Grid Selection

To reduce computation time for each design candidate, we use the solver in steady-state mode. Steady state may be achieved by using a half-grid with a symmetry boundary condition along the centerline, but this is not feasible for asymmetric cases with sideslip angle. Thus we need to balance mesh resolution, CFL number (which is effectively a time-step size), and accuracy. To accomplish steady state for flow physics that are inherently unsteady, as is the case for massive separation, vortex shedding, and recirculation zones behind a bluff body such as a truck, we use Cobalt's maximum CFL number, $1x10^6$, and time-average the solution output. Because of Cobalt's limiter, the solution residuals iteratively converge roughly eight orders of magnitude for the continuity equation and only two orders of magnitude for the turbulence equation, as shown in Fig. 8a, rather than the desired 12-14 orders for a double-precision computation. While we do not monitor residuals for convergence, we evaluate in Section 3.3 the difference between this steady-state assumption, which fails to resolve all the flow physics because of the large time-step, and a time-accurate simulation, which uses a time-step small enough to resolve both small- and large-scale eddy motion.

Instead of monitoring iterative residuals, we visually monitor the instantaneous force output until it has leveled, as shown in Fig. 8b, then we average the body-axis force, $F_x$, over the level region and use it to calculate $C_d$, per Eq. (4). To avoid the need to monitor each solution in this manner, we determine a sufficient number of iterations for a "worst case" (largest sideslip angle and flap design with adverse pressure gradients), apply that number to all cases, and perform solution spot checks to confirm convergence.

Concerning mesh resolution and solution accuracy, we generate four systematically refined grids (create a fine structured mesh then remove every other point in both spatial directions for each successively coarsened mesh), which we denote $h_1$ for the finest through $h_4$ for the coarsest, and evaluate whether their solutions display asymptotic behavior. We neglect $h_1$ because its force iterative history shows strong unsteady behavior even for zero sideslip, most likely because its resolution is fine enough to capture fine-scale turbulent motion and thus override the effect of using a large CFL number. From time-averaged $C_d$ values from $h_2$, $h_3$, and $h_4$ with respective average first cell $y^+$ = { 0.40, 0.84, 1.62 }, we use Eq. (7) to calculate an observed order of accuracy, $\hat{p} = 2.58$, that is not asymptotic but is indicative of the solution values being close for $h_2$ and $h_3$; they differ by 0.7%. For the mesh of interest, $h_2$, we use Eqs. (5) and (6) to obtain $U_{Numerical} = 0.74\%$. Thus, we select $h_2$ based on the following rationale: (1) the observed order of accuracy is reasonable and total numerical uncertainty is less than 1%; (2) computed values for $C_d$ on $h_2$ and $h_3$ differ by less than 1%; (3) while the computed iterative force oscillates, the amplitude is smaller for $h_2$ than for the coarser and finer solutions; (4) its fully turbulent predicted boundary layer thickness, defined as the distance between the surface and where 99% of the freestream velocity is attained, is roughly equivalent to the thickness estimated by an empirically-based integral method (Schetz 1993), while the solution on $h_3$ estimates a boundary layer 50% larger; and (5) this mesh features 97 nodes to resolve the flap geometry, where $h_3$ provides 49, which may not adequately resolve a quartic polynomial curve.

### 2.6 Validation of SAE Wind-Averaging Method

SAE developed and has used for several decades a method for calculating the wind-averaged drag coefficient for wind-tunnel testing of trucks and buses (SAE J1252 1981). We use this wind-averaging method in the optimization

process to approximate the inner loop, which propagates the aleatory uncertainty of wind speed and direction. In other words, to obtain an ideal wind-averaged value for the body-axis drag coefficient, $\bar{C}_d$, we would run simulations for a specific design at 1,000s of sideslip angles, sampled from a normal distribution, and average those values. A slightly inferior approach would average solutions from perhaps 50-100 normally distributed sideslip angles. The SAE method, however, uses just six sideslip angles and applies a weighting function, $\psi$, to average them, as shown in Eq. (8), where $i$ corresponds to the six angles and $C_d(\beta_i)$ is calculated in Eq. (4).

$$\bar{C}_d = \frac{1}{6}\sum_{i=1}^{6} \psi_i C_d(\beta_i) \tag{8}$$

Using the SAE J1252 method (1981) and based on average wind speed (9.06 mph or 4.05 m/s) and truck speed (67.1 mph or 30 m/s), we calculate $\beta$ = { 1.770, 2.301, 4.980, 6.024, 7.180, 7.694° } and $\psi$ = { 1.2790, 0.7575, 1.2091, 0.8273, 1.0881, 0.9484 }. Rather than blindly using this process, we show in the remainder of this subsection that the sampling using six angles with appropriate weights is comparable to using a larger statistical sampling and that the sampling is sufficiently close to a normal distribution.

In Fig. 9a, we plot the empirical distribution function (EDF) of NOAA average monthly wind data from 250 cities in the continental US from 1927 to 2002 (Dellinger 2008), where each of the 3,000 data points are given an equal probability of occurrence; the distribution is close to normal, the average wind speed is 9.06 mph (4.05 m/s), and standard deviation, $\sigma$ = 2.26 mph (1.01 m/s). We randomly sample 1,000 points from the population of NOAA wind data and combine the wind speed, $V_{wind}$, with 1,000 randomly generated samples from a uniform distribution of wind direction, $0 \leq \theta_{wind} \leq 180°$ (for a symmetric vehicle), since we assume the vehicle direction is uniform random. We obtain a distribution of wind normal to the direction of tractor-trailer motion, $V_y$, and convert it to sideslip angle, $\beta$, according to Eqs. (9) and (10); $V_\infty$ is the truck speed. This results in the black curve in Fig. 9b.

$$V_y = V_{wind} \sin(\theta_{wind}) \tag{9}$$

$$\beta = \sin^{-1}\left(\frac{V_y}{V_\infty}\right) \tag{10}$$

To create a reasonable sample size for computations, we randomly generate 50 normally distributed values for $\beta$ (gray curve in Fig. 9b), based on the mean and standard deviation of the 1,000-point $\beta$-distribution, and use them as input to compute $C_d$ for a fixed design configuration of the tractor-trailer with straight flaps ($\theta_1 = \theta_2 = \theta_3 = \delta$ = 16°, $L_1$ = 0.909 m, $H_1$ = 1.2904 m). These 50 values for body-axis $C_d$ are shown as the black EDF in Fig. 9c. We compare with results from the six SAE-determined $\beta$ values (SAE J1252 1981) that are normally distributed and are shown as black squares in Fig. 9b.

These SAE sideslip angles have a standard deviation 14% smaller than for the 1,000-point distribution, and we show next whether that difference is significant. We use these six $\beta$ values for computing $C_d$ then apply the SAE weights according to Eq. (8). These results are shown as the dashed gray EDF in Fig. 9c. Results from both normally distributed and SAE-determined $\beta$ values show a log-normal distribution, since values for $C_d$ must be positive. For comparing log-normal distributions, we use geometric mean and geometric standard deviation (Weisstein 2012), where the SAE geometric mean and standard deviation for the weighted values of $C_d$ differ from those of the larger sampling by 0.2% and 2.9%, respectively. We consider these differences an acceptable trade for computing six samples per design candidate rather than 50 or more for modeling the uncertain wind speed and direction.

To further reduce computation time, we compute the solution for a given design candidate at the smallest sideslip angle, $\beta$=1.770°, using a larger number of processors (64 cores) until it is well converged (80,000 iterations). We then use that solution as the initial state for each of the other five sideslip angles, such that each of those restarted solutions requires half the number of iterations to converge and about 1/3 the number of processors (24 cores). This process facilitates greater concurrent processing efficiency on a shared computing platform with 1,000s of cores, dozens of users, and shared software licenses. Following this process, 20 design points at six $\beta$ values (an average of 42,000 core-hours) require 2-10 days, depending on availability of shared cores and licenses. We use two platforms at the Department of Defense (DoD) US Army Engineer Research and Development Center in Mississippi: *Diamond* and *Garnet*. *Diamond* is an SGI Altix ICE with 1,920 Intel Xeon dual quad-cores, 11.2 GFLOPS, and 3 GB RAM per core; *Garnet* is a Cray XE6 with 1,260 AMD Opteron dual 8-cores, 9.6 GFLOPS, and 2 GB RAM per core (US DoD High Performance Computing Modernization Program 2012).

### 2.7 Optimization Under Uncertainty and Total Predictive Uncertainty

In this problem, one of the primary inputs – coupled wind speed and direction – is stochastic. Because of this, we are compelled to conduct the design optimization under an uncertain parameter, or optimization under uncertainty (OUU). Traditionally, aleatory uncertainty may be propagated through the model via statistical sampling of the model input, which may be a normal or other probability distribution; this comprises an inner loop. Since engineering problems of interest typically have a combination of aleatory and epistemic uncertainty, the outer loop

includes the epistemic uncertain parameters that are typically characterized as an interval, resulting in interval-valued probabilities for the drag, or p-boxes. For example, we use sampling within an interval (i.e., stratified Latin hypercube sampling) to select each value for the outer loop, then at each of those values we calculate the inner loop. This process could easily require thousands to hundreds of thousands of samples evaluated with the truth model. See Oberkampf and Roy (2010) and Roy and Oberkampf (2011) for greater detail and examples.

Since this OUU process is computationally demanding and because we are primarily interested in a mean value, $\bar{C}_d$, rather than a distribution, we consider two reduced approaches: the nested method discussed above but with the novel approach of using the six SAE $\beta$ values (see Section 2.6), and a surrogate-based method that we discuss in Section 2.8.

Table 4 lists and categorizes, for this problem, uncertainty in model input, model form, and numerical approximation. In this study, we address the sources of uncertainty highlighted in the Table with bold italics. We include the aleatory uncertainty associated with wind speed and direction in the inner loop, and the epistemic uncertainties in model input are propagated through the model as an outer loop. Ideally, we desire to include both aleatory and epistemic uncertainty within the design optimization loop, and we accomplish this in our 3-D study (Freeman and Roy 2013); however, for greater simplicity in this 2-D study, we include aleatory uncertainty in the optimization loop and later include the combined epistemic and aleatory uncertainty only for the best design candidate.

To combine the effects of aleatory and epistemic uncertainty, we employ probability bounds analysis techniques to quantify these uncertainties in the form of a probability box (or p-box). For every epistemic sample or bound, we generate an EDF, each with normally distributed aleatory input values, as shown in Figs. 9a and 9c. The ensemble of these EDFs, or the extents thereof, create the resultant p-box of model input uncertainty that is shown in Section 3.3. To complete the uncertainty quantification (UQ), model form and numerical approximation uncertainty values are added to the right side and subtracted from the left side of the p-box. Total predictive uncertainty thus includes propagated uncertainty from model input, model form, and numerical approximation. This information helps the user understand relationships between model input and model output and may be used to make decisions about ways to improve the model and reduce uncertainty. (Oberkampf and Roy 2010; Roy and Oberkampf 2011)

## 2.8 Surrogate-Based Global Optimization (SBGO)

Surrogate-based global optimization (SBGO) combines the accuracy of the nonlinear, coupled, and possibly discontinuous computational flow solutions (or the truth model results) with the computational efficiency of searching a simpler, potentially smooth representation of the truth model output. To obtain the surrogate model, otherwise known as a data fit or a response surface approximation, we start with a dataset of solutions that is generated by the truth model; the design points may be determined by stochastic sampling, design of experiment, user-determined methods, or by some combination of these three approaches (as we do in this study). Based on the nature of the dataset, if it is known, the user may select an appropriate data fitting scheme; since in our case the dataset is not smooth due to the discontinuous behavior associated with flow separation at larger flap deflection angles, we try numerous data fitting methods available in DAKOTA to determine which one provides the best data fit or surrogate model. The optimization algorithm of choice is then able to inexpensively query or evaluate the surrogate millions of times, if needed, to determine a minimum or set of minima. We next use the more expensive and more accurate truth model to evaluate this design point or points, update the surrogate model with those values, and repeat until the global or an acceptable minimum is located. (Renaud and Gabriele 1993; Adams et al. 2009; Swiler et al. 2006)

For this portion of the study – assessing surrogate models, sampling methods, and SBGO methods – we significantly reduce computational expense by using a surrogate model in place of the truth model (viscous computational simulations). For example, one sampling method may specify 100 design points. We query the surrogate model at those points and, in less than one second, receive 100 values for $\bar{C}_d$. Those returned values are used to generate the various surrogate models, or secondary surrogates. We may then evaluate the secondary surrogates by comparing them with the initial surrogate model, and we may use the secondary surrogates as the starting point for the various SBGO methods.

### *2.8.1 Data Fitting Algorithms*

We compare surrogate models generated by 12 DAKOTA data fitting algorithms, namely, polynomial regression models (linear, quadratic, and cubic) (Gergonne 1974 [1815]), Gaussian process fits (constant, linear, and reduced-quadratic) (Giunta and Watson 1998), kriging spatial interpolation (constant, linear, and quadratic), artificial neural network (Zimmerman 1996), and multivariate adaptive regression spline or MARS (linear and cubic) (Friedman 1991); we do not evaluate the moving least squares method because the DAKOTA team notes it does not yet work well for global optimization (Adams et al. 2009). For all of the data fitting methods, we provide a database of the combined truth-model evaluations from COLINY-EA and NCSU-DIRECT (or solutions at 289 design points).

To determine which surrogate model is best for this particular set of data, we start by using DAKOTA to conduct a multidimensional parameter study to locate the global minimum on the response surface (Adams et al. 2009). For

the parameter studies, we first specify relatively coarse resolution of the design-variable space that results in 3.4 million evaluations of the surrogate model and 2-12 minutes on a single processor; DAKOTA is currently unable to parallelize these computations. This search returns the minimum point, and we next iteratively refine the surface around that point to better resolve the input variable values at that minimum. With this best design from each of the surrogate models, we compare it with the best design obtained from the COLINY-EA optimization study – comparing both the predicted value for $\bar{C}_d$ and the form of the predicted design.

Since it is not our purpose to conduct a comprehensive assessment of each fitting method, we briefly discuss only the two data fitting algorithms that yield the best fits for our specific datasets. The most accurate fits for our data come from DAKOTA's implementation of Gaussian process (GP) and kriging interpolation. Both GP and kriging algorithms are interpolation based and are designed to handle surfaces that are multimodal, discontinuous, and noisy – such as we expect in this study. Both algorithms assume a multivariate normal distribution in the dataset, and we specify DAKOTA's zeroth-order additive correction that forces the surrogate model to match the truth data points. The kriging method uses the maximum likelihood estimation procedure (Law and Kelton 1982) that is effective for fitting data with slope discontinuities and multiple minima/maxima. (Adams et al. 2009)

### *2.8.2 Sampling Methods*

For a complex engineering problem, the quality of the surrogate model is a direct function of the dataset upon which it is based. Therefore, we must find an acceptable balance between a large, more representative dataset and one that is smaller, less computationally expensive, and sufficiently accurate. With this balance in mind, we evaluate the following sampling methods that are available in DAKOTA: Latin hypercube sampling (LHS); orthogonal array sampling (OAS); combined OAS and LHS (OA-LHS); Box-Wilson central composite design (CCD); Box-Behnken design (BB); and problem solving environment for uncertainty analysis and design exploration with Morris one-at-a-time sampling (PSUADE-MOAT). LHS randomly samples from a uniform distribution within discrete intervals in the design space (Oberkampf and Roy 2010). OAS creates orthogonal arrays of the inputs where any two of the columns contain an equal number of all possible combinations, and it is well suited to sensitivity analysis (Hedayat et al. 1999). CCD is based on a factorial design with additional center points and selects one point at the center of the design space, at each of the constraint endpoints, and at the constraint midpoints (Box and Wilson 1951). BB is a quadratic design and selects one point at the center of the design space and at each of the constraint endpoints (Box and Behnken 1960). PSUADE is a more encompassing tool for optimization, UQ, sensitivity analysis, and surrogate modeling, but we use only its MOAT sampling procedure, designed to discriminate input variables that insignificantly affect the output (Morris 1991).

We target a sample size of about 100, while some methods are limited to fewer than 100, because we seek an SBGO method that can locate the minimum with fewer total design points or function evaluations than are used by the COLINY-EA study, which found the best design within 180 design points. For each sampling method, we specify a seed value (we arbitrarily choose *seed* = 38) to ensure repeatability for each method and relative consistency among the methods.

We do not separately evaluate each sampling method, rather we evaluate the 72 possible combinations of sampling method with data fitting algorithm (12 data fitting types and six sampling methods). These combinations create a secondary surrogate model, or a surrogate from a surrogate; we then conduct a multidimensional parameter study on each of these surrogates to locate the likely global minimum and compare that design value and form with the best design from the initial surrogate. From a few of the most promising combinations, we proceed with the optimization studies, which again are based on querying the initial surrogate model in place of the computational simulations.

### *2.8.3 SBGO Methods*

In our earlier study (Freeman and Roy 2012b), we use the linear GP data fit of the flow solver results (289 design points) as the truth model and compare nine of DAKOTA's gradient-free SBGO algorithms after one global iteration; within that single global iteration, each optimizer queries the surrogate between 70 and 20,000 times, requiring only seconds of physical time on a single processor. Because there is one objective function, each DAKOTA-implemented optimization algorithm returns one design point that should be the minimum point in the surrogate model. While six of the optimizers fare better than the other three after a single global iteration, we believe that with enough global iterations, all nine would likely arrive at the truth design (in the case where it is known *a priori*) – and there is no significant computational penalty because this would require seconds or minutes, not days or weeks. This approach has merit in the sense of automation, but the outcome is the same, which is a recommendation for one design point that needs to be assessed with the truth model (flow solver or initial data fit) and returned to the database to create an updated surrogate model; the optimizer then repeats the process on this updated response surface (Renaud and Gabriele 1993). Therefore, we abandon this process in favor of evaluating each updated surrogate model using a multidimensional parameter study, which is known to compute within a few minutes. The SBGO methods that merit further investigation should predict a design point similar in form and close in value to the surrogate model minimum design point.

# 3 Results: Optimization Under Uncertainty

## 3.1 Caveat for 2-D Flow

We begin this discussion with the caveat that all drag coefficient results are larger than they would be for a 3-D study due to pressure relief that is absent in 2-D. For example, Storms et al. (2001) conducted wind tunnel tests using the test article on which our 2-D geometry is based. Their measurements indicate, for cases of $\beta$ = 0° and $\beta$ = ±10°, that the flow separates near the front of the simplified tractor-trailer at $x/W \approx 0.05$ and reattaches at $x/W \approx 0.13$, where total vehicle length is $7.65W$. By contrast, we show in Figs. 10a and 10b the 2-D simplified tractor-trailer without base flaps at two sideslip angles compared at the same angles to a case with flaps in Figs. 10c and 10d; the images show contours of gauge pressure overlaid with velocity streamlines to highlight regions of reversed flow. At $\beta$ = 2.30° for the case without flaps (Fig. 10a), the flow reattaches but well beyond the experimentally observed location. For $\beta$ = 4.98° (Fig. 10b), much less than the 10° in experiment, the boundary layer fails to reattach. With the addition of flaps, the reattachment point for the $\beta$ = 2.30° case (Fig. 10c) moves forward by about 20%, and at $\beta$ = 4.98° (Fig. 10d) the flow manages to reattach just ahead of the base. This issue may further be related to the forebody radius of curvature. Also, for the case with flaps in the experiment (albeit a considerably different shape from those of our study), $\bar{C}_D$ = 0.23 (Storms et al. 2001), whereas our best designs yield $\bar{C}_d$ = 0.56. Hence, this study focuses on OUU and design-trait survival based on ***relative*** improvement, more than on potential improvement of the actual flow physics or on accurate estimates of $\bar{C}_d$.

## 3.2 Evolutionary Algorithm and NCSU-DIRECT

We exercise caution in comparing COLINY-EA with NCSU-DIRECT because their sampling approaches differ, particularly in that COLINY-EA permits larger concurrent evaluations, $n$ (we select $n$ = 20), and is more likely to converge to an optimum design point, whereas NCSU-DIRECT is limited in this study to $n \leq 12$ (or twice the number of design variables). In Fig. 11, we roughly normalize the comparison by collecting NCSU-DIRECT results into groups of 20, where its box sampling uses as few as two samples. We permit COLINY-EA to continue for 12 generations, by which point we are satisfied that further improvements in fitness are minimal. Barring the infeasible design candidates (where the stowed base flap overlaps the doors centerline), this corresponds to 213 feasible design points, where each point requires six function evaluations for the wind-averaging. While the COLINY-EA solutions complete within eight weeks, we run NCSU-DIRECT until the minimum volume limit is reached with 28 iterations and after 16 weeks, corresponding to 140 feasible design points.

In Fig. 11, the dashed black line shows $\bar{C}_d$ = 0.8810 for the baseline configuration without flaps, the black diamonds show feasible COLINY-EA wind-averaged values in each generation, the solid black line with circle markers shows the minimum COLINY-EA value for each generation, and the gray diamonds and line show the corresponding values for NCSU-DIRECT. The NCSU-DIRECT algorithm generally has less variation within its ($n$ = 20)-groups of $\bar{C}_d$ values because once it locates an improved design candidate, the algorithm clusters the ensuing design points around that candidate, searching for a local minimum. While COLINY-EA results show more variance because of its many randomization processes and anti-elitism, the results converge more quickly to a smaller value. Both algorithms generally show improvement with each successive generation or group of samples, but COLINY-EA is more successful at locating the design candidates with greater fitness.

COLINY-EA's best candidate (EA.174) shows 36.3% improvement over the no-flaps baseline $\bar{C}_d$, while the NCSU-DIRECT and Doyle et al. (2008) best candidates improve 33.3% and 29.1%, respectively, over the baseline. The best design from Doyle et al. (2008) shows 59% reduction in $C_d$, but that is for $\beta$ = 0° and a slightly different design space (fewer design variables and tighter constraints); our best design shows 79% reduction in $C_d$ (and 72% reduction for the best NCSU-DIRECT design) compared with the no-flaps baseline at $\beta$ = 0°. We further compare the best design from the present study with the best design from our preliminary, straight-flap study ($\delta$ = 18°, $L_1$ = 0.909 m, $H_1$ = 1.2904 m): $\bar{C}_d$ for the curved-flap EA.174 is only 3.1% smaller, a difference of 181 drag counts. This makes a strong case for the simplicity and relative effectiveness of the straight deflected flap design in two dimensions.

Regarding design evolution, we first consider the COLINY-EA design candidates. Figure 12 plots all 240 COLINY-EA base flap designs, including the infeasible designs, and shows how the designs concentrate toward the outer edge of the trailer base; it further illustrates the wide variations evaluated within the design space. The top 10 design candidates, whose range of values for $\bar{C}_d$ varies by only 2.4%, are relatively similar: distance beyond the centerline, $H_1$ = 1.2904 m, is the same for all; axial $L_1$ varies between $0.38W$ and $0.44W$; flap leading edge $\theta_1$ varies between 6 and 15°; mid-chord $\theta_2$ varies between 19 and 23°; deflection $\delta$ ranges between 17 and 23°; and trailing edge $\theta_3$ appears to curve inward or outward, ranging between either -23 and -22° or 27 and 30°. We note the same trends in Fig. 13, showing all variable points within the constrained design space for COLINY-EA. Figure 13a suggests the flap should be moved as close to the trailer edge as possible. Figure 13b suggests the flap axial length shies away from the maximum allowed length ($0.47W$) and targets closer to $0.4W$. Figure 13d indicates the best flap design should include a gradual ramp off the trailer base, steeper than 0° but less than the deflection angle. Figures

13c, 13e, and 13f suggest a relatively straight flap after the leading edge slope ($\theta_1$), deflected inward a little more than 20°; this helps make the case for eliminating $\theta_2$ from the design variables, since it tends to mimic $\delta$. The $\theta_3$ plot in Fig. 13f illustrates a clear bimodality of this design parameter, where the hollow diamonds and shaded circle, square, and triangle highlight the variable values associated with the 10 best design points. The $\delta$ plot in Fig. 13c is also bimodal, but the best designs are clearly with the larger deflection angles.

We examine in Fig. 14 the bimodal orientation of the flap trailing edge. We compare two flap designs where $\theta_1$, $\theta_2$, and $\delta$ differ by 1 or 2°; in Fig. 14a (design candidate EA.82), the flap tips curve outward 23°, and in Fig. 14b (design candidate EA.174), the flap tips curve inward 30°. On the windward side (bottom of graphic) of EA.82, the flow slows more than it does for EA.174 in the same region, and this deceleration results in slightly larger static pressure and less pressure drag. On the other hand, the overall structure of the base flow for EA.174 moves slower than for EA.82, likely because flow over the EA.174 flap remains fully attached, such that its overall base static pressure is higher and results in less pressure drag. The differences are subtle, but it appears the inward-curved flap tips prevail slightly over the outward-curved flap tips; this is confirmed in Fig. 13c that indicates the top three designs have the inward-curved flap or positive $\theta_3$. We temper these observations with the fact that 3-D flow at this sideslip angle does not separate near the base of the trailer along the leeward side, according to the Storms et al. (2001) experiment and our 3-D computational study (Freeman and Roy 2013).

We explore the incremental design improvements with successive COLINY-EA generations in Fig. 15. In the 1st generation, almost anything is better than the case without flaps, where 22% improvement over the baseline is attained by placing this small-deflection $0.28W$-length flap to disrupt the base flow. With the 2nd generation, the flap gains an additional 7.5% improvement by moving as close as permitted to the trailer edge, greatly reducing the region of separation and recirculation coincident with the flap outer surface; some of that improvement comes also from decreasing the strength of the adverse pressure gradient by increasing the deflection angle to 22°. Generation 3 augments the improvement by 5% by increasing the flap length to $0.41W$. The 5th generation brings a small increment of 0.4% for a total reduction of 35.1% from the baseline; this design reduces $\theta_1$ to 6°, further weakening the adverse pressure gradient by providing a more gradual slope off the trailer base. For a 0.1% gain, Generation 7 flips the flap trailing edge inflection from a negative (outward curve) to a positive angle. The last adjustments in Generation 9 are minor and add 1.1%, to give the total 36.3% improvement. No further improvements surface from the next three generations.

In Figs. 16 and 17, we consider the NCSU-DIRECT design evolution. We notice a more discrete and systematic exploration of the design space in Fig. 16, highlighting its combined global-local search algorithm. This systematic approach is further demonstrated in Fig. 17, illustrating that only one or two variables change with each iteration. In Fig. 17a, we observe that NCSU-DIRECT also locates the most promising designs near the trailer edge, but here its methodical approach proves counterproductive by not discovering this fact until relatively late in its design evolution; further, for this specific parameters of this study, where the best designs are at this constraint boundary, the DIRECT algorithm can in principle never exactly reach it. Aside from that limitation in this case, the other variables show relatively close agreement with those of COLINY-EA: the best axial flap lengths are $0.45W$ (Fig. 17b), with $\delta$ = 15° (Fig. 17c), more curvature than the COLINY-EA best designs (Figs. 17d and 17e), and inward curving flap trailing edge (Fig. 17f). While Fig. 17 highlights the top 10 NCSU-DIRECT designs, the $\bar{C}_d$ values for these designs are all 2-3% larger than the #10 design from COLINY-EA.

We show in Fig. 18 the graphic and in Table 5 the tabular variable values comparing the best COLINY-EA and NCSU-DIRECT designs from this study with the best optimizer-based result from Doyle et al. (2008). The COLINY-EA and Doyle designs present the idea of a gradual slope off the trailer base, followed by a relatively straight flap deflected inward, while the NCSU-DIRECT design has a steeper leading-edge slope with a stronger favorable pressure gradient, but it recovers with the flap curvature at mid-chord. The NCSU-DIRECT design would likely be the most challenging and expensive to manufacture. The COLINY-EA design's closeness to the trailer edge, greater length, and deeper overall deflection angle result from minimizing $\bar{C}_d$ versus $C_{d,\beta=0°}$, where the design must perform well both at the benign no cross-flow state and with cross-winds. Thus, the longer flaps from our study maintain a greater region of larger static pressure, and the larger inward deflection results in improved performance at all of the sideslip angles. We observe a clear benefit also from relaxing the constraints on the geometric angles when possible, as $\theta_1$, $\theta_2$, $\theta_3$, and $\delta$ in our study reach or exceed the limits imposed in the earlier study of Doyle et al. (2008). We do not calculate the predicted $\bar{C}_d$ for the design of Doyle et al. (2008).

Thus, it appears for the parameters, constraints, and limited sample size of this particular study that COLINY-EA is able to locate with fewer function evaluations a design that performs better than the design located by NCSU-DIRECT. However, we do not claim that COLINY-EA located the optimum design, and we allow that NCSU-DIRECT, given enough iterations and smaller box-size tolerances, may eventually locate a comparable or better design.

### 3.3 Total Predictive Uncertainty

Due to finite time and computational resources, we limit the amount of UQ conducted in this study. Because it directly affects fitness of the design candidates, we include for every feasible design the uncertainty due to wind speed and direction; however, we accomplish this in an approximate manner by employing the SAE method (SAE

J1252 1981) of distributed sideslip angles to estimate $\bar{C}_d$. Regarding the other sources of uncertainty, we select the most fit design and subject only that design to more detailed UQ. In our case, we select an earlier design, EA.82, and infer that its uncertainty measures will be relatively comparable to those of the final best design, EA.174, since the best design candidates after generation 5 only further reduce $\bar{C}_d$ by as much as 1.9%. For model input uncertainty, we investigate the effects of variation in truck speed and elevation (coupled into Reynolds number) and of variation in the turbulence model inputs. For model form uncertainty, we consider the differences between computation and experiment and assess the effect of modeling this case as steady RANS rather than time accurate. We complete the total predictive uncertainty analysis by then summing the effects of numerical approximation uncertainty with those of model input and model form uncertainty.

### *3.3.1 Model Input Uncertainty*

Based on data from more than 500,000 trucks, the US Federal Highway Administration (2011) provides Fig. 19 that shows average speeds for tractor-trailers on select US interstate highways in 2010. These data indicate that average truck speeds dip below 55 mph (24.6 m/s) in and around major cities, in the mountains, and at border crossings. To model the Reynolds number (*Re*) effects, we analyze industry-generated raw data used for Fig. 19 (US Federal Highway Administration and American Transportation Research Institute 2011). Data are collected from 3-mile segments along 25 US interstate highways, as illustrated in Fig. 19, and include a wide variation in density and temperature – nearly 21,000 geographic data points; for each geographic location, truck speeds are averaged in 3-hour periods for each day of the year. We verify the data have a normal distribution, following the same process we use in Section 2.6, and calculate for US truck highway speeds in 2010: $V_{truck,avg}$ = 57.2 mph (25.6 m/s) with a standard deviation of 4.2 mph (1.9 m/s). For standard-day conditions at sea level, ±3 standard deviations of this average truck speed correspond to $44.6 \leq V_{truck} \leq 69.8$ mph or $1.3\text{x}10^6 \leq Re_{/x} \leq 2.1\text{x}10^6$ m$^{-1}$. In Fig. 20, we show the results for EA.82 at the six SAE sideslip angles and at five different values for $Re_{/x}$, compared with the Storms et al. (2001) experimental data; the experimental data are 3-D wind-tunnel results, without flaps and at zero sideslip, and are included for comparison of trends rather than for validation of model accuracy. The experimental results show only mild *Re*-dependence for $Re_{/x}$ between 1.2 and $2.1\text{x}10^6$ m$^{-1}$, where the values differ by 0.8-5.2%. The computational results at each respective sideslip angle differ by 0.02-0.7% for $1.3\text{x}10^6 \leq Re_{/x} \leq 2.0\text{x}10^6$ m$^{-1}$. Nonlinearity occurs for $Re_{/x}$ roughly below $1\text{x}10^6$ and above $2\text{x}10^6$ m$^{-1}$; computational and experimental behavior appears relatively comparable. Thus, we bracket the near-constant *Re* effects with results from $Re_{/x} = 1.3\text{x}10^6$ m$^{-1}$ and the baseline $Re_{/x} = 2.0\text{x}10^6$ m$^{-1}$.

For this study, we use the RANS S-A turbulence model, but there is epistemic uncertainty with respect to its boundary condition for ratio of S-A viscosity (a coefficient specific to the S-A model) to reference or freestream viscosity: $\tilde{\nu}/\nu_\infty$. Based on their own findings, combined with results from multiple flow solvers and users, Spalart and Rumsey (2007) recommend this ratio should range between 3 and 5 for external flow of air at high *Re*, typically for an aircraft at flight speed, suggesting 3 for a fully turbulent boundary layer at lower *Re*. A ratio of $\tilde{\nu}/\nu_\infty = 3$ corresponds to $\mu_t/\mu_\infty = 0.2$, where $\mu_t$ is turbulent eddy viscosity. Since our case involves lower *Re* flow, we vary the ratio between 1 and 10 and find little sensitivity to this parameter. We find for the two smallest SAE sideslip angles for EA.82 that $C_d$ values obtained for $\tilde{\nu}/\nu_\infty = 1$ and 10 are both smaller than for the default case of $\tilde{\nu}/\nu_\infty = 3$, though by no more than 0.1%. At the larger sideslip angles, $C_d$ values for $\tilde{\nu}/\nu_\infty = 1$ and 10 bracket those for $\tilde{\nu}/\nu_\infty = 3$ but only slightly, with values differing between 0.003 and 0.1%. This insensitivity may result from the boundary layer being largely detached and thereby being essentially unaffected by variations in turbulent viscosity.

In Fig. 21, we display EDFs resulting from model input uncertainty – Reynolds number variation (dashed black line), wind speed and direction (incorporated within results), turbulence model input (dashed gray and dotted black lines), and results from the initial flaps design EA.82 (gray line). Effects from variation in both *Re* and $\tilde{\nu}/\nu_\infty$ are small. The smaller *Re* changes $C_d$ for various angles by 0.3-0.7%, and the different $\tilde{\nu}/\nu_\infty$ ratios change it by 0.003-0.1%. We conclude the model is only mildly dependent on variations in truck speed, elevation, temperature, and the RANS S-A turbulence model boundary condition.

### *3.3.2 Model Form Uncertainty*

While other studies have evaluated many of the sources of model form uncertainty listed in Table 4, in this study we focus on the differences between computation and experiment, of which a part is the difference between flow calculated as time-accurate RANS and flow approximated as steady RANS, where the time-accurate simulations use a smaller time-step and thereby capture more of the flow physics. Since the designs in this study are original, there are no experimental data for comparison. However, for the next level of fidelity, we develop a validation metric by comparing computation with experiment for cases that involve RANS turbulence models and simplified tractor-trailers at zero and non-zero sideslip angles. Table 6 compares results from several computational studies with wind-tunnel test data using 3-D simplified tractor-trailer geometry. These results indicate poor performance by the RANS S-A turbulence model in 3-D, while other steady RANS turbulence models perform with an acceptable degree of accuracy (see noted references for details of these turbulence models), not greater than 12% difference from experiment. We also include some time-accurate, Detached Eddy Simulation (DES) comparisons to show that

steady RANS models (except S-A) perform as well as or better than a time-accurate model for this case and under these conditions. Thus, for the current model and since the RANS S-A turbulence model *in 2-D* performs suitably well under similar flow conditions (Freeman and Roy 2012a; Spalart and Rumsey 2007), we apply ±5% model form uncertainty for the results at $\beta$ = 1.770 and 2.301° and ±10% for the other four SAE angles.

Generally by assuming steady flow, we conserve computation time and resources, but we may sacrifice accuracy in proper modeling of the flow physics. Therefore, for one of the best design cases, EA.82, we evaluate the difference with computing the solution at a smaller time-step in hopes of better resolving the flow features. Since Cobalt essentially calculates time-accurate flow for all cases, the difference comes in effective time-step size or CFL number; a large CFL number does not allow for computing the small eddy structures. Cummings et al. (2008) indicate that a maximum Strouhal number, $St$ = 20, for flow with shear layer instability or massively separated flow, as is the case for many of our design candidates, corresponds to a non-dimensional time-step, $\Delta t^*$ = 0.025, where the time-step used in Cobalt can then be calculated as

$$\Delta t = \Delta t^* W / V_\infty. \tag{11}$$

We conduct a time-step sensitivity study using the EA.82 mesh, $\beta$ = 1.770°, and $\Delta t^*$ = { 0.025, 0.01, 0.005 }. Computed $C_d$ values differ by 0.28% between $\Delta t^*$ = 0.025 and 0.005, so we have confidence that $\Delta t^*$ = 0.025 is adequate to resolve the flow features. Comparing $C_d$ values from the six SAE sideslip angles for $\Delta t^*$ = 0.025 against CFL = 1x10$^6$, we find differences ranging from 0.05% at the smaller angles to 5.5% at the larger angles. As expected, the unsteady, turbulent behavior in 2-D is more pronounced with the larger angles and a steady solution loses some accuracy. Since the difference between time-step sizes falls under the more general category of computation vs. experiment, we include them inside the 5-10% model form uncertainty noted above. For example, of the +10% uncertainty in model form at $\beta$ = 7.694°, 5.5% is contributed by the RANS approximation uncertainty; the two uncertainties are not additive because the experiment is conducted in the equivalent of time accuracy. We further note that the time-accurate simulations require roughly the same amount of physical time for a converged solution as do the steady simulations. We attribute this to the relatively fine resolution of the mesh.

### *3.3.3 Numerical Approximation Uncertainty*

We are unable to compute quadruple precision to assess the error in using double precision, but we compare solutions using single and double precision for the EA.82 mesh at $\beta$ = 1.770°. These solutions differ by 0.36%. However, since we may assume the difference would be smaller between solutions using quad and double precision and we assume a large portion of this difference between single- and double-precision solutions is related to unsteadiness in the flow, we estimate uncertainty due to round-off error as no more than 1% of the discretization error. As noted previously, there is zero uncertainty due to sampling error.

Following a process similar to that of Section 2.4, we assess uncertainty due to numerical approximation error. To estimate the discretization error, we encounter some difficulty because the solutions at $\beta \neq 0°$ on the coarsest grid yield non-physical results (negative $C_d$). Thus, we use the solutions from the 2$^{nd}$ finest grid (note that we use the 3$^{rd}$ finest grid for almost all of this study) and estimate discretization error based on Richardson Extrapolation (Oberkampf and Roy 2010; Roy and Oberkampf 2011). Using Eq. (7), we calculate observed orders of accuracy, $\hat{p} =$ 3.78 and 2.76 for $\beta$ = 6.024 and 7.180°, respectively. Since these solutions do not show asymptotic behavior, they yield larger numerical uncertainty, even though the solutions on the two finest grids for the three largest sideslip angles are within 2% of each other. Using Eqs. (5) and (6), we calculate $U_{Numerical}$ = { 1.5, 2.9, 2.0% } for design EA.82 at $\beta$ = { 6.024, 7.180, 7.694° }. Because the smaller sideslip angles, $\beta$ = { 1.770, 2.301, 4.980° }, for the coarser grids also give non-physical results, we cannot directly calculate numerical error; while we would expect them to have less error than for the larger angles, we conservatively apply to them roughly the same numerical uncertainty, or 2.0%. Applying the wind-averaging procedure to these values and considering only uncertainty due to numerical error, we apply this total numerical error to our best design, EA.174, and predict $\bar{C}_d$ = 0.5613 ± 0.0119. We expect smaller numerical uncertainty for the 3-D case, where non-physical behavior should be less significant, if it exists at all.

### *3.3.4 Bringing It Together*

To compose Fig. 22, we generate the p-box for model input uncertainty (small black area in the center regions) from the minimum and maximum values of Fig. 21. To those values we add (upper bound) or subtract (lower bound) the model form uncertainty that for this case includes the difference at each sideslip angle between the EA.82 steady results (CFL = 1x10$^6$) and the time-accurate solutions ($\Delta t^*$ = 0.025); the medium gray region in Fig. 22 shows the model form uncertainty due to time-step size. The dark gray region shows the remainder of the model form uncertainty approximation from the 3-D experimental comparisons of Table 6, where the total uncertainty due to model form does not exceed the 5-10% discrepancy between computation and experiment. We finish the p-box of total predictive uncertainty by adding/subtracting the numerical uncertainty, shown in light gray. We observe that the largest model form and numerical uncertainty are associated with the largest angles, where the 2-D flow exhibits the greatest unsteadiness.

The p-box of Fig. 22 may be used for probabilistic observations, understanding of input/output relationships, and assessment of ways to improve the model. Probabilistic interpretation is precarious for such small sample sizes, so we focus on model assessment and understanding. Following are some observations that may be gained from the p-box. Decision-makers may realize from this p-box that epistemic uncertainty grows with increasing sideslip angle and decide to accept the computational expense of running the solutions at a smaller time-step for the larger sideslip angles, in exchange for reduced uncertainty at those angles and in the overall prediction. They may choose to conduct additional wind tunnel or other ground testing to reduce model form uncertainty. They may see the effects of highway speed and elevation as they relate to drag predictions and make decisions about truck fleet operating speeds to reduce probabilities of higher fuel consumption.

Since we are most interested in $\bar{C}_d$, we predict a total uncertainty estimate by using the SAE weights to wind-average the left and right extents shown in the p-box of Fig. 22. These values relate specifically to design EA.82; however, since the current best design, EA.174, falls within the same family of designs with EA.82, we convert them to a fraction and apply that fraction to design EA.174 to obtain our estimate of total predictive uncertainty,

$$\bar{C}_d = 0.5613\ ^{+0.0633}_{-0.0626} = 0.5613\ ^{+11.3\%}_{-11.2\%}.$$

Table 7 shows percentages of the components of total uncertainty, highlighting the slight asymmetry in model input uncertainty. The overall model form uncertainty is completely independent of specific design parameters; numerical uncertainty is lightly based on the design shape and may readily be extrapolated to similar designs; and model input uncertainty is also lightly based on design parameters, but it demonstrates only slight sensitivity to truck-speed variations. Clearly, the largest contributions (98-99%) to total uncertainty in this 2-D study come from model form and numerical approximation. In the follow-on 3-D study (Freeman and Roy 2013), we see no separated flow along the trailer body and less unsteadiness, which reduces that aspect of the numerical uncertainty; however, coarseness of the 3-D mesh for pragmatic reasons adds significant numerical error. Model form uncertainties for the 3-D study are comparable to the values in Table 7.

# 4 Results: Surrogate-Based Global Optimization

## 4.1 Selection of Surrogate Model and Sampling Method

We use surrogate modeling in two ways: initially, we use it to create an approximation of the truth model, or computational simulations, that may then be used inexpensively for further evaluations; and secondly, we use it in conjunction with sampling and an optimization method for SBGO, where the function evaluations query the initial surrogate model instead of the flow solver.

For the first case, DAKOTA builds a surrogate model by data-fitting the tabular $\bar{C}_d$ results from both COLINY-EA and NCSU-DIRECT designs, 289 design points. Of the 12 surrogate models noted in Section 2.8.1 and based on results of the multidimensional parameter studies, we exclude the models that yield predictions with non-physical meaning (negative $C_d$), namely, all three kriging and the cubic polynomial models. We present in Fig. 23 the flap designs associated with the minimum $\bar{C}_d$, according to the multidimensional parameter study queries of the surrogate models. In the legend, we quantify the difference (percent smaller in all cases) between predicted $\bar{C}_d$ from the surrogate data-fit and the best design in the truth data, EA.174, that we designate the truth design for this discussion. We expect a good data fit to supply a value within perhaps 10% of the truth design value. We also expect the surrogate best design to be within the same family as the truth design, but we need to be careful to not rule out an unconventional design based on preconception. Based on these two criteria, we rule out the polynomial and MARS surrogate models and select the linear Gaussian process (GP) surrogate model. To evaluate optimizer efficiency and accuracy, we also proceed with the artificial neural network (ANN) surrogate model because its prediction is close to the truth design, and its less conventional design merits consideration. Based on flow solver evaluation, the ANN and quadratic polynomial (QP) designs in Fig. 23 predict $\bar{C}_d$ = 0.7171 and 0.6611, respectively – 18-28% larger than the truth design and 1.4 to 2.1 times larger than the surrogate predicted values; so the outside-the-box designs and their surrogate models prove unfit for further consideration. We also use the flow solver to evaluate two minor variations each of the ANN and QP designs that we then add to the dataset for the surrogate model, thereby reducing the future likelihood of similar designs being selected. In contrast, the GP design flow-solver value for $\bar{C}_d$ is 4.9% larger than its surrogate-predicted value and 0.5% larger than the truth design; thus, it is not an improvement, but it is a reasonable prediction for the design space minimum.

To further evaluate the goodness of the surrogate data fit, we would ideally like to inspect a visual representation such as a curve for two variables or a carpet plot for three. Since that is impossible with six variables, we construct a set of curves from the surrogate model by fixing five variables and allowing the 6$^{th}$ to vary within its constrained range. In Fig. 24a, we use the design variable values at the surrogate model minimum (as located with the parameter study) and normalize the constraint values to range from 0 to 1. This figure provides 2-D snapshots of the multidimensional design space and shows that the data fit is smooth. The squares mark the normalized variable values from the surrogate minimum design point; e.g., $\delta$ = 18.1° for the GP minimum design point, so the square marks $\delta_{normalized}$ = 18.1/30 = 0.603 on the $\delta$-curve. Thus, for each of the six design variables in the surrogate model,

Fig. 24a confirms at least that a local minimum is located in the design space and that it tends to avoid local minima. We demonstrate in Fig. 24b the power of the surrogate model. The surrogate of Fig. 24b uses the body-axis $C_d$ values, as a function of sideslip angle, rather than the wind-averaged $C_d$ values, and it presents a continuous cumulative distribution function for $C_d$ values that is much better resolved than the discrete EDF of the truth data. We could extend this process to generate a relatively smooth p-box to show the effect of varying each design variable within this range of sideslip angles.

For the second case for using a surrogate model, we couple it with a sampling method to create a starting point for the SBGO study. Of the 72 possible surrogate-sampling combinations described in Section 2.8.2, again where we locate the best design using a multidimensional parameter study, we show the three with most promise in Fig. 25. We select the combinations of constant GP with PSUADE-MOAT sampling and of constant kriging with LHS because their best designs return a $\bar{C}_d$ value (noted in parentheses in the figure legend) within 10% of the truth design value and their designs appear to be within the truth design family. While its $\bar{C}_d$ value is nearly 17% larger than the truth design value, we also select the combination of constant kriging with BB sampling because it is within the truth design family and because its sampling method requires many fewer samples; this invites the possibility of more efficient convergence (i.e., fewer function evaluations) to an optimum design.

### 4.2 Optimization Strategy

Starting with the three secondary surrogate-sampling models noted in Section 4.1, and having automated the method, we create the results shown in Fig. 26; each SBGO study, limited to about 300 function evaluations (same order of magnitude as the original COLINY-EA study with its 240 design points), completes within a couple hours. In the figure, the curves show the difference between the SBGO minimum value and the truth design value. All three SBGO studies converge to a design value within 0.003% of the truth design value, and they all converge exactly to the design variable values of the truth design. The constant kriging-LHS and constant GP-PSUADE combinations converge more efficiently to the optimum, but they start with an apparently better surrogate model that is based on more data points. The constant kriging-BB combination converges to the truth design with fewer total function evaluations but with more post-initial-sampling function evaluations – about 70, compared with about 40 for the other two methods. We show also in Fig. 26 the results of using the COLINY-EA optimizer (filled black squares) without a surrogate-sampling foundation; it queries the approximate truth model (initial linear GP surrogate) rather than using the flow solver and, with this small number of iterations, converges to within 3.6% of the truth design value. This suggests that COLINY-EA may not have located the global minimum with the 240 design points of our initial 2-D OUU study, but we are confident that it at least located a local minimum and a design candidate with excellent performance. We further discover with these surrogate-based evaluations that COLINY-EA converges more quickly to the known minimum when CHC = 1, compared with CHC = 0 and 2; that is, it appears beneficial for the next generation to include mating and/or mutations from the best design candidate from the current and past pool of candidates. We implement this setting value in our 3-D study.

On one hand, we demonstrate the efficiency of using SBGO for a small number of function evaluations; but on the other hand, this approach is infeasible for our more expensive 3-D OUU study because it defeats the advantage of concurrent computing. That is, after the initial surrogate-sampling process that may be computed concurrently on a large processing platform, the SBGO process – as implemented by DAKOTA – limits each iteration to a single design point for updating the surrogate model. Based on computing times for our 3-D cases (Freeman and Roy 2013) and limiting the population to 140 design points, the SBGO methods would require between 23 weeks (LHS or PSUADE sampling) and 46 weeks (BB sampling), while the non-surrogate-based COLINY-EA method requires 14 weeks. A potentially improved approach involves using SBGO with parallel or concurrent capacity that would accelerate the process after the initial sampling-surrogate is created. Currently, however, this capability does not exist in DAKOTA. Until then and since neither approach guarantees locating the global minimum for such a limited population size, we recommend a non-surrogate-based, gradient-free, global optimization method for this and similar optimization studies.

# 5 Summary and Conclusions

In this study we conducted design optimization under conditions of uncertain wind speed and direction for a base-flap drag-reduction device, defined by six design variables, on a simplified 2-D full-scale tractor-trailer geometry at highway speed (67 mph or 108 km/h and $Re_W$ = 5.2x10$^6$). We used the DAKOTA optimization framework to manage the interface of optimizers, surrogate models, grid generator, and flow solver (Cobalt with S-A RANS turbulence model). Along the way, we conducted grid and time-step sensitivity studies; estimation of total predictive uncertainty that included the effects of Reynolds-number variation, turbulence model boundary-condition variation, steady RANS approximation, difference from experiment, and numerical approximation; and evaluation and comparison of two nonlinear, gradient-free, global optimization algorithms (COLINY-EA and NCSU-DIRECT), 12 surrogate models used to fit the data generated by those optimizers, and surrogate-based global optimization (SBGO) using various combinations of sampling methods and surrogate models.

The COLINY-EA optimization algorithm located a design that resulted in 36.3% reduction in $\bar{C}_d$, compared with the no-flaps baseline. However, this best design outperforms a simple straight flap deflected inward 18° by only 3.1%, raising the question of whether a more complex and expensive curved flap is justified. Our 3-D study shows a similar result (Freeman and Roy 2013). The NCSU-DIRECT optimization algorithm performed almost as well – with 30% fewer function evaluations but requiring twice the amount of physical time – resulting in a design with 33.3% reduction in $\bar{C}_d$; we believe NCSU-DIRECT came up short because its algorithm limits its ability to select constraint boundaries for the design variables, which in this case the best flap designs were as close as permitted to the trailer edge. Because of the potential efficiency of DIRECT methods, we recommend that future work include evaluation of VTDIRECT by He et al. (2009), since it has improved upon the NCSU-DIRECT algorithm and may concurrently evaluate a large number of points in the design space.

We successfully incorporated for every design candidate in the optimization study, by using the SAE wind-averaging process, the aleatory uncertain effects of wind speed and direction; we also included several additional sources of input uncertainty, both aleatory and epistemic, as a post-processing step. With lessons learned from this study, we incorporate in our follow-on 3-D study both aleatory and epistemic uncertainty for every design candidate in the optimization process, in addition to post-processing other sources of uncertainty for the best design (Freeman and Roy 2013). Further, this study identified that the trailer base flap should be as close as possible to the trailer edges and that mid-chord slope ($\theta_2$) was not a defining design variable and is excluded from the 3-D study.

For the best 2-D design, we estimated total predictive uncertainty as $^{+11.3\%}_{-11.2\%}$, consisting of 8.9% model form (due to the difference between the steady RANS computations and experiment), 2.1% numerical approximation (due to flow unsteadiness and separated flow at the larger sideslip angles), and 0.2-0.3% model input (due to variation in highway speed and turbulence model boundary condition parameter). Total predictive uncertainty analysis is similar for the 3-D study, but we see a smaller level of numerical uncertainty because of less unsteadiness and boundary-layer separation in the 3-D flow.

We determined that the best data fit for this case and under these flow conditions came from the linear Gaussian process surrogate model, and the best surrogate-sampling combinations for SBGO include GP and kriging interpolation data fitting with LHS, PSUADE-MOAT, and BB sampling methods. Despite their ability to converge to a good design with fewer function evaluations, surrogate-based methods proved unfruitful in this DAKOTA-based application because of serial limitations. Future algorithms capable of concurrent evaluation of points within the design space to update the surrogate would greatly enhance SBGO feasibility for computationally expensive engineering applications. Until then we recommend a non-surrogate-based, gradient-free global optimization method for future studies with similar setup and conditions.

# Acknowledgments

The authors gratefully acknowledge support from DAKOTA developers, Brian Adams, William Bohnhoff, Keith Dalbey, John Eddy, and Laura Swiler. This work was supported in large part by a generous grant of computer time and software usage from the DoD High Performance Computing Modernization Program at the US Army Engineer Research and Development Center, a DoD Supercomputing Resource Center in Vicksburg, Mississippi.

# References

Adams BM, Bohnhoff WJ, Dalbey KR, Eddy JP, Eldred MS, Gay DM, Haskell K, Hough PD, Swiler LP (2009) DAKOTA, a multilevel parallel object-oriented framework for design optimization, parameter estimation, uncertainty quantification, and sensitivity analysis: version 5.0 user's manual. Sandia Technical Report SAND2010-2183, December 2009. Updated December 2010 (Version 5.1)

Arora JS (2004) Introduction to optimum design, 2nd edn. Elsevier Academic Press, San Diego, California

ATDynamics (2012) Aerodynamics 101: aerodynamics at work. ATDynamics, Inc. http://www.atdynamics.com/aero.htm. Accessed 18 May 2012

Basara B, Tibaut P (2004) Time dependent vs. steady state calculations of external aerodynamics. In: McCallen R, Browand F, Ross J (eds) Lecture notes in applied and computational mechanics vol. 19: The aerodynamics of heavy vehicles: trucks, buses, and trains. Springer, Berlin, pp 107-117

Box GEP, Behnken D (1960) Some new three level designs for the study of quantitative variables. Technometrics 2(4):455-475

Box GEP, Wilson KB (1951) On the experimental attainment of optimum conditions. J Roy Statist Soc B13:1-38

Browand F, Radovich C, Boivin M (2005) Fuel savings by means of flow attached to the base of a trailer: Field test results. SAE Technical Paper 2005-01-1016. doi: 10.4271/2005-01-1016

Cobalt Solutions (2010) Cobalt version 5.0 user's manual. Cobalt Solutions, LLC., Ohio

Cooper KR (1985) The effect of front-edge rounding and rear-edge shaping on the aerodynamic drag of bluff vehicles in ground proximity. SAE Technical Paper 850288. doi: 10.4271/850288

Cooper KR (2003) Truck aerodynamics reborn – lessons from the past. SAE Technical Paper 2003-01-3376. doi: 10.4271/2003-01-3376
Cummings RM, Morton SA, McDaniel DR (2008) Experiences in accurately predicting time-dependent flows. Prog Aerosp Sci 44:241-257. doi: 10.1016/j.paerosci.2008.01.001
Dellinger D (2008) Average wind speed. National Oceanic and Atmospheric Administration. http://lwf.ncdc.noaa.gov/oa/climate/online/ccd/avgwind.html. Accessed 19 June 2012
Doyle JB, Hartfield RJ, Roy CJ (2008) Aerodynamic optimization for freight trucks using a genetic algorithm and CFD. AIAA Paper 2008-0323
Eddy J, Lewis K (2001) Effective generation of Pareto sets using genetic programming. In: Proceedings ASME design engineering technical conference, September 2001, pp 783-791
Finkel DE (2003) DIRECT optimization algorithm user guide. North Carolina State University. http://www4.ncsu.edu/~ctk/Finkel_Direct/DirectUserGuide_pdf.pdf. Accessed 27 May 2011
Forsythe JR, Strang WZ, Hoffmann KA (2000) Validation of several Reynolds-averaged turbulence models in a 3D unstructured grid code. AIAA Paper 2000-2552
Freeman JA, Roy CJ (2012a) Verification and validation of RANS turbulence models in commercial flow solvers. AIAA Paper 2012-0462; also Verification and validation of Reynolds-averaged Navier-Stokes turbulence models for external compressible flow. (submitted to AIAA J, July 2012).
Freeman JA, Roy CJ (2012b) Application of optimization under uncertainty: 2-D tractor-trailer base flaps. AIAA Paper 2012-0671
Freeman JA, Roy CJ (2013) Global optimization under uncertainty for tractor-trailer base flaps. (submitted for 51st AIAA Aerospace Sciences Meeting for January 2013; and submitted to Comput Fluids, August 2012)
Friedman JH (1991) Multivariate adaptive regression splines. Annals of Statistics 19(1):1-141
Gergonne JD (1974 [1815]) The application of the method of least squares to the interpolation of sequences. Historia Mathematica 1(4):439-447. doi: 10.1016/0315-0860(74)90034-2
Giunta AA, Watson LT (1998) A comparison of approximation modeling techniques: polynomial versus interpolating models. AIAA Paper 1998-4758
Gottlieb JJ, Groth CPT (1988) Assessment of Riemann solvers for unsteady one-dimensional inviscid flows of perfect gases. J Comput Phys 78:437-458
Grismer MJ, Strang WZ, Tomaro RF, Witzeman FC (1998) Cobalt: a parallel, implicit, unstructured Euler/Navier-Stokes solver. Adv Eng Softw 29(3-6):365-373
He J, Watson LT, Sosonkina M (2009) Algorithm 897: VTDIRECT95: serial and parallel codes for the global optimization algorithm DIRECT. ACM Trans on Mathematical Softw 36(3):17.1-17.24. doi: 10.1145/1527286.1527291
Hedayat AS, Sloane NJA, Stufken J (1999) Orthogonal arrays: theory and applications. Springer-Verlag, New York
Hsu F-H, Davis RL (2010) Drag reduction of tractor-trailers using optimized add-on devices. ASME J Fluids Eng 132(8):084504:1-6. doi: 10.1115/1.4001587
Hsu T-Y, Hammache M, Browand F (2004) Base flaps and oscillatory perturbations to decrease base drag. In: McCallen R, Browand F, Ross J (eds) Lecture notes in applied and computational mechanics vol. 19: The aerodynamics of heavy vehicles: trucks, buses, and trains. Springer, Berlin, pp 303-316
Lanser WR, Ross JC, Kaufman AE (1991) Aerodynamic performance of a drag reduction device on a full-scale tractor/trailer. SAE Technical Paper 912125. doi: 10.4271/912125
Law AM, Kelton WD (1982) Simulation modeling and analysis. McGraw Hill, New York.
Leuschen J, Cooper KR (2006) Full-scale wind tunnel tests of production and prototype, second-generation aerodynamic drag-reducing devices for tractor-trailers. SAE Technical Paper 2006-01-3456. doi: 10.4271/2006-01-3456
Lozano M, Herrera F, Krasnogor N, Molina D (2004) Real-coded memetic algorithms with crossover hill-climbing. Evolutionary Comput 12(3):273-302. doi: 10.1162/1063656041774983
Maddox S, Squires KD, Wurtzler KE, Forsythe JR (2004) Detached-eddy simulation of the ground transportation system. In: McCallen R, Browand F, Ross J (eds) Lecture notes in applied and computational mechanics vol. 19: The aerodynamics of heavy vehicles: trucks, buses, and trains. Springer, Berlin, pp 89-104
Mason WT Jr, Beebe PS (1978) The drag related flowfield characteristics of trucks and buses. In: Symposium on aerodynamic drag mechanisms of bluff bodies and road vehicles, General Motors Research Laboratories, Plenum Press.
Morris MD (1991) Factorial sampling plans for preliminary computational experiments. Technometrics 33(2):161-174
Oberkampf WL, Roy CJ (2010) Verification and validation in scientific computing. Cambridge University Press, Cambridge, England
Ortega JM, Salari K (2004) An experimental study of drag reduction devices for a trailer underbody and base. AIAA Paper 2004-2252
Pointer D, Sofu T, Chang J, Weber D (2009) Applicability of commercial CFD tools for assessment of heavy vehicle aerodynamic characteristics. In: Browand F, McCallen R, Ross J (eds) Lecture notes in applied and

computational mechanics vol. 41: The aerodynamics of heavy vehicles II: trucks, buses, and trains. Springer, Berlin, pp 349-361
Pointwise (2006) Gridgen version 15 user manual. Pointwise, Inc., Texas
Renaud JE, Gabriele GA (1993) Improved coordination in nonhierarchic system optimization. AIAA J 31(12):2367-2373. doi: 10.2514/3.11938
Roy CJ, Ghuge HA (2009) Detached eddy simulations of a simplified tractor/trailer geometry. In: Browand F, McCallen R, Ross J (eds) Lecture notes in applied and computational mechanics vol. 41: The aerodynamics of heavy vehicles II: trucks, buses, and trains. Springer, Berlin, pp 363-381
Roy CJ, Oberkampf WL (2011) A comprehensive framework for verification, validation, and uncertainty quantification in scientific computing. Comput Methods Appl Mechanics Eng 200: 2131-2144. doi: 10.1016/j.cma.2011.03.016
Roy CJ, Payne JL, McWherter-Payne MA (2006) RANS simulations of a simplified tractor/trailer geometry. ASME J Fluids Eng 128(5):1083-1089. doi: 10.1115/1.2236133
SAE J1252 (1981) SAE wind tunnel test procedure for trucks and buses. SAE Recommended Practice, July 1981
SAE J1321 (2012) Fuel consumption test procedure – type II. SAE Standard, February 2012
Schetz JA (1993) Boundary layer analysis. Prentice-Hall, New Jersey, ch. 2 and 7
Spalart PR, Rumsey CL (2007) Effective inflow conditions for turbulence models in aerodynamic calculations. AIAA J 45(10):2544-2553. doi: 10.2514/1.2973
Sreenivas K, Mitchell B, Nichols S, Hyams D, Whitfield D (2009) Computational simulation of the GCM tractor-trailer configuration. In: Browand F, McCallen R, Ross J (eds) Lecture notes in applied and computational mechanics vol. 41: The aerodynamics of heavy vehicles II: trucks, buses, and trains. Springer, Berlin, pp 325-338
Storms BL, Ross JC, Heineck JT, Walker SM, Driver DM, Zilliac GG (2001) An experimental study of the ground transportation system (GTS) model in the NASA Ames 7- by 10-ft wind tunnel. NASA/TM-2001-209621
Swiler LP, Slepoy R, Giunta AA (2006) Evaluation of sampling methods in constructing response surface approximations. AIAA Paper 2006-1827
Toro EF, Spruce M, Speares W (1994) Restoration of the contact surface in the HLL-Riemann solver. Shock Waves 4(1):25-34
US Code of Federal Regulations (2004) Truck size and weight, route designations – length, width and weight limitations: Exclusions from length and width determinations. Title 23, ch. 1, part 658.b.4
US DoD High-Performance Computing Modernization Program (2012) Available hardware by DoD supercomputing resource centers. http://www.afrl.hpc.mil/consolidated/hardware.php. Accessed 27 June 2012
US Federal Highway Administration (2011) Freight facts and figures 2011: Chapter 3, freight transportation system. Department of Transportation, FHWA-HOP-12-002
US Federal Highway Administration and American Transportation Research Institute (2011) Freight performance measures integrated query tool (FPMweb). https://www.freightperformance.org/fpmweb/default.aspx. Accessed 16 December 2011
Visser KD, Grover K, Marin LE (2011) Sealed aft cavity drag reducer. US Patent 8,079,634. http://patft.uspto.gov. Accessed 27 June 2012
Weisstein EW (2012) Log normal distribution. MathWorld – A Wolfram Web Resource. http://mathworld.wolfram.com/LogNormalDistribution.html. Accessed 19 June 2012
Wurtzler KE, Morton SA (2004) Accurate drag prediction using Cobalt. AIAA Paper 2004-0395
Yao W, Chen X, Luo W, Tooren M, Guo J (2011) Review of uncertainty-based multidisciplinary design optimization methods for aerospace vehicles. Prog Aerosp Sci 47: 450-479. doi:10.1016/j.paerosci.2011.05.001
Zimmerman DC (1996) Genetic algorithms for navigating expensive and complex design spaces. In: Final report for Sandia National Laboratories contract AO-7736 CA 02

# Figures

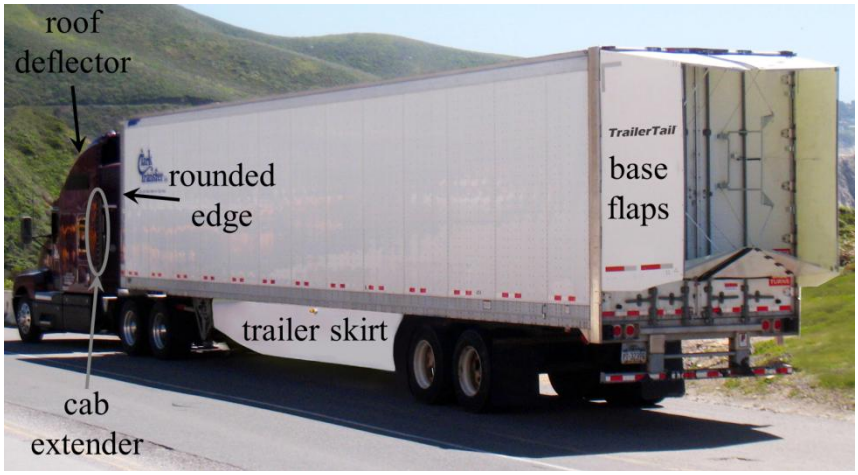


**Fig. 1** Example of straight trailer base flaps and other aerodynamic drag-reduction devices (Used with permission of Steven Rodger, 2012, ATDynamics, www.ATDynamics.com)

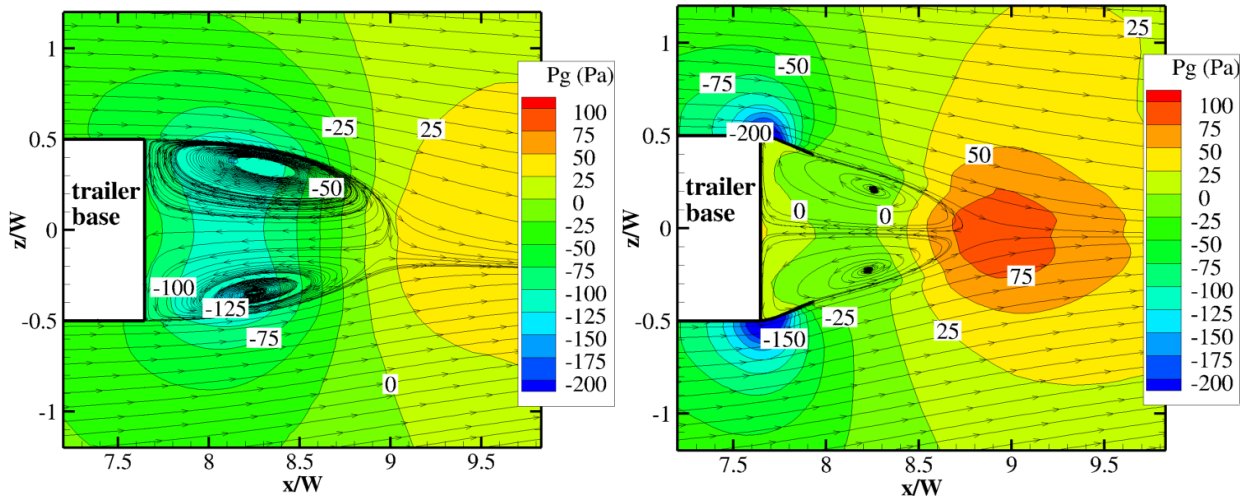


**a)** Baseline configuration, no flaps, $C_D$ = 0.3287 **b)** Side flaps deflected inward 20°, $C_D$ = 0.2005

**Fig. 2** Time-averaged 3-D computational solutions of simplified tractor-trailer with and without base flaps, showing reduced region of low pressure and stabilized base flow. Horizontal slice at $y/W$ = 0.695 for $\beta$ = 9.1° showing velocity streamlines atop contours of gauge pressure. Highway speed, $V_\infty$ = 57.2 mph (25.6 m/s), and trailer-width-based Reynolds number, $Re_W$ = 4.4 x $10^6$

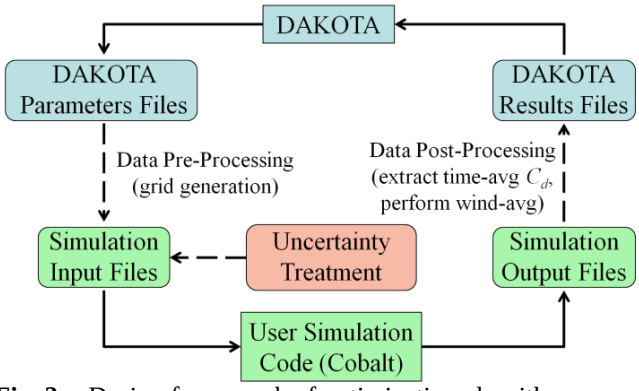


**Fig. 3** Design framework of optimization algorithm, pre-processing, simulation, and post processing

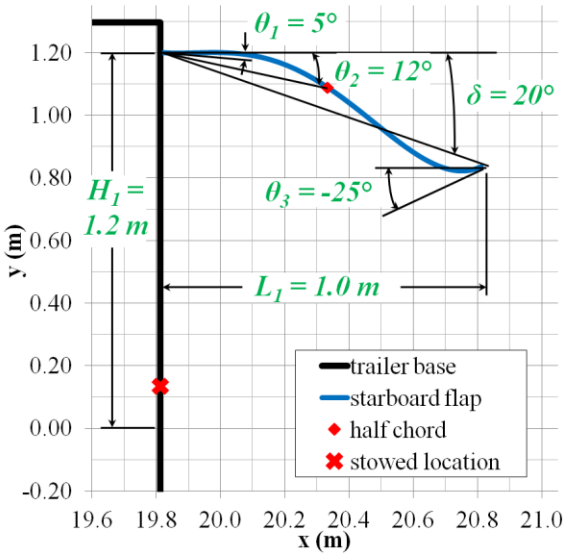


**Fig. 4** Trailer base flap schematic with design-variable values for one possible configuration. View of starboard flap as seen looking down from above the trailer

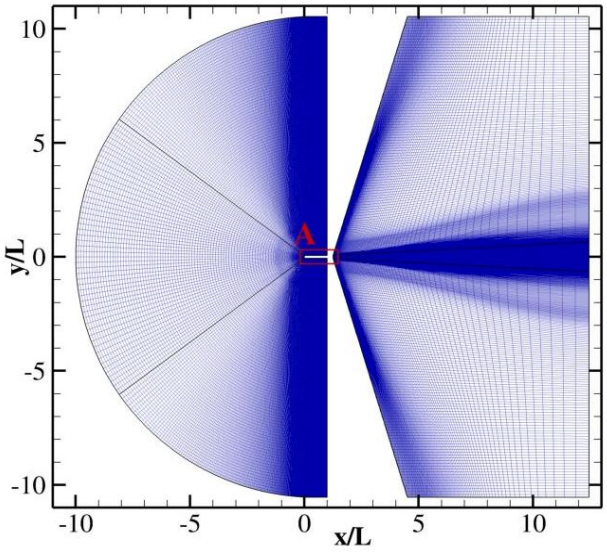


**a)** Entire domain minus flaps region

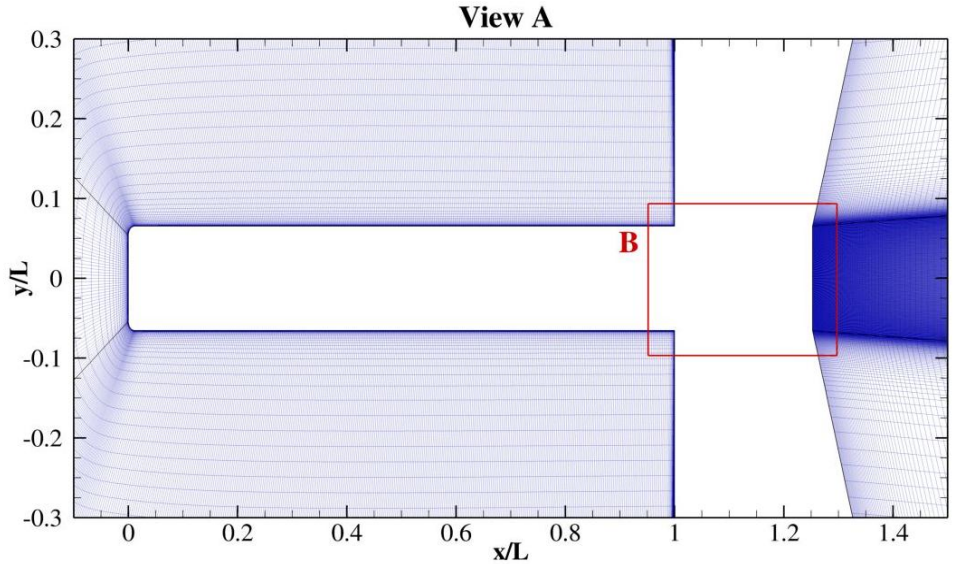


**b)** Closer view of simplified tractor-trailer and base flaps region

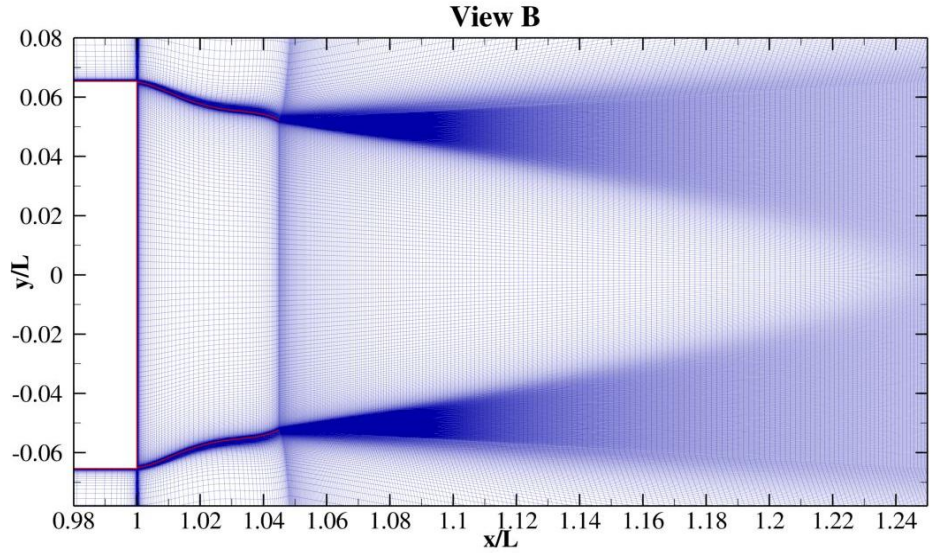


**c)** Close view of completed grid, base flaps region

**Fig. 5** Modified C-grid of simplified 2-D tractor-trailer geometry. 637,264 structured cells, first-cell average $y^+ \approx 0.4$

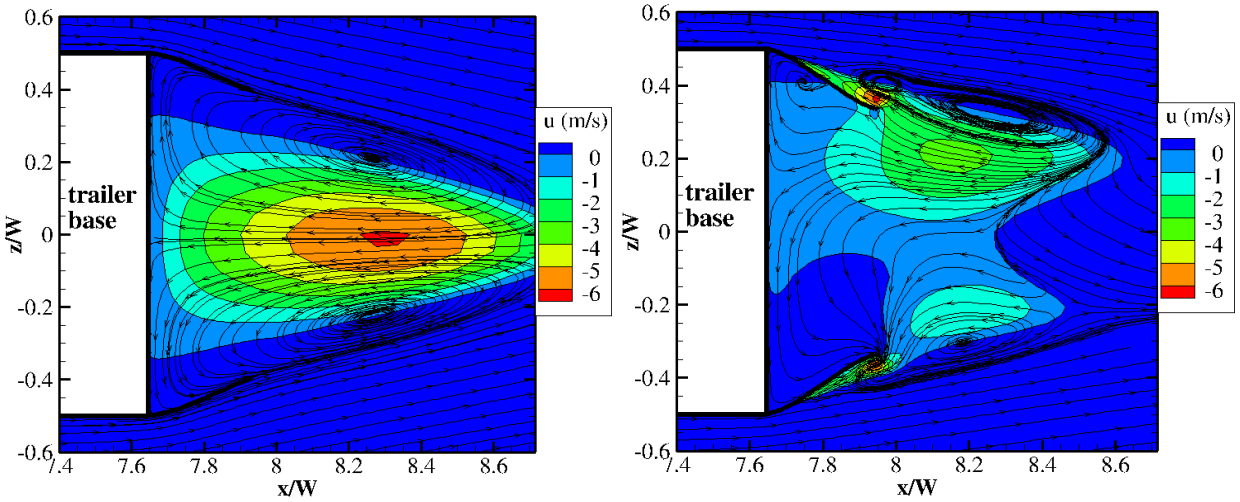


**a)** Attached flow for $\delta = 20°$, $C_D = 0.2083$ **b)** Separated flow for $\delta = 29°$, $C_D = 0.2669$

**Fig. 6** Time-averaged 3-D computational solutions of simplified tractor-trailer showing sensitivity of base-flap boundary layer to flap deflection angle. Horizontal slice at $y/W = 0.695$ for $\beta = 2.0°$ showing velocity streamlines atop contours of velocity in the $x$-direction. Highway speed, $V_\infty = 57.2$ mph (25.6 m/s), and $Re_W = 4.4 \times 10^6$

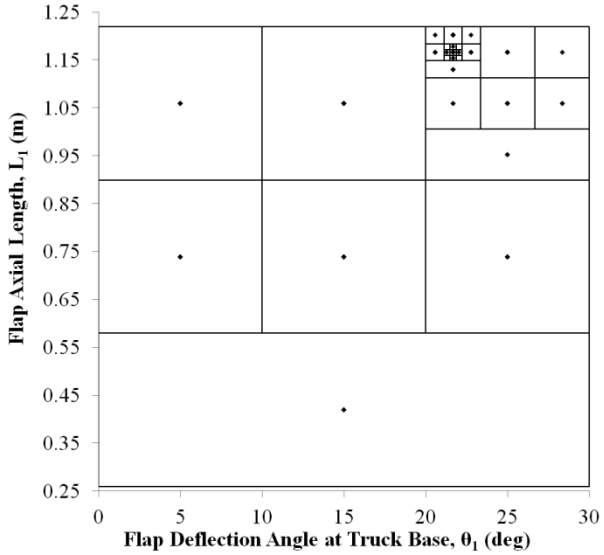


**Fig. 7** Illustration of DIviding RECTangles (DIRECT) algorithm, showing two of six design variables for the 2-D optimization study, representing 28 iterations of the DIRECT algorithm or 140 design points

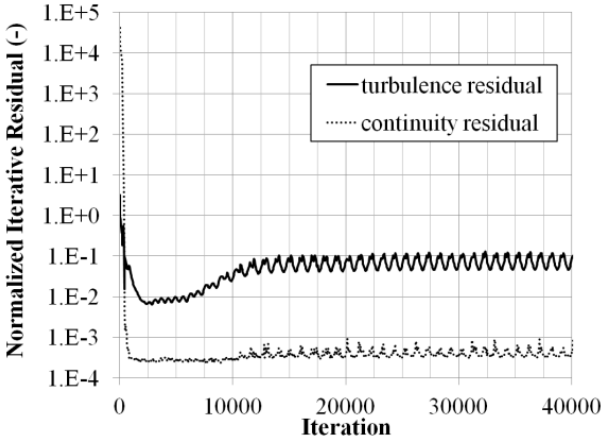


**a)** Residuals for continuity and turbulence

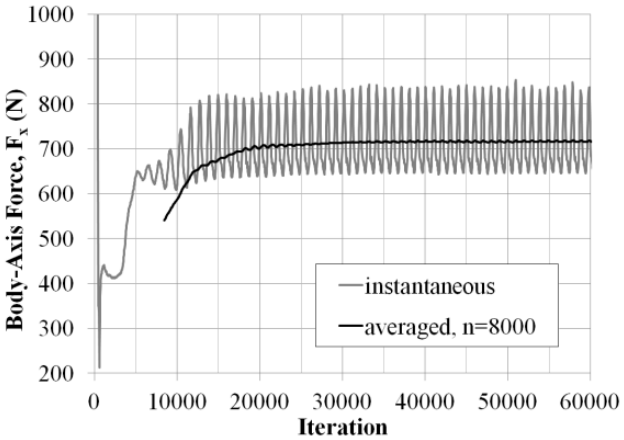


**b)** Instantaneous and averaged (running average of previous 8,000 iterations) body-axis force

**Fig. 8** Convergence history of iterative residuals and forces for simplified tractor-trailer. 637k-cell grid, $y^+ = 0.4$, Cobalt v. 5.0, S-A turbulence model, COLINY-EA design 124, $\beta = 1.8°$

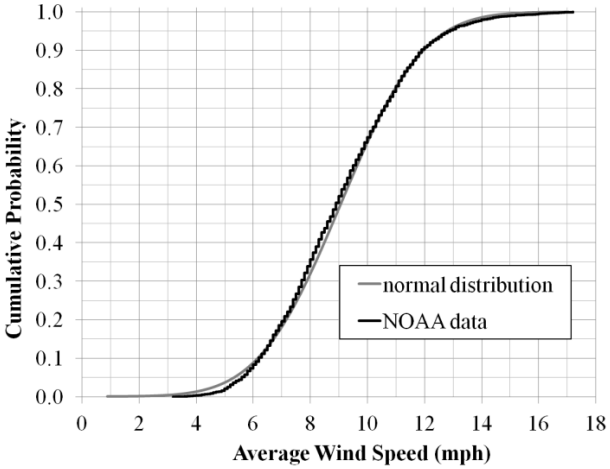


**a)** Cumulative distribution of monthly average wind speed in 250 continental US cities (Dellinger 2008) showing a normal distribution

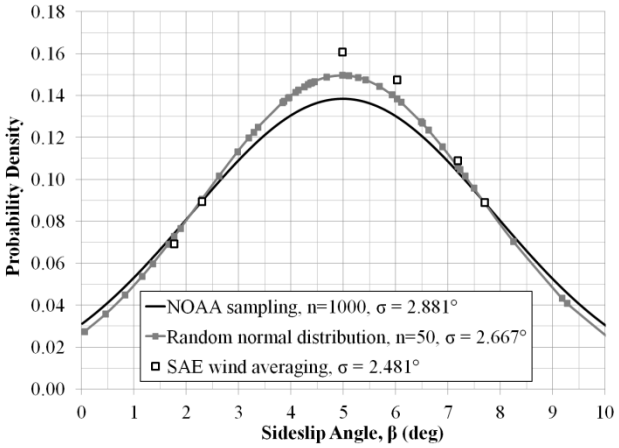


**b)** Probability density function of sideslip-angle input for flow computations, based on random sampling of monthly average wind speed and on random uniform distribution of wind direction

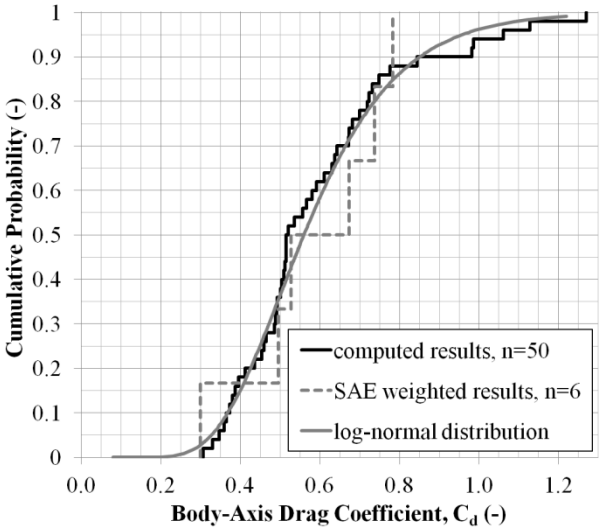


**c)** Empirical and cumulative distributions show log-normal form for body-axis $C_d$. 637k cell grid, straight flap ($\delta$ = 16°, 0.5 cm from trailer edge), Cobalt v5.0, S-A turbulence model

**Fig. 9** Validation of SAE wind-averaging method for approximating rigorous statistical sampling

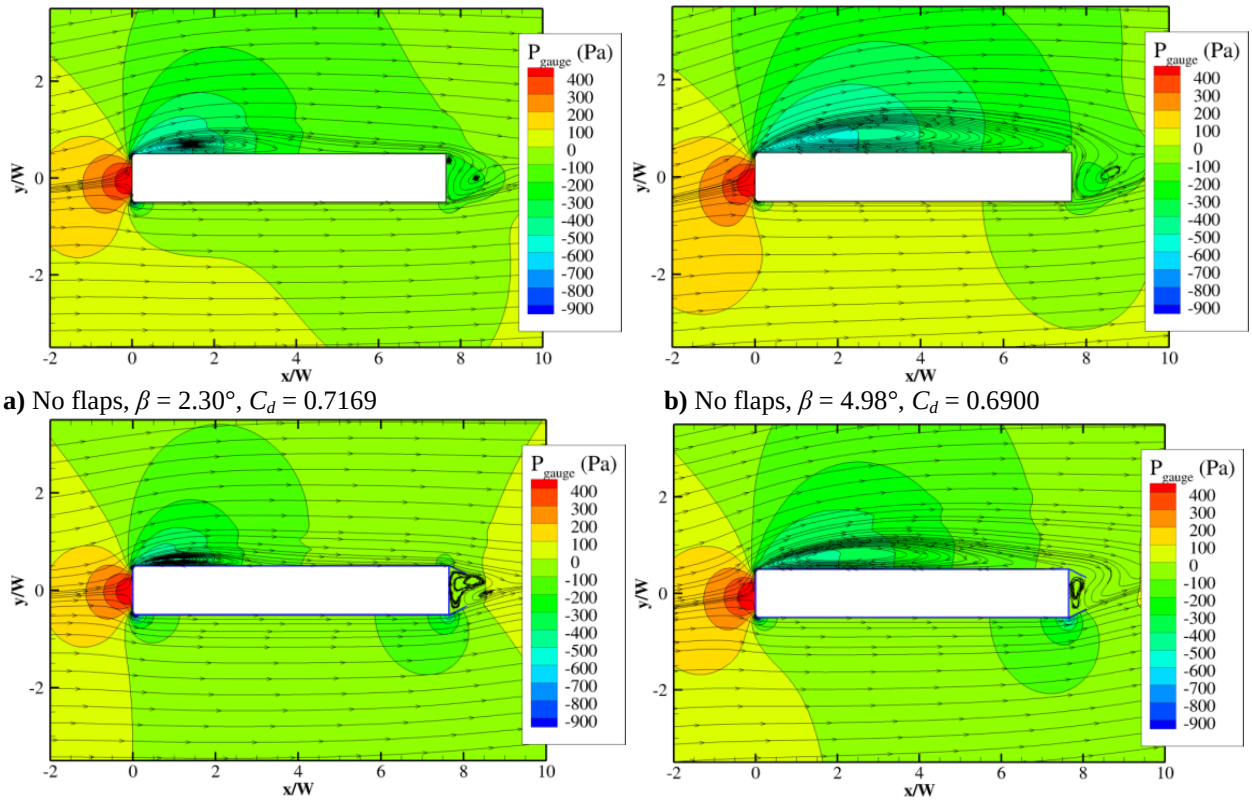


**a)** No flaps, $\beta$ = 2.30°, $C_d$ = 0.7169

**b)** No flaps, $\beta$ = 4.98°, $C_d$ = 0.6900

**c)** With flaps, $\beta$ = 2.30°, $C_d$ = 0.3555

**d)** With flaps, $\beta$ = 4.98°, $C_d$ = 0.5417

**Fig. 10** Effect of using base flaps for simplified 2-D tractor-trailer geometry, velocity streamlines atop contours of gauge pressure. $Re_W$ = 5.2x10$^6$, 637k grid, Cobalt v5.0, S-A turbulence model

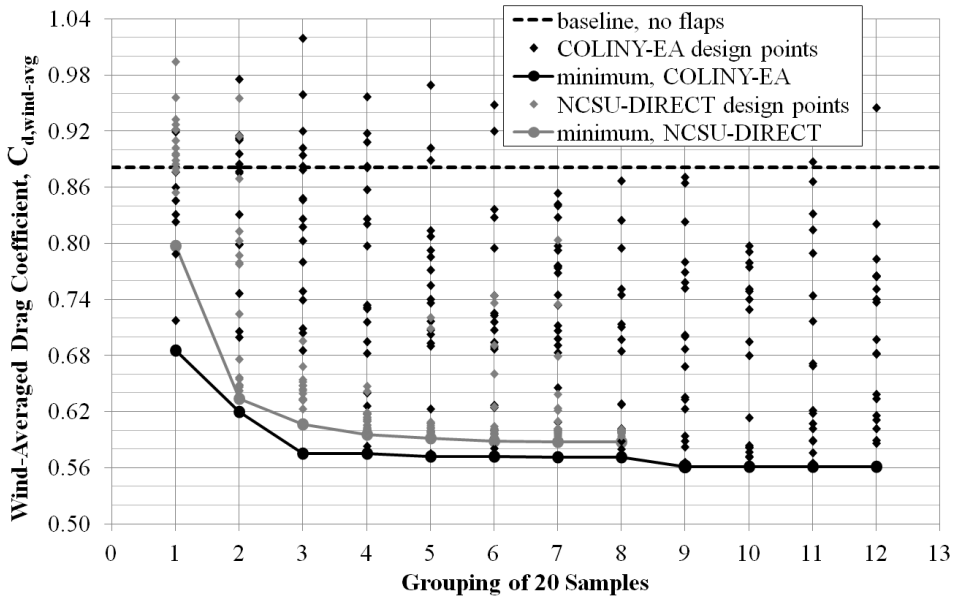


**Fig. 11** Wind-averaged drag coefficient results for 2-D simplified truck from DAKOTA-implemented design optimization algorithms: COLINY Evolutionary Algorithm and NCSU-DIRECT

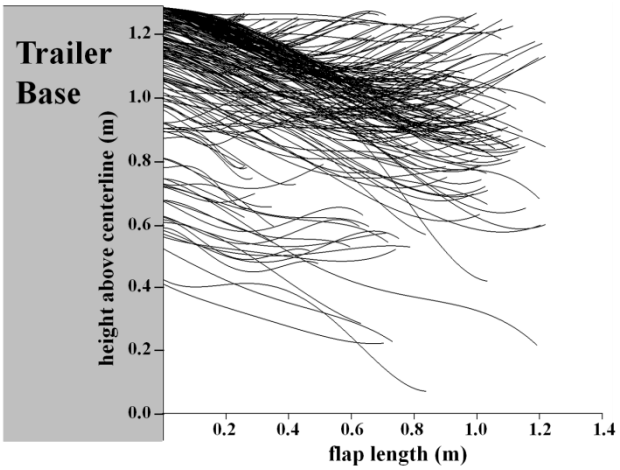


**Fig. 12** 240 COLINY-EA base-flap designs for 2-D simplified tractor-trailer, including infeasible designs

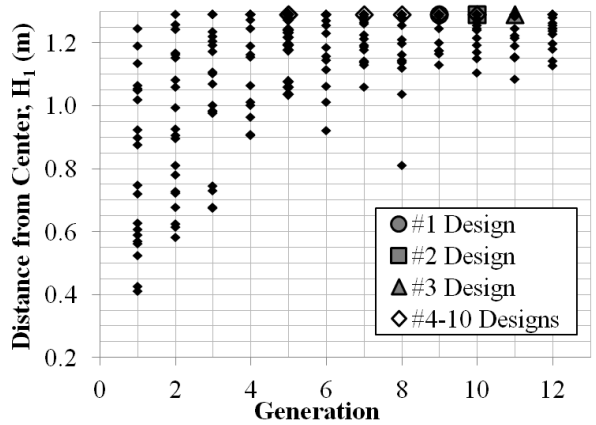


**a)** distance between centerline and flap

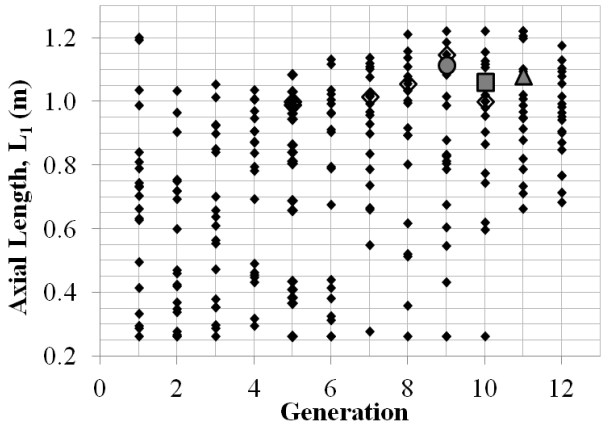


**b)** axial length of flap

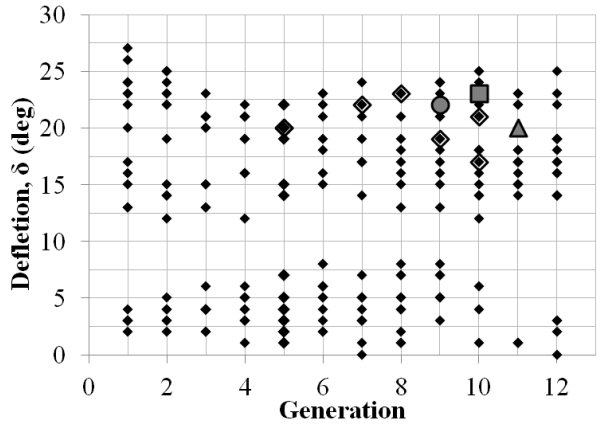


**c)** inward deflection angle of flap

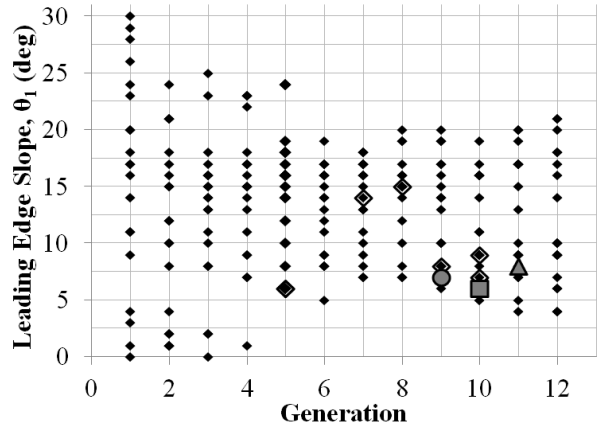


**d)** slope of flap at leading edge

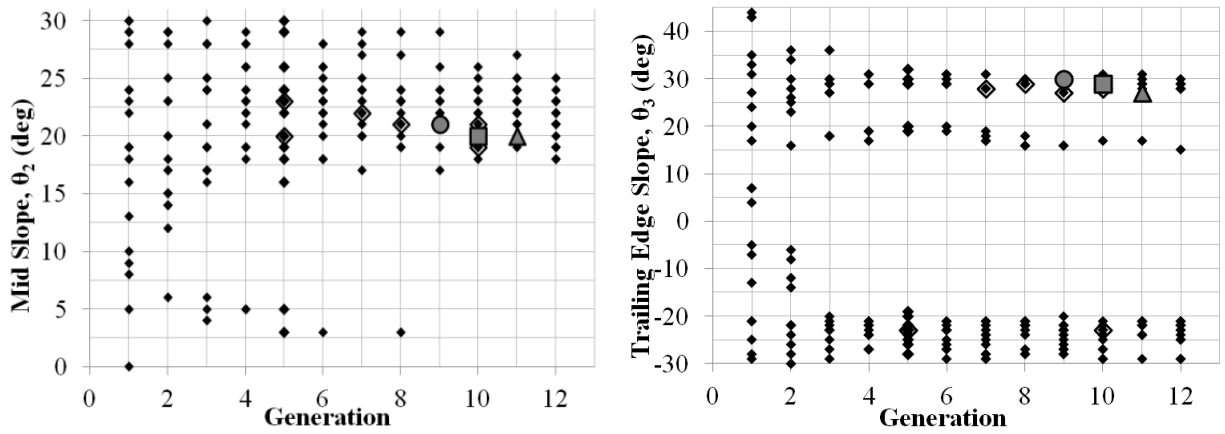


**e)** slope of flap at mid-chord **f)** slope of flap at trailing edge

**Fig. 13** Design variable tracker by generation for COLINY-EA base flaps on 2-D simplified tractor-trailer. Filled shapes highlight 10 best-performing EA designs

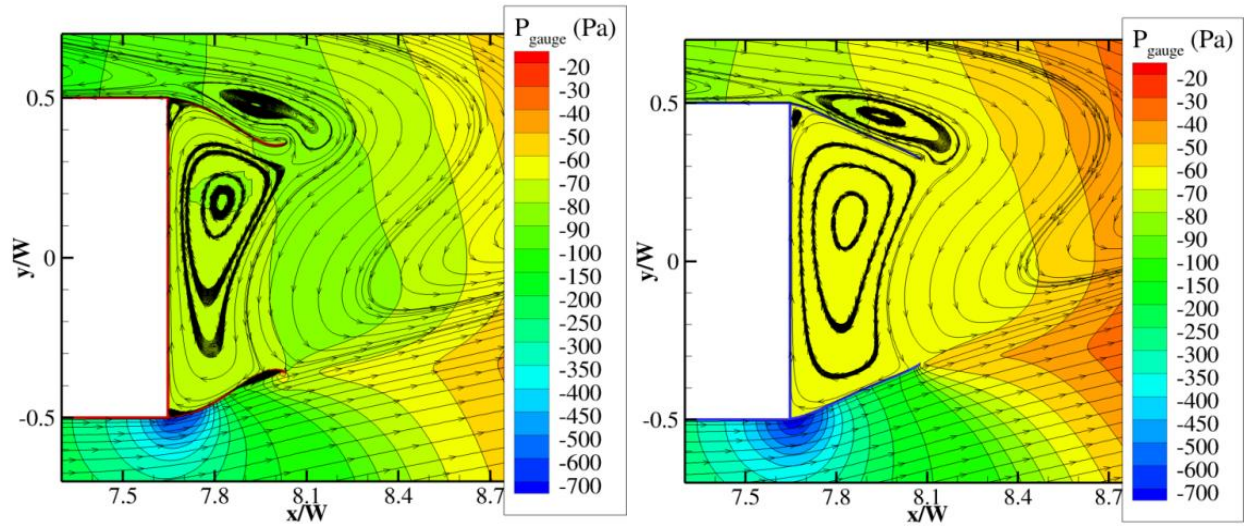


**a)** $\theta_3$ = -23°, $C_d$ = 0.5497 **b)** $\theta_3$ = 30°, $C_d$ = 0.5417

**Fig. 14** Comparison of base-flap trailing edge orientation on simplified 2-D tractor-trailer for $\beta$ = 4.98°. $Re_W$ = 5.2x10$^6$, Cobalt S-A turbulence model. Legend scale is nonlinear for visual effect

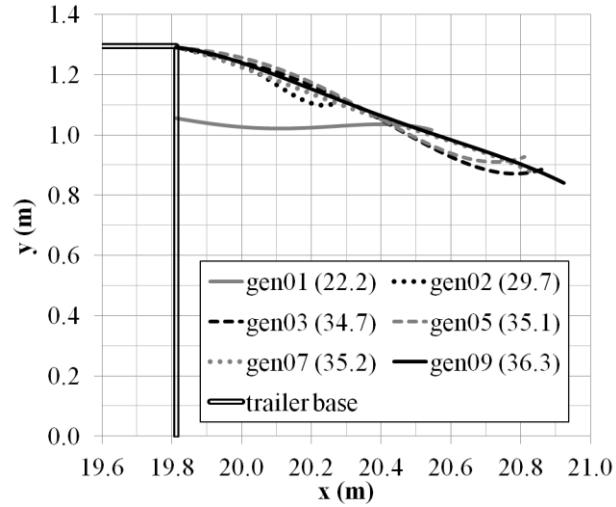


**Fig. 15** 2-D simplified tractor-trailer design evolution by Evolutionary Algorithm generations. Percent improvement over no-flaps baseline $\bar{C}_d$ shown in parentheses. $Re_W$ = 5.2x10$^6$, Cobalt S-A turbulence model

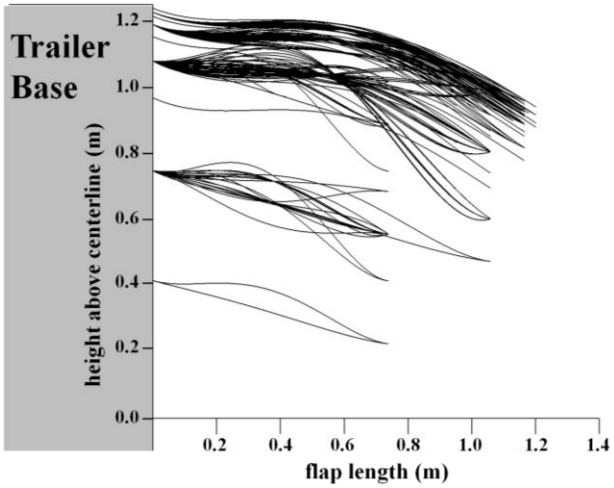


**Fig. 16** 157 NCSU-DIRECT base-flap designs for 2-D simplified tractor-trailer, including infeasible designs

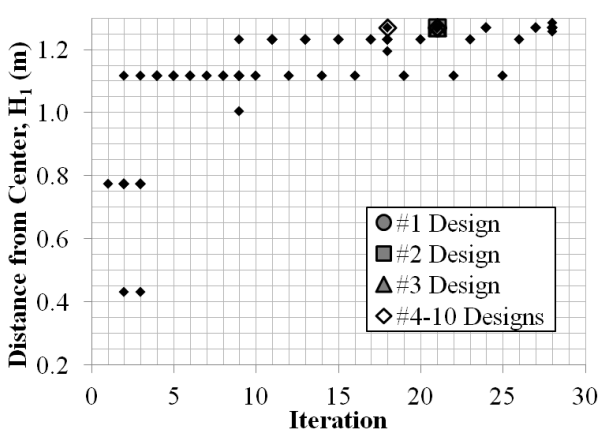


**a)** distance between centerline and flap

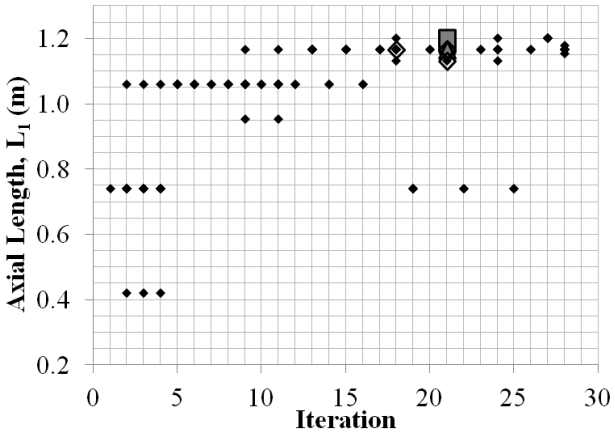


**b)** axial length of flap

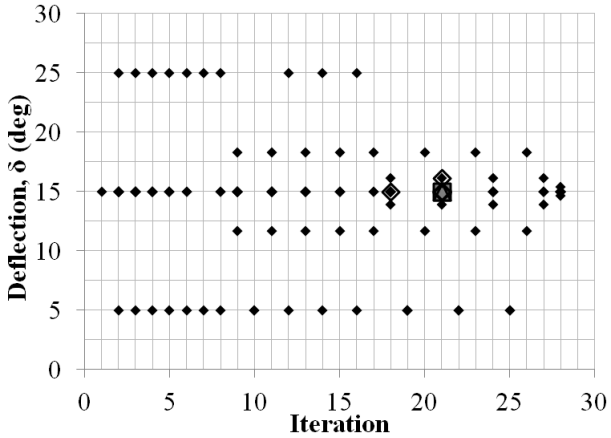


**c)** inward deflection angle of flap

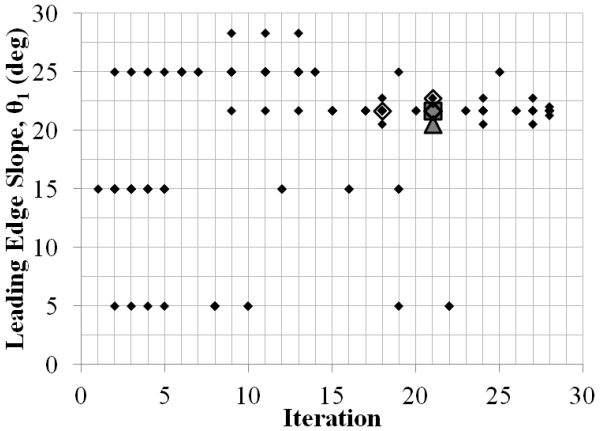


**d)** slope of flap at leading edge

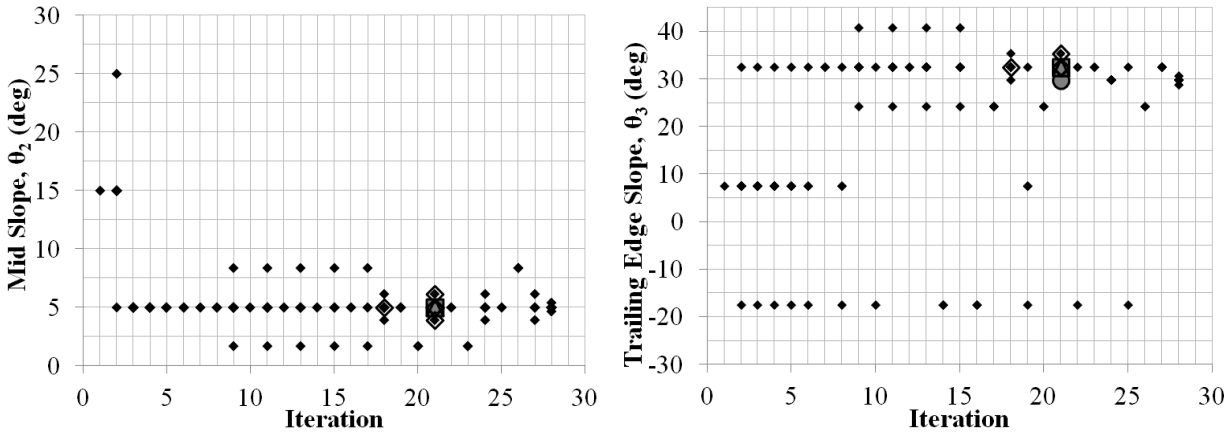


**e)** slope of flap at mid-chord **f)** slope of flap at trailing edge

**Fig. 17** Design variable tracker by iteration for NCSU-DIRECT base flaps on 2-D simplified tractor-trailer. Filled shapes highlight 10 best-performing DIRECT designs

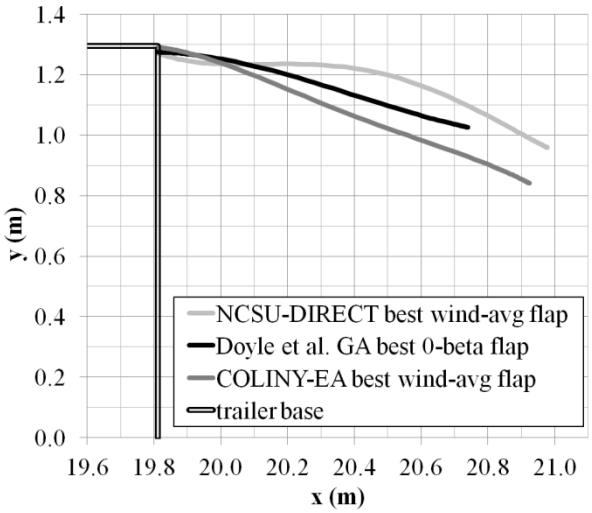


**Fig. 18** Comparison of best-performing optimizer-generated base-flap designs for 2-D simplified tractor-trailer: Doyle et al. (2008) Genetic Algorithm (not wind-averaged) vs. current study COLINY-EA and NCSU-DIRECT (wind-averaged)

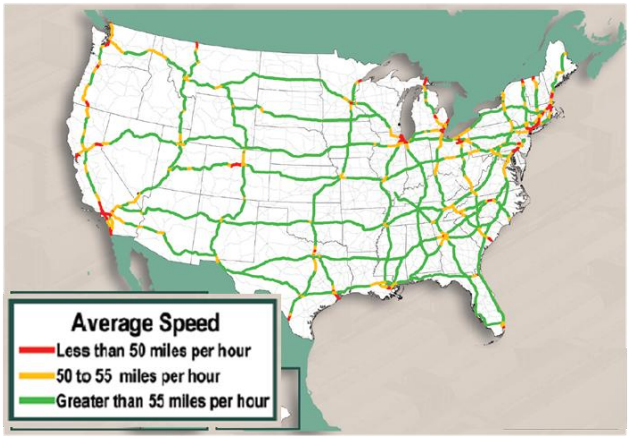


**Fig. 19** Average truck speeds on US interstate highways in 2010, based on data from 500,000+ trucks (Used with permission of Edward Strocko, 2012, Federal Highway Administration)

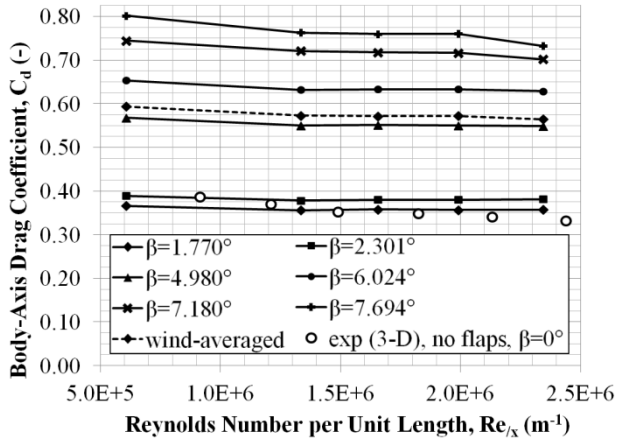


**Fig. 20** Reynolds number effect on $C_d$ for 2-D simplified tractor-trailer with base flaps (design EA.82) at several sideslip angles, compared with wind-tunnel test results from 3-D simplified truck without base flaps (Storms et al. 2001). 637k grid, Cobalt S-A turbulence model

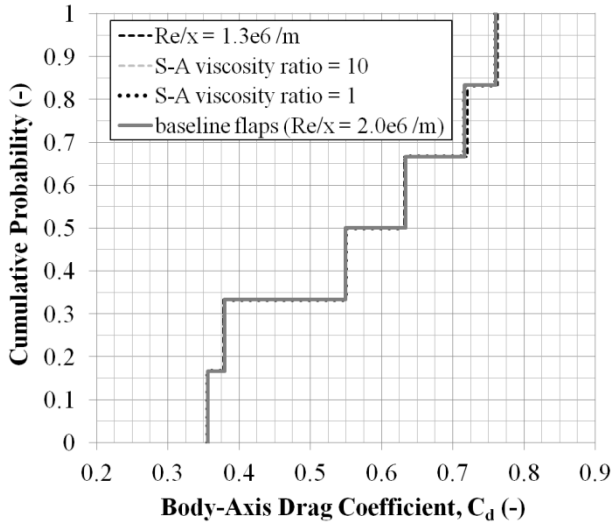


**Fig. 21** Ensemble of EDFs of $C_d$ for model-input uncertain parameters: wind speed and direction (aleatory), truck speed and elevation (aleatory), turbulence model boundary condition (epistemic). All results are from 2-D simplified tractor-trailer with base flaps design EA.82, 637k grid, $Re_W = 5.2 \times 10^6$, Cobalt S-A turbulence model

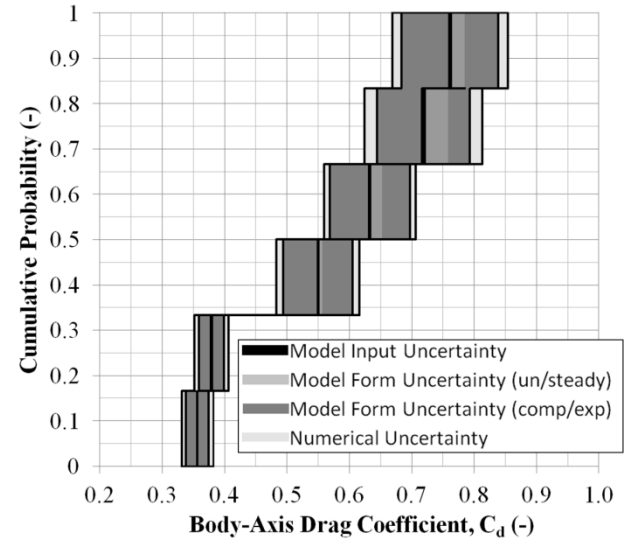


**Fig. 22** Probability-box showing total predictive uncertainty that includes uncertainty due to model input, model form, and numerical approximation, for the 2-D simplified truck with base flaps design EA.82. $Re_W = 5.2 \times 10^6$, Cobalt S-A turbulence model

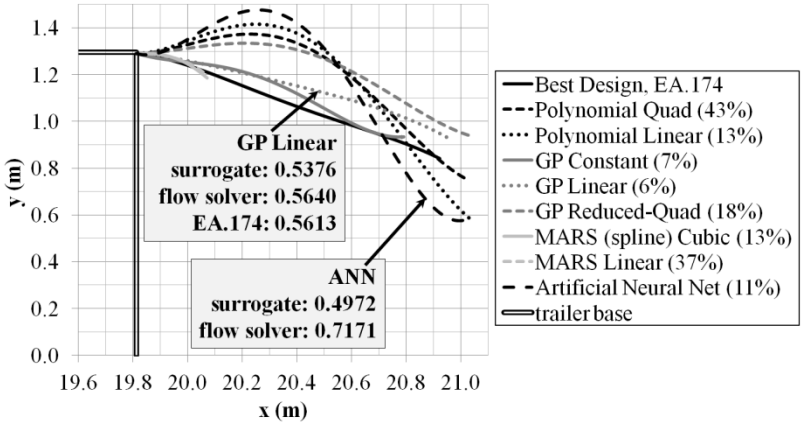


**Fig. 23** Various base flap designs for a 2-D simplified tractor-trailer, from results of a multidimensional parameter study using several surrogate models. 3.4 million function evaluations on each surrogate model for parameter study. Percentage in parentheses is difference between surrogate and truth design

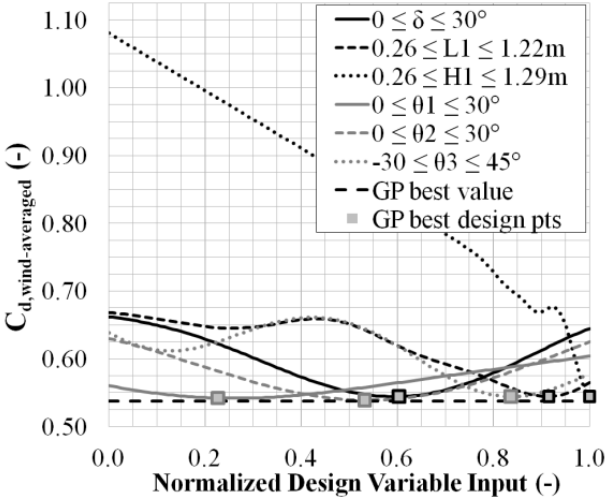


**a)** decoupled design variables in surrogate model; while several of the variables have multiple minima, a parameter search successfully locates a global minimum for each variable

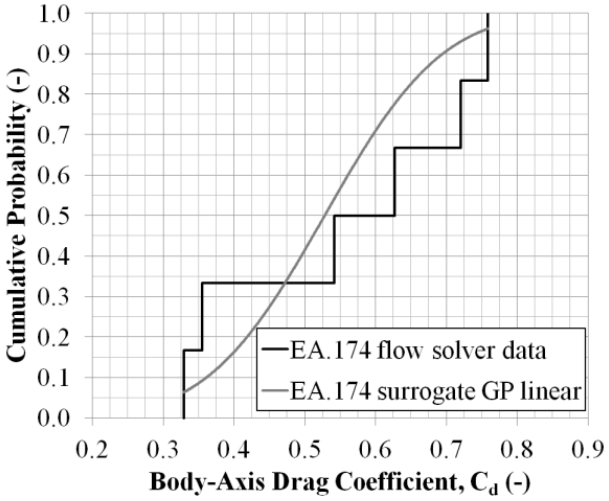


**b)** strength of surrogate model – may be used to approximate a continuous distribution vs. a discrete empirical probability distribution

**Fig. 24** Goodness of surrogate model – linear Gaussian process (GP) data fit from database of computational flow solutions for 289 design points from COLINY-EA and NCSU-DIRECT studies

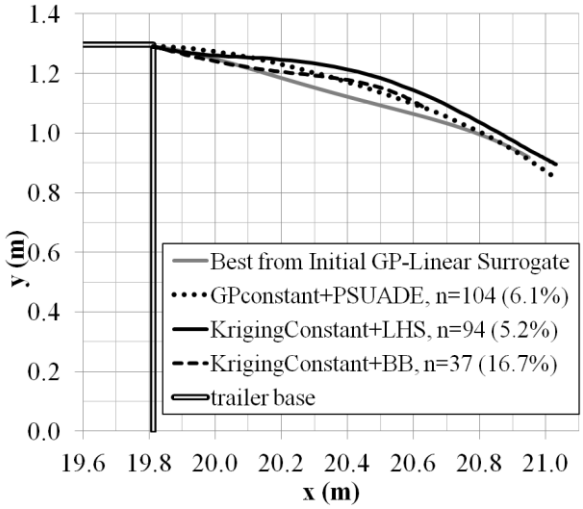


**Fig. 25** Best three of 72 surrogate-sampling combinations, chosen based on closeness to truth design value (noted in parentheses in legend) and to truth design form (gray curve). Truth model is based on the linear GP surrogate model

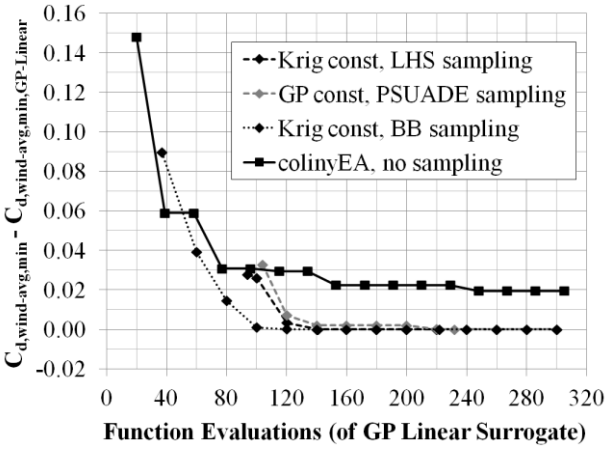


**Fig. 26** SBGO brings these three secondary surrogate-sampling models (dashed and dotted lines) to convergence with the truth design (within 0.003%) with about 140 function evaluations. Compare with non-surrogate-based approach (solid line) that comes within 3.6% of truth design

# Tables

**Table 1.** Trailer Base Flap Design Variables and Constraints

| Design Variable | Description | Constraint |
|---|---|---|
| $H_1$ | distance from trailer base centerline to flap attachment point (m) | $L_1/\cos\delta \le H_1 \le W/2$ |
| $L_1$ | axial length of trailer base flap (m) | $0.1W \le L_1 \le 1.219$ m |
| $\theta_1$ | deflection angle at flap leading edge (deg) | $0 \le \theta_1 \le 30°$ |
| $\theta_2$ | deflection angle at flap mid-chord (deg) | $0 \le \theta_2 \le 30°$ |
| $\theta_3$ | deflection angle at flap trailing edge (deg) | $-30 \le \theta_3 \le 45°$ |
| $\delta$ | flap incidence angle or angle of flap chord line (deg) | $0 \le \delta \le 30°$ |

**Table 2.** COLINY Evolutionary Algorithm Input Parameters (Adams et al. 2009)

| Parameter | Value | Description |
|---|---|---|
| seed | 38 | arbitrary starting point but fixed for repeatability |
| population size | 20 | population for 1st generation only |
| initialization type | unique_random | random generation of design candidates, duplicates rejected |
| mutation type | offset_normal | adds random zero-mean variability within normal distribution to design point variables |
| mutation rate | 1.0 | probability of mutation being performed on candidate |
| crossovers | uniform | crosses random combination of values from two parent design candidates to form new candidate |
| crossover rate | 0.8 | crossover rate * population size = number of crossovers |
| replacement type | chc = 0 | retains no past candidate in the current mating pool |

**Table 3.** NCSU-DIviding RECTangles Algorithm Input Parameters (Adams et al. 2009; Finkel 2003)

| Parameter | Value | Description |
|---|---|---|
| solution target | 0.12 | small desired target value |
| convergence tolerance | 0.01 | use with solution target; percent difference allowed from target |
| minimum boxsize limit | 0.001 | algorithm stops if smallest sub-region falls below this limit, preventing “tiny” hyper-rectangles |
| volume boxsize limit | $1x10^{-9}$ | algorithm stops if percent of original hyper-cube falls below this threshold |

**Table 4.** Sources of Uncertainty from Model Input, Model Form and Numerical Approximation

| | | |
|---|---|---|
| **Model Input** | | |
| ***Tractor-Trailer Geometry*** | ***L, W, H*** | ***deterministic*** |
| Height above ground (trailer loaded/ empty, tire inflation, trailer dimensions) | | epistemic/aleatory uncertainty |
| Tractor forebody shaping | | epistemic uncertainty |
| Trailer front-edge rounding | | epistemic uncertainty |
| Aerodynamic add-on devices (side skirts, wheel fairings, cab roof deflector, etc.) | | epistemic uncertainty |
| ***Tractor-Trailer Base Flaps*** | $H_1, L_1, \theta_1, \theta_2, \theta_3, \delta$ | ***design variables*** |
| Flap Gaps | | epistemic uncertainty |
| Aeroelasticity/flutter (truck vibration, wind gusts, hardware mounting) | | epistemic uncertainty |
| ***Truck Speed & Elevation*** | ***Reynolds Number, Re*** | ***aleatory uncertainty*** |
| ***Wind Speed & Direction*** | ***Sideslip Angle, β*** | ***aleatory uncertainty*** |
| ***Turbulence Model Boundary Conditions*** | $1 \leq \tilde{\nu}/\nu_\infty \leq 10$ ***(for S-A)*** | ***epistemic uncertainty*** |
| | *I* (turbulence intensity near ground: for k-ω, SST) | epistemic uncertainty |
| Effect of Traffic / Drafting (lateral, aft) | | epistemic uncertainty |
| Surface Roughness | | |
| Distributed: aluminum, cloth, wood | | aleatory uncertainty |
| Discrete: dirt, ice, damage, insects | | epistemic uncertainty |
| Driving Conditions (dry, rain, snow, ice, unusual wind, unusual terrain) | | epistemic uncertainty |
| **Model Form** | | |
| ***Computation vs. Experiment*** | | ***epistemic uncertainty*** |
| ***Steady RANS Approximation*** | | ***epistemic uncertainty*** |
| ***Turbulence Model*** | | ***epistemic uncertainty*** |
| Wheels: moving, stationary, none | | epistemic uncertainty |
| Effects of Complex Truck Geometry on $\Delta C_d$: | | |
| With/without base flaps (wheels, wheel flaps, exhaust stack, side mirrors, front grill) | | epistemic uncertainty |
| **Numerical Approximation** | | |
| ***Discretization Error*** | $U_{discretization}$ | ***estimated*** |
| ***Round-Off Error*** | $U_{round\text{-}off}$ | ***estimated*** |
| ***Statistical Sampling Error*** | $U_{sampling}$ | ***zero in this study*** |

[a] Items in bold italics are addressed in this 2-D study.

**Table 5.** Comparison of Best Designs from Doyle et al. (2008) and Current Study (Design EA.174 and DIRECT.121)

| Design Variable | Doyle et al. optimum (max) | EA.174 optimum (max) | DIRECT.121 optimum (max) |
|---|---|---|---|
| $H_1$ (m) | 1.2747 *(1.2889)* | 1.2904 *(1.2904)* | 1.2713 *(1.2904)* |
| $L_1$ (m) | 0.9283 *(1.2192)* | 1.1117 *(1.2192)* | 1.1659 *(1.2192)* |
| $\theta_1$ (deg) | 1.5 *(15.0)* | 7 *(30)* | 21.67 *(30)* |
| $\theta_2$ (deg) | - | 21 *(30)* | 5 *(30)* |
| $\theta_3$ (deg) | 13.5 *(15.0)* | 30 *(45)* | 29.72 *(45)* |
| $\delta$ (deg) | 15.0 *(15.0)* | 22 *(30)* | 15 *(30)* |
| $C_d$ Improvement over No-Flaps Design, $\beta = 0°$ | 59% | **79%** | 72% |
| $\bar{C}_d$ Improvement over No-Flaps | 29% | **36%** | 33% |

**Table 6.** Computational predictions vs. experiment for 3-D simplified tractor-trailer at varied sideslip angles

| Turbulence Model, 3-D Cases | $C_D$ Difference from Experiment (%) | | | |
|---|---|---|---|---|
| | $\beta = 0°$ | $\beta = 1\text{-}2°$ | $\beta = 4\text{-}8°$ | $\beta = 10°$ |
| **RANS S-A** (Roy et al. 2006; Maddox et al. 2004) | 49 - 65 | | | 58 |
| **RANS k-ω** (Roy et al. 2006) | 4.4 - 8 | | | |
| **RANS k-ε** (Basara and Tibaut 2004; Pointer et al. 2009)[a] | 2.3 - 10 | 0.5 - 1.0 | 10 - 12 | 9 |
| **RANS Reynolds Stress** (Basara and Tibaut 2004) | 0.6 | | | |
| **RANS SST** (Pointer et al. 2009)[a] | 0.8 - 2.6 | 0.5 - 1.0 | 10 - 12 | 9 |
| **DES, unsteady** (Maddox et al. 2004; Roy and Ghuge 2009; Sreenivas et al. 2009) | 2 - 12 | | | 12 - 39 |

[a] Pointer et al. (2009) do not specify which turbulence model is used for results at $\beta \neq 0°$.

**Table 7.** Percentages of Components of Total Predictive Uncertainty Estimate for Design EA.174

| Total Predictive Uncertainty for Best Design (EA.174) | Upper Bound (%) | Lower Bound (%) |
|---|---|---|
| model input (Re, S-A input) | 0.12 | 0.23 |
| model form (unsteady, exp) | 8.92 | 8.92 |
| numerical | 2.12 | 2.12 |
| TOTAL | 11.16 | 11.27 |

**Chapter 4**: Accepted for publication in *AIAA 51st Aerospace Sciences Meeting, January 2013*. Modified format in review for publication in *Computers & Fluids*.

# Global Optimization Under Uncertainty for Tractor-Trailer Base Flaps

Major Jacob A. Freeman, USAF* and Christopher J. Roy†
*Virginia Tech, Blacksburg, Virginia 24061*

**Using a global optimization evolutionary algorithm, propagating aleatory and epistemic uncertainty within the optimization loop, and using computational fluid dynamics, this study determines a design for 3-D tractor-trailer base-drag reduction devices that reduces the wind-averaged drag coefficient by 41% at 57 mph (92 km/h). Because it is optimized under uncertainty, this design is relatively insensitive to uncertain wind speed and direction and uncertain deflection angles due to mounting accuracy and static aeroelastic loading. The model includes five design variables with generous constraints, and this study additionally includes the uncertain effects on drag prediction due to truck speed and elevation, steady Reynolds-averaged Navier-Stokes (RANS) approximation, and numerical approximation. This study uses the DAKOTA optimization and uncertainty quantification framework to interface the RANS flow solver, grid generator, and optimization algorithm. The computational model is a simplified full-scale tractor-trailer with flow at highway speed. For the optimized design, the estimate of total predictive uncertainty is $^{+15\%}_{-42\%}$; 8-10% of this uncertainty comes from model form (computation vs. experiment); 3-7% from model input (wind speed and direction, flap angle, and truck speed); and +0.0/-28.5% from numerical approximation (due to the relatively coarse, 6-million cell grid). Relative comparison of designs to the no-flaps baseline should have considerably less uncertainty because numerical error and input variation are nearly eliminated and model form differences are reduced. The total predictive uncertainty is also presented in the form of a probability box, which may be used to decide how to improve the model and reduce uncertainty.**

# 1 Introduction

With no indication of future reduction in global fuel prices, commercial transportation companies and the US Department of Energy have for decades been working to reduce aerodynamic drag on tractor-trailers. More recently global commercial, government and military sectors are focusing effort on reducing consumption of fossil fuels. For tractor-trailers, aerodynamic drag occurs primarily in four areas [1]: tractor forebody; tractor-trailer gap; trailer underbody; and trailer base. The trailer underbody and base account for more than half of that aerodynamic drag [1]. While many drag-reduction shapes and devices have been designed and analyzed, such as a cab roof deflector, cab side extenders, skirt between cab and trailer, trailer front-end fairing, trailer front-end edge-rounding, trailer side skirts, wheel fairings, trailer underbody fairing, trailer vortex generators, slotted wheel flaps, wheel coverings, and trailer boat-tail or flaps on the trailer base [2, 3], most companies have focused on modifications to the tractor, where the largest return-on-investment is achieved. Figure 1 illustrates several tractor and trailer modifications and add-on devices.

* Graduate Student, jacobf72@vt.edu, Department of Aerospace & Ocean Engineering, Senior Member AIAA.
† Associate Professor, cjroy@vt.edu, Department of Aerospace & Ocean Engineering, Associate Fellow AIAA.

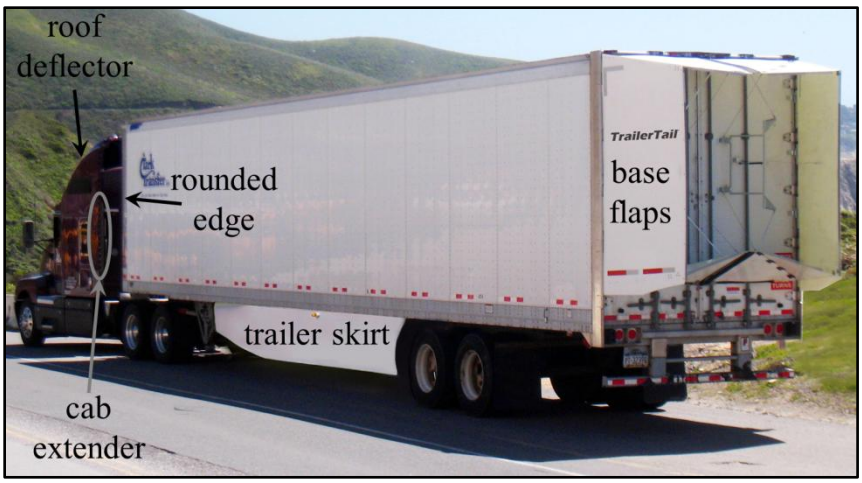


**Fig. 1.** Example of straight trailer base flaps and other aerodynamic drag-reduction devices [4] (Used with permission of Steven Rodger, 2012, ATDynamics, www.ATDynamics.com).

A wind-tunnel study using a full-scale truck at highway speed of 65 mph (105 km/h) has shown that the combination of roof-mounted deflector, cab side extenders, and rounding the trailer front edges, which we term the "modified configuration," reduces the wind-averaged drag coefficient, $\bar{C}_D$, by 17%, compared with an unmodified baseline configuration [2]. (We explain wind averaging in Section 2.1, and more detail is available in Ref. 5.) Relative to the unmodified configuration, the addition of front trailer skirts (similar to those in Fig. 1), tractor-trailer gap seal, and base flaps (straight; axial length, $L_1 = 0.20W$, where $W$ is trailer width; and deflected inward 15°), results in an additional 17% reduction in $\bar{C}_D$ at 65 mph (9% from the side skirts, 3% from the gap seal, and 5% from the base flaps) [2]. Note that the base flaps reduce $\bar{C}_D$ by 6% when compared with the modified configuration. Using the Society of Automotive Engineers (SAE) road-test procedures for heavy trucks [6] and with base flaps of $L_1 = 0.47W$, a commercial company claims 12% reduction in $\bar{C}_D$ at 65 mph from the base flaps and relative to the modified configuration [4].

At the base of a tractor-trailer, flow features include massive separation and turbulent shear flow that lower the static pressure and generate significant pressure drag because of the pressure differential between tractor front and trailer base. While base flaps add skin-friction drag and regions of adverse pressure gradient, more significantly they force the trailing wake to shrink and stabilize, resulting in a region with pressure a little larger than the freestream, which in turn creates less pressure drag [7] and allows for a safer driving environment for trailing and nearby vehicles. Figure 2 illustrates this with flow visualization from 3-D computational time-averaged solutions at highway speed 57.2 mph (92.1 km/h) and sideslip angles, $\beta = 9.1°$ for Figs. 2a and 2b, and $\beta = 0°$ for Figs. 2c and 2d. Random winds can result in different flow angles seen by the tractor-trailer, and these uncertainties are propagated from input to output by considering different sideslip angles. Figure 2a shows streamlines and gauge pressure ($P_{gauge} = P - P_\infty$, where $P_\infty$ is freestream pressure) contours for the trailer base without flaps, and Fig. 2b shows results for the trailer with base flaps; Figs. 2c and 2d show stream traces for the two different configurations. Addition of the base flaps visibly reduces the wake size and strength, as indicated by the smaller region of recirculating flow and higher static pressure, resulting in 39% reduction in body-axis drag coefficient, $C_D$, at that sideslip angle and 36% reduction in $\bar{C}_D$. Because the geometry for the computational simulation is simplified and includes forebody rounding, we expect a geometrically complex, full-scale tractor-trailer to experience roughly half that amount of drag reduction; this observation is based on comparing wind-tunnel experiments with nearly identical base flaps for 1/8-scale simplified geometry, which showed 19% reduction in $\bar{C}_D$ [8], and for an actual full-scale tractor-trailer, which showed 10% reduction in $\bar{C}_D$ [9]. Ten percent reduction in $\bar{C}_D$ translates to about 5% reduction in fuel consumption [2, 4].

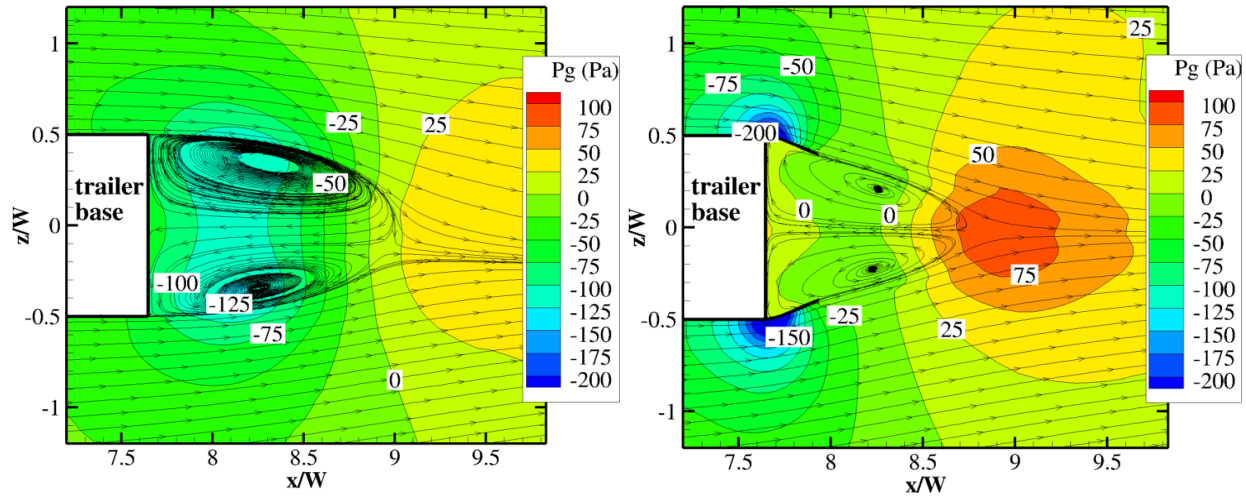


(a) Baseline configuration, no flaps, $C_D$ = 0.3287.

(b) Side flaps deflected inward 20°, $C_D$ = 0.2005.

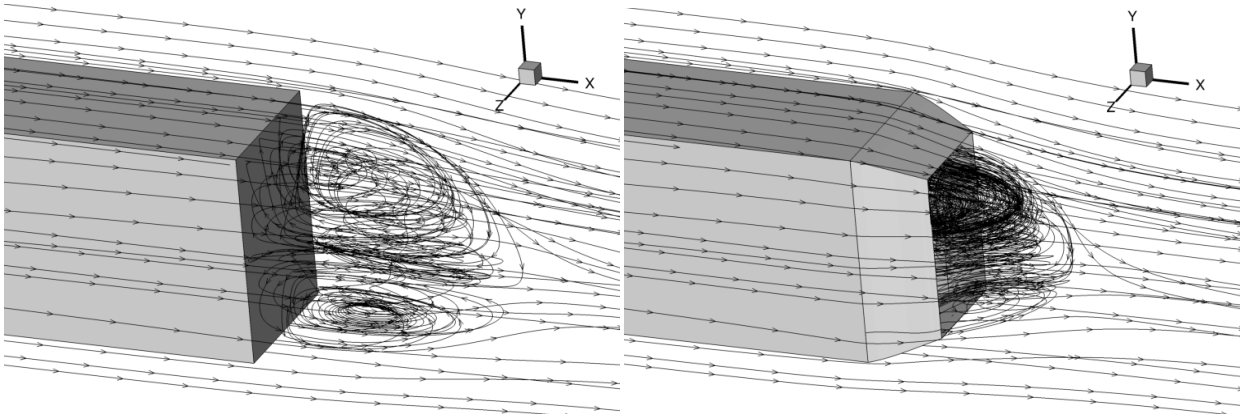


(c) Stream traces, no flaps.

(d) Stream traces, all flaps deflected inward 18°.

**Fig. 2.** Time-averaged 3-D computational solutions of simplified tractor-trailer with and without base flaps, showing reduced region of low pressure and stabilized base flow. Horizontal slice at $y/W$ = 0.695 for $\beta$ = 9.1° showing velocity streamlines atop contours of gauge pressure (for (a) and (b)). $\beta$ = 0° for (c) and (d). Highway speed, $V_\infty$ = 57.2 mph (92.1 km/h), and trailer-width-based Reynolds number, $Re_W$ = 4.4 x $10^6$.

Numerous experimental and some computational studies have been conducted to quantify the drag reduction associated with base flaps. Using a full-scale truck at highway speed of 65 mph, wind-tunnel testing of Cooper [2, 7] shows 6-8% reduction in $\bar{C}_D$ for straight flaps with $0.19W \le L_1 \le 0.25W$ and inward deflection of the flaps, $10 \le \delta \le 18°$. Using the SAE road-test procedures [6], with base flaps of $L_1 = 0.47W$ and $\delta$ = 15°, a commercial company claims 12% reduction in $\bar{C}_D$ at 65 mph [4, 10]. Road testing of Browand et al. [11] shows 8% reduction in $\bar{C}_D$ (compared with the baseline from Cooper [2]) for straight flaps of $L_1 = 0.24W$ and $\delta$ = 13°. Wind-tunnel testing of Hsu et al. [12], with streamlined geometry and at 1/12 full-scale Reynolds number, shows 30% reduction in $C_D$ at zero sideslip (assuming baseline $C_D = 0.25$) for straight flaps of $L_1 = 0.27W$ and $0.53W$ and for $9 \le \delta \le 12°$. Wind-tunnel testing of Ortega and Salari [13], with streamlined geometry and non-rotating wheels, shows 16% reduction in $\bar{C}_D$ for straight flaps of $L_1 = 0.35W$, $\delta_{side\ flaps}$ = 10°, $\delta_{top\ flap}$ = 11°, and $\delta_{bottom\ flap}$ = 0°. Ortega and Salari [13] further show 19% reduction in $\bar{C}_D$ for flaps with constant-radius curvature and $L_1 = 0.30W$. The 3-D computational study of Hsu and Davis [14] with streamlined geometry (for both tractor and trailer portions of the simplified geometry, instead of only for the tractor forebody) and curved flaps shows 51% reduction in zero-sideslip $C_D$ for $L_1 = 0.20W$ and $\delta$ = 9°; we expect a traditional, straight trailer body, with comparable base-drag reduction devices, to yield a smaller reduction in drag.

One of the moving targets in a base-flap optimization study is the deflection angle, where there is a "sweet spot" for each flap shape; this optimum deflection angle maximizes the effect of wake modification and enables the flow

to remain attached at the various sideslip angles. Figure 3 demonstrates this sensitivity, where Fig. 3a shows the boundary layer attached to the flap and a smooth reduction of the wake size and strength, whereas Fig. 3b shows the boundary layer separated from the flap (for a design similar to the one in Fig. 3a). The boundary layer separates because of the larger deflection angle and greater adverse pressure gradient, and this results in a 28% larger $C_D$.

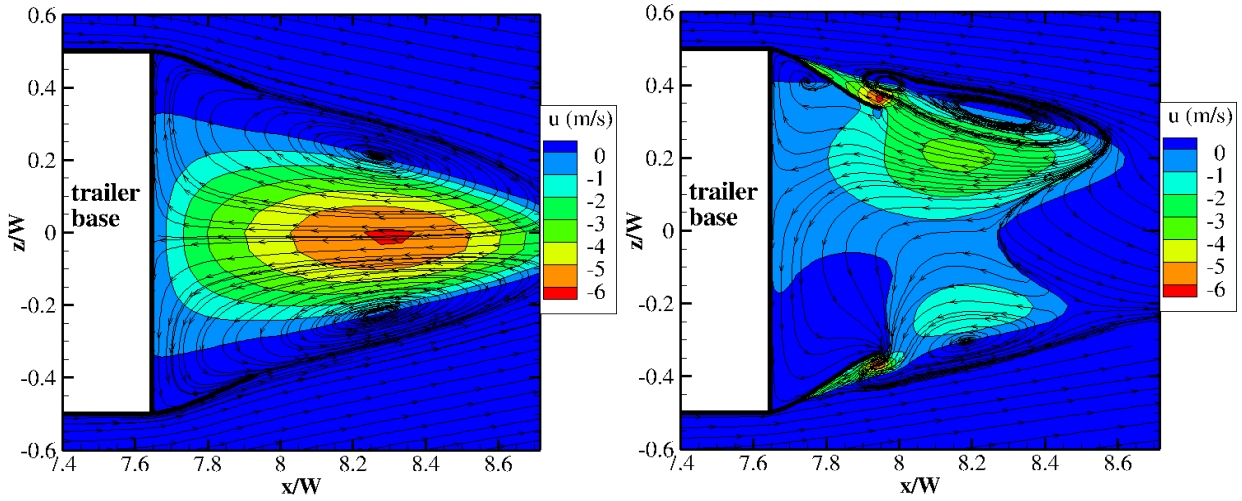


(a) Attached flow for $\delta$ = 20°, $C_D$ = 0.2083. (b) Separated flow for $\delta$ = 29°, $C_D$ = 0.2669.

**Fig. 3.** Time-averaged 3-D computational solutions of simplified tractor-trailer showing sensitivity of base-flap boundary layer to flap deflection angle. Horizontal slice at $y/W$ = 0.695 for $\beta$ = 2.0° showing velocity streamlines atop contours of velocity in the $x$-direction. Highway speed, $V_\infty$ = 57.2 mph (25.6 m/s), and $Re_W$ = 4.4 x $10^6$.

Numerous results confirm the observation that drag reduction from add-on devices and aerodynamic shaping is greater for geometries with front-edge rounding [7, 12, 13, 14]. All of these studies test a relatively small number of design configurations, and most of them include wind-averaging to account for variability in wind speed and direction. Cooper [7] shows that straight deflected flaps are slightly better than curved flaps (for 35 different configurations of each type), while Ortega and Salari [13] show that a curved flap is better. Most of these studies show that a flap length of 0.25$W$ is best, but ATDynamics [4] and Hsu et al. [12] show good results for a length closer to 0.5$W$. Thus, we conduct a computational optimization study to maximize drag reduction due to the addition of trailer base flaps that may have relatively wide ranges of curvature, length, and deflection angles (to include holding side flap angles independent of top and bottom flap angles). In addition, because some of the model input variables are uncertain, whether aleatory (inherent randomness) or epistemic (due to a lack of knowledge) in form [15], we propagate some sources of uncertainty within the design optimization loop. Specifically, we include within the optimization loop the aleatory uncertainty associated with wind direction and speed to predict a wind-averaged drag coefficient and the epistemic uncertainty associated with flap deflection angles – variability due to mechanical mounting and/or static aeroelasticity.

# 2 Methods

## 2.1 Framework and model

The optimization framework is managed by Sandia National Laboratories' Design Analysis Kit for Optimization and Terascale Applications (DAKOTA) [16] and includes automated computational mesh generation using Gridgen [17], flow calculations via the Cobalt computational fluid dynamics (CFD) solver version 5.2 [18], and design optimization by DAKOTA's common optimization library interface (COLINY) evolutionary algorithm (EA). Based on user-specified input parameters, the EA optimization scheme determines appropriate design candidates (base flap shape and orientation) then awaits the returned flow solver output, $\bar{C}_D$. While it waits, we generate the model geometry and flow solver input file, feed that grid and input deck to the flow solver at the appropriate flow conditions, extract $\bar{C}_D$, and return that value to the EA. These design candidates are executed concurrently in generations with a population of 20, of which one is the best candidate from the previous generation. The algorithm

then assesses these returned values, determines the next design points, and repeats. We illustrate this process in Fig. 4, where dashed lines represent user activity.

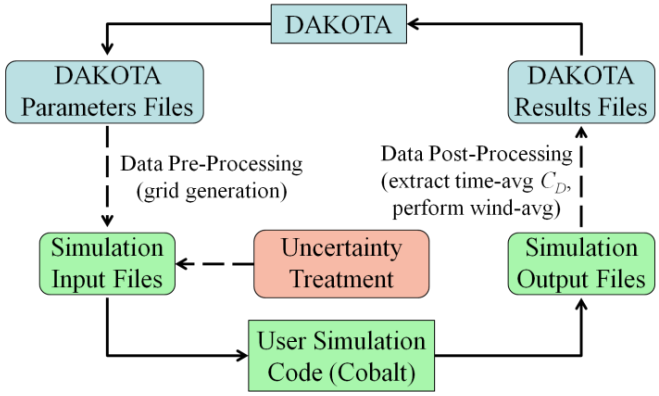


**Fig. 4.** Framework of optimization algorithm, pre-processing, simulation, and post processing.

For the physical model, we assume a constant freestream velocity ($V_\infty$ = 57.2 mph = 25.6 m/s) which is the average truck speed in 2010 on 25 interstate highways in the US [18], standard temperature ($T_\infty$ = 293.15 K), pressure ($P_\infty$ = 101.325 kPa), and density ($\rho_\infty$ = 1.204 kg/m$^3$) – corresponding to Reynolds number, $Re_\lambda = 1.698\text{x}10^6$ m$^{-1}$, or $Re_W = 4.4\text{x}10^6$ (Reynolds number based on trailer width), and Mach number, $M_\infty$ = 0.0745. We use the vehicle geometry of the Sandia National Laboratories Ground Transportation System (GTS), which models a Class-8 cab-over-engine tractor-trailer and uses the standard length ($L$ = 19.812 m = 65 ft*)* and width ($W$ = 2.5908 m = 8 ft 6 in.) for US trucks [8]. The trailer height is modified ($H$ = 3.6068 m = 11 ft 10 in., or 28 in. greater than the standard 9 ft 6 in.) to represent some of the effects of a trailer skirt and the cab being closer to the ground than the trailer, while the top of the trailer maintains the standard 13 ft 6 in. (4.11 m) above ground [8, 20]. To simplify the model and flow physics in regions not being investigated, the GTS geometry neglects the cab-trailer gap, other excrescence drag components (side mirrors, exhaust stack, underbody elements, etc.), and we further choose to remove the wheels. The experimental results of Ortega and Salari [13] and Gutierrez et al. [20] show that the presence of wheels increases the magnitude of $C_D$ but maintains roughly the same behavior (or shape of the curve) for $C_D$ vs. $\beta$; thus, for this comparative study, we neglect the effect of wheels.

The physical model accounts for two uncertain inputs which are included within the design optimization loop, hence this study is aerodynamic shape optimization under uncertainty (OUU). First, we include the effects of uncertain wind speed and direction, based on the National Oceanic and Atmospheric Administration (NOAA) collection of average monthly wind speed measurements in 250 continental US cities between 1927 and 2002 [21] and on the SAE standard practice for wind-averaging drag coefficients for trucks [5]. Freeman and Roy [22] show that the SAE wind-averaging practice of using weighted $C_D$ values from six determined sideslip angles is sufficiently representative of averaging the values from a much larger set of angles; thus, the SAE wind-averaging method is an adequate approximation of the more statistically robust method. Second, we include the effects of uncertainty in the base flap deflection angles, where the physical mounting angle may be inaccurate and/or where side winds may create static aeroelastic loading on the flaps and result in off-design deflection angles. We select $\delta \pm 2°$ for the epistemic uncertainty bounds, based on engineering judgment for mounting tolerance and reasonable displacement from wind gusts and based on results using the 2-D GTS model of our prior investigation [22], where this displacement corresponds to ± 5% difference in the $C_D$ values at a given $\beta$. Some 3-D results indicate ± 12% difference in $C_D$ for cases where $\delta$ hovers around the angle at which flow separates from the flaps (refer to Fig. 3). Hence, $\delta \pm 2°$ results in enough sensitivity to merit design consideration. Using the SAE wind-averaging method [5] for $V_\infty$ = 57.2 mph and average wind speed of 9.06 mph [21], we obtain $\beta$ = { 2.036, 2.770, 5.751, 7.187, 8.360, 9.063° } and weights, $\psi$ = { 1.3310, 0.7191, 1.2490, 0.8011, 1.1071, 0.9431 }. Cooper [7] points out that a truck moving at this ground speed has 10% probability of experiencing $\beta > 9°$; thus, the range noted above covers 90% of what any given tractor-trailer will experience on the highway. $\bar{C}_D$ is then calculated according to

$$\bar{C}_D = \frac{1}{6}\sum_{i=1}^{6} \psi_i C_D(\beta_i) \tag{1}$$

where

$$C_D(\beta_i) = \frac{F_x(\beta_i)}{\frac{1}{2}\rho_\infty V_\infty^2 HW} > 0 \tag{2}$$

where $F_x(\beta_i)$ is the axial force (N) at the respective sideslip angle, $\beta_i$ (deg), which includes both pressure and skin friction forces acting over the body surface and flaps. This force is predicted using the Cobalt flow solver [18].

We systematically select design variables and specify constraints based on previous research. We fix the flaps flush with the trailer base sides, top, and bottom, based on results of the 2-D GTS optimization studies of Freeman and Roy [22] and Doyle et al. [23] and on the wind-tunnel results of Lanser et al. [9] and Gutierrez et al. [20]. We specify that side-flap deflection angles are independent of top- and bottom-flap angles based on the experimental results of Ortega and Salari [13]. We specify an equation for flap shape that allows for straight or curved flaps, based on the findings of Cooper [7], Ortega and Salari [13], and Hsu and Davis [14]. And we allow variable flap length based on all studies discussed above. Figure 5a shows notional side base-flap geometry with four design variables: $L_1$, $\theta_1$, $\theta_2$, and $\delta_{side}$ (while not shown in the figure, $\delta_{top}$ is specified for the top/bottom flap). In our earlier study [22], we find that an additional slope specification at the mid-chord location does not significantly affect the results. We use $W$ or $H$, $L$, $L_1$, and $\delta_{side}$ or $\delta_{top}$ to determine two points in Cartesian space, according to Eqs. (3) and (4), where point 1 is the flap intersection at the trailer base and point 2 is the flap trailing edge.

$$x_{1_{side}} = x_{1_{top}} = L; \quad y_{1_{side}} = y_{1_{top}} = H; \; z_{1_{side}} = z_{1_{top}} = W/2 \tag{3}$$

$$\begin{aligned} x_{2_{side}} &= x_{2_{top}} = L + L_1; \quad y_{2_{side}} = H; \; y_{2_{top}} = H - L_1 \tan\delta_{top}\,; \\ z_{2_{side}} &= \frac{W}{2} - L_1 \tan\delta_{side}\,; \; z_{2_{top}} = W/2 \end{aligned} \tag{4}$$

These two points are then used with slopes, $\theta_1$ and $\theta_2$, to solve a system of four equations to determine the four coefficients of a cubic polynomial describing the flap geometry, $y$ (for top/bottom) or $z$ (for sides) = $Ax^3 + Bx^2 + Cx + D$. With each 2-D curve, we generate one flap surface and mirror it to the opposite edge of the base; thus, the side flaps are mirrored, and the top and bottom flaps are mirrored, all with the same axial length and with zero thickness. We then remove the ends of each side 3-D flap to where it intersects the top or bottom 3-D flap to form a sealed flaps cavity, as shown in Fig. 5b.

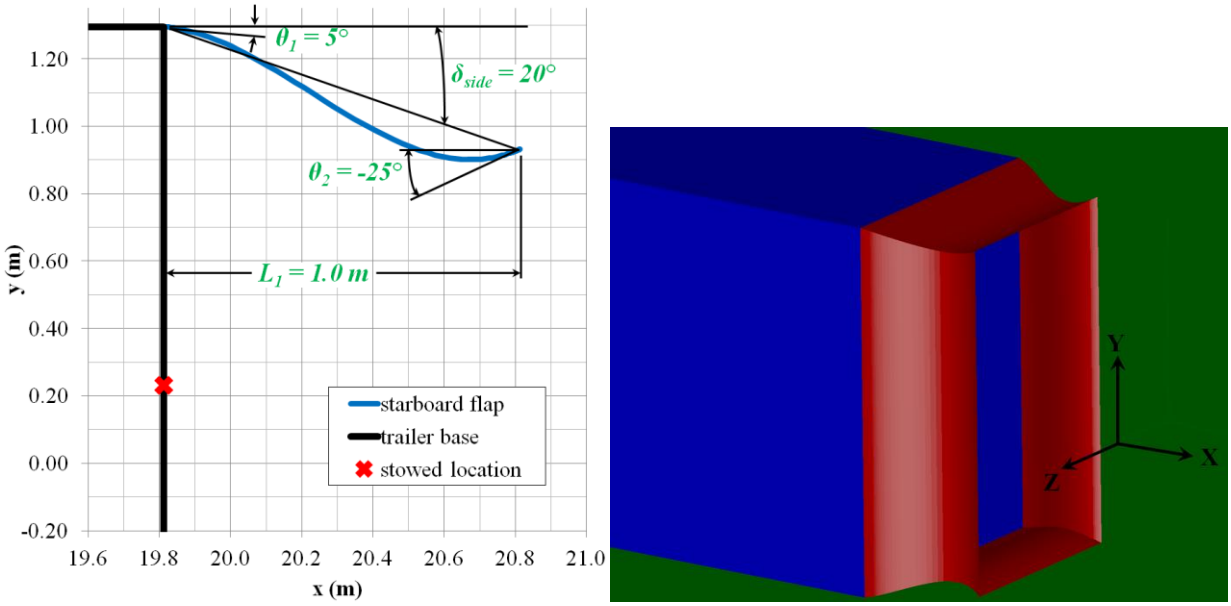


(a) 2-D side flap with variable labels; view looking down from top. (b) 3-D flaps at trailer base.

**Fig. 5.** Trailer-base flaps with design-variable values for one possible configuration.

We seek to minimize the objective function, which is the 3-D wind-averaged drag coefficient, taking into account the worst-case result from $\delta \pm 2°$ at each $\beta$; that is, two deflections and six sideslip angles for a total of 12 CFD solutions per design candidate.

$$minimize \quad \bar{C}_{D_{\delta\pm2°}} = \left\{ \frac{1}{6} \sum_{i=1}^{6} \psi_i \, max\left[ \left( C_{D,\delta-2°}(\beta_i) \right), \left( C_{D,\delta+2°}(\beta_i) \right) \right] \right\} \tag{5}$$

The non-load-bearing flaps are constrained by US federal regulation to not extend more than 5 ft (1.524 m) from the trailer base [24], but we further constrain the axial length, $L_1$, to 4 ft (1.219 m or 0.471$W$) to prevent the side flaps from overlapping the trailer base vertical centerline; the top and bottom flaps, in practice, must split axially in the center to accommodate the opening trailer doors (refer to Fig. 1), so they are limited by the side-flap length. If a design candidate includes side flaps which overlap the doors centerline, we assign it a large value, $\bar{C}_{D_{\delta\pm2°}} = 10$, thereby penalizing that combination of design parameters. The 10 best designs from the 2-D study [22] influence the constraints for the 3-D optimization study and are summarized in Table 1. We address in Section 3 the bi-modal result in 2-D for $\theta_2$.

**Table 1** 3-D Trailer base flaps design variables and constraints.

| Design Variable | Description | 2-D Top-10 Designs | 3-D Constraint |
|---|---|---|---|
| $L_1$ | axial length of trailer base flaps | $0.381 \le L_1/W \le 0.442$ | $0.235 \le L_1/W \le 0.471$ ($2 \le L_1 \le 4$ ft) |
| $\theta_1$ | slope at flap leading edge | $6 \le \theta_1 \le 15°$ | $0 \le \theta_1 \le 20°$ |
| $\theta_2$ | slope at flap trailing edge | $-23 \le \theta_2 \le -22°$<br>$27 \le \theta_2 \le 30°$ | $-35 \le \theta_2 \le 35°$ |
| $\delta_{side}$ | side flaps deflection angle | $17 \le \delta \le 23°$ | $10 \le \delta_{side} \le 28°$ |
| $\delta_{top}$ | top/bottom flaps deflection angle | - | $10 \le \delta_{top} \le 28°$ |

The computational domain extends approximately 10 tractor-trailer lengths in all spatial directions, shown in Fig. 6a. The fully structured mesh used for the optimization study, shown partly in Figs. 6c and 6d, is relatively coarse with $5.75 \times 10^6$ hexahedral cells. Figure 6b shows the vehicle surface geometry, with rounded front edges and base flaps. There are 20 cells within the estimated boundary layer region and computations reveal an average first-cell $y^+ = 1.3$; we would prefer a smaller value for first-cell $y^+$, but we make this trade-off between potentially better accuracy and smaller cell count because of the large total number of required computations (about 25 wall-clock hours for each of nearly 2,000 solutions). Figure 6 shows one of the design candidates; while each base flap candidate may have a different axial length, each is defined by 61 *tanh*-spaced coordinates in the axial direction. In the flaps cavity and the region within 5 m aft of the cavity, cell size away from the surfaces is generally less than 15 cm (0.06$W$) in each direction, and in most places it is less than 5 cm, as seen in Fig. 6d. All vehicle surfaces and flaps have a no-slip, adiabatic wall boundary condition; the grid "floor" or road models highway driving conditions, or no boundary layer, with a slip wall boundary condition; and the remaining boundaries are modified Riemann farfield at the specified $P_\infty$, $T_\infty$, and $M_\infty$. All values for $\beta$ are positive, such that the simplified tractor-trailer port side is windward for $\beta > 0°$. We select this grid based on the grid resolution study in Section 2.4.

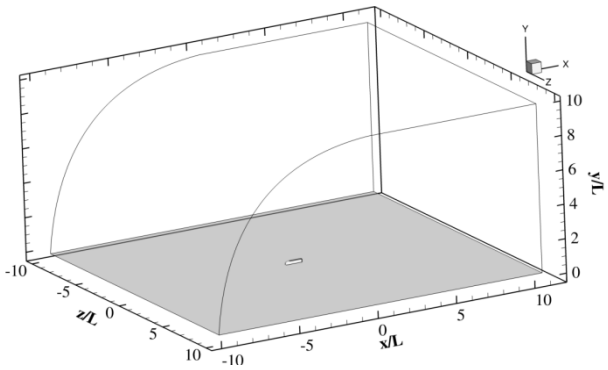


(a) Complete computational domain.

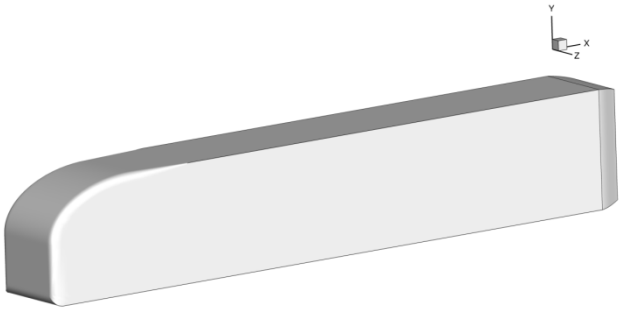


(b) Surface geometry with base flaps.

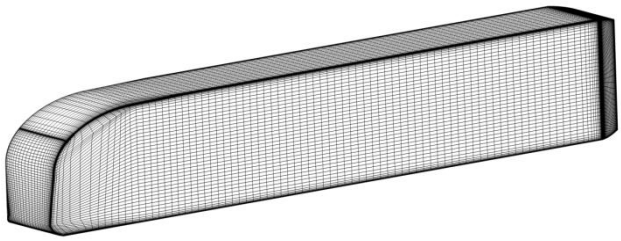

(c) Surface mesh with base flaps.

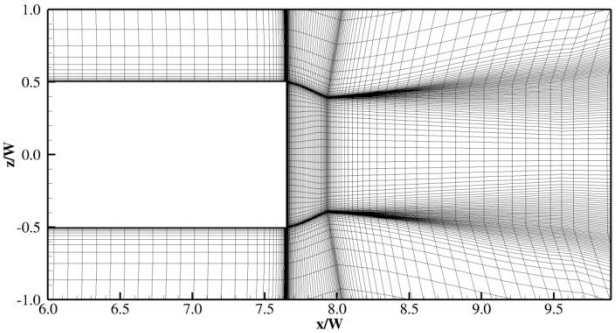


(d) Base and flaps, horizontal slice at $y/W = 0.69$.

**Fig. 6.** Computational mesh for simplified 3-D tractor-trailer geometry (GTS model), $5.75 \times 10^6$ hexahedral cells, average first-cell $y^+ \approx 1.3$ (for combined GTS and flaps).

### 2.2 Flow solver and turbulence model

Cobalt [18, 25] solves the 3-D unsteady, compressible Euler and Navier-Stokes equations at cell centers, uses the method of finite volumes, is parallelized, and is designed to use structured or unstructured mesh topologies. Cobalt formally achieves 2nd-order accuracy in space, and for an approximately steady, time-averaged solution we specify 1st-order accuracy in time and maximum Courant-Friedrichs-Lewy (CFL) number of $1 \times 10^6$. To reduce computational mesh cell count and overall computation time for applications with large Reynolds-number flow, all scales of turbulent flow are modeled with the two Menter shear-stress transport (SST) [26] Reynolds-averaged Navier-Stokes (RANS) equations.

We justify our selection of the two-equation SST turbulence model based on the following three findings. First, the SST model is commonly employed for cases which include wall-bounded, separated, and free-shear flows, as well as regions of adverse pressure gradient [26], all of which are present in the flow behavior around a tractor-trailer. Second, for 2-D cases which are representative of the flow properties of interest in the current study (a turbulent flat plate, a planar jet, and an NACA 0012 airfoil, all in low subsonic flow), Freeman and Roy [27] verify that Cobalt has correctly implemented the SST model, compared with implementations by two separate NASA codes; they verify that Cobalt SST solutions display nearly asymptotic behavior (as the computational mesh is refined, the solution observed order of accuracy approaches the code formal order of accuracy [15]) and maintain total numerical uncertainty less than 0.8%; and they validate the Cobalt SST solutions against experimental data – within an average of 0.9% (3.1% maximum) for the local skin friction coefficient on the flat plate, within 1% for ¾ of the shear layer velocity profile for the planar jet (and within 10% for the rest), and within 0.1% for the drag coefficient of the airfoil at 0° angle of attack. Last, Table 2 summarizes computational predictions versus experimental results for $C_D$ at several sideslip angles for the GTS and similar geometries. The SST model combines the positive attributes of both k-ω and k-ε models [26] and includes two transport equations versus seven for the Reynolds Stress Model (RSM); thus, SST may be slightly less accurate than RSM, but it is more computationally efficient (requires half the time [28]) for a large number of solutions. These results suggest the RANS SST turbulence model is suitable for this optimization study.

**Table 2** Computational predictions vs. experiment for 3-D simplified tractor-trailer at varied sideslip angles.

| RANS Turbulence Model, 3-D Cases | $C_D$ Difference from Experiment (%) | | | |
|---|---|---|---|---|
| | $\beta = 0°$ | $\beta = 1\text{-}2°$ | $\beta = 4\text{-}8°$ | $\beta = 10°$ |
| **S-A** [29, 30] | 49 - 65 | | | 58 |
| **k-ω** [29] | 4.4 - 8 | | | |
| **k-ε** [28, 31][a] | 2.3 - 10 | 0.5 - 1.0 | 10 - 12 | 9 |
| **Reynolds Stress** [28] | 0.6 | | | |
| **SST** [31][a] | 0.8 - 2.6 | 0.5 - 1.0 | 10 - 12 | 9 |
| **DES** [30, 32, 33][b] | 2 - 12 | | | 12 - 39 |

[a] Pointer et al. [31] do not distinguish which turbulence model was used for results at $\beta \neq 0°$.
[b] Time accurate simulations. All others are time averaged.

Further, the user may specify in Cobalt values for the freestream turbulent kinetic energy, $k$, and turbulence specific dissipation rate, $\omega$, which may be calculated as [34]

$$k = {}^{3}/_{2}\,(V_\infty I)^2 \tag{6}$$

$$\omega = {}^{k}/_{\nu(\mu_t/\mu)} \tag{7}$$

where $\boldsymbol{I}$ is turbulence intensity (-), $\nu$ is kinematic viscosity (which is $1.506\text{x}10^{-5}$ m$^2$/s at standard sea level), $\mu$ is dynamic viscosity (Pa·s), and $\mu_t$ is turbulent viscosity (Pa·s). A typical value for external, unobstructed flow [34] is $\mu_t/\mu = 1$, so for the ground we assume $\mu_t/\mu = 5$. Based on the methods of Holmes [35] and Socolofsky and Jirka [36], $\boldsymbol{I}$ may be calculated, respectively, as Eqs. (8) or (9),

$$I = 1.441/\ln\,(z/z_0) \tag{8}$$

$$I = 1.341/\ln\,(z/z_0) \tag{9}$$

where $z$ is the height above ground (m) and $z_0$ is the surface roughness length (m). We let $z$ = 2 m, which is half the height of a tractor-trailer, but $z_0$ may vary between 0.001 for desert terrain with no trees or other vegetation and 5.0 m for a dense, urban environment with numerous, tall buildings. If we assume relatively open terrain with few trees, $z_0$ = 0.01, and if we average the two methods above, we obtain $\boldsymbol{I}$ = 0.27, which yields $k$ = 71.5 m$^2$/s$^2$ and $\omega$ = 949,442 sec$^{-1}$. However, if we look at a range of surface roughness lengths for feasible truck routes in the US, we consider $0.001 \leq z_0 \leq 0.4$; for the two methods combined we obtain $0.18 \leq \boldsymbol{I} \leq 0.90$. (For reference, in a modern wind tunnel, we might expect $\boldsymbol{I}$ = 0.005 or smaller.) From our 2-D evaluation at these bounds of turbulence intensity, we find that $\bar{C}_d$ differs by 0.4%; and for the 3-D case, the difference in $C_D$ is less than 0.08%. Since this difference is small, we evaluate each design candidate only at the "typical" values, $k$ = 71.5 m$^2$/s$^2$ and $\omega$ = 949,442 sec$^{-1}$.

### 2.3 Optimization schemes and surrogate models

With our earlier study [22], we show that surrogate-based global optimization (SBGO) is an appealing option for optimization studies that can afford only dozens of design points; however, we conclude that SBGOs are not feasible as implemented for this study using DAKOTA because design points for the surrogate-model updates are computed serially. A possibility that we did not evaluate, however, may include the parallel, combined global-local search algorithm of He et al. [37]. Compared with concurrent computing for 140 design points, we estimate that serial computations require 2-3 times as much physical time (23-46 weeks versus 14 weeks with concurrent evaluations). Thus, a different approach must be considered.

Because this problem is non-convex [22], nonlinear, non-gradient-based, discontinuous among the solutions, and computationally expensive, we elect to use a genetic algorithm with global search for optimization, specifically DAKOTA's evolutionary algorithm (EA). Genetic algorithms such as the EA are based on Darwin's theory of

"survival of the fittest," in that the most fit candidates – in this case, those with the smallest $\bar{C}_{D_{\delta\pm2^\circ}}$ – survive from one generation to the next, while the others are eliminated. See Refs. 16, 38, and 39 for further explanation and detail. In addition to our 2-D down-selection of the EA method [22], Janiga [40] and Dumas [41] provide examples of conducting optimizations using EA for relatively complex engineering problems, based on using CFD for the function evaluations.

Table 3 details the specific settings within the EA input file, which we select to increase the likelihood of "discovering" or capturing the global minimum. We select the DAKOTA-recommended crossover hill-climber (CHC) genetic algorithm, incorporated within EA, for engineering applications and specify that the best design candidate from the existing population be included in the "mating" pool, thereby ensuring the best traits are passed to the next generation. EA allows a mix of continuous and discrete design variables, so we specify continuous $L_1$ and discrete $\theta_1$, $\theta_2$, $\delta_{side}$, and $\delta_{top}$, in increments of 1°.

**Table 3** COLINY evolutionary algorithm input parameters [16].

| Parameter | Value | Description |
|---|---|---|
| seed | 38 | arbitrary starting point but fixed for repeatability |
| population size | 20 | population for 1st generation only |
| initialization type | unique_random | random generation of design candidates, duplicates rejected |
| mutation type | offset_normal | adds random zero-mean variability within normal distribution to design point variables |
| mutation rate | 1.0 | probability of mutation being performed on candidate |
| crossovers | uniform | crosses random combination of values from two parent design candidates to form new candidate |
| crossover rate | 0.8 | crossover rate * population size = number of crossovers |
| replacement type | chc = 1 | moves best current/past candidate to current pool |

Using the EA in our 2-D GTS study [22], we locate a design within 2.5% of the final best design $\bar{C}_d$ with 60 design-point evaluations and locate that best design $\bar{C}_d$ with 180 evaluations; an additional 60 design points show no further improvement. For the 3-D study, we propose following the same method, hoping to obtain a reasonably efficient design within six or seven generations (115-134 design evaluations). Each evaluation requires 12 flow solutions, and each solution runs on 32 processing cores for 15-26 hours. Each generation requires roughly 150,000 core hours and, with hardware glitches and shared resources, completes in two to three weeks, for a total of nearly four months to complete seven generations. We use two platforms at the US Army Engineer Research and Development Center in Mississippi: *Diamond* and *Garnet*. *Diamond* is an SGI Altix ICE with 1,920 Intel Xeon dual quad-cores, 11.2 GFLOPS and 3 GB RAM per core; *Garnet* is a Cray XE6 with 1,260 AMD Opteron dual 8-cores, 9.6 GFLOPS and 2 GB RAM per core [42].

### 2.4 Solution convergence and computational grid selection

Because of Cobalt's in-house flux limiter [18], the solution residuals iteratively converge a little more than seven orders of magnitude for the continuity and turbulence transport equations, as shown in Fig. 7a, rather than the desired 12-14 orders for a double-precision computation. Figure 7b shows the iterative history for the body-axis force, $F_x$, for one particular base-flap design. This shows a fairly rapid convergence to a relatively steady value because there is flow separation neither along the trailer body nor along the flaps; designs with boundary layer separation off the flaps require more iterations for convergence but typically fewer than 8,000 iterations. We visually monitor the instantaneous force output, as in Fig. 7b, until it has leveled, then we average $F_x$ over the level region and use Eq. (2) to calculate $C_D$. To avoid the need to monitor each solution in this manner, we determine a sufficient number of iterations for a "worst case" (mid-range sideslip angle and flap design with strong adverse pressure gradient), apply that number to all cases, and perform solution spot checks to confirm convergence.

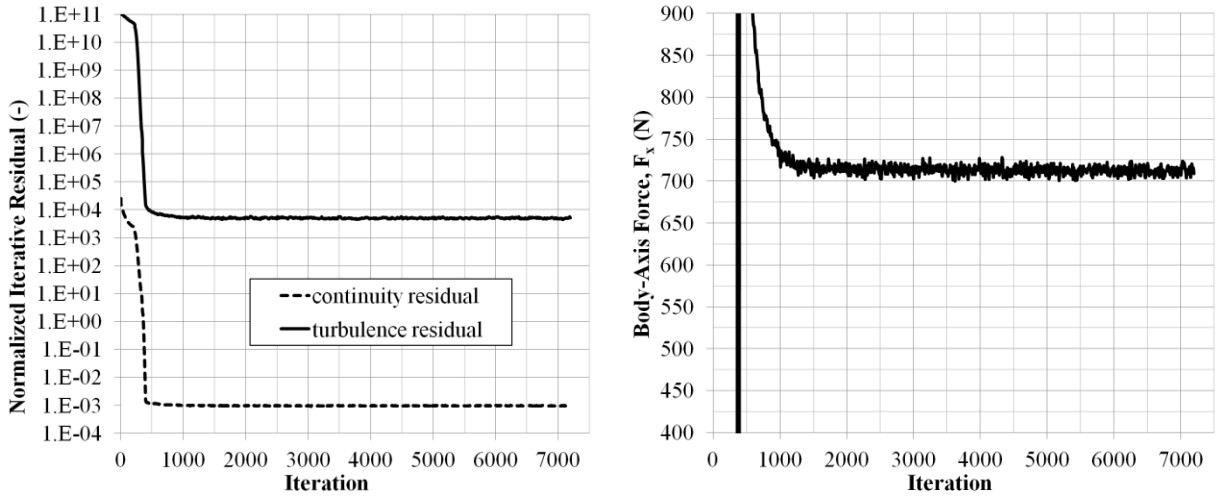


(a) Seven orders of magnitude for continuity and turbulence. (b) Body-axis force.

**Fig. 7.** Convergence history of iterative residuals and forces for 3-D simplified tractor-trailer. 5.75 million cell structured grid, Cobalt v5.2, SST turbulence model. History shown for design 45, $\beta = 2°$.

Concerning mesh resolution and solution accuracy, we generate three systematically refined grids (create a fine structured mesh then remove every other point in the three spatial directions for each successively coarsened mesh) of the GTS geometry without base flaps, which we denote fine, medium, and coarse, and evaluate whether their solutions display asymptotic behavior. We create half-grids which are symmetric about $z = 0$ (tractor-trailer vertical center plane) to maintain a smaller cell count and enable steady flow behavior; the fine mesh has 147.6 million cells with $y^+ = 0.36$, the medium grid has 18.4 million cells with $y^+ = 0.70$, and the coarse mesh has 2.3 million cells with $y^+ = 1.34$. Based on the computed $C_D$ values and according to the methods of Oberkampf and Roy [15], we calculate an observed order of accuracy, $\hat{p} = 2.66$ for the fine grid, that is not asymptotic but is indicative of the solution values being close for the fine and medium grids; they differ by 3.6%. We estimate total numerical uncertainty (due to discretization and round-off errors) [15, 43] for the fine grid, $U_{Numerical,Fine}$ = 1.6%. Based on Richardson Extrapolation, we estimate $U_{Numerical,Medium}$ = 6.1% and $U_{Numerical,Coarse}$ = 28%.

Ideally we would select the fine grid for the optimization study because its solution behavior is relatively close to asymptotic and its uncertainty due to numerical error is small. However, each solution would require at least two weeks on 1,024 cores, and that is infeasible for a study that may require 1,600 solutions (551 million core-hours). The coarse mesh is the only practical and acceptable option for a study that is comparative in nature and that requires more than a few CFD solutions. Nonetheless, we observe for the coarse grid that its fully turbulent predicted boundary layer thickness, defined as the distance between the surface and where 99% of freestream velocity is attained, is roughly equivalent to the thickness estimated by an empirically-based integral method [44]. Additionally, we justify use of the coarse grid because comparative values between designs are still expected to be accurate, even if the actual drag values are off by as much as 28%. To obtain a more accurate answer for an optimized design candidate, we may refine the mesh and compute the solution associated with that design. To further reduce computation time, we compute the solution for a given design candidate at the smallest sideslip angle, $\beta$=2.0°, until it is well converged then use that solution as the initial state for each of the other five sideslip angles; each of those restarted solutions requires 10-25% fewer iterations to converge.

In addition to our estimates for the GTS geometry without flaps, we estimate the uncertainty due to numerical error for the most promising candidate design. We accomplish this by using the geometry for the best design to create a medium grid and coarsen it by a factor of two in all spatial directions; in case this new coarse grid is slightly different from the original, we run computations for both of these new coarse (still 5.75 million cells) and medium (46.0 million cells) grids. We then use the coarse- and medium-grid solutions to estimate (via Richardson Extrapolation) the uncertainty due to discretization error [15, 43]. We could obtain a more accurate estimate with three grid levels but the 368-million-cell fine mesh would not be easily handled; compared with the coarse-grid solution, the medium grid requires more than 50 times the number of core hours for a converged solution.

### 2.5 Optimization under uncertainty and total predictive uncertainty

We classify this study as aerodynamic shape OUU because two primary inputs are uncertain: (1) the aleatory uncertainty of wind speed and direction, which have a normal distribution, are coupled using the six sideslip angles with their associated weights to calculate $\bar{C}_D$ [5]; and (2) the epistemic uncertainty of flap deflection angles, which have no statistical distribution, are represented by discrete bounds of ± 2° and are used to calculate $\bar{C}_{D_{\delta\pm2^\circ}}$. To include both forms of uncertainty, the rigorous approach involves a nested-loop process. Starting with an epistemic parameter value for the outer loop, we generate a large sampling of model input values (aleatory) using an appropriate distribution (e.g., random or normal) and propagate those through the model as an inner loop. We repeat this inner loop process for each value of the outer loop, determined by sampling within an interval (i.e., stratified Latin hypercube sampling) [15, 43]. This process could easily require thousands of samples evaluated with the truth model. Because function evaluations are computationally expensive and because we are primarily interested in a mean value, $\bar{C}_{D_{\delta\pm2^\circ}}$, we consider an approximate approach rather than a distribution. We use for the inner aleatory loop the six samples at the according sideslip angles, and we use for the outer epistemic loop the two bounds for the flap angles, $\delta \pm 2°$. Thus, rather than using hundreds or thousands of samples per iteration of the optimization loop, we approximate the statistical sampling with 12 computational simulations per design candidate.

For a tractor-trailer traveling at highway speeds on the open road and for our model of that system, there are many sources of uncertainty that may be categorized as model input, model form, or numerical approximation. Freeman and Roy [22] list many of those sources, and in addition to the uncertainty associated with wind speed and direction and with flap deflection angles, we address the following sources of uncertainty in this study: truck speed and elevation (coupled in Reynolds-number sensitivity and combined with flap deflection sensitivity), steady RANS approximation, and numerical approximation. We quantify these uncertain sources only for the best design, and we present the total prediction uncertainty in the form of a "final answer" plus or minus the uncertainty and graphically with a probability box (or p-box) [15, 43]. For every epistemic sample or bound, we generate an empirical distribution function (EDF), as shown in Section 3.2, Figs. 12 and 14. The extents of this ensemble of EDFs create the resultant p-box of model input uncertainty. To this p-box we add (to the right side) or subtract (from the left side) model form and numerical approximation uncertainty values. Therefore, total predictive uncertainty includes propagated uncertainty from model input, model form, and numerical approximation. This information helps the user understand relationships between model input and model output and may be used to make decisions about ways to improve the model and reduce uncertainty.

# 3 Results and discussion

### 3.1 Optimized design

After seven EA generations, 130 feasible design candidates, and 1,560 flow solutions using CFD, we have determined a design that reduces $\bar{C}_D$ more than any other published trailer base-flap design. We do not claim this design is the global minimum because the sampling size is small, but it is worthy of further evaluation in ground and road testing. In Fig. 8a, the solid black line shows $\bar{C}_D = 0.3303$ for the baseline configuration without flaps (the Storms et al. [8] wind tunnel experiment using the 1/8-scale no-flaps GTS measured $\bar{C}_D = 0.277 \pm 0.01$), the black diamonds show feasible EA design values for $\bar{C}_{D_{\delta\pm2^\circ}}$ in each generation, and the gray line with circle markers shows the minimum EA value to that point. Each of the first five generations produces a design with improved value for $\bar{C}_{D_{\delta\pm2^\circ}}$: generation 6 does not yield a new minimum design, and generation 7 determines a design that improves the previous best design by one drag count. These developments strengthen the assertion that design EA.127 from generation 7 is a good design minimum. We display design EA.127 graphically in Fig. 8b.

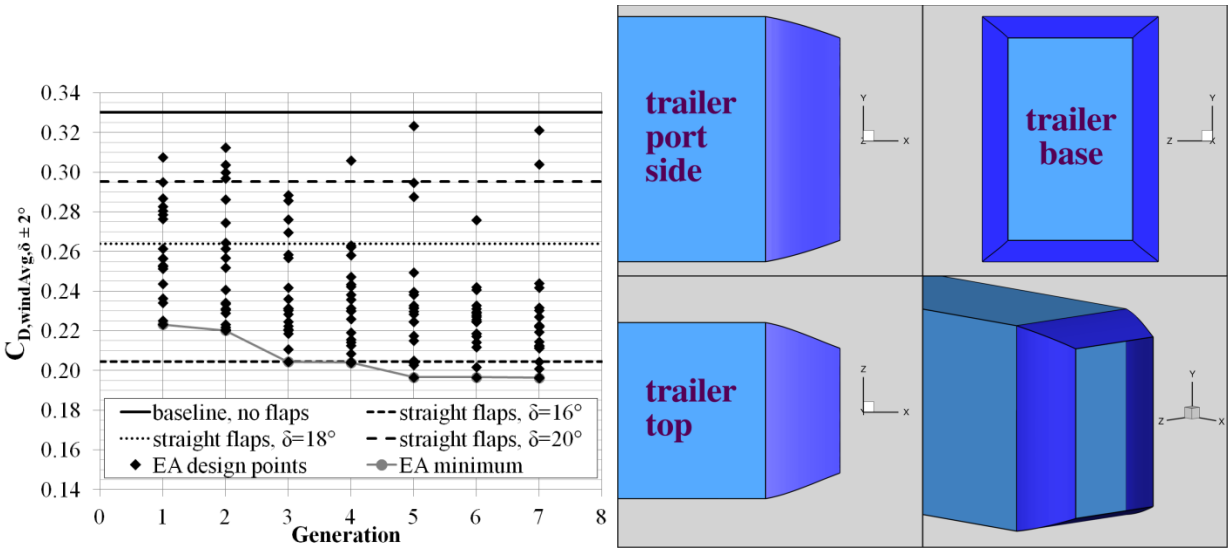


(a) Design tracking over seven generations. (b) Graphic of best design, EA.127.

**Fig. 8.** $\bar{C}_{D_{\delta\pm2^\circ}}$ results for 3-D simplified tractor-trailer using the DAKOTA-implemented COLINY evolutionary algorithm and five design variables ($L_1$, $\theta_1$, $\theta_2$, $\delta_{side}$, and $\delta_{top}$); seven generations represent 130 feasible design candidates and 1,560 flow solutions; compared with straight flap design at various deflection angles. 5.75 million cell structured grid, Cobalt v5.2 flow solver, SST turbulence model.

The EA.127 design, with $\bar{C}_{D_{\delta\pm2^\circ}} = 0.1964$, shows 41% improvement over the no-flaps baseline; for this best design, note that $\bar{C}_D = 0.1927$, which does not include the epistemic uncertainty of flap deflection angle, is a 42% improvement over the no-flaps baseline. With the 50% cut to drag reduction numbers discussed in Section 1, we might reasonably expect 20-21% reduction in $\bar{C}_D$ for an actual tractor-trailer, which is a vast improvement over the current best claim of 12% [4]. Twenty percent reduction in drag for a tractor-trailer results in about 10% reduction in fuel consumption [2, 4]. According to data collected for 2010 by the US Federal Highway Administration, combination trucks (category that includes tractor-trailers but not single-unit trucks) averaged 5.9 miles per gallon (2.5 km/l) and traveled 85.0 billion miles (136.9 billion km) on US rural and urban interstate highways [45]. If we conservatively estimate that 1/3 of that travel would include trailer flaps of our design and based on average US diesel prices for 2011 ($3.84/gal) [46], the 10% reduction in fuel consumption would result in an annual US fuel savings of $1.84 billion and 480 million gallons of diesel; it would also reduce carbon emissions by 10% from the tractor-trailers that use this device.

For comparison purposes with Hsu and Davis [14], who report 51% reduction for zero-sideslip $C_D$, our best design shows 39% reduction for the no-sideslip $C_D$; our tractor-trailer configuration is considerably less streamlined, so we expect a smaller relative reduction, but our design is more robust, considering the uncertain effects of wind speed and direction, static aeroelastic loading, mounting inaccuracy, and allowing for different deflection angles on each of the flaps. Compared with straight-flap designs ($L_1 = 0.46W$) at $16 \leq \delta \leq 20°$ (see black dashed and dotted lines in Fig. 8a), where all flaps are deflected the same angle, our best design $\bar{C}_{D_{\delta\pm2^\circ}}$ is 3.9% smaller (79 drag counts) than the $\delta = 16°$ design and 25.6% smaller (674 drag counts) than the $\delta = 18°$ design; thus, performance of competing designs and our own is quite sensitive to the mounted deflection angle. The summarized results in Table 4 emphasize that our best design, with some curvature, provides modest but significant improvements over a straight flap; careful consideration should be given to the tradeoff between performance and manufacturing complexity and cost. For the straight flap of $\delta = 18°$ in Table 4, we note the dramatic decrease in $\bar{C}_{D_{\delta\pm2^\circ}}$ performance (with only 20% improvement over the no-flaps baseline); this is because flow has separated from the flaps at the perturbed deflection, $\delta + 2 = 20°$.

**Table 4** Comparison of trailer base flap designs from ATDynamics [4] and current study.

| Design Variable | ATDynamics | EA.127 optimum (max) | Straight Flap 1 | Straight Flap 2 | Top 10 Designs |
|---|---|---|---|---|---|
| $L_1$ (m) | 0.47$W$ | 0.42$W$ *(0.47W)* | 0.46$W$ | 0.46$W$ | 0.38 - 0.45$W$ |
| $\theta_1$ (deg) | 15 | 10 *(20)* | 16 | 18 | 2 - 15 |
| $\theta_2$ (deg) | 15 | 20 *(± 35)* | 16 | 18 | 16 - 20 |
| $\delta_{sides}$ (deg) | 15 | 19 *(28)* | 16 | 18 | 18 - 22 |
| $\delta_{top/bottom}$ (deg) | 15 | 16 *(28)* | 16 | 18 | 11 - 18 |
| $\bar{C}_D$ Improvement over No-Flaps Design | - | 42% | 40% | 41% | |
| $\bar{C}_{D_{\delta\pm2^\circ}}$ Improvement over No-Flaps | 12% [a] | 41% | 38% | 20% | 37 - 41% |

[a] Measurement from track and road testing [4, 6]. The other results (EA.127, straight flaps, and Top 10) are simulation based with streamlined forebody and underbody.

Regarding design evolution, Fig. 9 shows all the variable points within the constrained design space using the EA for aerodynamic shape OUU study. Shaded circle, square, triangle, and diamonds highlight the variable values associated with the 10 best design points. These best designs show the following variable ranges: axial flap length $L_1$ varies between 0.38$W$ and 0.45$W$; flap leading edge $\theta_1$ varies between 2 and 15°; trailing edge $\theta_2$ varies between 16 and 20°, with one exception at 32°; side flap deflection $\delta_{side}$ ranges between 18 and 22°; and top and bottom flap deflection $\delta_{top/bottom}$ ranges between 11 and 18°, of which six of the top 10 vary between 15 and 18°. The top 10 designs values for $\bar{C}_{D_{\delta\pm2^\circ}}$ vary between 0.1964 and 0.2084, a range of 6%. With more generations we expect to see convergence to smaller ranges of variable values. Figure 9a suggests the flap axial length shies away from the maximum allowed length (0.47$W$), indicating a better design is not necessarily longer than our 4-ft constraint. Figure 9b indicates the best flap design should include a gradual ramp off the trailer base, steeper than 0° but less than the deflection angle. Figures 9c, 9d, and 9e suggest a relatively straight flap after the leading edge slope $\theta_1$. Figures 9d and 9e confirm the findings of Ortega and Salari [13] that the side flap deflection angles need not match those of the top and bottom flaps. The relatively wide ranges of values for $\theta_1$ and $\theta_2$ occur not necessarily due to a limited number of generations but possibly because we constrain all four flaps to maintain the same effective form, while flow behavior is not the same in all four regions. That is, the top and sides see free turbulent shear flow, whereas the bottom flow experiences underbody/road interaction and is more like planar shear. To increase the fidelity of a future study, we recommend allowing $\delta$, $\theta_1$, and $\theta_2$ for the top flap to be independent of the bottom and both top and bottom to be independent of the side flaps. Figure 9 also shows the next proposed batch of design candidates, generation 8, though we terminate the study after seven generations due to time and resource limitations.

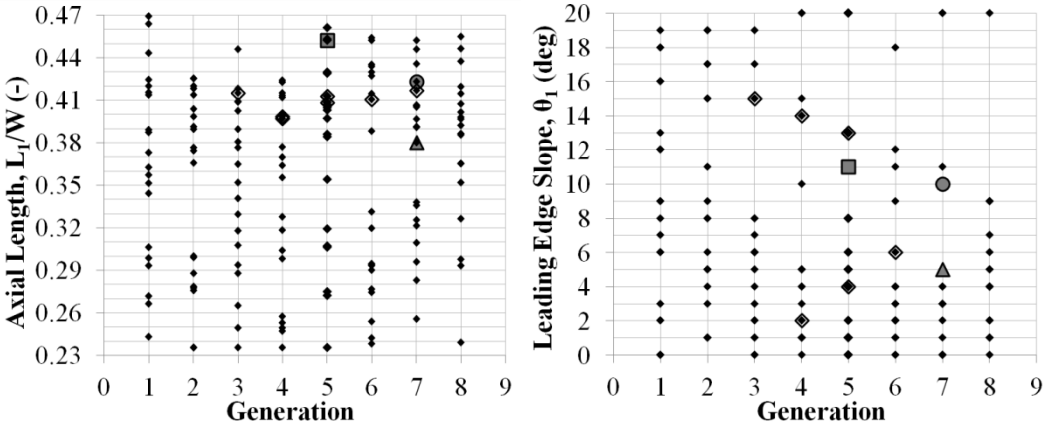


(a) Axial length of flap. (b) Slope at trailer-flap interface.

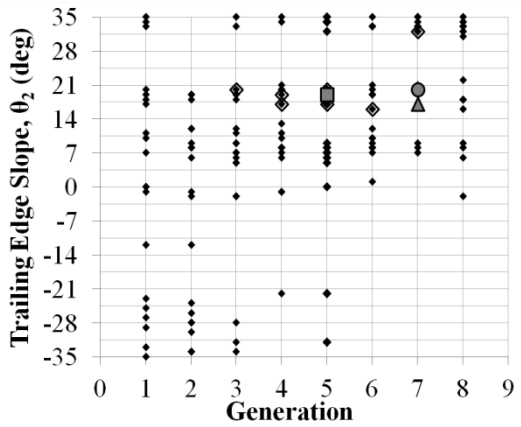


(c) Slope at flap trailing edge.

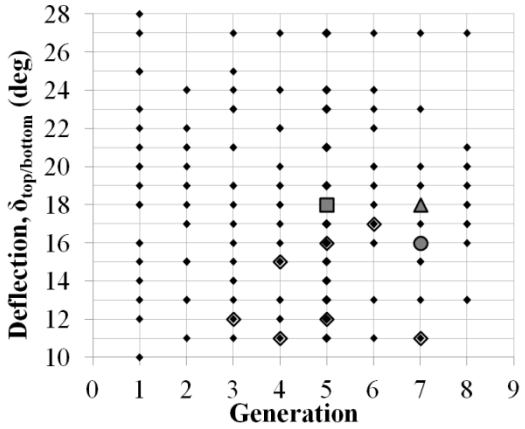


(d) Inward deflection angle for top, bottom flaps.

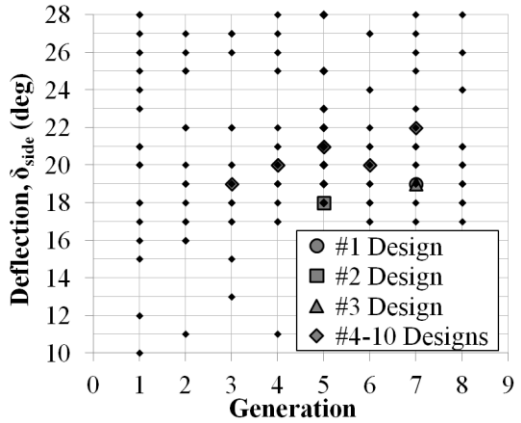


(e) Inward deflection angle for both side flaps.

**Fig. 9.** Design variable tracker by generation for EA base flaps on 3-D GTS. Filled shapes highlight the 10 best-performing designs.

We provide a healthy range of ±35° for the trailing edge slope based on the bi-modal outcome from our 2-D study [22]; however, the 3-D results indicate clear preference for a positive slope, or flap end curved inward. Results shown in Fig. 10 illustrate the differing flow behavior for these two configurations (inward and outward inflection at the flap trailing edge), where separated recirculating flow on the negative-$\theta_2$ flaps counteract any benefit from the larger deflection angle. The 2-D optimization study indicates nearly equal $\bar{C}_d$ values for negative and positive trailing edge inflection on the best design candidates [22]. However, the results shown in Fig. 10 stand to reason, where we would expect to see adverse performance from the negative trailing edge inflection. Figure 9c supports this observation, where the EA eliminates designs with negative $\theta_2$ after the 5$^{th}$ generation (with one exception in the proposed 8$^{th}$ generation).

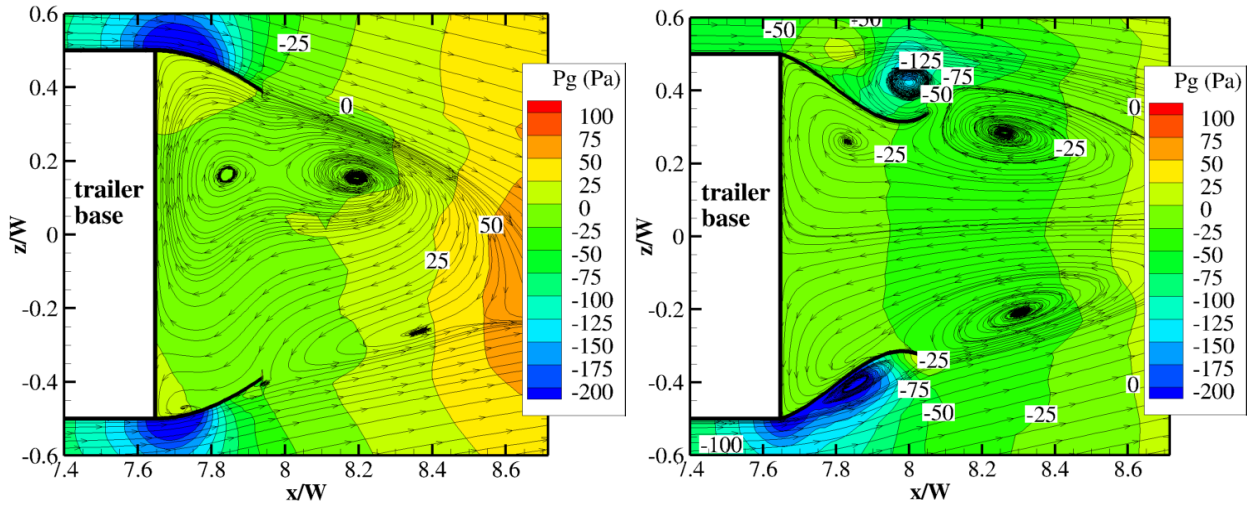


(a) Design 1, $\theta_2$ = 35°, $C_D$ = 0.2315 (b) Design 24, $\theta_2$ = -34°, $C_D$ = 0.3133

**Fig. 10.** Negative angle at flap trailing edge results in large regions of separated flow and larger $C_D$. Horizontal slice at $y/W$ = 0.695 for $\beta$ = 5.8° showing velocity streamlines atop contours of gauge pressure. Highway speed, $V_\infty$ = 57.2 mph (25.6 m/s), and $Re_W$ = 4.4 x $10^6$.

We explore the incremental design improvements with successive EA generations in Fig. 11. In the 1st generation (dark gray solid line), the algorithm starts with a fortuitous guess for a good design, where 32.4% improvement over the baseline is attained by disrupting the flow with these 0.41*W*-length flaps with $\delta_{side}$ = 18° and $\delta_{top/bottom}$ = 21° and with outward inflection at the trailing edge. With the 2nd generation (black dotted line), the flaps lose some advantage by being shorter at 0.29*W* but gain advantage with the straighter form, for a net improvement of 33.3%. For generations 2 through 4, $\delta_{top/bottom}$ hovers at the shallower angles of 12-15° before moving to 16° for the best design. For the side flaps, the best designs maintain $\delta_{sides}$ = 18-22°. Generation 3 (black dashed line) augments the improvement by 4.8% by increasing the flap length to 0.42*W*. Generation 4 (dark gray dashed line) brings an almost negligible improvement, then the 5th generation (dark gray dotted line) brings another 2.3% improvement by lengthening the flaps to 0.45*W*, increasing the side deflection angles and decreasing the top/bottom deflections. Generation 6 produces no improved design, and generation 7 (black solid line) makes slight modifications to all the variables for reduction by a single drag count. We include the straight flap design (light gray solid) for visual comparison with the EA designs. No improvement with generation 6 and almost negligible improvement with generation 7 suggest the algorithm has determined a good design, certainly a local minimum, but we do not declare it has found the global minimum design.

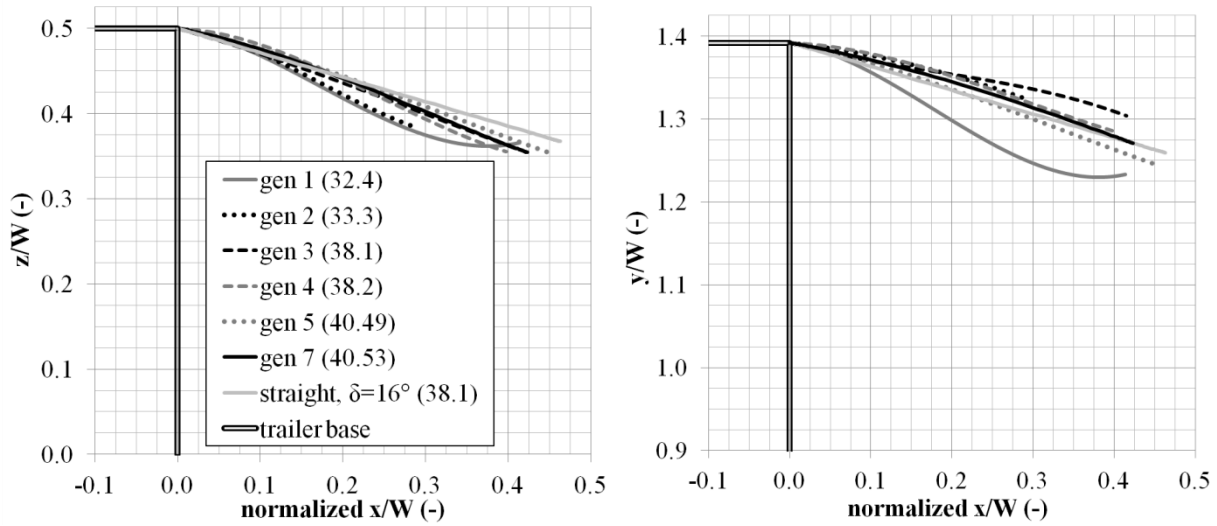


(a) Side flaps. (b) Top/bottom flaps.

**Fig. 11.** 3-D simplified tractor-trailer design progression by evolutionary algorithm generations. Percent improvement over no-flaps baseline $\bar{C}_D$ shown in parentheses. Seven generations are completed. $Re_W$ = 4.4x10$^6$, Cobalt SST turbulence model.

## 3.2 Total predictive uncertainty

Due to finite time and computational resources, we limit the amount of uncertainty quantification (UQ) conducted in this study. Because it directly affects fitness of the design candidates, we include for every feasible design the uncertainty due to wind speed and direction and the uncertainty associated with flap deflection angle, as affected by static aeroelastic loading and installation accuracy. Regarding other sources of uncertainty, we select the most fit design and subject only that design to more detailed UQ. For model input uncertainty, in addition to those sources of uncertainty already noted, we investigate the effects of variation in truck speed and elevation (coupled into Reynolds number). For model form uncertainty, we consider the differences between computation and experiment and assess the effect of modeling this case as steady RANS rather than time accurate. We complete the total predictive uncertainty analysis by then summing the effects of numerical approximation uncertainty with those of model input and model form uncertainty.

### *3.2.1 Model input uncertainty*

While we show in our 2-D study that tractor-trailer average speeds on US interstate highways have a normal distribution and could be treated as aleatory uncertainty, we approximate the distribution by treating these average speeds as epistemic uncertainty, bracketing plus and minus two standard deviations of the population mean; this gives truck speed, 48.8 (78.5) ≤ $V_{truck}$ ≤ 65.6 mph (105.6 km/h) or 3.8x10$^6$ ≤ $Re_W$ ≤ 5.0x10$^6$ [19, 22]. For the 2-D simplified tractor-trailer with base flaps, we determine that body-axis drag coefficients for the six different sideslip angles vary by 0.3-0.7% when applying these two input values for $Re_W$ [22]. In the wind tunnel experiment of Storms et al. [8] using the GTS geometry without base flaps, the variations in $C_D$ from these values for $Re_W$ correspond to 1-2%.

We assumed – in retrospect, incorrectly – for this study that *Re* effects would similarly be small and should be treated in post processing. Figure 12 shows the effects of variations in $\delta$ and the combination of $Re_W$ and $\delta$. The solid black line shows results at the baseline $Re_W$ = 4.4x10$^6$ and with no perturbation of $\delta$; the gray and black dashed lines show the results for the same $Re_W$ at $\delta$ + 2° and $\delta$ - 2°, respectively. These results confirm the effectiveness of the optimization process that minimizes the effect of variations in deflection angles; the results vary from the baseline within ± 2%, with one exception at +4%. The gray and black dotted lines show the results for $Re_W$ = 5.0x10$^6$ at $\delta$ + 2° and $Re_W$ = 3.8x10$^6$ at $\delta$ - 2°, respectively. These show that trucks traveling at higher highway speeds can expect to receive greater reductions in drag coefficient, where the $C_D$ values decrease by 3-5% from the unperturbed baseline $Re_W$ = 4.4x10$^6$; $\bar{C}_D$ decreases by 3.4%. At the slower speed, the $C_D$ values and $\bar{C}_D$ all increase by 7%. If we decrease

the truck speed by three standard deviations, $C_D$ values and $\bar{C}_D$ all increase by 10-11%; if we increase the truck speed by three standard deviations, $C_D$ values decrease by 1-6% and $\bar{C}_D$ decreases by 5%. These results show there is greater drag-coefficient sensitivity to speed reduction than to speed increase. When we consider more of the effects on tractor-trailer fuel economy, including aerodynamic (pressure and skin friction) drag, rolling friction, and engine and transmission losses, where travel at greater highway speed requires more power than at lower speeds [47], we find that total "drag" savings are larger at the lower speed than at the higher highway speed. Thus, greater highway speed results in smaller drag coefficient but not in smaller total "drag."

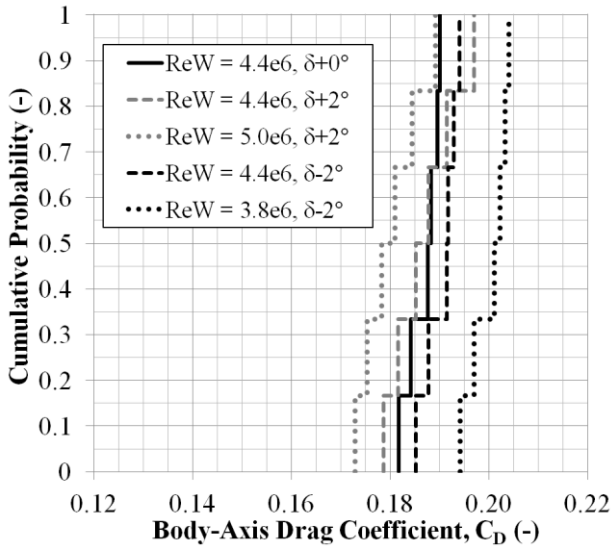


**Fig. 12.** Ensemble of EDFs of $C_D$ for model-input uncertain parameters: wind speed and direction (aleatory), truck speed and elevation (aleatory treated as epistemic), and flap deflection variation (epistemic). All results are from 3-D simplified tractor-trailer with base flaps design EA.90, $5.75 \times 10^6$ cell grid, Cobalt SST turbulence model.

Thus we see that *Re* effects are significant for the 3-D CFD solutions. We attribute the less pronounced 2-D *Re* effects to the presence of an artifact in the 2-D CFD solutions, a massive separation on the leeward side of the trailer for $\beta > 3$ or 4° [22]. We could optimize for an even more robust design, including *Re* effects in the optimization loop, by coupling $Re_W$ and $\delta$ perturbations as we do for Fig. 12. We conclude the model is moderately sensitive to variations in truck speed, elevation, and temperature – all factors that affect $Re_W$ – and perturbations of the flap deflection angle.

### *3.2.2 Model form uncertainty*

While there are many sources of model form uncertainty, we focus on the differences between computation and experiment, which includes the difference between flow calculated as time-accurate RANS and flow approximated as steady RANS. The time-accurate simulations use a smaller time step and thereby capture more of the flow physics. Since the designs in this study are original, there are no experimental data for comparison. However, for the next level of fidelity, we estimate model form uncertainty by comparing computation with experiment for cases that involve RANS turbulence models and simplified tractor-trailers at zero and non-zero sideslip angles. Table 2 (Section 2.2) compares results from several computational studies with wind-tunnel test data using 3-D simplified tractor-trailer geometry. These results indicate poor performance by the RANS S-A turbulence model in 3-D, while other steady RANS turbulence models perform with an acceptable degree of accuracy, not greater than 12% difference from experiment. We also include some time-accurate, detached-eddy simulation (DES) comparisons to show that steady RANS models (except S-A) perform as well as or better than a time-accurate model for this case and under these conditions. Thus, for the current cases that use the SST turbulence model we apply ±3% model form uncertainty for the results at $\beta = 2.036$ and 2.770° and ±11% for the four larger SAE angles.

By assuming steady flow, we conserve computation time and resources, but we may sacrifice accuracy in proper modeling of the flow physics. Therefore, we evaluate the effect on the solution associated with computing at a smaller time step in hopes of better resolving the flow features. Since Cobalt essentially calculates time-accurate

flow for all cases, the difference comes in effective time-step size or CFL number; a large CFL number does not usually allow for computing the small eddy structures. Cummings et al. [48] indicate that a maximum Strouhal number, $St$ = 20, for flow with shear layer instability or massively separated flow, as is the case for many of our design candidates, corresponds to a non-dimensional time step, $\Delta t^* = 0.025$, where the time step used in Cobalt can then be calculated as

$$\Delta t = \Delta t^* W / V_\infty. \tag{10}$$

We conduct a time-step sensitivity study using the EA.45 mesh (similar to the best design, EA.90), $\beta$ = 2.036°, and $\Delta t^*$ = { 0.025, 0.0125, 0.00625, 0.003125 } and show the results in Fig. 13. Between the two smallest time-step sizes, the computed $C_D$ values differ by 0.9%. More resolution in $\Delta t^*$ brings a more accurate estimate, but we select $\Delta t^*$ = 0.00625 for the evaluation of RANS approximation versus time-accurate solution because finer temporal resolution brings only a slight improvement in accuracy and comes at an increased computational expense. Specifically, solutions using $\Delta t^*$ = 0.00625 require four times the number of core hours for a converged solution; a time step at twice that resolution requires at least eight times the number of core hours, and so on. We use $\Delta t^*$ = 0.00625 even though it is inconsistent with the experimentally expected $St$ value [47]; the inconsistency is due to the mesh coarseness. Comparing $C_D$ values from the six SAE sideslip angles for $\Delta t^*$ = 0.00625 against CFL = $1x10^6$, we find the time-accurate results are smaller by a range of 7% at the smallest angle to 13% at the largest. These relatively large differences indicate two things: (1) flow features and behavior are better resolved with the finer temporal resolution; and (2) the finer time step compensates somewhat for the relatively coarse mesh resolution. We expect there would be a smaller difference in results if we make comparisons based on a finer mesh; using a fine mesh in our 2-D study, the differences in $C_d$ between time accurate and steady are less than 6% for all angles, and the number of core hours for a converged solution is nearly equivalent [22].

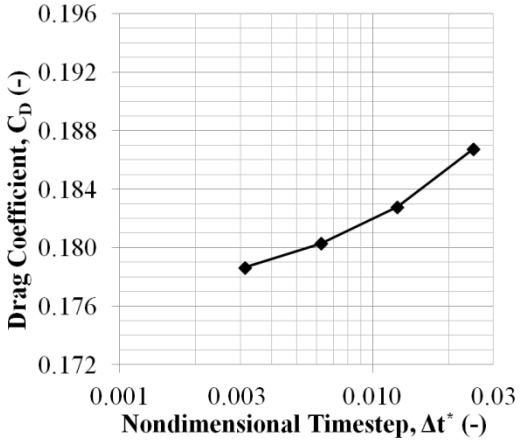


**Fig. 13.** Time-step sensitivity study, showing $C_D$ for the 5.75 million cell grid at $\beta$ = 2.036°, Cobalt SST turbulence model.

Both the effect of finer time-step sizes and the validation metric of computation vs. experiment fall within the category of model form, but they are not necessarily independent of each other because the experiment is conducted in the equivalent of time accuracy. Therefore, we represent them by applying the more conservative of the two estimates. For example, at $\beta$ = 2.770°, experimental validation indicates the uncertainty estimate is ±3%, and the RANS approximation indicates the uncertainty estimate is -8/+0%; so we represent the uncertainty at that angle as -8/+3%.

### *3.2.3 Numerical approximation uncertainty*

The medium grid has eight times more cells than the coarse mesh and requires more iterations to converge, such that its solutions require 56 times the number of core hours. Thus, we compute medium-grid CFD solutions only for the end and middle sideslip angles, $\beta$ = { 0, 5.751, 9.063° }, and interpolate the numerical uncertainty estimates for the rest. Following the process of Section 2.4 in Freeman and Roy [22] and Appendix 4 in Freeman [49], with two meshes of refinement factor, $r$ = 2, and using a factor of safety of 1.5 instead of three because we apply the

uncertainty to the coarse mesh, we estimate uncertainty due to numerical approximation error, $U_{Numerical}$ = { 17.6, 14.6, 14.6% }. Based on the behavior of this and similar solutions, we interpolate linearly and apply the wind-averaging procedure to predict uncertainty due to numerical error for the second-best design, EA.90, $\bar{C}_{D_{\delta\pm2^\circ}} = 0.1965\ ^{+0.00}_{-0.0560}$ (or +0.0/-28.5%). The wind-averaged numerical uncertainty estimate is ±14.2%, but since all $C_D$ estimates on the finer grid are smaller, we estimate zero uncertainty for the upper bound and double that uncertainty for the lower bound. This is a significant amount of uncertainty, but we are not surprised due to the relative coarseness of the grid. We could expect smaller numerical uncertainty, closer to the ±2% estimate in the 2-D study [22], for solutions using the medium and fine meshes – but at the price of considerable computational expense.

### *3.2.4 Total predictive uncertainty*

To compose Fig. 14, we generate the p-box for model input uncertainty (black area in the center regions) from the minimum and maximum values of Fig. 12. To those values we add (upper bound) or subtract (lower bound) the model form uncertainty, shown in light gray, that combines the difference between the EA.90 steady results (CFL = $1x10^6$) and the time-accurate solutions ($\Delta t^*$ = 0.00625) with the difference between computation and experiment. We finish the p-box of total predictive uncertainty by subtracting the numerical uncertainty, shown in dark gray. This p-box may be used for probabilistic observations, understanding of input/output relationships, and assessment of ways to improve the model. Probabilistic interpretation is precarious for such small sample sizes, so we focus on model assessment and understanding. Following are some observations that may be gained from the p-box. Decision-makers would likely notice the large numerical and model form uncertainty. A potential investigation that may yield reductions in both numerical and model form uncertainty would be to conduct the UQ using time-accurate CFD rather than steady; this would cause a 4x increase in all computations, but that is considerably less than the 56x increase incurred by running the medium grid. This would likely reduce the model form uncertainty, and it would reduce the numerical error if there were a significantly smaller difference between coarse and medium solutions computed at the smaller time step. The decision-makers may choose to conduct additional wind tunnel or other ground testing to reduce model form uncertainty. Since the design performance is clearly dominated by epistemic uncertainty, they may notice the effects of highway speed and elevation as they relate to drag predictions and make decisions about truck fleet operating speeds to reduce probabilities of higher fuel consumption. After pondering Fig. 12, they may also consider the possibility of variable, controlled flap deflection angles as a function of truck speed.

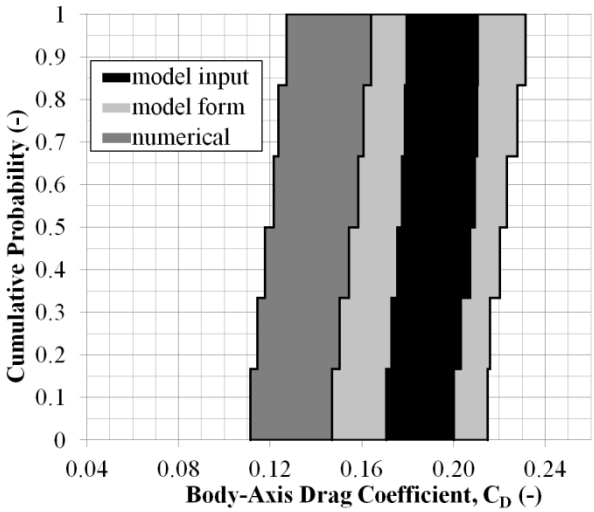


**Fig. 14.** Probability box showing total predictive uncertainty that includes uncertainty due to model input, model form, and numerical approximation, for the 3-D simplified tractor-trailer with base flaps design EA.90. $Re_W$ = $4.4x10^6$, Cobalt SST turbulence model.

Since we are most interested in $\bar{C}_{D_{\delta\pm2^\circ}}$, we predict a total uncertainty estimate for design EA.90 by using the SAE weights to wind-average the left and right extents shown in the p-box of Fig. 14. These values relate specifically to design EA.90; however, since the best design, EA.127, falls within the same family of designs with EA.90, we

convert them to a fraction and apply that fraction to design EA.127 to obtain our estimate of total predictive uncertainty:

$$\bar{C}_{D_{\delta\pm2^\circ}} = 0.1964\ ^{+0.0300}_{-0.0832} = 0.1964\ ^{+15.3\%}_{-42.4\%}.$$

Table 5 shows percentages of the components of total uncertainty, highlighting the asymmetry in all three forms of uncertainty. This uncertainty estimate may be extrapolated to similar designs because the overall model form uncertainty is completely independent of specific design parameters and because numerical uncertainty is only lightly based on the design shape due to minor variations in grid form (specifically in the trailer base and wake region). The majority of the total uncertainty (92% lower bound, 53% upper bound) in this 3-D study comes from model form and numerical approximation, both of which may be reduced through computational and experimental measures. We note also that both a finer grid and a smaller time step yield solutions with smaller, more desirable predictions for $C_D$, hence the greater uncertainty and larger potential range for values to be less than the estimated value for $\bar{C}_{D_{\delta\pm2^\circ}}$.

**Table 5** Components of total predictive uncertainty estimate for design EA.90.

| **Total Predictive Uncertainty for Design EA.90** | **Upper Bound (%)** | **Lower Bound (%)** |
|---|---|---|
| model input (*Re*, $\delta$) | 7.19 | 3.44 |
| model form (unsteady, exp) | 8.11 | 10.45 |
| numerical (coarse grid) | 0.00 | 28.44 |
| TOTAL | 15.30 | 42.37 |

As a final observation for this CFD-based 3-D OUU study, the relative comparison between designs with flaps and the baseline without flaps has considerably less uncertainty than we note in Table 5. That is, our final design predicted drag coefficient may not be accurate, but its relative improvement over the no-flaps baseline should be approximately the same if we use a finer mesh and/or smaller time step. Both baseline and flaps design candidates use precisely the same flow conditions, sideslip angles, turbulence model parameters, CFL number, and post-processing technique. The primary sources of remaining uncertainty are due to model input, which still includes variability in the coupled flap deflection and *Re*; separation location, if it exists for the given configuration; and slightly different grid form in the flap/wake region. Thus, our absolute predictions for $\bar{C}_{D_{\delta\pm2^\circ}}$ have 15-42% uncertainty, but our comparative predictions, $(\bar{C}_{D_{\delta\pm2^\circ}} - \bar{C}_{D,no\ flaps})/\bar{C}_{D,no\ flaps}$, have less uncertainty, in our judgment on the order of 3-9% (about 3-7% model input and 0-2% numerical). Continuing with that reasoning, we expect that relative comparison between two base-flap designs (e.g., straight flap versus curved flap) has even less uncertainty than the 3-9% estimate.

# 4 Summary and Conclusions

In this study we conducted aerodynamic shape optimization under conditions of uncertain wind speed and direction and uncertain device mounting and static aeroelastic loading, for base-flap drag-reduction devices, defined by five design variables, on a simplified 3-D full-scale tractor-trailer geometry at highway speed (57 mph or 92 km/h and $Re_W$ = 4.4x10$^6$). We used the DAKOTA optimization framework to manage the interface of optimizers, grid generator, and flow solver (Cobalt with the two-equation SST RANS turbulence model).

We successfully incorporated for every design candidate in the optimization study, by using the SAE wind-averaging process, the aleatory uncertain effects of wind speed and direction and the epistemic uncertainty associated with the base flap mounting accuracy and operational perturbations. We also included an additional and significant source of aleatory input uncertainty – variation in truck speed and elevation, or Reynolds number effect – as a post-processing step; we treated this aleatory uncertainty as epistemic, resulting in less computational expense but in greater uncertainty. We conducted grid and time-step sensitivity studies and estimated total predictive uncertainty that included the effects of Reynolds-number variation, steady RANS approximation, difference from experiment, and numerical approximation.

The COLINY EA optimization algorithm located a design that resulted in 41% reduction in $\bar{C}_{D_{\delta\pm2^\circ}}$ at 57 mph, compared with the no-flaps baseline. This best design outperforms simple straight flaps with inward deflection by between 4 and 26%, depending on the nominal angle at which the flap is mounted (16 or 18° for these two cases, respectively); this sensitivity and potentially large benefit merit wind tunnel and road testing consideration. We estimate that our design, incorporated on an actual, full-scale tractor-trailer will provide 20% reduction in drag coefficient; this is 8% greater reduction than what is currently advertised by industry [4].

For the best design, we estimated total predictive uncertainty in $\bar{C}_{D_{\delta\pm2^\circ}}$ as $^{+15.3\%}_{-42.4\%}$, consisting of 8-10% model form (due to the difference between the steady RANS computations and experiment), 3-7% model input (due to variation in highway speed and flap mounting angle), and +0.0/-28.4% numerical approximation (due primarily to grid coarseness). While this total uncertainty is large, relative uncertainty between the design of interest and the no-flaps baseline should be considerably smaller, particularly for designs that effectively curtail separated flow on the flaps; thus, the relative performance of a given design should be comparable even with finer grids. Nonetheless, if a more accurate prediction is required, we suggest using a smaller time step ($\Delta t^* = 0.00625$ rather than CFL = $1\text{x}10^6$) that we showed requires four times the computing time, instead of using a finer grid (eight times the cell count) that requires 56 times the computing time.

To develop a more robust design, future studies should include any or all of the following, in order of anticipated significance of the contribution:

(1) Validate the design predicted performance with wind tunnel and road testing.

(2) Optimize the shape according to the combined input of *Re* and flap deflection angle, in addition to the uncertain wind speed and direction. This should not require more simulations per design point. From our 2-D OUU results, we were misguided into neglecting *Re* sensitivity in the design loop for the 3-D study.

(3) While maintaining one axial length for a more efficient sealed cavity, allow separate forms and deflection angles for side, top, and bottom flaps. A 9-variable option could include $\theta_{1,sides}$, $\theta_{2,sides}$, $\delta_{sides}$, $\theta_{1,top}$, $\theta_{2,top}$, $\delta_{top}$, $\theta_{1,bottom}$, $\theta_{2,bottom}$, and $\delta_{bottom}$; and an alternative 6-variable option could include $\theta_{1,sides/top}$, $\theta_{2,sides/top}$, $\delta_{sides/top}$, $\theta_{1,bottom}$, $\theta_{2,bottom}$, and $\delta_{bottom}$. It is uncertain whether the 9-variable approach would necessarily require more design points to find a good design because the algorithm may prove more efficient with decoupled variables.

(4) Consider the potentially more efficient local-global search algorithm, VTDIRECT95 by He et al. [37].

All things considered, we have developed a design that performs well in the face of uncertain wind speed and direction and uncertain flap deflection angles, and one that, if it performs as well as designed, has the potential to save billions of dollars in commercial trucking fuel consumption.

# Acknowledgments

This work was supported significantly and could not have been completed without the generous grant of computer time from the Department of Defense (DoD) High Performance Computing Modernization Program at the US Army Engineer Research and Development Center, a DoD Supercomputing Resource Center in Vicksburg, Mississippi.

# References

[1] Mason WT Jr, Beebe PS. The drag related flowfield characteristics of trucks and buses. In: Symposium on aerodynamic drag mechanisms of bluff bodies and road vehicles, General Motors Research Laboratories, Plenum Press, 1978.

[2] Cooper KR. Truck aerodynamics reborn – lessons from the past. SAE technical paper 2003-01-3376, 2003. DOI: 10.4271/2003-01-3376

[3] Leuschen J, Cooper KR. Full-scale wind tunnel tests of production and prototype, second-generation aerodynamic drag-reducing devices for tractor-trailers. SAE technical paper 2006-01-3456, 2006. DOI: 10.4271/2006-01-3456

[4] Aerodynamics 101: aerodynamics at work. ATDynamics, Inc. http://www.atdynamics.com/aero.htm [cited 18 May 2012]

[5] SAE wind tunnel test procedure for trucks and buses. SAE J1252, SAE Recommended Practice, July 1981.

[6] Fuel consumption test procedure – type II. SAE J1321, SAE standard, February 2012.

[7] Cooper KR. The effect of front-edge rounding and rear-edge shaping on the aerodynamic drag of bluff vehicles in ground proximity. SAE technical paper 850288, February 1985. DOI: 10.4271/850288

[8] Storms BL, Ross JC, Heineck JT, Walker SM, Driver DM, Zilliac GG. An experimental study of the ground transportation system (GTS) model in the NASA Ames 7- by 10-ft wind tunnel. NASA/TM-2001-209621, February 2001.

[9] Lanser WR, Ross JC, Kaufman AE. Aerodynamic performance of a drag reduction device on a full-scale tractor/trailer. SAE technical paper 912125, September 1991. DOI: 10.4271/912125

[10] Visser KD, Grover K, Marin LE. Sealed aft cavity drag reducer. US Patent 8,079,634; 2011. http://patft.uspto.gov [cited 27 June 2012]

[11] Browand F, Radovich C, Boivin M. Fuel savings by means of flow attached to the base of a trailer: field test results. SAE technical paper 2005-01-1016, 2005. DOI: 10.4271/2005-01-1016

[12] Hsu T-Y, Hammache M, Browand F. Base flaps and oscillatory perturbations to decrease base drag. In: McCallen R, Browand F, Ross J (eds.). Lecture notes in applied and computational mechanics, vol. 19: The aerodynamics of heavy vehicles: trucks, buses, and trains, pp. 303-316. Berlin: Springer; 2004.

[13] Ortega JM, Salari K. An experimental study of drag reduction devices for a trailer underbody and base. 34th fluid dynamics conference, AIAA 2004-2252, Portland, OR: June 28 - July 1, 2004.

[14] Hsu F-H, Davis RL. Drag reduction of tractor-trailers using optimized add-on devices. ASME J Fluids Eng 2010; 132(8):084504:1-6. DOI: 10.1115/1.4001587

[15] Oberkampf WL, Roy CJ. Verification and validation in scientific computing. Cambridge, England: Cambridge University Press; 2010.

[16] Adams BM, Bohnhoff WJ, Dalbey KR, Eddy JP, Eldred MS, Gay DM, Haskell K, Hough PD, Swiler LP. DAKOTA, a multilevel parallel object-oriented framework for design optimization, parameter estimation, uncertainty quantification, and sensitivity analysis: version 5.0 user's manual. Sandia Technical Report SAND2010-2183, December 2009.

[17] Gridgen version 15 user manual. Pointwise, Inc., Texas, 2006.

[18] Cobalt version 5.2 user's manual. Cobalt Solutions, LLC., Ohio, 2011.

[19] Freight performance measures integrated query tool (FPMweb). Federal Highway Administration and American Transportation Research Institute. https://www.freightperformance.org/fpmweb/default.aspx [cited 16 December 2011]

[20] Gutierrez WT, Hassan B, Croll RH, Rutledge WH. Aerodynamics overview of the ground transportation systems (GTS) project for heavy vehicle drag reduction. SAE Technical Paper 960906, February 1996. DOI: 10.4271/960906

[21] Dellinger D. Average wind speed. National Oceanic and Atmospheric Administration, 2008. http://lwf.ncdc.noaa.gov/oa/climate/online/ccd/avgwind.html [cited 19 June 2012]

[22] Freeman JA, Roy CJ. Application of optimization under uncertainty: 2-d tractor-trailer base flaps. 50th aerospace sciences meeting, AIAA 2012-0671, Nashville, TN: January 9-12, 2012. Also: Freeman JA, Roy CJ. Optimization under uncertainty: 2-d tractor-trailer base flaps. Int J Numer Methods Fluids (in review) 2012.

[23] Doyle JB, Hartfield RJ, Roy CJ. Aerodynamic optimization for freight trucks using a genetic algorithm and CFD. 46th aerospace sciences meeting, **A**IAA 2008-0323, Reno, NV: January 7-10, 2008.

[24] Truck size and weight, route designations – length, width and weight limitations: exclusions from length and width determinations. Code of federal regulations title 23, ch. 1, part 658.b.4, April 2004.

[25] Grismer MJ, Strang WZ, Tomaro RF, Witzeman FC. Cobalt: a parallel, implicit, unstructured Euler/Navier-Stokes solver. Advances Eng Softw 1998: 29(3-6):365-373.

[26] Forsythe JR, Strang WZ, Hoffmann KA. Validation of several Reynolds-averaged turbulence models in a 3d unstructured grid code. Fluids 2000 conference, AIAA 2000-2552, Denver, CO: June 19-22, 2000.

[27] Freeman JA, Roy CJ. Verification and validation of RANS turbulence models in commercial flow solvers. 50th aerospace sciences meeting, AIAA 2012-0462, Nashville, TN: January 9-12, 2012. Also Freeman JA, Roy CJ. Verification and validation of Reynolds-averaged Navier-Stokes turbulence models for external compressible flow. AIAA J (in review) 2012.

[28] Basara B, Tibaut P. Time dependent vs. steady state calculations of external aerodynamics. In: McCallen R, Browand F, Ross J (eds.). Lecture notes in applied and computational mechanics, vol. 19: The aerodynamics of heavy vehicles: trucks, buses, and trains, pp. 107-117. Berlin: Springer; 2004.

[29] Roy CJ, Payne JL, McWherter-Payne MA. RANS simulations of a simplified tractor/trailer geometry. ASME J Fluids Eng 2006; 128(5):1083-1089. DOI: 10.1115/1.2236133

[30] Maddox S, Squires KD, Wurtzler KE, Forsythe JR. Detached-eddy simulation of the ground transportation system. In: McCallen R, Browand F, Ross J (eds.). Lecture notes in applied and computational mechanics, vol. 19: The aerodynamics of heavy vehicles: trucks, buses, and trains, pp. 89-104. Berlin: Springer; 2004.

[31] Pointer D, Sofu T, Chang J, Weber D. Applicability of commercial CFD tools for assessment of heavy vehicle aerodynamic characteristics. In: Browand F, McCallen R, Ross J (eds.). Lecture notes in applied and computational mechanics, vol. 41: The aerodynamics of heavy vehicles II: trucks, buses, and trains, pp. 349-361. Berlin: Springer; 2009.

[32] Roy CJ, Ghuge HA. Detached eddy simulations of a simplified tractor/trailer geometry. In: Browand F, McCallen R, Ross J (eds.). Lecture notes in applied and computational mechanics, vol. 41: The aerodynamics of heavy vehicles II: trucks, buses, and trains, pp. 363-381. Berlin: Springer; 2009.

[33] Sreenivas K, Mitchell B, Nichols S, Hyams D, Whitfield D. Computational simulation of the GCM tractor-trailer configuration. In: Browand F, McCallen R, Ross J (eds.). Lecture notes in applied and computational mechanics, vol. 41: The aerodynamics of heavy vehicles II: trucks, buses, and trains, pp. 325-338. Berlin: Springer; 2009.

[34] Determining turbulence parameters. Fluent 6.3 user's guide, section 7.2.2. Fluent, Inc., Pennsylvania, September 2006.

[35] Holmes JD. Atmospheric boundary layers and turbulence. Hurricane engineering, Louisiana State University. http://www.hurricaneengineering.lsu.edu/CourseMat/03Lect6BoundLayer.ppt [cited 27 September 2011]

[36] Socolofsky SA, Jirka GH. Atmospheric mixing. Coastal and Ocean Engineering Division, Texas A&M University. http://ceprofs.civil.tamu.edu/ssocolofsky/cven489/Downloads/Book/Ch6.pdf [cited 27 September 2011]

[37] He J, Watson LT, Sosonkina M. Algorithm 897: VTDIRECT95: serial and parallel codes for the global optimization algorithm DIRECT. ACM Trans Mathematical Softw 2009; 36(3):17.1-17.24. DOI: 10.1145/1527286.1527291

[38] Arora JS. Introduction to optimum design, 2nd ed. San Diego, CA: Elsevier Academic Press; 2004.

[39] Eddy J, Lewis K. Effective generation of Pareto sets using genetic programming. In: Proceedings ASME Design Engineering Technical Conference, pp. 783-791. 2001.

[40] Janiga G. A few illustrative examples of CFD-based optimization: heat exchanger, laminar burner and turbulence modeling. In: Thévenin D, Janiga G (eds.). Optimization and computational fluid dynamics. Berlin: Springer-Verlag; 2008, pp. 17-59.

[41] Dumas L. CFD-based optimization for automotive applications. In: Thévenin D, Janiga G (eds.). Optimization and computational fluid dynamics. Berlin: Springer-Verlag; 2008, pp. 191-215.

[42] Available hardware by DoD supercomputing resource centers. Department of Defense High-Performance Computing Modernization Program. http://www.afrl.hpc.mil/consolidated/hardware.php [cited 13 December 2011]

[43] Roy CJ, Oberkampf WL. A comprehensive framework for verification, validation, and uncertainty quantification in scientific computing. Comput Methods Appl Mech Eng 2011; 200:2131-2144. DOI: 10.1016/j.cma.2011.03.016

[44] Schetz JA. Boundary layer analysis. New Jersey: Prentice-Hall; 1993.

[45] Annual vehicle miles of travel by highway category and vehicle type. Table VM-1, highway statistics 2010, Office of Highway Patrol Information, Federal Highway Administration, US Department of Transportation. http://www.fhwa.dot.gov/policyinformation/statistics/2010/vm1.cfm [cited 21 July 2012]

[46] US on-highway diesel fuel prices. US Energy Information Administration, 2011. http://www.eia.gov/petroleum/gasdiesel [cited 21 May 2012]

[47] McCallen R, Couch R, Hsu J, Browand F, Hammache M, Leonard A, Brady M, Salari K, Rutledge W, Ross J, Storms B, Heineck JT, Driver D, Bell J, Zilliac G. Progress in reducing aerodynamic drag for higher efficiency of heavy duty trucks (class 7-8). Office of Scientific and Technical Information, US Department of Energy, December, 1999. DOI: 10.2172/771211

[48] Cummings RM, Morton SA, McDaniel DR. Experiences in accurately predicting time-dependent flows. Prog Aerosp Sci 2008; 44:241-257. DOI: 10.1016/j.paerosci.2008.01.001

[49] Freeman JA. Optimization under uncertainty and total predictive uncertainty for a tractor-trailer base-drag reduction device. PhD dissertation, Virginia Polytechnic Institute and State University; August, 2012.

# Chapter 5: Conclusion

## 5.1 Summary and Conclusions

This research contributes new findings to the state-of-the-practice in the combination of verification and validation, uncertainty quantification, and aerodynamic shape optimization under uncertainty (OUU) (including both aleatory and epistemic uncertainty) for a complex, engineering problem of interest – reducing aerodynamic drag for a tractor-trailer. Starting at the foundation, this study conducts code and solution verification and validation for four Reynolds-averaged Navier-Stokes (RANS) turbulence models (S-A, SARC, SST, and Wilcox 1998 k-ω) in two commercial CFD flow solvers (Cobalt and RavenCFD), using three cases whose combined flow physics roughly represent the complexities of tractor-trailer aerodynamics. While the turbulence models are not formally verified, adequate evidence is provided that they are implemented correctly for these flow conditions and they are validated with appropriate experimental data. The S-A turbulence model is selected for the 2-D OUU study and the SST model for the 3-D OUU study. Grid and time-step sensitivity studies are conducted for the geometries of interest to select appropriate computational grids and time step, as well as to assess numerical accuracy of the associated solutions. The study includes development of automated grid generation and assembly to accommodate the hundreds (400 for 2-D, 130 for 3-D) of tractor-trailer base flap design configurations; and data-mining and wind-averaging processes [66] are automated for the CFD flow solutions. Rigorous justification is provided for using the approximate wind-averaging technique in place of a more statistically robust sampling method. The 2-D study includes six design variables, indicates the best designs are flush with the trailer edges and that one of the variables has little influence on the design; thus, one new variable is introduced and two old ones are removed for the 3-D study, allowing the side flap deflections to be independent of the top and bottom flaps. Wind-averaging is used to approximate propagation of aleatory uncertain wind speed and direction, and the wind-averaging is modified to employ a worst-case condition for propagation of epistemic uncertainty in flap deflection angles. The design optimization process is developed and refined by initially reducing the problem to two dimensions then expanding it to three dimensions after the most accurate and efficient optimization approach is selected for this specific application; this proves to be the DAKOTA version of evolutionary algorithm. This selection process involves several non-gradient-based optimization methods, 12 surrogate models with six data sampling methods, and nine SBGO algorithms. While SBGO appears to be most efficient in determining a minimum design with fewer design candidates, the approach is discarded because it is computationally inefficient with its serial evaluations, as implemented in DAKOTA.

The final answer is a 3-D flap that has some curvature but is mostly straight and reduces the wind-averaged drag coefficient by 41% from the baseline configuration with no flaps. The design is relatively robust – fairly insensitive to small perturbations in wind speed, wind direction, and flap deflection. The magnitude of many other uncertain effects is estimated (Reynolds-number variation, turbulence model boundary-condition variation, steady RANS approximation, difference from experiment, and numerical approximation), helping decision-makers know where and how to apply resources to reduce the uncertainty. The final design fares better than a straight flap with deflection by between 4 and 26%, depending on the precise angle at which the flap is mounted. Due to the large number of tractor-trailers on US highways, even 4% may translate into significant savings of oil, money, and carbon emissions. Wind-tunnel and

road testing may prove the curved flaps are no better than the straight flaps, but this research strongly suggests it is worth testing.

For the 2-D study, total predictive uncertainty is estimated at ±11%: 9% model form (due to the difference between the steady RANS computations and experiment), 2% numerical approximation (due to flow unsteadiness and separated flow at the larger sideslip angles), and 0.3% model input (due to variation in highway speed and turbulence model boundary condition parameter). The large region of separated flow on the trailer leeward side that was an artifact of the 2-D CFD solution (neither experiment nor the 3-D solutions indicate this separation region) overwhelmed any possible effects from Reynolds number variation or freestream turbulence parameters; thus, model input uncertainty is small. The mesh is fine, and the time-accurate solutions also predict the large region of separated flow, so numerical uncertainty is small. Based on the 2-D performance, Reynolds number variation is not included in the optimization loop; however, in the post-processing stage this is discovered to be an oversight, such that Reynolds number effects should be coupled with flap deflection perturbations in the design loop. This oversight is manifest in the 3-D estimate for total predictive uncertainty, $^{+15.3\%}_{-42.4\%}$: 8-10% model form (basically the same as for 2-D), 3-7% model input (due to variation in highway speed and flap mounting angle), and +0.0/-28.4% numerical approximation (due primarily to grid coarseness). While this total uncertainty is large, relative uncertainty between the design of interest and the no-flaps baseline is considerably smaller, particularly for designs that effectively curtail separated flow on the flaps; thus, the relative performance of a given design should be comparable even with finer grids. Nonetheless, if a more accurate prediction is required, this study suggests using a smaller time step that is shown to require four times the computing time, instead of using a finer grid that requires 56 times the computing time. All things considered, this research effort has developed a design that performs well in the face of uncertain wind speed and direction and uncertain flap deflection angles, and one that, if it performs as well as designed, has the potential to save billions of dollars in commercial trucking fuel consumption.

### 5.2 Recommendations for Future Work

To develop a more robust design, future studies should include any or all of the following, in order of anticipated significance of the contribution:

(1) Validate the design predicted performance with wind tunnel and road testing.

(2) Optimize the shape according to the combined input of *Re* and flap deflection angle, in addition to the uncertain wind speed and direction. This should not require more simulations per design point.

(3) While maintaining one axial length for a more efficient sealed cavity, allow separate forms and deflection angles for side, top, and bottom flaps. A 9-variable option could include $\theta_{1,sides}$, $\theta_{2,sides}$, $\delta_{sides}$, $\theta_{1,top}$, $\theta_{2,top}$, $\delta_{top}$, $\theta_{1,bottom}$, $\theta_{2,bottom}$, and $\delta_{bottom}$; and an alternative 6-variable option could include $\theta_{1,sides/top}$, $\theta_{2,sides/top}$, $\delta_{sides/top}$, $\theta_{1,bottom}$, $\theta_{2,bottom}$, and $\delta_{bottom}$. It is uncertain whether the 9-variable approach would necessarily require more design points to find a good design because the algorithm may prove more efficient with decoupled variables.

(4) Consider the potentially more efficient local-global DIRECT search algorithm, VTDIRECT95 by He et al. [54].

(5) How can this OUU process be applied to an aircraft that does not have a convenient SAE method for wind averaging? There are a few possibilities.

a. Follow the theoretical approach of Cooper [2] that is the basis for the SAE empirical model, making minor adjustments for the change in reference frame, but this approach would still require a large sampling.
b. Follow the method discussed in Section 2.6 of Chapter 3 but devise a separate weighting function that would need to be validated with several times the number of simulations completed for that study. If panel methods or low-fidelity inviscid solutions are sufficient for this validation, such an effort would be manageable.
c. The more mathematically complex but computationally efficient polynomial chaos sampling may eventually become an option. Refer to Section 1.2.3 for several examples: Zhang et al. [41], Han and Hosder [42], and Schillings et al. [45]. However, all of these studies use gradient-based optimization.

(6) For future code verification studies, whether pure or comparative like this one:
a. An additional consideration is 2-D versus 3-D code verification. While flow velocities are low and geometries are simple in these cases, both turbulent flow and experimental measurement are fundamentally 3-D; thus, 2-D turbulence models may not accurately or correctly represent the actual flow physics, such that 3-D models should be considered for further verification and validation.
b. This study highlights the need for case models that are free of singularities and/or potentially coupled or conflicting boundary conditions. Even so, the absence of singularities and intersecting boundary conditions does not guarantee clean verification.

# References for Chap 1, Chap 5, and Appendices


[1] Dahm, W.J.A. "Technology Horizons: A Vision for Air Force Science & Technology During 2010-2030," Vol. 1, AF/ST-TR-10-01-PR, 15 May 2010.

[2] Cooper, K.R., "Truck Aerodynamics Reborn – Lessons from the Past," SAE Technical Paper 2003-01-3376, 2003. DOI: 10.4271/2003-01-3376

[3] Leuschen, J. and Cooper, K.R., "Full-Scale Wind Tunnel Tests of Production and Prototype, Second-Generation Aerodynamic Drag-Reducing Devices for Tractor-Trailers," SAE Paper 06CV-222, 2006. DOI: 10.4271/2006-01-3456

[4] "Aerodynamics 101: Aerodynamics at Work," ATDynamics, Inc., URL: http://www.atdynamics.com/aero.htm [cited 18 May 2012].

[5] "Annual Vehicle Miles of Travel by Highway Category and Vehicle Type," Table VM-1, Highway Statistics 2001-2010, Office of Highway Patrol Information, Federal Highway Administration, US Department of Transportation, URL: http://www.fhwa.dot.gov/policyinformation/statistics [cited 9 April 2012].

[6] "US On-Highway Diesel Fuel Prices," US Energy Information Administration, URL: http://www.eia.gov/petroleum/gasdiesel [cited 21 May 2012].

[7] Oberkampf, W.L. and Roy, C.J., *Verification and Validation in Scientific Computing*, Cambridge University Press, Cambridge, England, 2010.

[8] Veluri, S.P., Roy, C.J. and Luke, E.A., "Comprehensive Code Verification Techniques for Finite Volume CFD Codes," *Computers & Fluids*, 2012 (accepted manuscript). DOI: 10.1016/j.compfluid.2012.04.028

[9] Grismer, M.J., Strang, W.Z., Tomaro, R.F. and Witzeman, F.C., "Cobalt: A parallel, implicit, unstructured Euler/Navier-Stokes solver," *Advances in Engineering Software*, Vol. 29, No. 3-6, 1998, pp. 365-373. DOI: 10.1016/S0965-9978(97)00075-6

[10] "Cobalt Version 5.0 User's Manual," Cobalt Solutions, LLC, Ohio, 2010.

[11] Carpenter, J.R., "RavenCFD by Corvid Technologies," Flow Solver Documentation, URL: http://fileserver.corvidtec.com/dokuwiki/doku.php?id=ravencfd [cited 20 December 2011].

[12] "Computational Fluid Dynamics," Corvid Technologies, URL: http://www.corvidtec.com/index.html [cited 7 June 2012].

[13] Rumsey, C.L., "Turbulence Modeling Resource," NASA-Langley Research Center, 2012, URL: http://turbmodels.larc.nasa.gov/index.html [cited 7 June 2012].

[14] Rumsey, C.L. and Thomas, J.L., "Application of FUN3D and CFL3D to the Third Workshop on CFD Uncertainty Analysis," NASA/TM-2008-215537, November 2008.

[15] Storms, B.L., Ross, J.C., Heineck, J.T., Walker, S.M., Driver, D.M. and Zilliac, G.G., "An Experimental Study of the Ground Transportation System (GTS) Model in the NASA Ames 7- by 10-Ft Wind Tunnel," NASA/TM-2001-209621, February 2001.

[16] Heineck, J.T., Walker, S.M. and Satran, D., "The Measurement of Wake and Gap Flows Generic Conventional Truck Model (GCM) Using Three-Component PIV," Lecture Notes in Applied and Computational Mechanics, Vol. 19: *The Aerodynamics of Heavy Vehicles: Trucks, Buses, and Trains*, Springer, Berlin, 2004, pp. 173-184.

[17] Spalart, P.R. and Rumsey, C.L., "Effective Inflow Conditions for Turbulence Models in Aerodynamic Calculations," *AIAA Journal*, Vol. 45, No. 10, 2007, pp. 2544-2553. DOI: 10.2514/1.2973

[18] Freeman, J.A. and Roy, C.J., "Verification and Validation of RANS Turbulence Models in Commercial Flow Solvers," AIAA Paper 2012-0462, January 2012. Also Freeman J.A. and Roy C.J., "Verification and Validation of Reynolds-Averaged Navier-Stokes Turbulence Models for External Compressible Flow," *AIAA Journal*, 2012 (in review).

[19] Roy, C.J., Payne, J.L. and McWherter-Payne, M.A., "RANS Simulations of a Simplified Tractor/Trailer Geometry," *ASME Journal of Fluids Engineering*, Vol. 128, No. 5, 2006, pp. 1083-1089. DOI: 10.1115/1.2236133

[20] Maddox, S., Squires, K.D., Wurtzler, K.E. and Forsythe, J.R., "Detached-Eddy Simulation of the Ground Transportation System," Lecture Notes in Applied and Computational Mechanics, Vol. 19: *The Aerodynamics of Heavy Vehicles: Trucks, Buses, and Trains*, Springer, Berlin, 2004, pp. 89-104.

[21] Veluri, S.P, Roy, C.J., Ahmed, A., Rifki, R., Worley, J.C. and Recktenwald, B., "Joint Computational/Experimental Aerodynamic Study of a Simplified Tractor/Trailer Geometry," *ASME Journal of Fluids Engineering*, Vol. 131, No. 8, 2009, pp. 2011-2019. DOI: 10.1115/1.3155995

[22] Basara, B. and Tibaut, P., "Time Dependent vs. Steady State Calculations of External Aerodynamics," Lecture Notes in Applied and Computational Mechanics, Vol. 19: *The Aerodynamics of Heavy Vehicles: Trucks, Buses, and Trains*, Springer, Berlin, 2004, pp. 107-117.

[23] Pointer, D., Sofu, T., Chang, J. and Weber, D., "Applicability of Commercial CFD Tools for Assessment of Heavy Vehicle Aerodynamic Characteristics," Lecture Notes in Applied and Computational Mechanics, Vol. 41: *The Aerodynamics of Heavy Vehicles II: Trucks, Buses, and Trains*, Springer, Berlin, 2009, pp. 349-361.

[24] Roy, C.J. and Ghuge, H.A., "Detached Eddy Simulations of a Simplified Tractor/Trailer Geometry," Lecture Notes in Applied and Computational Mechanics, Vol. 41: *The Aerodynamics of Heavy Vehicles II: Trucks, Buses, and Trains*, Springer, Berlin, 2009, pp. 363-381.

[25] Sreenivas, K., Mitchell, B., Nichols, S., Hyams, D. and Whitfield, D.L., "Computational Simulation of the GCM Tractor-Trailer Configuration," Lecture Notes in Applied and Computational Mechanics, Vol. 41: *The Aerodynamics of Heavy Vehicles II: Trucks, Buses, and Trains*, Springer, Berlin, 2009, pp. 325-338.

[26] Pankajakshan, R., Mitchell, B. and Whitfield, D.L., "Full-Scale Simulations of Drag Reduction Devices for Class 8 Trucks," Lecture Notes in Applied and Computational Mechanics, Vol. 41: *The Aerodynamics of Heavy Vehicles II: Trucks, Buses, and Trains*, Springer, Berlin, 2009, pp. 339-348.

[27] Ortega, J.M. and Salari, K., "An Experimental Study of Drag Reduction Devices for a Trailer Underbody and Base," AIAA Paper 2004-2252, June 2004.

[28] Gutierrez, W.T., Hassan, B., Croll, R.H. and Rutledge, W.H., "Aerodynamics Overview of the Ground Transportation Systems (GTS) Project for Heavy Vehicle Drag Reduction," SAE Technical Paper 960906, February 1996. DOI: 10.4271/960906.

[29] Lanser, W.R., Ross, J.C. and Kaufman, A.E., "Aerodynamic Performance of a Drag Reduction Device on a Full-Scale Tractor/Trailer," SAE Technical Paper 912125, September 1991. DOI: 10.4271/912125.

[30] Doyle, J.B., Hartfield, R.J. and Roy, C.J., "Aerodynamic Optimization for Freight Trucks Using a Genetic Algorithm and CFD," AIAA Paper 2008-0323, January 2008.

[31] Hsu, F.-H. and Davis, R.L., "Drag Reduction of Tractor-Trailers Using Optimized Add-On Devices," *ASME Journal of Fluids Engineering*, Vol. 132, No. 8, 2010. DOI: 10.1115/1.4001587

[32] Cooper, K.R., "The Effect of Front-Edge Rounding and Rear-Edge Shaping on the Aerodynamic Drag of Bluff Vehicles in Ground Proximity," SAE Technical Paper 850288, February 1985, DOI: 10.4271/850288.

[33] "Fuel Consumption Test Procedure – Type II," SAE J1321, SAE Standard, February 2012.

[34] Visser, K.D., Grover, K. and Marin, L.E., "Sealed Aft Cavity Drag Reducer," U.S. Patent 8,079,634; 2011, URL: http://patft.uspto.gov [cited 27 June 2012].

[35] Browand, F., Radovich, C. and Boivin, M., "Fuel Savings by Means of Flow Attached to the Base of a Trailer: Field Test Results," SAE Technical Paper 2005-01-1016, 2005. DOI: 10.4271/2005-01-1016

[36] Hsu, T.-Y., Hammache, M. and Browand, F. "Base Flaps and Oscillatory Perturbations to Decrease Base Drag," Lecture Notes in Applied and Computational Mechanics, Vol. 19: *The Aerodynamics of Heavy Vehicles: Trucks, Buses, and Trains*, Springer, Berlin, 2004, pp. 303-316.

[37] Roy, C.J. and Oberkampf, W.L., "A Comprehensive Framework for Verification, Validation, and Uncertainty Quantification in Scientific Computing," *Computer Methods in Applied Mechanics and Engineering*, Vol. 200, 2011, pp. 2131-2144. DOI: 10.1016/j.cma.2011.03.016

[38] Roy, C.J. and Balch, M.S., "A Holistic Approach to Uncertainty Quantification in Modeling and Simulation," *International Journal for Uncertainty Quantification*, Vol. 2, No. 4, 2012, pp. 363-381. DOI: 10.1615/Int.J.UncertaintyQuantification.2012003562

[39] Hills, R.G., Pilch, M., Dowding, K.J., Red-Horse, J., Paez, T.L., Babuska, I. and Tempone, R., "Validation Challenge Workshop," *Computer Methods in Applied Mechanics and Engineering*, Vol. 197, No. 29-32, May 2008, pp. 2373-2666.

[40] Yao, W., Chen, X., Luo, W., Tooren, M. and Guo, J., "Review of Uncertainty-Based Multidisciplinary Design Optimization Methods for Aerospace Vehicles," *Progress in Aerospace Sciences*, Vol. 47, 2011, pp. 450-479. DOI:10.1016/j.paerosci.2011.05.001

[41] Zhang, Y., Hosder, S., Leifsson, L. and Koziel, S., "Robust Airfoil Optimization Under Inherent and Model-Form Uncertainties Using Stochastic Expansions," AIAA Paper 2012-0056, January 2012.

[42] Han, D. and Hosder, S., "Inherent and Model-Form Uncertainty Analysis for CFD Simulation of Synthetic Jet Actuators," AIAA Paper 2012-0082, January 2012.

[43] Li, W., Huyse, L. and Padula, S., "Robust Airfoil Optimization to Achieve Consistent Drag Reduction Over a Mach Range," NASA/CR-2001-211042, ICASE Report No. 2001-22, August 2001.

[44] Gumbert, C., Newman, P. and Hou, G., "Effect of Random Geometric Uncertainty on the Computational Design of a 3-D Flexible Wing" AIAA Paper 2002-2806, June 2002.

[45] Schillings, C., Schmidt, S. and Schulz, V., "Efficient Shape Optimization for Certain and Uncertain Aerodynamic Design," *Computers and Fluids*, Vol. 46, 2011, pp. 78-87. DOI: 10.1016/j.compfluid.2010.12.007

[46] Arora, J.S., *Introduction to Optimum Design*, 2nd ed., Elsevier Academic Press, San Diego, California, 2004.

[47] Adams, B.M., Bohnhoff, W.J., Dalbey, K.R., Eddy, J.P., Eldred, M.S., Gay, D.M., Haskell, K., Hough, P.D. and Swiler, L.P., "DAKOTA, A Multilevel Parallel Object-Oriented Framework for Design Optimization, Parameter Estimation, Uncertainty Quantification, and Sensitivity Analysis: Version 5.0 User's Manual," Sandia Technical Report SAND2010-2183, December 2009. Updated December 2010, Version 5.1.

[48] Eddy, J. and Lewis, K., "Effective Generation of Pareto Sets Using Genetic Programming," Proceedings of ASME Design Engineering Technical Conference, 2001, pp. 783-791.

[49] Lozano, M., Herrera, F., Krasnogor, N. and Molina, D., "Real-Coded Memetic Algorithms with Crossover Hill-Climbing," *Evolutionary Computation*, Vol. 12, No. 3, 2004, pp. 273-302. DOI: 10.1162/1063656041774983

[50] Janiga, G., "A Few Illustrative Examples of CFD-based Optimization: Heat Exchanger, Laminar Burner and Turbulence Modeling," In: Thévenin, D. and Janiga, G. (eds.), *Optimization and Computational Fluid Dynamics*. Springer-Verlag, Berlin, 2008, pp. 17-59.

[51] Dumas, L., "CFD-based Optimization for Automotive Applications," In: Thévenin, D. and Janiga, G. (eds.), *Optimization and Computational Fluid Dynamics*. Springer-Verlag, Berlin, 2008, pp. 191-215.

[52] Finkel, D.E., "DIRECT optimization algorithm user guide," North Carolina State University, 2003, URL: http://www4.ncsu.edu/~ctk/Finkel_Direct/DirectUserGuide_pdf.pdf [cited 27 June 2012].

[53] Freeman, J.A. and Roy, C.J., "Application of Optimization Under Uncertainty: 2-D Tractor-Trailer Base Flaps," AIAA Paper 2012-0671, January 2012.

[54] He, J., Watson, L.T. and Sosonkina, M., "Algorithm 897: VTDIRECT95: Serial and Parallel Codes for the Global Optimization Algorithm DIRECT," *ACM Transactions on Mathematical Software,* Vol. 36, No. 3, 2009, pp. 17.1-17.24. DOI: 10.1145/1527286.1527291

[55] Renaud, J.E. and Gabriele, G.A., "Improved Coordination in Nonhierarchic System Optimization," *AIAA Journal*, Vol. 31, No. 12, 1993, pp. 2367-2373. DOI: 10.2514/3.11938

[56] Swiler, L.P., Slepoy, R. and Giunta, A.A., "Evaluation of Sampling Methods in Constructing Response Surface Approximations," AIAA Paper 2006-1827, May 2006.

[57] Gergonne, J.D., "The Application of the Method of Least Squares to the Interpolation of Sequences," *Historia Mathematica*, Vol. 1, No. 4, 1974 [1815], pp. 439-447. DOI: 10.1016/0315-0860(74)90034-2

[58] Giunta, A.A. and Watson, L.T., "A Comparison of Approximation Modeling Techniques: Polynomial Versus Interpolating Models," AIAA Paper 1998-4758, September 1998.

[59] Zimmerman, D.C., "Genetic Algorithms for Navigating Expensive and Complex Design Spaces," Final Report for Sandia National Laboratories Contract AO-7736 CA 02, 1996.

[60] Friedman, J.H., "Multivariate Adaptive Regression Splines," *Annals of Statistics*, Vol. 19, No. 1, 1991, pp. 1-141. DOI: 10.1214/aos/1176347963

[61] Law, A.M. and Kelton, W.D., *Simulation Modeling and Analysis*, McGraw-Hill, New York, 1982.

[62] Hedayat, A.S., Sloane, N.J.A. and Stufken, J., *Orthogonal Arrays: Theory and Applications*, Springer-Verlag, New York, 1999.

[63] Box, G.E.P. and Wilson, K.B., "On the Experimental Attainment of Optimum Conditions," *Journal of the Royal Statistical Society: Series B*, Vol. 13, No. 1, 1951, pp. 1-45.

[64] Box, G.E.P. and Behnken, D., "Some New Three Level Designs for the Study of Quantitative Variables," *Technometrics*, Vol. 2, No. 4, 1960, pp. 455-475.

[65] Morris, M.D., "Factorial Sampling Plans for Preliminary Computational Experiments," *Technometrics*, Vol. 33, No. 2, 1991, pp. 161-174.

[66] "SAE Wind Tunnel Test Procedure for Trucks and Buses," SAE J1252, SAE Recommended Practice, July 1981.

[67] "Gridgen Version 15 User Manual," Pointwise, Inc., Texas, 2006.

# Appendix 1: Tractor-Trailer Base Flap Geometry

## A1.1 Five-Variable Flap, Cubic Polynomial

From the method of Doyle et al. [30], the simplified tractor-trailer base flap geometry is a function of five variables: $H_1$, $L_1$, $\theta_1$, $\theta_2$ and $\delta$, with descriptions and constraints detailed in Table A1.1. One notional design is shown in Fig. A1.1. These constraints differ from those of Doyle et al. [30], where all three angles ranged between 0 and 15°. For the tractor-trailer, length $L$ = 19.812 m = 65 ft, width $W$ = 2.5908 m = 8.5 ft, and height $H$ = 3.6068 m = 11.833 ft.

**Table A1.1.** Trailer Base Five-Variable Flap Design Variables and Constraints

| Design Variable | Description | Constraint |
|---|---|---|
| $H_1$ | distance from trailer base centerline to flap attach point (m) | $L_1/\cos\delta \le H_1 \le W/2$ |
| $L_1$ | axial length of trailer base flap (-) | $0.1W \le L_1 \le 0.47W$ |
| $\theta_1$ | deflection angle at flap leading edge (deg) | $0 \le \theta_1 \le 30°$ |
| $\theta_2$ | deflection angle at flap trailing edge (deg) | $-30 \le \theta_2 \le 45°$ |
| $\delta$ | flap incidence angle or angle of flap chord line (deg) | $0 \le \delta \le 30°$ |

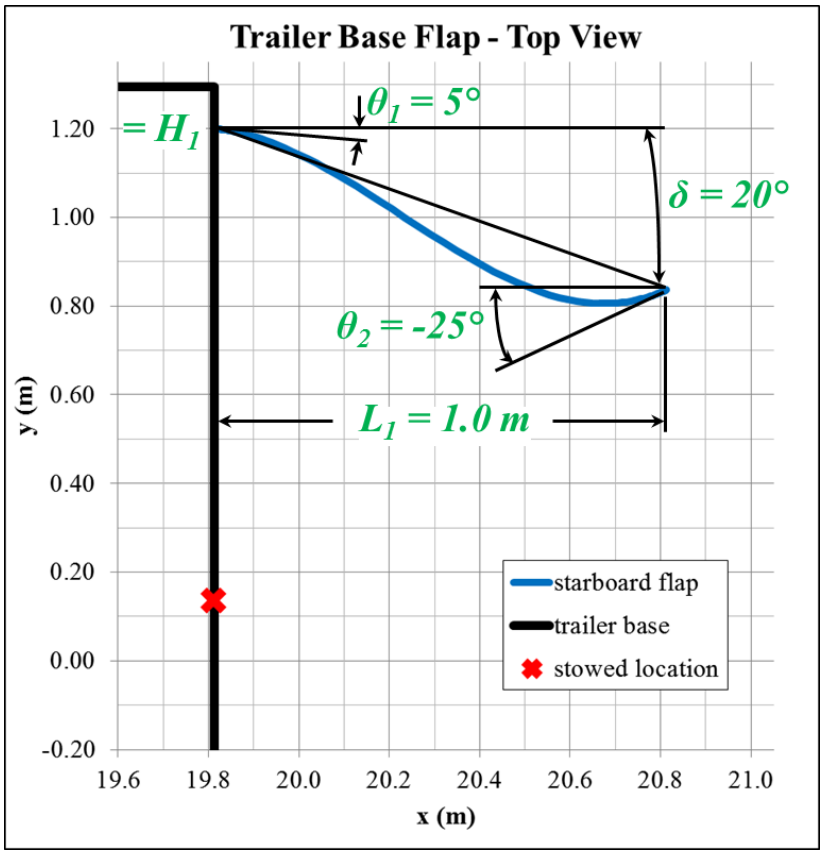


**Figure A1.1.** Cubic polynomial model of five-variable base flap for simplified tractor-trailer

We use $L$, $H_1$, $L_1$ and $\delta$ to determine two points in Cartesian space, according to Eqs. (A1.1) and (A1.2), where point 1 is the flap intersection at the trailer base and point 2 is the flap trailing edge. These two points are then used with slopes, $\theta_1$ and $\theta_2$, to solve a system of four equations

(Eq. (A1.3)) to determine the four coefficients of a cubic polynomial describing the flap geometry, $y = Ax^3 + Bx^2 + Cx + D$. The four coefficients are detailed in Eqs. (A1.4) through (A1.7).

$$x_1 = L; \quad y_1 = H_1 \tag{A1.1}$$

$$x_2 = L + L_1; \quad y_2 = H_1 - L_1 \tan\delta \tag{A1.2}$$

$$\begin{bmatrix} y_1 \\ y_2 \\ dy/dx)_1 = -tan\theta_1 \\ dy/dx)_2 = -tan\theta_2 \end{bmatrix} = \begin{bmatrix} Ax_1^3 + Bx_1^2 + Cx_1 + D \\ Ax_2^3 + Bx_2^2 + Cx_2 + D \\ 3Ax_1^2 + 2Bx_1 + C \\ 3Ax_2^2 + 2Bx_2 + C \end{bmatrix} \tag{A1.3}$$

$$A = \frac{-2(y_1 - y_2)}{(x_1 - x_2)^3} + \frac{-tan\theta_1 - tan\theta_2}{(x_1 - x_2)^2} \tag{A1.4}$$

$$B = \frac{3(x_1 + x_2)(y_1 - y_2)}{(x_1 - x_2)^3} + \frac{(x_1 + 2x_2)tan\theta_1 + (2x_1 + x_2)tan\theta_2}{(x_1 - x_2)^2} \tag{A1.5}$$

$$C = \frac{-6x_1x_2(y_1 - y_2)}{(x_1 - x_2)^3} + \frac{-x_2(2x_1 + 2x_2)tan\theta_1 - x_1(x_1 + 2x_2)tan\theta_2}{(x_1 - x_2)^2} \tag{A1.6}$$

$$D = \frac{x_1^2y_2(x_1 - 3x_2) + x_2^2y_1(3x_1 - x_2)}{(x_1 - x_2)^3} + \frac{x_1x_2^2tan\theta_1 + x_1^2x_2tan\theta_2}{(x_1 - x_2)^2} \tag{A1.7}$$

### A1.2 Six-Variable Flap, Quartic Polynomial for 2-D Design Optimization

For the 2-D tractor-trailer base-flap design optimization study (Chapter 3), we further modify the configuration of Doyle et al. [30] by adding a sixth design variable, giving: $H_1$, $L_1$, $\theta_1$, $\theta_2$, $\theta_3$ and $\delta$, with descriptions and constraints detailed in Table A1.2. We add a deflection angle at the mid-chord location on the flap. One notional design is shown in Fig. A1.2.

**Table A1.2.** Trailer Base Six-Variable Flap Design Variables and Constraints

| Design Variable | Description | Constraint |
|---|---|---|
| $H_1$ | distance from trailer base centerline to flap attach point (m) | $L_1/\cos\delta \le H_1 \le W/2$ |
| $L_1$ | axial length of trailer base flap (-) | $0.1W \le L_1 \le 0.47W$ |
| $\theta_1$ | deflection angle at flap leading edge (deg) | $0 \le \theta_1 \le 30°$ |
| $\theta_2$ | deflection angle at flap mid-chord (deg) | $0 \le \theta_2 \le 30°$ |
| $\theta_3$ | deflection angle at flap trailing edge (deg) | $-30 \le \theta_3 \le 45°$ |
| $\delta$ | flap incidence angle or angle of flap chord line (deg) | $0 \le \delta \le 30°$ |

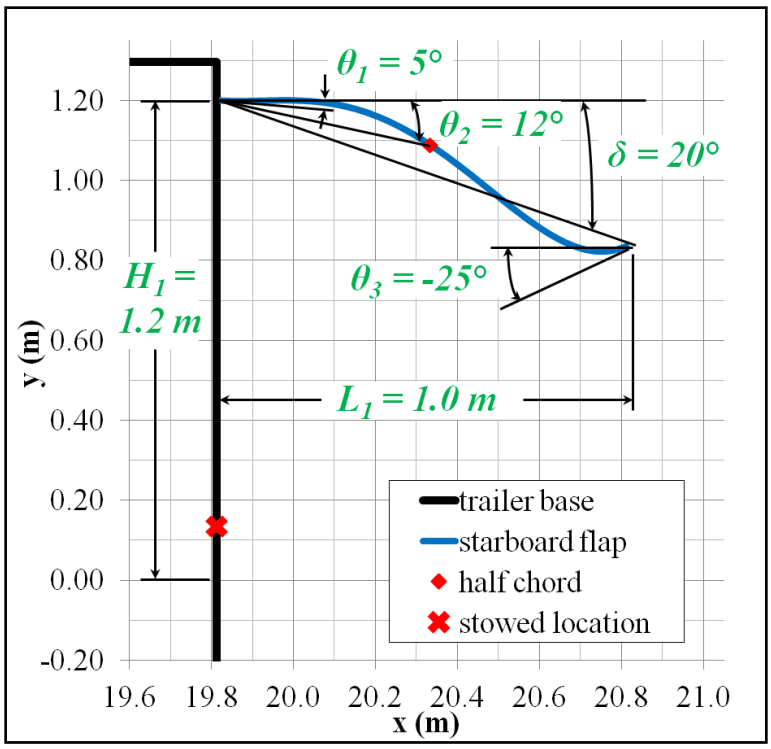


**Figure A1.2.** Trailer base flap schematic with six design-variable values for one possible configuration. View of starboard flap as seen looking down from above the trailer

We use $H_1$, $L_1$, $\theta_2$ and $\delta$ to determine three points in Cartesian space, according to Eqs. (A1.8) through (A1.10), where point 1 is the flap intersection at the trailer base, point 2 is the flap mid-chord, and point 3 is the flap trailing edge. These three points are then used with slopes, $\theta_1$ and $\theta_3$, to solve a system of five equations (Eq. (A1.11)) to determine the five coefficients of a quartic polynomial describing the flap geometry, $y = Ax^4 + Bx^3 + Cx^2 + Dx + E$. The five coefficients are detailed in Eqs. (A1.12) through (A1.18).

$$x_1 = L; \quad y_1 = H_1 \tag{A1.8}$$

$$x_2 = L + \frac{L_1 \cos\theta_2}{2\cos\delta}; \quad y_2 = H_1 - \frac{L_1 \sin\theta_2}{2\cos\delta} \tag{A1.9}$$

$$x_3 = L + L_1; \quad y_3 = H_1 - L_1 \tan\delta \tag{A1.10}$$

$$\begin{bmatrix} y_1 \\ y_2 \\ y_3 \\ dy/dx)_1 = -tan\theta_1 \\ dy/dx)_3 = -tan\theta_3 \end{bmatrix} = \begin{bmatrix} Ax_1^4 + Bx_1^3 + Cx_1^2 + Dx_1 + E \\ Ax_2^4 + Bx_2^3 + Cx_2^2 + Dx_2 + E \\ Ax_3^4 + Bx_3^3 + Cx_3^2 + Dx_3 + E \\ 4Ax_1^3 + 3Bx_1^2 + 2Cx_1 + D \\ 4Ax_3^3 + 3Bx_3^2 + 2Cx_3 + D \end{bmatrix} \tag{A1.11}$$

$$den1 = (x_1 - x_3)^3 (x_1 - x_2)^2 (x_2 - x_3)^2 \tag{A1.12}$$

$$den2 = (x_1 - x_3)^2(x_1 - x_2)(x_2 - x_3) \tag{A1.13}$$

$$\begin{aligned} A = \Big(\frac{1}{den1}[&y_1(x_2 - x_3)^2(-3x_1 + 2x_2 + x_3) + y_2(x_1 - x_3)^3 \\ &- y_3(x_1 - x_2)^2(x_1 + 2x_2 - 3x_3)]\Big) \\ &- \Big(\frac{1}{den2}[tan\theta_1(x_2 - x_3) - tan\theta_3(x_1 - x_2)]\Big) \end{aligned} \tag{A1.14}$$

$$\begin{aligned} B = \Big(\frac{2}{den1}[&y_1(x_2 - x_3)^2(2x_1^2 + 2x_1x_3 - x_2^2 - 2x_2x_3 - x_3^2) - y_2(x_1 - x_3)^3(x_1 + x_3) \\ &+ y_3(x_1 - x_2)^2(x_1^2 + 2x_1x_2 - 2x_1x_3 + x_2^2 - 2x_3^2)]\Big) \\ &+ \Big(\frac{1}{den2}[tan\theta_1(x_2 - x_3)(x_1 + x_2 + 2x_3) \\ &- tan\theta_3(x_1 - x_2)(2x_1 + x_2 + x_3)]\Big) \end{aligned} \tag{A1.15}$$

$$\begin{aligned} C = \Big(\frac{1}{den1}[&y_1(x_2 - x_3)^2(-4x_1^2x_2 - 8x_1^2x_3 + 3x_1x_2^2 + 2x_1x_2x_3 + x_1x_3^2 + 3x_2^2x_3 \\ &+ 2x_2x_3^2 + x_3^3) + y_2(x_1 - x_3)^3(x_1^2 + 4x_1x_3 + x_3^2) \\ &- y_3(x_1 - x_2)^2(x_1^3 + 2x_1^2x_2 + x_1^2x_3 + 3x_1x_2^2 + 2x_1x_2x_3 - 8x_1x_3^2 \\ &+ 3x_2^2x_3 - 4x_2x_3^2)]\Big) \\ &- \Big(\frac{1}{den2}[tan\theta_1(x_2 - x_3)(x_1x_2 + 2x_1x_3 + 2x_2x_3 + x_3^2) \\ &- tan\theta_3(x_1 - x_2)(2x_1x_2 + 2x_1x_3 + x_2x_3 + x_1^2)]\Big) \end{aligned} \tag{A1.16}$$

$$\begin{aligned} D = \Big(\frac{2x_1x_3}{den1}[&-y_1(x_2 - x_3)^2(3x_2^2 - 4x_1x_2 - 2x_1x_3 + 2x_2x_3 + x_3^2) \\ &- y_2(x_1 - x_3)^3(x_1 + x_3) \\ &+ y_3(x_1 - x_2)^2(x_1^2 + 2x_1x_2 - 2x_1x_3 - 4x_2x_3 + 3x_2^2)]\Big) \\ &+ \Big(\frac{1}{den2}[x_3tan\theta_1(x_2 - x_3)(2x_1x_2 + x_1x_3 + x_2x_3) \\ &- x_1tan\theta_3(x_1 - x_2)(x_1x_2 + x_1x_3 + 2x_2x_3)]\Big) \end{aligned} \tag{A1.17}$$

$$E = \left(\frac{1}{den1}[y_1x_2x_3^2(x_2-x_3)^2(-4x_1^2+3x_1x_2+2x_1x_3-x_2x_3)+y_2x_1^2x_3^2(x_1-x_3)^3 + y_3x_1^2x_2(x_1-x_2)^2(x_1x_2-2x_1x_3-3x_2x_3+4x_3^2)]\right) - \left(\frac{x_1x_2x_3}{den2}[x_3tan\theta_1(x_2-x_3)-x_1tan\theta_3(x_1-x_2)]\right) \quad \text{(A1.18)}$$

We created the following Fortran code to generate the 2-D flap geometry. The code receives two input files: one contains the requested values for the six flap variables, generated by the DAKOTA optimization algorithm; the other contains coordinates for a unit-length straight line, where the nodes are spaced according to Gridgen's hyperbolic tangent function [67], which is then dimensionalized according to $L_1$ and $L$.

```
! Code for Generating 2D GTS Trailer Base Flaps, Version 1.0
!  - quartic polynomial, y = Ax^4 + Bx^3 + Cx^2 + Dx + E
!  - creates starboard flap (positive y) ==> port flap is mirrored in Gridgen
! 30 June 2011, Maj Jacob A Freeman
! 9 August 2011 - Modified for 'params.in.$num' input file from DAKOTA;
!                 note input angles in radians.

!*******************************************************************************
!*************************  MODULES  ***********************************
!*******************************************************************************

Module Select_Precision

! Specify computing precision
! Selected_Real_Kind = select desired kinds of real variables in processor-indep manner
  Implicit None
  Save

  ! Declare parameters
  Integer, Parameter :: Single = Selected_Real_Kind(p=6,r=37)
  Integer, Parameter :: Double = Selected_Real_Kind(p=13,r=200)
  Integer, Parameter :: Prec = Double     ! Precision for computations is set on this line

End Module

!*******************************************************************************

Module Set_Inputs

Use Select_Precision
  Implicit None
  Save

  Character(LEN=20) ::     gridname = 'tanhSpacing_97pts'
  Integer, Parameter ::    imax = 97     ! no. nodes, x-dir (imax-1 = number of cells in x-dir)
  Real(kind=Prec) ::       pi            ! pi = 3.14159265358...
  Real(kind=Prec) ::       L1            ! flap length in x-direction (m)
  Real(kind=Prec) ::       H1            ! position of flap above y=0 (m)
  Real(kind=Prec) ::       theta1        ! slope of flap leading edge (rad)
  Real(kind=Prec) ::       theta2        ! slope of flap at mid-chordlength (rad)
```

```
  Real(kind=Prec) ::          theta3          ! slope of flap trailing edge (rad)
  Real(kind=Prec) ::          delta           ! flap incidence angle (rad)
  Real(kind=Prec), Parameter :: length = 19.812_Prec          ! GTS length (m)

End Module

!*******************************************************************************

Module Geometry

Use Select_Precision
Use Set_Inputs
  Implicit None
  Save

  Integer ::                                  i               ! looping index for x-direction
  Real(kind=Prec),Dimension(imax) ::  x               ! x-coordinates for flap (m)
  Real(kind=Prec),Dimension(imax) ::  x_norm          ! normalized x-coords from 0 to 1
  Real(kind=Prec),Dimension(imax) ::  y               ! y-coordinates for flap (m)
  Real(kind=Prec) ::                          chordlength     ! (m)
  Real(kind=Prec), Parameter ::           one   = 1.0_Prec
  Real(kind=Prec), Parameter ::          two   = 2.0_Prec
  Real(kind=Prec), Parameter ::           three = 3.0_Prec
  Real(kind=Prec), Parameter ::           four  = 4.0_Prec
  Real(kind=Prec), Parameter ::           five  = 5.0_Prec
  Real(kind=Prec), Parameter ::           six   = 6.0_Prec
  Real(kind=Prec), Parameter ::           seven = 7.0_Prec
  Real(kind=Prec), Parameter ::           eight = 8.0_Prec
  Real(kind=Prec), Parameter ::           zero  = 0.0_Prec

End Module

!*******************************************************************************
!*********************    SUBROUTINES  & FUNCTIONS    ************************
!*******************************************************************************

Subroutine Write_Precision_Info

Use Select_Precision
  Implicit None

  ! Let user know precision for current computations
  write (*,*) '*****************************************************************'
  if (Prec == Single) then
    write (*,*) 'Currently using Single precision'
  elseif (Prec == Double) then
    write (*,*) 'Currently using Double precision. Why use Single?!'
  else
    write (*,*) 'Error: Precision must be specified as single or double.'
  endif
  write (*,*) '*****************************************************************'
  write (*,*)

End Subroutine

!*******************************************************************************
```

```
Subroutine Initialize_Constants

Use Set_Inputs, Only: pi
Use Geometry, Only: one
  Implicit None
  Save

  pi = acos(-one) ! sets pi

End Subroutine

!*******************************************************************************

Subroutine Set_Geometry

Use Geometry
  Implicit None

  Real(kind=Prec) :: theta1_deg, theta2_deg, theta3_deg, delta_deg  ! (deg)
  Real(kind=Prec) :: x1, x2, x3, y1, y2, y3                         ! (m)
  Real(kind=Prec) :: den1, den2, term1, term2, term3, term4, term5
  Real(kind=Prec) :: coeffA, coeffB, coeffC, coeffD, coeffE

  theta1_deg = theta1/pi*180.0_Prec
  theta2_deg = theta2/pi*180.0_Prec
  theta3_deg = theta3/pi*180.0_Prec
  delta_deg = delta/pi*180.0_Prec

  ! output to screen to verify input parameters
  write(*,*) 'Calculating geometry from DAKOTA input file, params.in'
  write(*,*) '(0.25908 <= L1 <= 1.2192 m)      : ',L1
  write(*,*) '(L1/cos(delta) <= H1 <= 1.2904 m): ',H1
  write(*,*) '(  0 <= theta1 <= 30 deg)        : ',theta1_deg
  write(*,*) '(  0 <= theta2 <= 30 deg)        : ',theta2_deg
  write(*,*) '(-30 <= theta3 <= 45 deg)        : ',theta3_deg
  write(*,*) '(  0 <=  delta <= 30 deg)        : ',delta_deg

  x1 = length
  y1 = H1
  x2 = length + L1*cos(theta2)/two/cos(delta)
  y2 = H1 - L1*sin(theta2)/two/cos(delta)
  x3 = L1 + length
  y3 = H1 - L1*tan(delta)

  chordlength = L1/cos(delta)

  den1 = ((x1-x3)**3)*((x1-x2)**2)*((x2-x3)**2)
  den2 = ((x1-x3)**2)*(x1-x2)*(x2-x3)

  term1 = y1*(x2-x3)**2
  term2 = y2*(x1-x3)**3
  term3 = y3*(x1-x2)**2
  term4 = tan(theta1)*(x2-x3)
  term5 = tan(theta3)*(x1-x2)
```

```
 coeffA = (one/den1)*( term1*(two*x2 + x3 - three*x1) + &
       term2 - term3*(x1 + two*x2 - three*x3) ) - (one/den2)*( term4 - term5 )

 coeffB = (two/den1)*( term1*(two*x1**2 + two*x1*x3 - x2**2 - two*x2*x3 - x3**2) &
     - term2*(x1 + x3) + term3*(x1**2 + two*x1*x2 - two*x1*x3 + x2**2 - two*x3**2) ) &
     + (one/den2)*( term4*(x1 + x2 + two*x3) - term5*(two*x1 + x2 + x3) )

 coeffC = (one/den1)*( term1*(-four*x2*x1**2 - eight*x3*x1**2 + three*x1*x2**2 &
     + two*x1*x2*x3 + x1*x3**2 + three*x3*x2**2 + two*x2*x3**2 + x3**3) &
     + term2*(x1**2 + four*x1*x3 + x3**2) - term3*(x1**3 + two*x2*x1**2 + x3*x1**2 &
     + three*x1*x2**2+two*x1*x2*x3 - eight*x1*x3**2 + three*x3*x2**2 - four*x2*x3**2))&
     - (one/den2)*( term4*(x1*x2 + two*x1*x3 + two*x2*x3 + x3**2) &
     - term5*(two*x1*x2 + two*x1*x3 + x2*x3 + x1**2) )

 coeffD = (two*x1*x3/den1)*( -term1*(three*x2**2 + two*x2*x3 - four*x1*x2 + x3**2 &
     - two*x1*x3) - term2*(x1 + x3)+term3*(x1**2 + two*x1*x2 - two*x1*x3 + three*x2**2 &
     - four*x2*x3) ) + (one/den2)*( term4*x3*(two*x1*x2 + x1*x3 + x2*x3) &
     - term5*x1*(x1*x2 + x1*x3 + two*x2*x3) )

  coeffE = (one/den1)*( term1*x2*(x3**2)*(three*x1*x2 + two*x1*x3 - x2*x3 &
      - four*x1**2) + term2*(x1**2)*(x3**2) + term3*x2*(x1**2)*(x1*x2 - two*x1*x3 &
      - three*x2*x3 + four*x3**2) ) - (x1*x2*x3/den2)*( term4*x3 - term5*x1 )

 x = x_norm*L1 + length
 do i = 1, imax
   y(i) = coeffA*x(i)**4 + coeffB*x(i)**3 + coeffC*x(i)**2 + coeffD*x(i) + coeffE
 enddo

End Subroutine

!**************************************************************************

Subroutine Write_Flap_Geometry

Use Geometry
Implicit none

 open(70,file='params.in.p3d',status='replace')
 180 Format(E23.15,E23.15,E23.15)
  write(70,*)imax
  do i = 1, imax
    write(70,180) x(i),y(i),zero
  enddo
 close(70)

End Subroutine

!**************************************************************************

Subroutine Read_Tanh_Spacing

Use Geometry
 Implicit none
 Logical :: connected

 inquire(file=trim(gridname)//'.dat',exist=connected)
```

```
  if (connected .eqv. .false.) then
    write(*,*) trim(gridname)//'.dat has a typo or cannot be found. Stopping...'
    stop
  endif

  open(80, file=trim(gridname)//'.dat', status = 'unknown')
    ! read tanh-spaced points, from 0 to 1
    read(80,*)
    read(80,*)
    read(80,*) (x_norm(i),i=1,imax)
  close(80)

End Subroutine

!*******************************************************************************

Subroutine Read_Design_Variables

Use Geometry
  Implicit none
  Logical :: connected

  open(90, file='params.in', status = 'unknown')
    ! read design variable input values
    read(90,*)
    read(90,*)
    read(90,*) L1
    read(90,*) H1
    read(90,*) theta1_deg
    read(90,*) theta2_deg
    read(90,*) theta3_deg
    read(90,*) delta_deg
  close(90)

End Subroutine
! *******************************************************************************
! ************************   MAIN PROGRAM   ********************************
! *******************************************************************************
Program Main

Use Select_Precision
Use Set_Inputs
Use Geometry
  Implicit None

  call Write_Precision_Info
  call Initialize_Constants
  call Read_Tanh_Spacing
  call Read_Design_Variables
  call Set_Geometry
  call Write_Flap_Geometry

End
! *******************************************************************************
! ************************   END OF PROGRAM   *****************************
! *******************************************************************************
```

### A1.3 Five-Variable Flaps, Cubic Polynomial for 3-D Design Optimization

For the 3-D tractor-trailer base-flap design optimization study (Chapter 4), we profit from the results of the 2-D study (Chapter 3) to determine that $H_1$ may be fixed at the trailer edges for minimum $\bar{C}_D$. We further conclude that $\theta_2$ does not play a significant role in determining the flap form, since it tends to conform with $\delta$, so we exclude it from the 3-D study but identify $\theta_2$ again with the flap trailing edge slope. Thus, we proceed with five design variables: $L_1$, $\theta_1$, $\theta_2$, $\delta_{side}$ and $\delta_{top}$, with descriptions and modified constraints detailed in Table A1.3. We use Eqs. (A1.1) through (A1.7) to determine the cubic polynomial coefficients, but we fix $H_1$ as a constant (for the side flaps, $H_1 = W/2$; for the top/bottom flaps, $H_1 = H/2$) and iterate for the second prescribed value for $\delta$. The side flaps are mirrored, and the top and bottom flaps are mirrored, all flaps with the same axial length. The Fortran code is lightly modified to generate two flap geometries: one in the *x-y* plane for the top/bottom flaps, the other in the *x-z* plane for the side flaps; we do not include a copy of these Fortran files because the differences from the one above are trivial. One notional design is shown in Fig. A1.3.

**Table A1.3.** 3-D Trailer Base Five-Variable Flap Design Variables and Constraints

| Design Variable | Description | Constraint |
|---|---|---|
| $L_1$ | axial length of trailer base flap (-) | $0.235W \le L_1 \le 0.471W$ ($2 \le L_1 \le 4$ ft) |
| $\theta_1$ | slope at flap leading edge (deg) | $0 \le \theta_1 \le 20°$ |
| $\theta_2$ | slope at flap trailing edge (deg) | $-35 \le \theta_2 \le 35°$ |
| $\delta_{side}$ | side flaps deflection angle (deg) | $10 \le \delta_{side} \le 28°$ |
| $\delta_{top}$ | top/bottom flaps deflection angle (deg) | $10 \le \delta_{top} \le 28°$ |

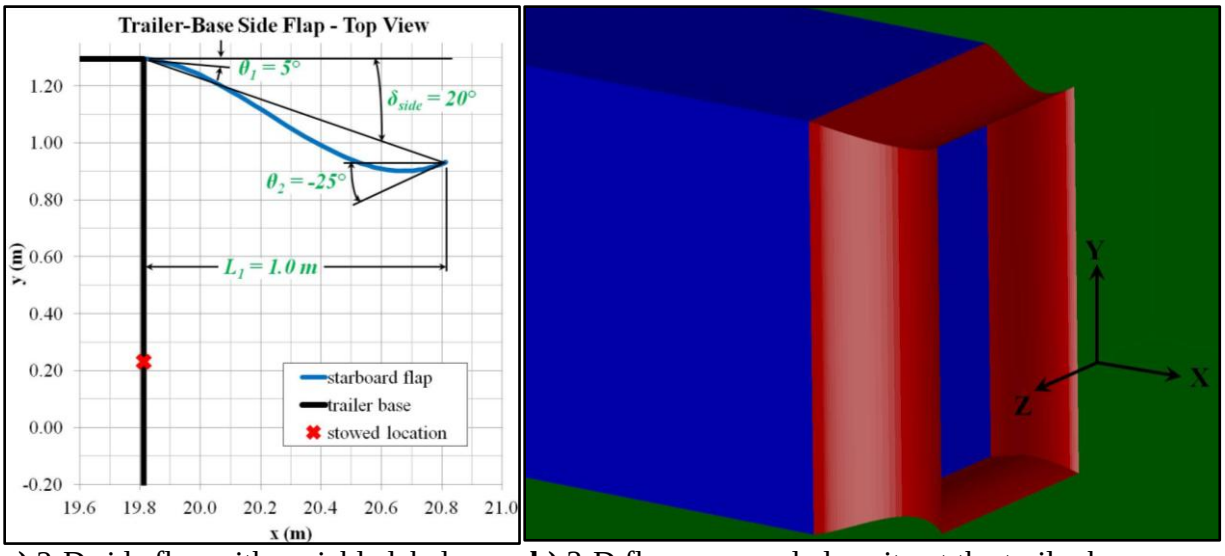


**a)** 2-D side flap with variable labels **b)** 3-D flaps as a sealed cavity at the trailer base

**Figure A1.3**. Trailer-base flaps with design-variable values for one possible configuration

# Appendix 2: Input Files, Executables, and Automation Scripts for Optimization Framework

In Fig. A2.1 we provide an expansion of Fig. 3 in Chapter 3 for 2-D or Fig. 4 in Chapter 4 for 3-D. The blue boxes contain input files and executables that are fixed for the entire optimization but that differ between the 2-D and 3-D studies. The red box contains the output of each iteration of the optimization, where the tabular data include design variable values and their according response value calculated by the flow solver and the optimizer output includes information about each design point, as well as statistical information at the end of the specified number of iterations. Purple boxes contain files created as output from one process that are then used as input for the next process. Gray boxes contain automation scripts that we developed for convenience and efficiency. Green boxes contain commercially or governmentally developed software. The numbers in parentheses correspond to the Appendix section number with a representative file.

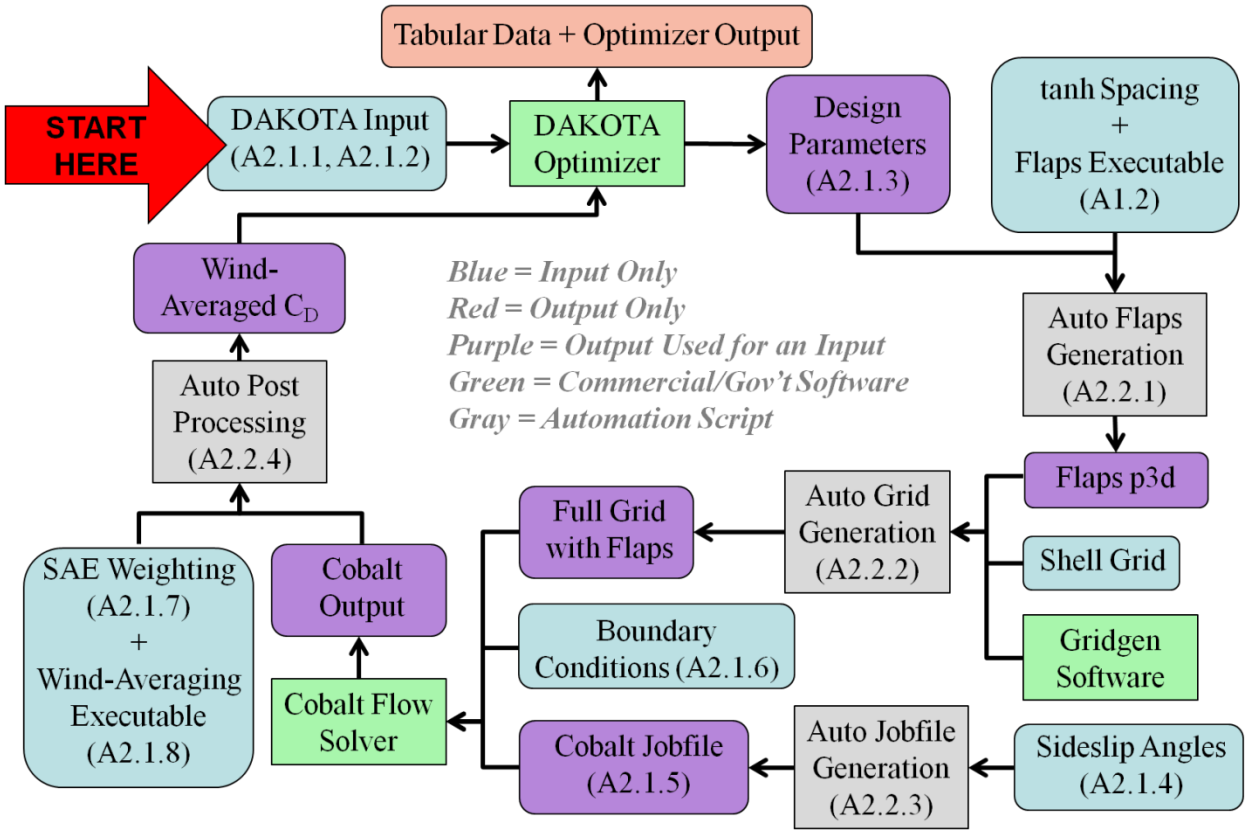


**Figure A2.1**. Flow chart of design optimization process details. Parentheses note location of according file in Appendix 2

## A2.1 Input Files and Executables

### A2.1.1 Evolutionary Algorithm (COLINY-EA) Input File for DAKOTA Optimization

```
# DAKOTA INPUT FILE - ea_dakota_full3Dopt.in
#  Evolutionary Algorithm for global optimization of single objective function
#  Uses continuous and/or discrete design variables
# 3D GTS model - Rev02 h4 full grid, variable flaps (5 design variables or DVs)

strategy,
  single_method
     tabular_graphics_data                  # tabular output gives ID#, DV values, and output value
                                            #   (CD_windAvg in this case)
method,
  coliny_ea
     max_iterations = 6                     # number of generations beyond initial sampling
     max_function_evaluations = 2000
     seed = 38                              # initial seed, ensures common starting point & same result if
                                            #    all other input same
     population_size = 20
     initialization_type unique_random      # random generation but successive gens reject candidate if duplicate
     fitness_type merit_function            # penalizes infeasible designs
     mutation_type offset_normal            # offset adds random var to given coord value; adds zero-mean random
                                            #     var w/normal dist
     mutation_rate 1.0
     crossover_type uniform                 # random combo of coordinates from parent1 and parent2
     crossover_rate 0.8                     # no. crossovers = crossover_rate * population size
     replacement_type chc = 1               # selects best individuals from combo of current pop & newly
                                            #    generated individs
model,
  single

variables,
  continuous_design = 1                     # continuous DV, L1, with specified bounds
     lower_bounds           0.6100
     upper_bounds           1.2192
     descriptors            'L1'
  discrete_design_range = 4                 # discrete DVs with specified range, default unit increments for resol'n
     lower_bounds            0        -35      10       10
     upper_bounds            20        35      28       28
     descriptors            'theta1'  'theta2'  'dside'   'dtop'

interface,
  fork
     asynchronous                           # allows selection of concurrent design points
     evaluation_concurrency = 20
     analysis_driver = './full3Dopt.sh'
       parameters_file = 'params.in'        # generates parameters input file, used by full3Dopt.sh to make flap
                                            #    geometry (plot3d files)
       results_file    = 'results.out'      # waits for results file number to match parameters input file number,
                                            #    then evaluates and starts next generation
       file_tag
       file_save

responses,
  num_objective_functions = 1
```

```
    response_descriptors = 'Cd_windAvg_epiFlaps'
    no_gradients
    no_hessians
################################
###            End of File            ###
################################
```

### A2.1.2 NCSU-DIRECT Input File for DAKOTA Optimization

```
#  DIRECT (DIviding RECTangles) Algorithm for global optimization by North Carolina State University
#  Uses continuous design variables only
#  Uses bound constraints only
# 2D GTS model - Rev05 h2 full grid, variable flap (6 DVs)

strategy,
        single_method
          tabular_graphics_data
method,
        ncsu_direct
          max_iterations = 200                    # algorithm appears to not respect this input
          max_function_evaluations = 2000         # algorithm appears to not respect this input
          solution_target = 0.12                  # desired global min value; default = 0.0
          convergence_tolerance = 0.01            # use with solution_target; % diff from known/specified value
          min_boxsize_limit = 1.0e-5              # alg stops if smallest subregion falls below this limit
          volume_boxsize_limit = 1.0e-9           # alg stops if % of original hypercube falls below this; unique
                                                  #    to NCSU not coliny
model,
        single
variables,
        continuous_design = 6
          lower_bounds    0.25908         0.25908         0       0       -30     0
          upper_bounds    1.2192          1.2904          30      30      45      30
          descriptors     'L1'            'H1'            'theta1' 'theta2' 'theta3' 'delta'
interface,
        fork
          asynchronous
            evaluation_concurrency = 20
          analysis_driver = './full2Dopt.sh'
            parameters_file = 'params.in'
            results_file    = 'results.out'
            file_tag
            file_save
responses,
        num_objective_functions = 1
        response_descriptors = 'Cd_windAvg_bodyAxis'
        no_gradients
        no_hessians
################################
###            End of File            ###
################################
```

### A2.1.3 Parameters Input File

```
                        5 variables
 1.171265512122849e+00 L1              # continuous design variable
                       11 theta1       # discrete design variable
                       19 theta2
                       18 dside
                       18 dtop
                        1 functions    # one objective function
                        1 ASV_1
                        1 derivative_variables
                        1 DVV_1
                        0 analysis_components
################################
###          End of File       ###
################################
```

### A2.1.4 Sideslip Angles File

These are the sideslip angles for the 3-D optimization study, determined by the SAE wind-averaging method [66] for truck speed, $V_\infty$ = 57.2 mph, and average wind speed of 9.06 mph.

```
id      beta (for wind-averaging)
 1   2.036
 2   2.770
 3   5.751
 4   7.187
 5   8.360
 6   9.063
################################
###          End of File       ###
################################
```

### A2.1.5 Flow Solver Input File

We provide below one representative example of the input deck with comments for the Cobalt [10] flow solver; we do not include a sample input file for RavenCFD [11] because it is quite similar, with a few additional options for solver parameters. Notable differences for the 2-D and 3-D input values include the following: for 2-D, 80,000 iterations were required to obtain converged steady solutions for the smallest sideslip angle, $\beta$, with 40,000 iterations required for the solutions (restarted from the smallest $\beta$ solution) at the other $\beta$ values; 3-D required 7,200 iterations for the smallest $\beta$ and 5,000 to 6,800 for the other $\beta$ values. This was most likely due to relative resolution and flow behavior, where the 2-D meshes were finely resolved and had large regions of artificially separated and unsteady flow, and the 3-D meshes were relatively coarse and had little or no unsteadiness in the flow; and for 2-D, we used the Spalart-Allmaras turbulence model (option "1"), while we used Menter SST turbulence model (option "4") for the 3-D study.

```
#!/bin/csh
#################################################################
# THIS IS FOR ERDC DIAMOND: SGI ALTIX ICE, 11.2 GFLOPS
#  Note: the PBS commands, binary/license file locations differ for other computing platforms
#################################################################
#PBS -A USAFA32092TPU                  ## project ID
#PBS -l walltime=32:00:00              ## number of wall hours requested for job
```

```
#PBS -l select=4:ncpus=8:mpiprocs=8      ## select=number of nodes requested; ncpus=8 for 8cpus per node
#PBS -l place=scatter:excl               ##   mpiprocs=number of cores/node requested
#PBS -l cobalt=32                        ## place=selects any available nodes
#PBS -l application=cobalt               ## cobalt=32 number of license processing elements requested
#PBS -N EA.90.1.minus2                   ## job ID=COLINY_EA design 90 at beta1=2.1 deg (for 3D)
#PBS -q standard                         ## queue type
#PBS -e jaf.e                            ## error file
#PBS -o jaf.o                            ## processing output file, not solution data
#PBS -m e                                ## send user email at job completion
#PBS -M jacobf72@vt.edu

cd $PBS_O_WORKDIR                        ## moves to working directory
setenv NCPUS 32
echo Number of CPUs: $NCPUS

setenv CBLTLOC /usr/local/applic/cobalt/5.2-rlm   ## specifies location of the Cobalt executables
setenv COBALT_LIC                                 ## Cobalt license info, details omitted
setenv RUN mpirun                                 ## specifies command to run job in parallel
source /usr/share/modules/init/csh
module swap mpi mpi/intelmpi-4.0.0
module load cobalt/5.2-rlm
module list

setenv CASE 3dGTSflaps.ea.grd.90.minus2.beta.1    ## case name
setenv CASEDIR $WORKDIR/3dGTS/colinyEA            ## case directory
setenv GRIDDIR $WORKDIR/3dGTS/grids               ## location of grid and boundary condition files
setenv SCRATCH $CASEDIR                           ## make a working directory
mkdir $SCRATCH

echo Running in $CASEDIR
echo Start `date`
cat > $CASEDIR/$CASE.inp << EOF
******************************************************
                     TITLE
******************************************************
Rev02 h4 grid, $CASE
******************************************************
          ALGORITHM PARAMETERS
******************************************************
 NO. PROCESSORS FOR COBALT   PROCESSOR GROUP SIZE FOR MESH PARTITIONING
   $NCPUS                          16.          ## group size may be smaller/larger, depending grid file size
 START OPTION (1=INITIAL RUN, 2=RESTART, 3=RESTART, RESET TIME TO 0)
   1
 EQUATION SET (1=EULER, 2=LAMINAR NS, 3=TURBULENT NS)
   3
 GAS MODEL (1=IDEAL GAS, 2=EQUILIBRIUM AIR)
   1
 TURBULENCE MODEL(1=SA, 2=DES-SA, 3=BSL, 4=SST, 5=DES-SST, 6=KW, 7=SARC, 8=DES-SARC)
   4
 SPATIAL ACCURACY (1 OR 2)   TEMPORAL ACCURACY (1 OR 2)
           2                   1              ## set temporal accuracy to 1 for steady, 2 for time-accurate
 OVERSET GRID (0=NO)
   0
 TEMPORAL DAMPING COEFFICIENTS (ADVECTION & DIFFUSION)
   0.01         0.0
 NO. TIME STEPS     NO. NEWTON SUB-ITERATIONS
```

```
   6800                                    1
 CFL              REQUESTED TIME STEP
   1.e6                                    -1.
 INITIAL CFL      RAMP START    RAMP LENGTH
   1.0              200           200     ## starts at CFL=1; at iteration 200, it ramps to 1.e6 over 200 iterations
************************************************************
          PHYSICAL & GAS CONSTANTS
************************************************************
 COORDINATE SYSTEM (1=FLO57, 2=PANAIR, 3=AXI-SYMMETRIC)
  1
 UNITS (1=MKS, 2=CGS, 3=FOOT-SLUG-SEC, 4=INCH-SNAIL-SEC)
  1                                       ## mks = meters, kilogram, second (SI units)
 GAMMA    GAS CONSTANT     GRAVITY
  -1.          -1.             0.        ## -1. reverts to default values
 SUTHERLAND LAW COEFFICIENTS (C1 & C2)   PRANDTL NO.
  -1.       -1.                                 -1.
************************************************************
           REFERENCE CONDITIONS
************************************************************
 MACH NO.   ANGLE OF ATTACK   ANGLE OF SIDESLIP
   0.0745       0.0          BVALUE   ## BVALUE is auto-scripted to be substituted with appropriate beta value
 STATIC PRESSURE    STATIC TEMPERATURE
   101325.0                    293.15          ## pressure in Pa, temp in Kelvin
************************************************************
            INITIAL CONDITIONS
************************************************************
 MACH NO.     ANGLE OF ATTACK     ANGLE OF SIDESLIP
  -1.              -370.              -370.     ## -370. is default angle value, reverts to reference conditions
 STATIC PRESSURE         STATIC TEMPERATURE
  -1.                        -1.
 K or Nu~            OMEGA
  71.50               9.4944e5               ## calculated freestream values for turbulence model
************************************************************
        POST-PROCESSING CONTROL PARAMETERS
************************************************************
------------------------------------------------------
            TURBULENCE STATISTICS
------------------------------------------------------
 TIME AT WHICH TO BEGIN CALCULATION OF TIME-AVERAGES
   100.
------------------------------------------------------
            RESTART/SOLUTION FILE
------------------------------------------------------
 FREQUENCY (IN TIME-STEPS) OF RESTART FILE OUTPUT
   1000
------------------------------------------------------
            FLOW VIZ DATA AND FILE
------------------------------------------------------
 FLOW VIZ FILE FORMAT (0=NONE, 1=COBALT, 2=ENSIGHT, 3=FIELDVIEW, 4=TECPLOT)
   4
 FLOW VIZ FILE NAME BASE
  $CASE
 LIST OF AUXILIARY VARIABLES
   4                                       ## output is rho, u, v, w, P; "4" requests eddy viscosity
 DATA IN LAB REF FRAME?    DATA TIME-AVERAGED?
   0                                       1
```

```
 FREQUENCY (IN TIME-STEPS) OF FLOW VIZ FILE OUTPUT
    -1.
-------------------------------------------------------
                 TAP DATA AND FILE
-------------------------------------------------------
 PROVIDE TAP DATA?    LIST OF TAP DATA
    0                2 3 4 5 6 7 9 10                  ## may be used to output specified values at a specified location
 DATA IN LAB REF FRAME?    DATA TIME-AVERAGED?
    0                                                  0
 FREQUENCY (IN TIME-STEPS) OF TAP FILE OUTPUT
    100.
-------------------------------------------------------
   INTEGRATED FORCES/MOMENTS AND CONVERGENCE DATA
-------------------------------------------------------
 DATA TIME_AVERAGED?
   1
 REFERENCE AREA
   9.3445
 X-, Y-, Z- COORDINATES OF MOMENT REFERENCE POINT
   0.0     0.0         0.0
 REFERENCE LENGTHS FOR MOMENTS ABOUT X-,Y- AND Z-AXIS
   2.5908            0.0         0.0
 IF AXI-SYMMETRIC, PROVIDE FORCES OVER FOLLOWING SECTOR SIZE (DEGREES)
   -1.
 FREQUENCY (IN TIME-STEPS) OF CONVERGENCE OUTPUT
   8
*******************************************************
         END OF INPUT INFORMATION
*******************************************************
EOF
#------------------ CoMPIRUN script argument list ------------------
#----- executable options -----
#  1: machine type            ! Options: compaq,ibm3,ibm4,linux,linuxgm
#                             !          sgir10k,sgir12k,sgir14k,sun64
#  2: precision switch        ! Options: double, single
#--------- input files ---------
#  3: Cobalt input file name (aka stdin)
#  4: bc file name
#  5: grid file name
#  6: motion file name
#  7: user-specified profile file name
#  8: tap location file name
#-------- output files --------
#  9: Cobalt output file name (aka stdout)
# 10: external controller HDF file (an input and output file)
# 11: 1-D heat equation restart file name (an input and output file)
# 12: movie tap file name
# 13: restart file name (an input and output file)
# 14: directory for convergence files
# 15: directory for flow viz files
#-----------------------------------------------------------------
 $CBLTLOC/CoMPIRUN \
amd64 \
double \
$CASEDIR/$CASE.inp \
$GRIDDIR/3dGTSwFlaps.cbc \
```

```
$GRIDDIR/90.minus2.grd \
$CASEDIR/$CASE.mtn \
$CASEDIR/$CASE.prf \
$GRIDDIR/$CASE.tap \
$CASEDIR/$CASE.out \
$CASEDIR/$CASE.hdf \
$CASEDIR/$CASE.ldhe \
$CASEDIR/$CASE.mtap \
$CASEDIR/$CASE.rst \
$CASEDIR/$CASE.convrg \
$CASEDIR/$CASE.movies
echo Finish `date`
##########################################
####                End of File       #######
##########################################
```

### A2.1.6 Flow Solver Boundary Condition File

```
#######################################
 Cobalt Boundary Condition File for:
 3D GTS with Base Flaps
#######################################
  1
GTS farfield
Farfield
Modified Riemann Invariants
 P_stat   T_stat   k  omega   Mach  alpha   beta
 -1.0     -1.0    -1.  -1.    -1.  -370.0  -370.0          ## defaults to reference conditions in primary job file
#######################################
  2
GTS surface
Solid-Wall
Adiabatic No Slip
No Trips
Yes                                                      ## yes force accounting on tractor-trailer surface
#######################################
  3
road
Solid-Wall
Slip
No                                                       ## no force accounting on road
#######################################
  4                                                      ## remove for case without base flaps
flaps
Solid-Wall
Adiabatic No Slip
No Trips
Yes                                                      ## yes force accounting on trailer base flaps
#######################################
#  4                                                     ## Use this option for symmetry case, no sideslip angles
#symmetry plane
#Solid-Wall
#Symmetry
#No
##########################################
####                End of File       #######
##########################################
```

### A2.1.7 SAE Weights for Wind-Averaging

Following is the file with weights for the 3-D optimization study, determined by the SAE wind-averaging method [66] for truck speed, $V_\infty$ = 57.2 mph, and average wind speed of 9.06 mph. These weights are used with Eq. (8) in Chapter 3 to calculate the wind-averaged drag coefficient.

```
id        M (SAE weight for V_wind = 9.06mph and V_truck = 57.2mph)
 1   1.331028
 2   0.719134
 3   1.249049
 4   0.801112
 5   1.107059
 6   0.943103
##########################################
####                End of File                 #######
##########################################
```

### A2.1.8 Code for Calculating Wind-Averaged Drag Coefficient

```
! Code for Wind-Averaging Drag Coefficient from Cobalt Calculations, Version 2.0
! 23 April 2012, Maj Jacob A Freeman
!  Modified from Version 1.0 to select max of plus2 or minus2 body-axis Cd

!*****************************************************************************
!****************************    MODULES    **********************************
!*****************************************************************************

Module Select_Precision
  Implicit None
  Save

  ! Declare parameters
  Integer, Parameter :: Single = Selected_Real_Kind(p=6,r=37)
  Integer, Parameter :: Double = Selected_Real_Kind(p=13,r=200)
  Integer, Parameter :: Prec = Single     ! Precision for computations is set on this line

End Module

!*****************************************************************************

Module Set_Inputs

Use Select_Precision
  Implicit None
  Save

  Integer ::                    i                   ! looping index
  Integer, Parameter ::         imax = 6            ! number of solutions for wind-averaging
  Integer, Dimension(imax) ::     id                ! identification number
  Real(kind=Prec), Dimension(imax) :: beta          ! sideslip angles from SAE method
  Real(kind=Prec), Dimension(imax) :: weight        ! weighting values from SAE method
  Real(kind=Prec), Dimension(imax) :: CD            ! max of CDm2 and CDp2
  Real(kind=Prec), Dimension(imax) :: CDm2          ! raw time-avg CD, calculated in Cobalt v5.2, minus2 value
  Real(kind=Prec), Dimension(imax) :: CDp2          ! raw time-avg CD, calculated in Cobalt v5.2, plus2 value
  Real(kind=Prec) ::            CD_windAvg          ! wind-averaged drag coefficient => simple average of
```

```
                                                    !   CD(i)*weight(i)
  Real(kind=Prec) ::            CD_windAvg_m2       ! wind-averaged drag coefficient => simple average of
                                                    !   CDm2(i)*weight(i)
  Real(kind=Prec) ::            CD_windAvg_p2     ! wind-averaged drag coefficient => simple average of
                                                    !   CDp2(i)*weight(i)
  Real(kind=Prec), Parameter ::       six  = 6.0_Prec
  Real(kind=Prec), Parameter ::       nine = 9.0_Prec

End Module

!*******************************************************************************
!INFORMATION ON ALL MODULES
! 1 --> Select_Precision
! 2 --> Set_Inputs     (contains Select_Precision)
!*******************************************************************************

!*******************************************************************************
!**********************  SUBROUTINES  & FUNCTIONS  **********************
!*******************************************************************************

!*******************************************************************************

Subroutine Wind_Averaging

Use Set_Inputs
  Implicit None

  Real(kind=Prec), Dimension(imax) :: term1, term2, term3

  ! output to screen to verify input parameters
!  write(*,*) 'Perform Wind-Averaging of Time-Averaged Raw Drag Coefficients'
!  write(*,*) '       id   beta(deg)      weight        CD '
!  do i = 1, imax
!    write(*,*) id(i),beta(i),weight(i),CD(i)
!  enddo

  do i = 1, imax
    term1(i) = CD(i)*weight(i)
    term2(i) = CDm2(i)*weight(i)
    term3(i) = CDp2(i)*weight(i)
  enddo

  CD_windAvg = (term1(1) + term1(2) + term1(3) + term1(4) + term1(5) + term1(6))/six
  CD_windAvg_m2 = (term2(1) + term2(2) + term2(3) + term2(4) + term2(5) + term2(6))/six
  CD_windAvg_p2 = (term3(1) + term3(2) + term3(3) + term3(4) + term3(5) + term3(6))/six

  if (CD(1) < nine) then
    write(*,*) 'Wind-Averaged CD = ',CD_windAvg
  else
    write(*,*) 'Wind-Averaged CD = Invalid Design'
  endif

End Subroutine

!*******************************************************************************
```

```
Subroutine Write_CD_WindAvg

Use Set_Inputs
 Implicit none

 open(10,file='cd_windAvg.dat',status='replace')
  if (CD(1) < nine) then
   write(10,*) '               ',CD_windAvg,'Cd_windAvg_epiFlaps'
  else
   write(10,*) '                 9.999999 Cd_windAvg_epiFlaps'
  endif
 close(10)

End Subroutine

!*******************************************************************************

Subroutine Write_CD_WindAvg_m2_p2

Use Set_Inputs
 Implicit none

 open(15,file='cd_windAvg_m2_p2.dat',status='replace')
  if (CD(1) < nine) then
   write(15,*) CD_windAvg_m2,'Cd_windAvg_minus2'
   write(15,*) CD_windAvg_p2,'Cd_windAvg_plus2'
  else
   write(15,*) '   9.999999 Cd_windAvg_minus2'
   write(15,*) '   9.999999 Cd_windAvg_plus2'
  endif
 close(15)

End Subroutine

!*******************************************************************************
Subroutine Read_Beta_and_SAE_Weighting

Use Set_Inputs

 Implicit none

 open(20, file='betaWindAvg-n6.dat',status='unknown')
  read(20,*)
  do i = 1, imax
   read(20,*) id(i), beta(i)
  enddo
 close(20)

 open(30, file='weightSAE.dat',status='unknown')
  read(30,*)
  do i = 1, imax
   read(30,*) id(i), weight(i)
  enddo
 close(30)
End Subroutine
```

```
!*******************************************************************************
Subroutine Read_TimeAvg_CD

Use Set_Inputs
  Implicit none

  open(40, file='Cd_timeAvg_temp.dat',status='unknown')
    do i = 1, imax
      read(40,*) id(i),CDm2(i),CDp2(i)
      CD(i) = max(CDm2(i),CDp2(i))
    enddo
  close(40)

End Subroutine

! ******************************************************************************
! INFORMATION ON ALL SUBROUTINES
! ******************************************************************************
! No.     Subroutine                  Modules Included                  Subroutines,Functions Included
! ============================================================================
! 1       Wind_Averaging              Select_Precision; Set_Inputs  none
! 2       Write_CD_WindAvg            Select_Precision; Set_Inputs  none
! 3       Write_CD_WindAvg_m2_p2            Select_Precision; Set_Inputs  none
! 4       Read_Beta_and_SAE_Weighting  Select_Precision; Set_Inputs  none
! 5       Read_TimeAvg_CD                   Select_Precision; Set_Inputs  none
! ****************************************************************************

! ****************************************************************************
! ************************   MAIN PROGRAM   *********************************
! ****************************************************************************
Program Main

Use Select_Precision
Use Set_Inputs
  Implicit None

  call Read_Beta_and_SAE_Weighting
  call Read_TimeAvg_CD
  call Wind_Averaging
  call Write_CD_WindAvg
  call Write_CD_WindAvg_m2_p2

End
! ****************************************************************************
! ************************   END OF PROGRAM   ********************************
! ****************************************************************************
```

## A2.2 Automation Scripts for Optimization Studies

Below are the automation scripts that we modified (A2.2.1) or developed to use within the DAKOTA optimization framework [45].

### A2.2.1 Generates 3-D Flaps Geometry

```
#!/bin/csh -f
# Filename: full3Dopt.sh (or full2Dopt.sh for 2-D optimization)
# Full 3D GTS optimization problem - rev02 h4 full grid
#  Maj Jacob Freeman, 10 April 2012
#  Variable flaps, 5 design variables (L1, theta1, theta2, dside, dtop)

# $argv[1] is params.in.(fn_eval_num) FROM Dakota
# $argv[2] is results.out.(fn_eval_num) returned to Dakota

# ------------------------
# Set up working directory
# ------------------------

# strip function evaluation number for making working directory
set num = `echo $argv[1] | cut -c 11-`
mkdir workdir.$num

# copy parameters file from DAKOTA into working directory
cp $argv[1] workdir.$num/params.in

# copy files for flap generation into workdir
cp gridstuff/3DflapCubicHi.exe workdir.$num/.
cp gridstuff/3DflapCubicLo.exe workdir.$num/.
cp gridstuff/tanhSpacing_61pts.dat workdir.$num/.

cd workdir.$num

# generate 3D flap database curves
#   This also calculates nonlinear constraint: overlapChecker = (L1/cos(delta) - H1). Okay if <= 0.
#   Inputs are params.in & tanhSpacing_61pts.dat
#   Outputs are params.in.top.hi.p3d, params.in.side.hi.p3d
#     and params.in.top.lo.p3d, params.in.side.lo.p3d & constraint.dat
./3DflapCubicHi.exe          ## These call the file detailed in Appendix A1.2, except we add/subtract 2 deg
./3DflapCubicLo.exe          ##    from deflection angle specified in params.in file, to generate flap geometry

# move for use by createGrids_Jobfiles.sh
mv params.in.top.hi.p3d ../flaps-p3d/flap.top.hi.$num.p3d
mv params.in.side.hi.p3d ../flaps-p3d/flap.side.hi.$num.p3d
mv params.in.top.lo.p3d ../flaps-p3d/flap.top.lo.$num.p3d
mv params.in.side.lo.p3d ../flaps-p3d/flap.side.lo.$num.p3d
mv constraint.dat ../constraint/constraint.$num.dat

# This step doesn't entirely make sense, but we need to copy Cobalt output
#  from outputResults to workdir as results.out, then move that back to
#  the main directory as results.out.num
cp ../outputResults/results.out.$num results.out
mv results.out ../$argv[2]

# cleanup
cd ..
```

```
mv params.in.$num parameterInputs/.
rm -rf workdir.$num
################################
###             End of File              ###
################################
```

### A2.2.2 Generates 3-D Grids with Simplified Tractor-Trailer with Base Flaps

```
#!/bin/bash
# Generates grids for 3D GTS optimization problem - rev02 h4 full grid
#  Maj Jacob Freeman, 12 April 2012
#  Variable flaps, 5 variables (L1, theta1, theta2, dside, dtop)

# some cleanup and temporary move of files until tar/gzip at end of this script
rm results.out.*

echo "Please enter population size for grid/job creation: "
read n_current

echo "Please enter total population count prior to these grids/jobs: "
read n_cumulative

imin=$((1 + $n_cumulative))
imax=$(($n_cumulative + $n_current))

# loop goes from generation start to (that number + population size)
for (( i = $imin ; i <= $imax ; i++ ))

  do

    # read overlap_checker
    overlap_checker=$(grep 'value' constraint/constraint.$i.dat | cut -c 18-38)
    overlap_flag=$(grep 'flag' constraint/constraint.$i.dat | cut -c 27-28)

    # create grid and jobfiles if overlap_checker <= 0, else do not create *.grd & *.job
    if [ "$overlap_flag" -eq "1" ]
      then
        echo "Overlap checker = $overlap_checker <= 0. It stays. Create grids."
        # Set up working directory
        mkdir workdir.$i

        # copy Gridgen glyph, p3d, job & betaWindAvg files for plus2deg flaps into workdir
        cp gridstuff/*.glf workdir.$i/.
        cp flaps-p3d/flap.top.hi.$i.p3d workdir.$i/params.in.top.p3d
        cp flaps-p3d/flap.side.hi.$i.p3d workdir.$i/params.in.side.p3d
        cd workdir.$i

        # generate 3D grids with GridgenV15.15
        # inputs are params.in.top.hi.p3d, params.in.side.hi.p3d, GTSfullSize_corrected.dba &
        #     3dGTSwFlaps.rev02.h4.shell.gg
        # outputs are params.in.gg, params.in.grd, params.in.bc
            # FIRST TRY makeFlaps_h4.glf. If it fails, TRY makeFlaps_h4_mod.glf. They account for different ways
            #    the connectors are applied to the DB entities.
        /aoe/gridgen/GridgenV15/gridgen -b makeFlaps_h4.glf
#       /aoe/gridgen/GridgenV15/gridgen -b makeFlaps_h4_mod.glf

        # move grids to common storage place for shipment to HPC computing with Cobalt
```

```
      mv params.in.gg ../gridgenGrids/$i.plus2.gg
      mv params.in.grd ../cobaltGrids/$i.plus2.grd

      # minor cleanup to be sure we don't read in incorrect p3d files
      rm params.in.top.p3d params.in.side.p3d

      # copy p3d files for minus2deg flaps into workdir
      cp ../flaps-p3d/flap.top.lo.$i.p3d params.in.top.p3d
      cp ../flaps-p3d/flap.side.lo.$i.p3d params.in.side.p3d

      # inputs are params.in.top.lo.p3d, params.in.side.lo.p3d, GTSfullSize_corrected.dba &
      #     3dGTSwFlaps.rev02.h4.shell.gg
      # outputs are params.in.gg, params.in.grd, params.in.bc
      /aoe/gridgen/GridgenV15/gridgen -b makeFlaps_h4.glf
#       /aoe/gridgen/GridgenV15/gridgen -b makeFlaps_h4_mod.glf

      # move grids to common storage place for shipment to HPC computing with Cobalt
      mv params.in.gg ../gridgenGrids/$i.minus2.gg
      mv params.in.grd ../cobaltGrids/$i.minus2.grd

      # cleanup
      cd ..
      rm -rf workdir.$i

    else
      echo "Overlap checker = $overlap_checker > 0. It goes. Neither grid nor jobfiles are created."
      mv flaps-p3d/flap.top.hi.$i.p3d exile-nonviable-p3d-params/.
      mv flaps-p3d/flap.top.lo.$i.p3d exile-nonviable-p3d-params/.
      mv flaps-p3d/flap.side.hi.$i.p3d exile-nonviable-p3d-params/.
      mv flaps-p3d/flap.side.lo.$i.p3d exile-nonviable-p3d-params/.
  fi

done

echo "Grids "$imin" through "$imax" complete!!"
################################
###            End of File            ###
################################
```

### A2.2.3 Generates Batch of Input Jobfiles for the Cobalt Flow Solver

We modify the flow solver input file, detailed in Appendix A2.1.5, with generic descriptors such as BVALUE in the reference conditions input for ANGLE OF SIDESLIP, then use the following script to substitute in the appropriate values for the respective input file.

```
#!/bin/bash
# Generates jobfiles for 3D GTS optimization problem - rev02 h4 full grid
#  Maj Jacob Freeman, 12 April 2012
#  Variable flaps, 5 variables (L1, theta1, theta2, dside, dtop)

# some cleanup and temporary move of files until tar/gzip at end of this script
mv cobaltGrids/*.job cobaltGrids/temp/.

echo "Please enter computing platform (diamond or garnet): "
read hpc
```

```
echo "Please enter population size for job creation: "
read n_current

echo "Please enter total population count prior to these jobs: "
read n_cumulative

echo "Please enter HPC queue (standard, debug, etc) or reservation number (Rxxxxx): "
read res

imin=$((1 + $n_cumulative))
imax=$(($n_cumulative + $n_current))

# loop goes from generation start to (that number + population size)
for (( i = $imin ; i <= $imax ; i++ ))

  do

    # read overlap_checker
    overlap_checker=$(grep 'value' constraint/constraint.$i.dat | cut -c 18-38)
    overlap_flag=$(grep 'flag' constraint/constraint.$i.dat | cut -c 27-28)

    # create jobfiles if overlap_checker <= 0, else do not create *.job
    if [ "$overlap_flag" -eq "1" ]
      then
        echo "Overlap checker = $overlap_checker <= 0. It stays. Create jobfiles."
        # Set up working directory
        mkdir workdir.$i

        # copy Gridgen glyph, p3d, job & betaWindAvg files for plus2deg flaps into workdir
        cp gridstuff/*.job workdir.$i/.
        cp gridstuff/betaWindAvg-n6.dat workdir.$i/.
        cd workdir.$i

        # Create jobfiles for initial runs, beta = 2.036 deg ONLY; others will restart from this case
        # read beta values for wind-averaging
        beta=$(grep " 1 " betaWindAvg-n6.dat | cut -c 6-11)

        # modify jobfile with correct job number and value for sideslip
        # replaces all instances of JNUM with $i, BVALUE with $beta, WINDAVGB with $j and FLAPPOSN with
        #    plus2 or minus2 in jobfile
        sed -e "s/JNUM/$i/" -e "s/BVALUE/$beta/" -e "s/FLAPPOSN/plus2/" -e "s/QUEUE/$res/" <$hpc.ea.init.job
            >../cobaltGrids/$hpc.ea.grd.$i.plus2.beta.1.job
        sed -e "s/JNUM/$i/" -e "s/BVALUE/$beta/" -e "s/FLAPPOSN/minus2/" -e "s/QUEUE/$res/" <$hpc.ea.init.job
            >../cobaltGrids/$hpc.ea.grd.$i.minus2.beta.1.job

        beta=$(grep " 2 " betaWindAvg-n6.dat | cut -c 6-11)
        sed -e "s/JNUM/$i/" -e "s/BVALUE/$beta/" -e "s/WINDAVGB/2/" -e "s/FLAPPOSN/plus2/" -e
            "s/QUEUE/$res/" -e "s/NSTEPS/5000/" -e "s/NAVG/73/" <$hpc.ea.rst.job
            >../cobaltGrids/$hpc.ea.grd.$i.plus2.beta.2.job
        sed -e "s/JNUM/$i/" -e "s/BVALUE/$beta/" -e "s/WINDAVGB/2/" -e "s/FLAPPOSN/minus2/" -e
            "s/QUEUE/$res/" -e "s/NSTEPS/5000/" -e "s/NAVG/73/" <$hpc.ea.rst.job
            >../cobaltGrids/$hpc.ea.grd.$i.minus2.beta.2.job

        beta=$(grep " 3 " betaWindAvg-n6.dat | cut -c 6-11)
        sed -e "s/JNUM/$i/" -e "s/BVALUE/$beta/" -e "s/WINDAVGB/3/" -e "s/FLAPPOSN/plus2/" -e
            "s/QUEUE/$res/" -e "s/NSTEPS/6800/" -e "s/NAVG/106/" <$hpc.ea.rst.job
```

```
        >../cobaltGrids/$hpc.ea.grd.$i.plus2.beta.3.job
    sed -e "s/JNUM/$i/" -e "s/BVALUE/$beta/" -e "s/WINDAVGB/3/" -e "s/FLAPPOSN/minus2/" -e
        "s/QUEUE/$res/" -e "s/NSTEPS/6800/" -e "s/NAVG/106/" <$hpc.ea.rst.job
        >../cobaltGrids/$hpc.ea.grd.$i.minus2.beta.3.job

    for (( j = 4 ; j <= 5 ; j++ ))
      do
        beta=$(grep " $j " betaWindAvg-n6.dat | cut -c 6-11)
        sed -e "s/JNUM/$i/" -e "s/BVALUE/$beta/" -e "s/WINDAVGB/$j/" -e "s/FLAPPOSN/plus2/" -e
          "s/QUEUE/$res/" -e "s/NSTEPS/6600/" -e "s/NAVG/102/" <$hpc.ea.rst.job
          >../cobaltGrids/$hpc.ea.grd.$i.plus2.beta.$j.job
        sed -e "s/JNUM/$i/" -e "s/BVALUE/$beta/" -e "s/WINDAVGB/$j/" -e "s/FLAPPOSN/minus2/" -e
          "s/QUEUE/$res/" -e "s/NSTEPS/6600/" -e "s/NAVG/102/" <$hpc.ea.rst.job
          >../cobaltGrids/$hpc.ea.grd.$i.minus2.beta.$j.job
    done

    beta=$(grep " 6 " betaWindAvg-n6.dat | cut -c 6-11)
    sed -e "s/JNUM/$i/" -e "s/BVALUE/$beta/" -e "s/WINDAVGB/6/" -e "s/FLAPPOSN/plus2/" -e
        "s/QUEUE/$res/" -e "s/NSTEPS/6400/" -e "s/NAVG/99/" <$hpc.ea.rst.job
        >../cobaltGrids/$hpc.ea.grd.$i.plus2.beta.6.job
    sed -e "s/JNUM/$i/" -e "s/BVALUE/$beta/" -e "s/WINDAVGB/6/" -e "s/FLAPPOSN/minus2/" -e
        "s/QUEUE/$res/" -e "s/NSTEPS/6400/" -e "s/NAVG/99/" <$hpc.ea.rst.job
        >../cobaltGrids/$hpc.ea.grd.$i.minus2.beta.6.job

    # cleanup
    cd ..
    rm -rf workdir.$i

  else
    echo "Overlap checker = $overlap_checker > 0. It goes. Neither grid nor jobfiles are created."
    mv parameterInputs/params.in.$i exile-nonviable-p3d-params/.
  fi

done

echo "Tar and gzip all .job files ..."
# zip batch of jobfiles for ftp to HPC
cd cobaltGrids
tar cf $hpc.ea.job.$imin.to.$imax.tar *.job
gzip $hpc.ea.job.$imin.to.$imax.tar
mv $hpc.ea.job.$imin.to.$imax.tar.gz ../.
cd ..

# put other grid and job files back
mv cobaltGrids/temp/*.job cobaltGrids/.
echo "Process complete!!"
################################
###             End of File              ###
################################
```

### A2.2.4 Post Processing of Output Files from the Cobalt Flow Solver

The following script extracts the time-averaged body-axis drag coefficient from the Cobalt output files then combines them with the weighted values and calls the wind-averaging code (Appendix A2.1.8) to complete the post processing.

```
#!/bin/bash
# Post processes Cobalt *.out files for 3D GTS optimization problem - rev02 h4 full grid
#  Maj Jacob Freeman, 23 April 2012
#  Variable flap, 5 variables (L1, theta1, theta2, dside, dtop)
#  Calculates modified wind-averaged value from body-axis drag coefficients
#    - Modification uses max of grd.minus2 and .plus2 in wind-averaging

echo "Please enter population size to be post-processed: "
read n_current

echo "Please enter total population count prior to these data: "
read n_cumulative

imin=$((1 + $n_cumulative))
imax=$(($n_cumulative + $n_current))

# establish file header, not to be repeated with subsequent generations
if [ "$imin" == "1" ]
  then
    echo "Cd Output Values from colinyEA, h4 full grid, variable flap" > Cd_results.3dGTSflaps.EA.SST.rawAll.dat
    echo "id  L1  theta1  theta2  dside  dtop  beta  Cd_body_minus2  Cd_body_plus2" >>
          Cd_results.3dGTSflaps.EA.SST.rawAll.dat
    echo "Wind-Averaged CD Values from colinyEA, h4 full grid, variable flap" >
          CdWindAvg_results.3dGTSflaps.EA.SST.dat
    echo "id  L1  theta1  theta2  dside  dtop  Cd_windAvg_minus2  Cd_windAvg_plus2" >>
          CdWindAvg_results.3dGTSflaps.EA.SST.dat
fi

# loop goes from generation start to (that number + population size)
for (( i = $imin ; i <= $imax ; i++ ))
  do
    mkdir postdir.$i
    cp gridstuff/betaWindAvg-n6.dat postdir.$i/.
    cp gridstuff/weightSAE.dat postdir.$i/.
    cp gridstuff/windAveraging.exe postdir.$i/.
    cp parameterInputs/params.in.$i postdir.$i/.
    cp exile-nonviable-p3d-params/params.in.$i postdir.$i/.
    cd postdir.$i

    L1=$(grep "L1" params.in.$i | cut -c 21-44)
    theta1=$(grep "theta1" params.in.$i | cut -c 40-44)
    theta2=$(grep "theta2" params.in.$i | cut -c 40-44)
    dside=$(grep "dside" params.in.$i | cut -c 40-44)
    dtop=$(grep "dtop" params.in.$i | cut -c 40-44)

    for (( j = 1 ; j <= 6 ; j++ ))
      do
        # read time-averaged drag coefficient
        #   -A 39 prints the 39 lines after 'ALL PATCHES' & writes to tempA. -A 5 prints the 5 lines after 'BODY-
            AXIS'
```

```
    #     from tempA & writes to tempB. Then we cut just the pertinent TOTAL CD value, which is body-axis CD
          for GTS+flaps.
    grep -A 39 'ALL PATCHES' ../outputResults/out/3dGTSflaps.ea.grd.$i.minus2.beta.$j.out > tempA.$j.dat
    grep -A 5 'BODY-AXIS' tempA.$j.dat > tempB.$j.dat
    Cdm2=$(grep 'TOTAL' tempB.$j.dat | cut -c 26-36)

    grep -A 39 'ALL PATCHES' ../outputResults/out/3dGTSflaps.ea.grd.$i.plus2.beta.$j.out > tempC.$j.dat
    grep -A 5 'BODY-AXIS' tempC.$j.dat > tempD.$j.dat
    Cdp2=$(grep 'TOTAL' tempD.$j.dat | cut -c 26-36)

    # read beta values and SAE weighting for wind-averaging
    beta=$(grep " $j " betaWindAvg-n6.dat | cut -c 6-11)
    weight=$(grep " $j " weightSAE.dat | cut -c 6-14)

    # write values to cumulative Cd_results raw file AND to temp file for input to fortran averaging .exe
    #   if run didn't complete or invalid design (no grd/job file), write large Cd value so it's out of consideration
    if [ "$Cdm2" == "" ]
      then
        echo "$i $L1 $theta1 $theta2 $dside $dtop $beta 9.999999 9.999999" >>
          ../Cd_results.3dGTSflaps.EA.SST.rawAll.dat
        echo "$j 9.999999 9.999999" >> Cd_timeAvg_temp.$i.dat
      else
        echo "$i $L1 $theta1 $theta2 $dside $dtop $beta $Cdm2 $Cdp2" >>
          ../Cd_results.3dGTSflaps.EA.SST.rawAll.dat
        echo "$j $Cdm2 $Cdp2" >> Cd_timeAvg_temp.$i.dat
    fi
  done

  # move time-averaged Cd values to generic format for input to fortran averaging .exe
  cp Cd_timeAvg_temp.$i.dat Cd_timeAvg_temp.dat

  # wind-averaging executable: selects max of plus2 or minus2, multiplies time-avg Cd with SAE weight, then
  #    averages those 6 values
  ./windAveraging.exe

  # convert generic output from fortran exe to file format used by DAKOTA
  cp cd_windAvg.dat ../outputResults/results.out.$i

  # write minus2 & plus2 wind-averaged CD values to file
  CdAvgm2=$(grep 'Cd_windAvg_minus2' cd_windAvg_m2_p2.dat | cut -c 1-12)
  CdAvgp2=$(grep 'Cd_windAvg_plus2' cd_windAvg_m2_p2.dat | cut -c 1-12)
  echo "$i $L1 $theta1 $theta2 $dside $dtop $CdAvgm2 $CdAvgp2" >>
          ../CdWindAvg_results.3dGTSflaps.EA.SST.dat

  # cleanup
  cd ..
  rm -rf postdir.$i
done
###########################################
####                End of File                #######
###########################################
```

# Appendix 3: Input Files for Data Fitting and Surrogate-Based Global Optimization

## A3.1 Generating and Searching the Surrogate Model

This DAKOTA file accomplishes three things. First, it starts by either reading in an existing data file with results (in our case, it reads in the combined results from computational simulations from the 2-D COLINY-EA and NCSU-DIRECT optimization studies, or solutions from 289 design points) or by specifying a sampling method that creates the design points and awaits the returned solution data. Second, we specify a data fitting method and the code creates a surrogate model from those data. Third, we specify a way of searching that surrogate model for the minimum value, either by using a global optimizer or by using a multidimensional parameter study to locate the minimum by discrete searching. We found the parameter study was the most accurate way to locate the minimum.

```
# DAKOTA INPUT FILE - surrogatePlusGlobalOpt.in
#  SBGO or parameter search to locate min, using combined EA & DIRECT initial data, single objective function
#  Maj Jacob A. Freeman, 15 December 2011

strategy,
   single
     tabular_graphics_file = 'filename.dat'
     method_pointer = 'SBGO'

variables,
   continuous_design = 6
     lower_bounds          0.25908          1.2504           0          0          -30          0
     upper_bounds          1.2192           1.2904           30         30         45           30
     descriptors           'L1'             'H1'             'theta1'   'theta2'   'theta3'     'delta'

##################################
###  Surrogate Search Specifications  ###
##################################
method,
   id_method = 'SBGO'
   model_pointer = 'surrogate_model'

   surrogate_based_global
#    approx_method_pointer = 'EA'                    ## each of these points to an SBGO method below
#    approx_method_pointer = 'PDS'
#    approx_method_pointer = 'COBYLA'
#    approx_method_pointer = 'SOLIS-WETS'
#    approx_method_pointer = 'PATTERN-SEARCH'
#    approx_method_pointer = 'ASYNCH-PATTERN-SEARCH'
#    approx_method_pointer = 'DIRECT'
#    approx_method_pointer = 'SOGA'
#    approx_method_pointer = 'EGO'
     max_iterations = 1
     replace_points
     output verbose

   multidim_parameter_study                        ## or we use a parameter study to search the surrogate
     partitions = 12  12  15  15  15  15           ## specifies how many subdivisions in each variable space
```

```
                                                ##   we can refine these more as we tighten the bounds
model,
   id_model = 'surrogate_model'
   responses_pointer = 'surrogate_response'
   surrogate global
##############################
###   Specify data fitting method   ###
##############################
#       polynomial quadratic                # linear, quadratic, cubic
       gaussian_process
          trend constant                    # constant, linear, reduced_quadratic, quadratic
          point_selection                   # use when points > 100 to help avoid ill-conditioning
#       kriging
#         trend constant                    # constant, linear, reduced_quadratic, quadratic
#         optimization_method = 'global'    # global, local, sampling, none
#       mars
#         max_bases 10
#         interpolation linear              # linear or cubic
#       neural_network
#         nodes 200
#       radial_basis
#       moving_least_squares
#         poly_order 3

################################################
###   Here is where we call the database for the data fit   ###
################################################
     reuse_samples all samples_file = './dataEA-DIRECT.full2d.windAvg.dat'
     dace_method_pointer = 'sampling'
     correction additive zeroth_order       # additive, multiplicative, or combined; zeroth_order, first_order, or
                                            #     second_order;  zeroth = match samples via scalar; 1st = match
                                            #     samples, gradient via linear function;  2nd = match samples,
                                            #     gradients, Hessians via quadratic function
     diagnostics = 'rsquared','cv'          # sum_squared, mean_squared, root_mean_squared, max_squared,
                                            #     sum_scaled, max_scaled, sum_abs, mean_abs, max_abs, press, cv,
                                            #     and rsquared
responses,
   id_responses = 'surrogate_response'
   response_descriptors = 'Cd_bodyAxis'
   num_objective_functions = 1
   no_gradients
   no_hessians

#################################
###  Sampling Method Specifications   ###
#################################
method,
   id_method = 'sampling'
   model_pointer = 'truth'
   dace
     lhs
       seed = 38
       samples = 0                          # set to zero to revert to datafile with previously sampled points
################################################
###  Global Search within Surrogate then Suggest Updates   ###
################################################
```

```
method,
  id_method = 'EA'
  model_pointer = 'truth'
  coliny_ea
    max_iterations = 10000                # number of generations
    max_function_evaluations = 20000
    seed = 38                             # initial seed, ensures common starting point & same result if all other
                                          #    input same
    population_size = 40                  # initial population only
    initialization_type unique_random     # random generation but successive gens reject candidate if duplicate
    fitness_type merit_function           # penalizes infeasible designs
    mutation_type offset_normal
    mutation_rate 1.0
    crossover_type uniform                # random combo of coordinates from parent1 and parent2
    crossover_rate 0.8                    # no. crossovers = crossover_rate * population size
    replacement_type chc = 1

method,
  id_method = 'PDS'
  model_pointer = 'truth'
  optpp_pds                               # OPT++ Parallel Direct Search, non-grad based
    search_scheme_size = 10000

method,
  id_method = 'COBYLA'
  model_pointer = 'truth'
  coliny_cobyla
    max_iterations = 10000
    max_function_evaluations = 20000
    seed = 38
    initial_delta = 1.0
    threshold_delta = 0.005

method,
  id_method = 'SOLIS-WETS'
  model_pointer = 'truth'
  coliny_solis_wets
    max_iterations = 10000
    max_function_evaluations = 20000
    seed = 38
    initial_delta = 1.0
    threshold_delta = 0.005

method,
  id_method = 'PATTERN-SEARCH'
  model_pointer = 'truth'
  coliny_pattern_search
    stochastic
    max_iterations = 10000
    max_function_evaluations = 20000
    seed = 38
    initial_delta = 1.0
    threshold_delta = 0.005
```

```
method,
   id_method = 'ASYNCH-PATTERN-SEARCH'
   model_pointer = 'truth'
   coliny_apps
     max_iterations = 200
     max_function_evaluations = 20000
     initial_delta = 1.0
     threshold_delta = 0.005

method,
   id_method = 'DIRECT'
   model_pointer = 'truth'
   ncsu_direct
     max_iterations = 10000
     max_function_evaluations = 20000
     solution_target = 0.12
     convergence_tolerance = 0.01
     min_boxsize_limit = 1.0e-3
     volume_boxsize_limit = 1.0e-6

method,
   id_method = 'SOGA'
   model_pointer = 'truth'
   soga
     max_iterations = 10000
     max_function_evaluations = 20000
     population_size = 40
     seed = 38
     initialization_type unique_random
     replacement_type favor_feasible
     fitness_type merit_function
     crossover_type multi_point_parameterized_binary 6
     mutation_type replace_uniform
       mutation_rate 0.1

method,
   id_method = 'EGO'
   model_pointer = 'truth'
   efficient_global
     seed = 38

model,
   id_model = 'truth'
   single
     interface_pointer = 'true_function'
     responses_pointer = 'true_response'
interface,
   id_interface = 'true_function'
   fork
     asynchronous
       evaluation_concurrency = 6
     analysis_driver = './full2Dopt.sh'
       parameters_file = 'params.in'
       results_file    = 'results.out'
       file_tag
       file_save
```

```
responses,
   id_responses = 'true_response'
   num_response_functions = 1
   response_descriptors = 'Cd_bodyAxis'
   no_gradients
   no_hessians
################################
###            End of File            ###
################################
```

## A3.2 Determine Sample Points for Secondary Surrogate

The surrogate model from A3.1 is now used as the truth model. The following file generates a group of sample design points, based on the various methods noted in Section 1.2.5, Sampling Methods. We then append these points to a file that queries the surrogate/truth model.

```
# DAKOTA INPUT FILE - sampling.in
#  Distributed Design & Analysis of Computer Experiments (DACE or DDACE)
#   - eliminates non-repeatability element of Design of Experiments since computational simulations are repeatable
#   - assumes uniform probability distributions
#   - runs only continuous design variables
#
# Use sampling method to generate design points for 6 design variables

strategy,
            single_method
              tabular_graphics_data
              tabular_graphics_file = 'psuade105-GPlinear.dat'
 method,
#    dace
#      lhs
#      oas
#      oa_lhs
#      box_behnken
#      central_composite
     psuade_moat           # samples = m*(NDV + 1); NDV = no. of design variables, m = integer (recommend ~10),
                           #     de-select "dace" & "samples"
       partitions = 5       # for psuade_moat, must be odd integer, equal division of bounds for design variables
       seed = 38
       samples = 105
#       symbols = 210

model,
            single
variables,
   continuous_design = 6
     lower_bounds            0.25908       0.25908       0             0            -30          0
     upper_bounds            1.2192        1.2904        30            30           45           30
     descriptors              'L1'          'H1'         'theta1'      'theta2'     'theta3'     'delta'
interface,
            fork
              asynchronous
                evaluation_concurrency = 10000
              analysis_driver = './full2Dopt.sh'
                parameters_file = 'params.in'
                results_file    = 'results.out'
```

```
            file_tag
            file_save
responses,
          num_objective_functions = 1
          response_descriptors = 'Cd_bodyAxis_windAvg'
          no_gradients
          no_hessians
################################
###            End of File            ###
################################
```

### A3.3 Sample the Initial Surrogate Model, Create and Update Secondary Surrogate

We write those data points to the following input file, which then queries the initial surrogate/truth model to create a secondary surrogate model. With the secondary surrogate, we then conduct a parameter study to locate the minimum. That point is appended to the file below, which creates an updated secondary surrogate. We automated this process using shell scripts and repeat until the design point converges, or the design variable values no longer change with each parameter search of the updated secondary surrogate.

```
# DAKOTA INPUT FILE - initialSurrogate.in
#  Generate database from surrogate model (Gaussian Process Linear, from CFD results from EA, DIRECT)
#  Maj Jacob A. Freeman, 13 February 2012
# NOTE: This runs only with Dakota v5.1, since v5.0 doesn't accept "samples = 0" --> gives an error message.

strategy,
   single
     tabular_graphics_data
     tabular_graphics_file = 'psuade105-GPlinear.dat'
     method_pointer = 'SBGO'
variables,
   continuous_design = 6
     lower_bounds          0.25908          0.25908          0          0          -30          0
     upper_bounds          1.2192           1.2904           30         30         45           30
     descriptors           'L1'             'H1'             'theta1'   'theta2'   'theta3'     'delta'

method,
   id_method = 'SBGO'
   model_pointer = 'surrogate_model'
  list_parameter_study
    list_of_points =                          ## this list actually needs to be at end of file, so easier to append
 4.51104e-01     6.71608e-01     6.00000e+00     6.00000e+00     4.50000e+01     6.00000e+00
 4.51104e-01     6.71608e-01     6.00000e+00     6.00000e+00     0.00000e+00     6.00000e+00
 4.51104e-01     6.71608e-01     2.40000e+01     6.00000e+00     0.00000e+00     6.00000e+00
 4.51104e-01     6.71608e-01     2.40000e+01     2.40000e+01     0.00000e+00     6.00000e+00
 4.51104e-01     1.2904e+00      2.40000e+01     2.40000e+01     0.00000e+00     6.00000e+00
      …                  …               …
      …

model,
   id_model = 'surrogate_model'
   responses_pointer = 'surrogate_response'
   surrogate global

#     Don't use point_selection when relatively few data points and 6 DVs.
```

```
      gaussian_process
        trend constant     # linear or constant or reduced_quadratic
#       point_selection

      reuse_samples all samples_file = './dataEA-DIRECT.full2d.windAvg.dat'
      dace_method_pointer = 'sampling'
#     correction additive zeroth_order
      correction combined second_order
      diagnostics = 'rsquared'

responses,
    id_responses = 'surrogate_response'
    response_descriptors = 'Cd_bodyAxis_windAvg'
    num_objective_functions = 1
    no_gradients
    no_hessians

method,
    id_method = 'sampling'
    model_pointer = 'truth'
    dace
      lhs
        seed = 38
        samples = 0

model,
    id_model = 'truth'
    single
      interface_pointer = 'true_function'
      responses_pointer = 'true_response'

interface,
    id_interface = 'true_function'
    fork
      asynchronous
        evaluation_concurrency = 6
      analysis_driver = './full2Dopt.sh'
        parameters_file = 'params.in'
        results_file    = 'results.out'
        file_tag
        file_save

responses,
    id_responses = 'true_response'
    num_response_functions = 1
    response_descriptors = 'Cd_bodyAxis_windAvg'
    no_gradients
    no_hessians
################################
###              End of File              ###
################################
```

# Appendix 4: Uncertainty Quantification for 3-D Design EA.90

The following is based on notes from Dr. Chris Roy, 27 July 2012.

$$GCI = \frac{F_s}{r^p - 1}|f_2 - f_1| \tag{A4.1}$$

GCI is Roache's grid convergence index, or an interval applied to the Richardson extrapolated discretization error; $f_1$ is the solution value on the medium grid; $f_2$ is the solution value on the coarse grid; $f_0$, used below, is the solution value on the fine grid; $F_s$ is factor of safety; $r$ is grid refinement factor; and $p$ is order of accuracy. Equation (A4.1) results in uncertainty to be placed about the medium grid solution, where the interval = $f_1 \pm$ GCI.

For the design EA.90, $\beta$ = 0°, $f_1$ = 0.12633 and $f_2$ = 0.19439, which results in 54% error relative to $f_1$. We substitute into Eq. (A4.1) to obtain

$$GCI = \frac{3}{2^2 - 1}|0.19439 - 0.12633| = |0.06806| \tag{A4.2}$$

This provides an interval on $f_1$: 0.12633 ± 0.06806, or $f_{min}$ = 0.05827 and $f_{max}$ = 0.19439.

The Richardson extrapolated value, $\bar{f}$, for the fine solution is

$$\bar{f}_{1,2} = f_1 + \frac{f_1 - f_2}{r^p - 1} = 0.12633 + \frac{-0.06806}{3} = 0.10364 \tag{A4.3}$$

This is shown graphically in Fig. A4.1. For $F_s$ = 3, we estimate numerical uncertainty as $f_1 \pm$ GCI or $f_2 \,{}^{+0}_{-2\ \mathrm{GCI}}$ or $f_2 \,{}^{+0\%}_{-70\%}$.

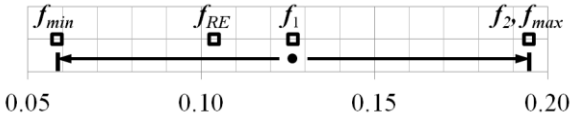


**Figure A4.1**. Graphical depiction of uncertainty interval on medium solution, with Richardson extrapolated fine solution value indicated

For the GTS baseline configuration with no flaps, symmetric grid, $\beta$ = 0°, we obtain $f_0$ = 0.23222, $f_1$ = 0.24090, and $f_2$ = 0.29582, which results in 3.7% error relative to $f_0$ and 22.8% error relative to $f_1$. From Eq. (A4.3), we obtain $\bar{f}_{0,1}$= 0.2293 and $\bar{f}_{1,2}$= 0.2226.

In conclusion, we need a fine grid solution for the EA.90 design to reduce numerical uncertainty. The actual drag coefficient for EA.90 at zero sideslip is probably closer to $\bar{f}_{1,2}$= 0.10364 than to $f_2$ = 0.19439, and the actual no-flaps baseline drag coefficient is close to $\bar{f}_{0,1}$= 0.2293; thus, there is a 55% reduction in drag compared between EA.90 and the no-flaps baseline. We could, therefore, use $F_s$ = 1.5 or 2 since the no-flaps baseline case (with solutions for three grid levels) is close to asymptotic, where $\hat{p} = 2.66$.